Effect of hybridization in CoDico-FRTPs: Orientation-dependent characterization and analytical modeling in various climatic conditions

Zur Erlangung des akademischen Grades eines

DOKTORS DER INGENIEURWISSENSCHAFTEN
(Dr.-Ing.)

von der KIT-Fakultät für
Maschinenbau des
Karlsruher Instituts für Technologie (KIT)

angenommene

DISSERTATION

von

M.Sc. Benedikt Marian Scheuring

geb. in Freiburg im Breisgau

Tag der mündlichen Prüfung: 30.08.2024
Hauptreferent: Prof. Dr.-Ing. Kay A. Weidenmann
Korreferenten: John Montesano, Ph.D., P.Eng
    Prof. Dr.-Ing. Frank Hennig

"Das Leben besteht nur aus Momenten aber mir kommt es auf jeden an. Denn die Momente dauern immerhin dein ganzes Leben lang."

-**Kurt Tallert**

Kurzfassung

Aufgrund der geringen Taktzeit bei der Prozessierung und der Fähigkeit, auch komplexe Geometrien inklusive Verrippung abzubilden, weisen langfaserverstärkte Thermoplaste (LFTs) ein signifikantes Leichtbaupotenzial für die Großserienproduktion in der Automobilindustrie auf. In Anbetracht der steigenden Nachfrage nach einer weiteren Gewichtsreduzierung von Fahrzeugen wurde in den vergangenen Jahren eine Optimierung der mechanischen Eigenschaften von LFT vorgenommen, um den Verbundwerkstoff für strukturelle Anwendungen zu qualifizieren. Daher wurden vermehrt Kohlenstofffasern eingesetzt, die eine hohe Festigkeit und Steifigkeit aufweisen. Im Rahmen dieser Forschungsarbeit werden insbesondere direkt inline compoundierte LFTs (LFT-D-ILC) mit anschließendem Fließpressen untersucht, da bei diesen eine relativ hohe Faserlänge erreicht werden kann, wodurch die Eigenschaften der Fasern besser zur Geltung kommen. Allerdings ist auch bei diesen LFTs durch die thermoplastische Matrix eine hohe Sensitivität der mechanischen Eigenschaften gegenüber erhöhter Temperatur und absorbiertem Wasser zu beobachten. Ein vielversprechender Ansatz, um dieses Problem zu adressieren und zusätzlich die mechanischen Eigenschaften weiter zu optimieren, ist Gegenstand des Graduiertenkollegs GRK 2078. Im Rahmen dessen wird die Kombination von diskontinuierlichen kohlenstofffaserbasierten LFT-Werkstoffen mit endlos kohlenstofffaserverstärkten Tapes untersucht. Die Herstellung festerer, steiferer und gegen Umwelteinflüsse robusterer Bauteile ist durch hybride Verbundwerkstoffe möglich, ohne dass die Vorteile von LFTs, wie die kurze Taktzeit und die hohe geometrische Designfreiheit, verloren gehen. In dieser Arbeit

werden zunächst die Prozess-Struktur-Eigenschaftsbeziehungen von LFT-D-ILC anhand von Fließgepressten Platten mit PA6 als Matrixmaterial und verschiedenen Verstärkungsfasern (CF, GF und eine Mischung aus CF und GF zu gleichen Teilen) und eines Hybriden Verbundwerkstoff aus CF-LFT verstärt mit undirektionalen Tapes unter zwei Belastungsarten (Zug und Biegung) untersucht. Im Weiteren wird durch DMA versuche im trockenen und feucht konditionierten zustand der Einfluss von Temperatur und absorbierten Wasser in 0 und 90° orientierung untersucht. Um ein tiefgreifendes Verständnis zu erlangen, wurden die verschiedenen LFT-Materialien mithilfe etablierter Homogenisierungsmethoden modelliert. Zudem wurde der temperaturabhängige Steifigkeitsverlauf von CF-LFT und dem Hybriden mit diesen Modellen abgebildet. Da beim Fließpressen durch die Fließbewegung der Faser-Matrix-Masse eine Orientierung der Fasern stattfindet, wurden alle Versuche mit Proben durchgeführt, die in unterschiedlicher Orientierung aus den Platten präpariert wurden. Bei allen drei LFT Materialien konnte eine starke Ausrichtung der Fasern in Fließrichtung festgestellt werden. Allerdings wich diese leicht von der erwarteten Fließrichtung ab, was auch auf Inhomogenitäten im LFT-Rohling vor dem Pressen zurückgeführt werden konnte. Im Rahmen einer Untersuchung mittels DIC- und Bruchflächenanalysen unter dem REM konnten bei mit CF verstärktem LFT Faserbündel, die während des Dispergierprozesses nicht vollständig aufgelöst wurden, als Schadensursachen für kritisches Versagen identifiziert werden. Diese Faserbündel führten zu einer deutlichen Überschätzung der Steifigkeit mit der angewandten Homogenisierungsmethode. Die Richtungsabhängigkeit der Materialkennwerte konnte auch unter dem Einfluss von Temperatur und Feuchte nachgewiesen werden. Es konnte gezeigt werden, dass die Temperaturempfindlichkeit durch Fasern reduziert werden kann, wobei der Grad der Faserorientierung in Belastungsrichtung, der Faservolumengehalt und die Faserlänge eine entscheidende Rolle spielen. Absorbiertes Wasser führte zu einer Absenkung der Glasübergangstemperatur im PA6, die auch in den Verbundwerkstoffen sichtbar wurde. Eine Versteifung der Matrix durch Wasser bei niedrigen Temperaturen hatte keinen Einfluss auf die Verbundwerkstoffe. Es konnte gezeigt werden, dass sich die mechanischen Eigenschaften von LFTs,

insbesondere die Steifigkeit, durch die Hybridisierung mit CoDico richtungsab-
hängig deutlich verbessern lassen. Zudem wird die Empfindlichkeit gegenüber
Temperatur und Feuchtigkeit reduziert. Die Hybridisierung mit CoDico er-
weitert somit das Anwendungsspektrum von LFT-Materialien in verschiedenen
realen Szenarien, ohne die Vorteile von LFTs einzuschränken.

Abstract

Due to the low cycle time during processing and the ability to create complex geometries including ribbing, long-fiber-reinforced thermoplastics (LFTs) have significant lightweight construction potential for large-scale production in the automotive industry. Against the backdrop of increasing demand for further weight reduction in vehicles, the mechanical properties of LFTs have been optimized in recent years in order to qualify the composite material for structural applications. As a result, carbon fibers with high strength and stiffness have been increasingly used. Directly inline compounded LFTs (LFT-D-ILC) with subsequent extrusion are particularly in focus here, as relatively long fiber lengths can be achieved here and the properties of the fibers can therefore be better exploited. However, the mechanical properties of these LFTs are also highly sensitive to increased temperature and absorbed water due to the thermoplastic matrix. A promising approach to address this problem and to further optimize the mechanical properties is the subject of the German-Canadian Research Training Group GRK 2078, which is investigating the combination of discontinuous carbon fiber-based LFT materials with continuous carbon fiber-reinforced tapes. The production of stronger, stiffer and more robust components against environmental influences is possible with hybrid composite materials without losing the advantages of LFTs, such as the short cycle time and the high geometric design freedom.

In this work, the process-structure-property relationships of LFT-D-ILC are first investigated using compression moulded sheets with PA6 as matrix material and different reinforcing fibers (CF, GF and a mixture of CF and GF in equal parts) and a hybrid composite material made of CF-LFT reinforced with undirectional carbon fiber-reinforced tapes under two types of loading (tension and bending).

Furthermore, the influence of temperature and absorbed water in 0 and 90° orientation is investigated by DMA tests in dry and wet condition. In order to gain an in-depth understanding, the various LFT materials were modelled using established homogenization methods. In addition, the temperature-dependent stiffness curve of CF-LFT and the hybrid was mapped using these models. Since the flow movement of the fiber-matrix mass during impact extrusion results in an orientation of the fibers, all tests were carried out with samples that were prepared from the plates in different orientations.

For all three LFT materials, a strong orientation of the fibers in the direction of flow was observed. However, this deviated slightly from the expected flow direction, which could also be attributed to inhomogeneities in the LFT initial charge before compression molding. As part of an investigation using DIC and fracture surface analyses under the SEM, fiber bundles that were not completely dissolved during the dispersion process were identified as the cause of critical failure in LFT reinforced with CF. These fibre bundles led to a significant overestimation of the stiffness with the homogenization method used. The directional dependence of the material properties could also be demonstrated under the influence of temperature and moisture. It could be shown that the temperature sensitivity can be reduced by fibers, whereby the degree of fiber orientation in the direction of loading, the fiber volume content and the fiber length play a decisive role. Absorbed water led to a reduction in the glass transition temperature in PA6, which was also visible in the composites. Stiffening of the matrix by water at low temperatures had no effect on the composites. It has been demonstrated that the mechanical properties, particularly stiffness, can be significantly enhanced in a direction-dependent manner through the hybridization to CoDico. This process also reduces sensitivity to temperature and moisture. Consequently, hybridization to CoDico expands the potential applications of LFT materials in various real-world scenarios, without limiting the advantages of LFTs.

Acknowledgement

First of all, I would like to sincerely thank my main supervisor, Prof. Kay André Weidenmann. His genuine interest, unwavering motivation, support and kindness were instrumental throughout my time as doctoral researcher. His prompt responses to emails and requests, along with his insightful discussions and dedication to problem-solving, provided immense guidance. Beyond his scientific mentorship, his approachable, honest, and enthusiastic demeanor made every conversation with him not only professionally rewarding but also personally enriching. I would also like to thank my co-supervisor Prof. Peter Elsner, who unfortunately passed away during my time as doctoral researcher. He was already the supervisor of my master's thesis and I was able to benefit greatly from the discussions in which he, through his enormous wealth of experience and his very caring and attentive manner, provided many suggestions that can be found in the final version of my work. At this point, I would also like to thank Prof. Frank Henning, who seamlessly assumed the role of Prof. Peter Elsner, ensuring that the defense and related matters proceeded smoothly. I would also like to express my special thanks to Prof. John Montesano, my Canadian supervisor, who has been very supportive throughout my doctoral studies and has enabled me to have two very enriching research stays in Canada. He was always a very helpful discussion partner who, through a mixture of trust and paise, coupled with high demands, always encouraged me to improve. He was also a great personal support to me beyond the professional supervision. My thanks also go to Prof. Thomas Böhlke, who, as spokesperson for the IRTG, ensured the smooth operation of the program and took over the leadership of the doctoral committee.

I would also like to thank my group leader, Dr. Wilfried Liebig. His interest in all scientific and personal topics, as well as his honest nature, were crucial to a warm group dynamic in which working was always fun. Also, the opportunity to take unconventional paths and, as soon as you were convinced of them, to have his unconditional support by your side was very enriching. I also always found it very a great opportunity to be able to launch so-called "U-Boot" projects, even if no submarine comes out of them. I would also like to thank the technicians at IAM-WK, in particular Ralf Rössler, Sebastian Hohne and Marc Brecht, who, with their many years of experience, made many unusual ideas possible in the first place and solved many a problem faster than expected. I am also very grateful for the support of the IAM-WK workshop, which has always reliably produced new test setups of excellent quality. I want to thank my office colleague Juliane Blarr for her friendship, patience, and composure. Together, we shared many fun and challenging moments that I will always treasure and never forget. A special thanks also goes to Nicolas Christ, who completes the characterization team of the IRTG's third generation. I was privileged to work with both of them in a consistently friendly and supportive manner, which made working at the IRTG so special. We shared wonderful moments together, especially during our time in Canada. Additionally, I'd like to thank all my colleagues for everything, especially those from HWL. You've made the good times even better and helped me through the tough times. Special thanks go to my students Jonas Wilhelm, Lennard Bechtloff, Maxim Meierhans, Jonas Hangel, Leo Hoffman, Saruka Muralitharan und Viola Wolf who have supported me greatly either by writing their theses and/or as student research assistants.

I would especially like to thank my circle of friends in Karlsruhe, with whom I fought my way through my mechanical engineering studies and without whom I probably would not have come so far and would not be the person I am today. The time with you was and is great and has made my time in Karlsruhe something special that I will not forget. Many thanks to my circle of friends in Freiburg, who form a strong foundation for my self-confidence and always provide a place of grounding. It's a space where we can look back on wonderful past times and look forward to new, exciting things to come. For over 20 years,

I've been able to count on you – no problem is too big to be resolved. No matter which paths we take in life, being there for one another is a certainty, and this sense of security feels truly good.

Finally, I would like to express my heartfelt gratitude to my family for their love and unwavering support. I will always be deeply thankful to my parents for their tireless encouragement, wise advice, and constant reassurance, as well as for teaching me to approach even significant challenges with a sense of ease. They have been the cornerstone of my success. I am also profoundly grateful to my siblings, Manuel and Annika, whose steadfast love and trust have given me a true sense of home and shaped me into the person I am today. Thank you, Lorena, for your endless support and unwavering love. You have always been by my side, especially in the most difficult moments, and I am deeply grateful to you for that. Your understanding and support were a wonderful help, especially when I was so absorbed in my work. You were always there for me, gently reminding me to prioritize my happiness and well-being, which means a lot to me. Knowing that I can always count on you gives me a special sense of security. I really appreciate that and I love you

Karlsruhe, September 2024 *Benedikt Scheuring*

Contents

Acronyms and symbols

Acronyms

CF	Carbon fiber
CF$_{\mathbf{LFT}}$	LFT reinforced with CF
CF + GF$_{\mathbf{LFT}}$	LFT reinforced with CF+GF
CLT	Classic Laminate Theory
Co	Continuous
CoDico	Continuous-discontinuous
DIC	Digital image correlation
Dico	Discontinuous
FLD	Fiber length distribution
FMC	Fiber mass content
FOD	Fiber orientation distribution
FOT	Fiber orientation tensor
FRP	Fiber-reinforced plastics
FVC	Fiber volume content
GF	Glass fiber

$\mathbf{GF_{LFT}}$	LFT reinforced with GF
$\mathbf{G-LFT}$	Granulated long fiber-reinforced thermoplastics
ILC	Inline compound
iRoM	Inverse rule of mixture
LFT	Long fiber-reinforced thermoplastics
$\mathbf{LFT-D}$	Long fiber-reinforced thermoplastics direct compounding process
PA6	Polyamide 6
RoM	Rule of Mixture
iRoM	inverse Rule of Mixture
ILC	Inline compounding
SFT	Short fiber-reinforced thermoplastics
TGA	Thermogravimetric analysis
TSE	Twin-screw extruders
TTS	Time temperature superposition
UD	Unidirectional
vol.%	Volume percent
wt.%	Weight percent
CT	Micro-computed tomography

Constants

π	Pi: $3{,}14159\ldots$

Latin symbols and variables

A Area

a Aspect ratio

a_{crit} Critical aspect ratio

b Width

D Distance of the fibers

E Modulus of elasticity

E' Storage modulus

E'' Loss modulus

f frequency

G Shear modulus

h Thickness

L Length

L_{crit} Critical fiber length

L_{sat} Saturation fiber length

L_{g} Gauge length

L_{n} Number-averaged length

L_{p} Weight-averaged length

M Mass

M_{e} Molecular weigh

M_{w} Saturation mass

r	Radius
T	Temperature
T_{g}	Glass transition temperature
T_α	Alpha transition temperature
T_β	Beta transition temperature
T_γ	Gamma transition temperature
T_{m}	Melting temperature
$\tan\delta$	Loss factor
V	Volume
v	Volume fraction
w	Weight fraction

Greek symbols and variables

ε	Strain
ε_b	Failure strain
ε_l	Longitudinal strain
ε_t	Transverse strain
ν	Poissons's ratio
ρ	Density
σ	Stress
σ_f	Tensile strength of fiber
σ_b	Tensile strength

xviii

τ	Shear stress
τ_y	Interfacial shear strength

Operators and math symbols

Δ	Difference

General deep indexes

11	Longitudinal
22	Transversal
33	Out of plane
c	Composite
f	Fiber
m	Matrix

1 Introduction and motivation

One of the most significant challenges of the 21st century is the mitigation of global warming. The transportation sector, including cars, trains, and aviation, is a significant contributor to greenhouse gas emissions, which are a primary driver of global warming. Despite the European Union's multi-sector efforts to cut greenhouse gas emissions over the past 30 years, carbon dioxide emissions from the transportation sector have steadily increased, comprising 23% of the European Union's total emissions in 2021, with passenger cars contributing over the half [1]. Consequently, reducing the fuel consumption of automobiles has become imperative to curb emissions, especially CO_2. This urgency has led to the implementation of stricter regulations on CO_2 emissions from automobiles in recent years. One solution to address this regulations are lightweight materials and design, which ideally has a positive, self-reinforcing effect. For example, mass reduction leads to a reduction in the inertia and operating loads of structures and machine parts, which in turn reduces the need for support structures, allowing further mass reduction. This mass reduction in turn leads to a reduction in primary energy consumption in all mass-related processes of the automobile, which for a weight reduction of 100 kg saves about $0.3\,l$ to $0.4\,l$ of gasoline and thus $0.85\,kg$ to $1.4\,kg$ of CO_2 per $100\,km$ [2, 3]. Composites offer promising lightweight construction solutions due to their exceptional weight-specific material properties and adaptability to specific applications. Fiber-reinforced polymers (FRPs), combining strong and stiff reinforcing fibers with a lightweight polymer matrix, are particularly important. Both thermoplastic and thermoset polymer matrices can be reinforced with discontinuous or continuous fibers [4, 5]. With the introduction of the EU's Circular Economy Package, which aims to move from a linear to a circular

economy in order to recycle waste and thus conserve resources and protect the climate, lightweight materials face further challenges. Until now, it has been difficult to break FRPs based on a thermoset matrix system down into their original raw materials after use, making recycling concepts almost impossible to implement. Consequently, there is a growing preference for composite materials with a thermoplastic matrix. While these materials may not be fully recyclable in a one-to-one manner, they offer the potential to be re-melted and further processed with the acceptance of fiber shortening, thereby contributing to the advancement of sustainability. The most widely used thermoplastic composites are based on glass fiber reinforcements, as these are sometimes even cheaper than the polymer matrix and can therefore be used very economically. Long glass fiber-reinforced thermoplastics (LFTs) are well-suited for automotive applications due to their advantages such as formability, impact resistance, rapid manufacturing, and recyclability. Glass fiber-reinforced PP and PA are already established in the automotive sector for various applications such as front ends, dashboard supports, door modules, and underbody structures. [6, 7, 8] Moreover, the more rigorous regulations regarding emissions have permitted greater financial flexibility, which has led to an increase in demand for FRPs based on a thermoplastic matrix with stiffer and stronger carbon fibers as reinforcement in recent years [9, 10]. Furthermore, the combination of injection/compression molding processes with structural inserts of pre-impregnated continuous unidirectional fibers to so called CoDico-FRPs represents a pioneering solution for applications that require superior strength and stiffness [11]. This work is an experimental investigation of CoDico-FRPs based on an LFT basis. Thermoplastics, which lack cross-linked main chains, exhibit a significant reduction in mechanical properties when subjected to temperature and environmental factors such as moisture. Consequently, these materials are subjected to testing under such conditions. To predict their stiffness behavior, established homogenization methods are employed to model the temperature and direction-dependent stiffness characteristics. The insights gleaned from this investigation should facilitate a more comprehensive comprehension of CoDico-FRPs, thereby clearing the path for the development of more structural applications that can effectively reduce primary energy consumption in a cost-effective manner [12].

2 State of the art

2.1 Mechanics of fiber-reinforced polymers

This thesis is dedicated to exploring fiber-reinforced polymers (FRP), with a specific emphasis on those utilizing a thermoplastic matrix, referred to as FRTP. As a result, this chapter is exclusively focused on discussions surrounding FRTP. Specialized topics, like the impacts of absorbed water, are confined to polyamides, the primary matrix system in this study.

2.1.1 Basic aspects of FRP

The fundamental concept of FRPs is the integration of the respective benefits of fibers and plastics (referred to as the matrix) to create a material with the desired characteristics for a specific application. Since the individual components cannot be discerned on a macroscopic scale, FRPs are macroscopically homogeneous multiphase materials which belong to the category of composite materials [13, 14, 4].

In a composite, the fiber and the matrix fulfill distinct functions. The matrix provides the external shape of the component, the geometric position of the fibers, the load transfer within and between the fibers, and protects the fibers from external influences. Conversely, the fibers, when certain conditions are met, increase the strength and stiffness of the material. [13, 15, 16].

In general, there are a number of criteria regarding the ratio of specific material properties of the fiber to the matrix that, according to Puck, must be met in order to achieve a reinforcing effect of the fibers in the composite [17, 18]:

- Reinforcement fibers have a higher strength than the matrix: $\sigma_{\mathrm{fb}} > \sigma_{\mathrm{mb}}$
- Reinforcement fibers should have higher stiffness than the matrix: $E_{\mathrm{f}} > E_{\mathrm{m}}$
- The matrix should not break before the fibers, requiring a higher elongation at break: $\varepsilon_{\mathrm{mb}} > \varepsilon_{\mathrm{fb}}$

The extent of the reinforcement is contingent upon the fiber content, fiber length distribution, and fiber orientation. However, these factors collectively result in a heterogeneous microstructure, which subsequently gives rise to anisotropic material behavior in FRPs [13, 19, 20].

FRPs are divided into two categories based on their fiber structure: continuously reinforced FRPs (Co-FRPs) and discontinuously reinforced FRPs (Dico-FRPs). Co-FRPs are defined by the fact that they consist of continuous fibers whose length spans the entire dimension of the component. By aligning the fibers along the loading direction, parts with high stiffness and strength can be produced. Consequently, the continuous fibers significantly constrain design freedom, rendering the manufacture of complex geometries such as ribs challenging and costly [21, 22, 5].

In contrast, DiCo-FRP comprises fibres of finite length. This renders the manufacture of DiCo-FRP components considerably more straightforward, as the finite length of the fibres confers upon the material an extended flow capability in comparison to Co-FRP. This results in enhanced formability and the ability to conform to curved surfaces, thus enabling the production of even complex geometries such as ribs. However, this is accompanied by a notable reduction in specific mechanical properties in comparison to Co-FRP [23, 24, 5]. Figure 2.1 shows a schematic comparison of the different properties of Co-FRP and Dico-FRP in terms of both mechanical properties and processability.
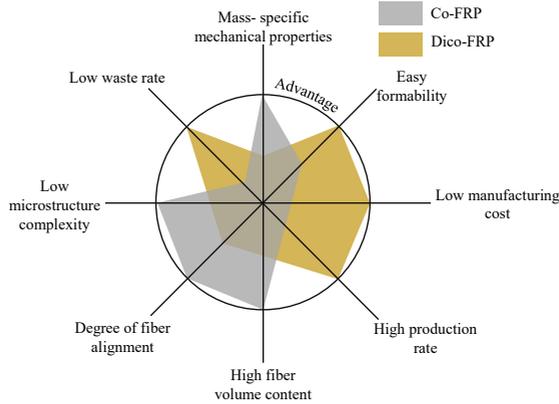
Figure 2.1: Schematic comparison of the advantages and disadvantages of Co- and Dico-FRP in accordance to [5].

2.1.2 Continuously fiber-reinforced polymers (Co-FRP)

A schematic representation of a Co-FRP is illustrated in Figure 2.2. Since the fibers are oriented in a single direction, this case is designated as a unidirectional (UD) Co-FRP. This serves as a useful illustration of the mechanics involved in Co-FRPs. In the case of UD-oriented fibers, the fiber volume fraction v_f of the composite can be determined using Equation (2.1) by calculating the area fractions of fiber A_f and matrix A_m and the sum of both A_c, as the depth is reduced from the equation.

$$v_f = \frac{V_f}{V_m + V_f} = \frac{A_f L}{(A_m + A_f) \cdot L} = \frac{A_f}{A_m + A_f} = \frac{A_f}{A_c}. \tag{2.1}$$

The fiber weight fraction w_f is a more frequently utilized metric to describe the fiber content of an FRP, given that it is often set in production technology and can also be determined experimentally. The correlation with v_f is provided in

5
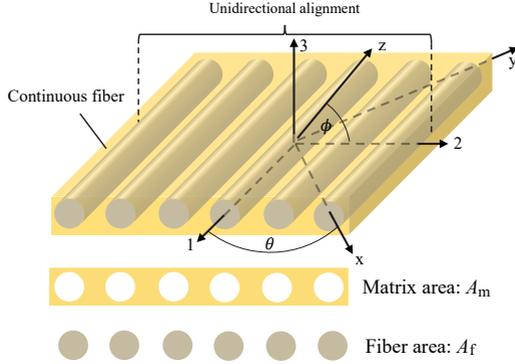
Figure 2.2: Schematic representation of a unidirectional continuous fiber-reinforced laminat, with definition of the longitudinal (1), transversal (2) and out of plane (3) direction and the rotation angle θ and ϕ in accordance to [25].

Equation 2.2 based on the density of the matrix ρ_m, the density of the fiber ρ_f and the assumption of non-porosity.

$$w_\mathrm{f} = \frac{M_\mathrm{f}}{M_\mathrm{c}} = \frac{M_\mathrm{f}}{M_\mathrm{m} + M_\mathrm{f}} = \frac{\rho_\mathrm{f} V_\mathrm{f}}{(\rho_\mathrm{m} V_\mathrm{m} + \rho_\mathrm{f} V_\mathrm{f})} = \frac{\rho_\mathrm{f} V_\mathrm{f}}{\rho_\mathrm{c} V_\mathrm{c}} = \frac{\rho_\mathrm{f}}{\rho_\mathrm{c}} \cdot v_\mathrm{f} \qquad (2.2)$$

In order to facilitate further discussion of the mechanical properties of such composites, it is necessary to define three orientations. The longitudinal direction, which is aligned with the fibers, is designated as 1, the orthogonal direction, which is perpendicular to the longitudinal direction, is designated as 2, and the out-of-plane direction, which is orthogonal to both 1 and 2, is designated as 3. For reference, please refer to Figure 2.2.

If the UD-Co-FRP from Figure 2.2 is now loaded in direction 1, it causes the fibers and the matrix to deform equally, assuming that both components exhibit elastic behavior and a perfect bond [26, 27]. The well-known Rule of Mixture (RoM) can be used to estimate the stiffness E_{11}:

$$E_{11} = E_\mathrm{m} \cdot (1 - v_\mathrm{f}) + E_\mathrm{f} v_\mathrm{f}, \qquad (2.3)$$

whereas E_m describes the stiffness of the matrix and E_f the stiffness of the fiber [28, 4, 25, 29]. Upon rotation of the fiber orientation by the angle θ, a notable change in stiffness is observed. To illustrate this phenomenon, the stiffness curves over the angle θ for varying fiber volume contents (v_f) are presented in Figure 2.3. This course can be described by the Halpin-Tsai method, which is
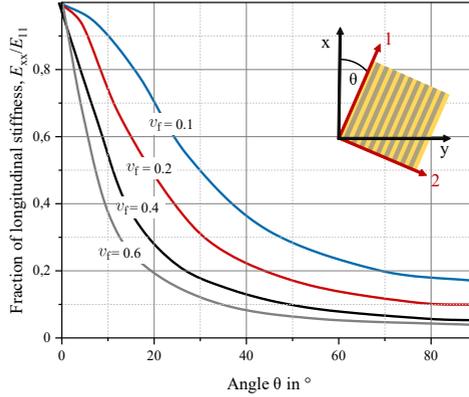
Figure 2.3: Schematic curve of the elasticity modulus over the angle of a unidirectional laminate for different fiber volume contents based on / in accordance to [25].

discussed in more detail in Section 2.1.4.

For the properties in transverse, 2 direction or for $\theta = 90°$, UD-Co-FRP can be described by equal stresses in both components, fibers and matrix. With Equation 2.5 it is now possible to determine the stiffness E_{22}, which represents the Reuss bound and is also called inverse RoM (iRoM) [4, 28, 30]:

$$\frac{1}{E_{22}} = \frac{v_f}{E_f} + \frac{1 - v_f}{E_m}. \tag{2.4}$$

From which follows:

$$E_{22} = \frac{E_f \cdot E_m}{v_f E_m + (1 - v_f) E_f}. \tag{2.5}$$

7

Given that such UD laminates exhibit a pronounced directional dependence, they are frequently stacked on top of one another in varying orientations forming a so-called laminate. The most prevalent layups are [0°/90°] and [±45°]. To ascertain the effective mechanical properties of such lay-ups, the classical laminate theory can be employed, which will be discussed in more detail in Section 2.1.4.3.

2.1.3 Discontinuously fiber-reinforced polymers (Dico-FRP)

2.1.3.1 Load transfer into the fiber

Figure 2.4 (a) depicts a schematic representation of a fiber with a finite length embedded in a cylindrical thermoplastic matrix element (referred to as the single-fiber model) in the unloaded state. When this element is loaded, the matrix transfers the load to the fiber by shear. The shear deformation is strongest at the fiber tips, i.e. the ends of the fiber (cf. Fig. 2.4 (b)). Since the shear is intended to transfer the entire load to the fiber, the goal is for the shear to reach zero before the center of the fiber is reached. For this, the fiber must have a certain length L_{crit}. Figure 2.4 (c) therefore shows the progression of shear stress and stress in the fiber along its length. The stress is continuously introduced into the fiber by the shear until the stress is applied in the fiber and the shear is zero [31, 32, 33, 22, 25].

To determine L_{crit} for a fiber matrix combination, Equation (2.8) according to Kelly and Tyson [34], which was originally developed for a copper-tungsten fiber composite, can be used. Thereby σ_f is the tensile strength of the fiber, r_f is the fiber radius, and τ_y is the interfacial shear strength between matrix and fiber [34].

$$L_{\mathrm{crit}} = \frac{\sigma_{\mathrm{f}} \cdot r_{\mathrm{f}}}{\tau_{\mathrm{y}}}. \tag{2.6}$$

Since both σ_f and τ_y are material constants, L_{crit} for a given fiber matrix combination depends directly on the fiber radius. Thus, the aspect ratio a,

(a)
Stress-free fiber in polymermatrix

(b)
Stressed fiber in polymermatrix

(c)
Load transfer from matrix (thermoplastic) to fiber in a composite
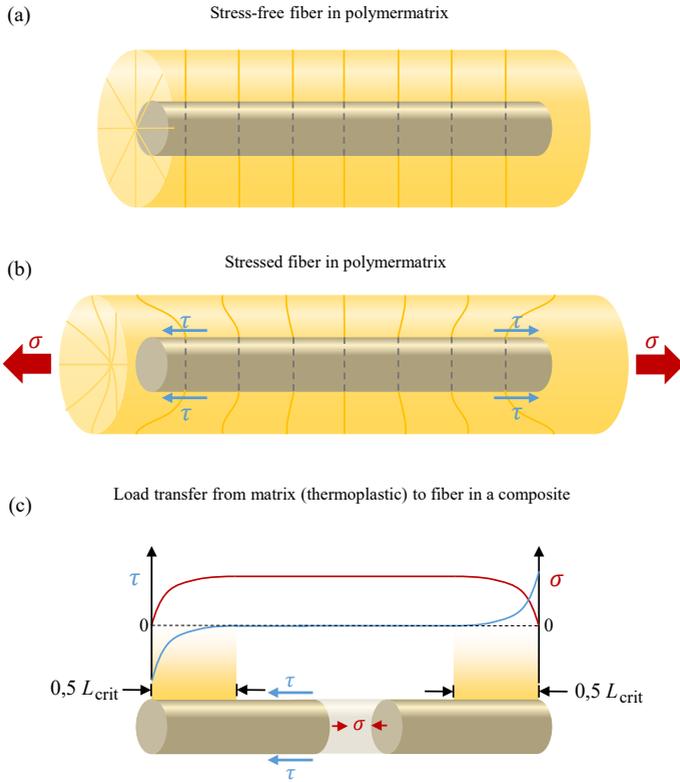
Figure 2.4: Schematic representation of a single fiber, with finite length, embedded in a cylindrical thermoplastic matrix element with (a) in a stress free state, (b) under stress and (b) the course of shear stress and and stress in the fiber over the length according to [25] based on the shear lag model from Cox[31].

which is given in Equation (2.7) gives a more sufficient geometric description of the fiber.

$$a = \frac{L_f}{2 \cdot r_f}. \tag{2.7}$$

This means that a critical aspect ratio a_{crit} can be defined with:

$$a_{\text{crit}} = \frac{L_{\text{crit}}}{2 \cdot r_{\text{f}}} = \frac{\sigma_{\text{f}}}{2\tau_{\text{y}}}. \tag{2.8}$$

In essence, the critical aspect ratio can be sufficiently approximated from the stiffness ratio $E_{\text{f}}/E_{\text{m}}$ and is approximately 100 for the most common FRTPs using GF as the reinforcing fiber [35].
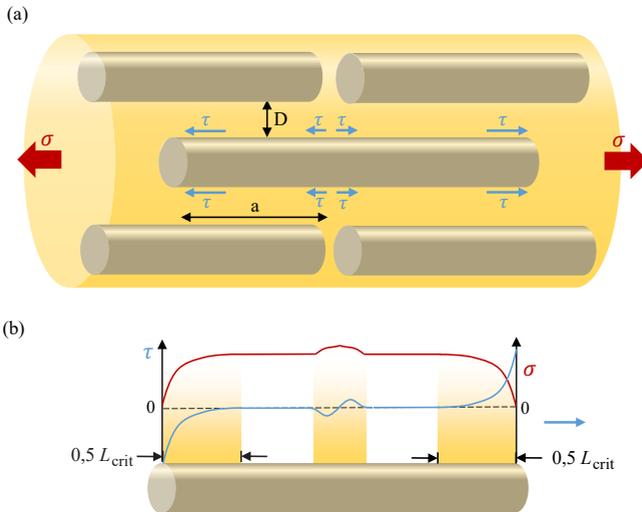
Figure 2.5: Schematic representation of a multi-fiber model with inspiration from [25] and with stress curve in a single fiber for $E_{\text{f}}/E_{\text{m}} \to \infty$ and the overlap a larger than $D\sqrt{2/3}$ based on [36, 37, 38, 39].

However, the single-fiber model only considers the redistribution of load between the matrix and the fiber. As previously stated in Section 2.1.1, the matrix is also responsible for transferring the load from one fiber to another, which is not considered in the single-fiber model [36, 37, 39].

The effect of fiber interaction can be described using the multi-fiber model shown in Figure 2.5 (a) with the distance of the fibers D and the overlap a. When a composite material with a specified overlap length a is subjected to load, the fibers within are pulled apart a small distance. Consequently, the matrix surrounding the fiber ends experiences tensile stress. As adjacent fibers displace relative to each other, pure shear stress persists throughout the remaining matrix region. When $E_{\mathrm{f}}/E_{\mathrm{m}} \to \infty$ and the overlap a is slightly larger than $D\sqrt{2/3}$, stress peaks are created by the discontinuities of adjacent fibers. Figure 2.5 (b) depicts a schematic representation of the mean tensile and shear stresses and their variation along the fiber in such a case. An in-depth derivation can be found in Schultrich et al. [36], Mohonee et al. [37] and Fu et al. [39].

2.1.3.2 Influence of fiber length and content on the effective mechanical properties

As demonstrated in the Section 2.1.3.1, the load transfer in the fiber is dependent on the fiber length in addition to the interfacial shear strength. Consequently, this correlation is also reflected in the effective mechanical properties of Dico-FRP. Figure 2.6 illustrates the fundamental relationship between fiber length and effective mechanical properties in terms of modulus of elasticity, strength and impact energy. For each load case above the 95 % line, a specific plateau can be identified, above which the incorporation of longer fibers does not result in noticeable improvements in the observed properties [40].

This plateau is also frequently referred to as the saturation length of the individual load case, L_{sat} [44]. According to the Kelly and Tyson model, there should be a match between L_{sat} and L_{crit} for the tensile strength. Thomas et al. compared the results of the tensile strength with the Kelly and Tyson model modified with a fitted numerical orientation factor after Chou [45] to account for multidirectional fiber orientation and showed good agreement [42]. This
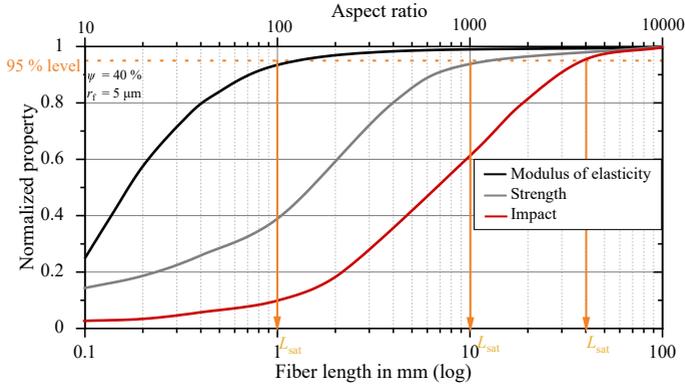
Figure 2.6: Qualitative progression of the normalized mechanical properties of over fiber length and aspect ratio according to [40] based on experimental data of 40 wt. % GF-reinforced polypropylene by Thomason et al. [41, 42, 43].

adjustment is necessary because in real Dico-FRP there is hardly any unidirectional orientation of all fibers, but rather a multidirectional orientation, which is described in more detail in Section 2.1.3.3. Nevertheless, the curves depicted in Figure 2.6 should be regarded as schematic and no special consideration should be given to the absolute values, as the transferability to other material systems or the general validity has not been proven [44].

It is crucial to recognize that Dico-FRPs frequently exhibit a lack of uniformity in fiber length, yet they are often characterized by a fiber length distribution. These fiber length distributions are typically depicted in a histogram, but they are often aggregated into representative average values for the purpose of material and process description. These values are defined in accordance with DIN EN ISO 22314 as number-averaged L_n and weight-averaged L_p [46, 47]:

$$L_\mathrm{n} = \frac{\sum_{i=1}^{i=n} L_i}{n} \tag{2.9}$$

and

$$L_\mathrm{p} = \frac{\sum_i n_i L_i^2}{\sum_i n_i L_i}. \tag{2.10}$$

Thereby L_{p} is emphasizing the proportion of longer fibers within the distribution, which is especially relevant in the case of molded LFT specimens. Typically, such specimens feature a length distribution with a noticeable peak followed by a substantial decline [48, 25].

Besides the fiber length, fiber content also has a significant effect on the effective mechanical properties [49]. Illustrated in Figure 2.7, Thomason et al. was able to show on long glass fiber-reinforced polypropylene that for the elasticity modulus there is a linear increase with fiber content, while there is a non-linear relationship for strength and impact performance, with a peak between 40 wt.% and 50 wt.%. A further increase leads to a reduction in tensile strength and impact strength [50, 51, 25].

In analogous studies, Ahn et al. demonstrated that the maximum tensile strength for both GF and CF-reinforced PA6 could be attained at approximately 25 vol.% [52]. The effects that can be held responsible for this drop at high FVCs are described in more detail in Section 2.3.5.
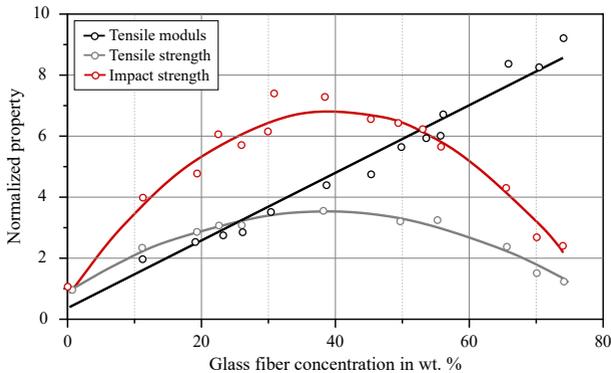
Figure 2.7: Experimentally determined mechanical properties normalized on the values of the unfilled matrix material as a function of fiber concentration (in wt. %): Tensile modulus, tensile strength and notched impact strength in accordance to [51] of GF reinforced PP.

13

2.1.3.3 Influence of fiber orientation

The influence of fiber orientation on the effective mechanical properties has already been shown for the elasticity modulus in Co-FRP for a rotation by θ (cf. Fig. 2.3). Considering the three-dimensional orientation capability of fibers in Dico-FRP, it becomes necessary to introduce an additional angle for accurate characterization. The definition of this angle is given in Figure 2.8. The orientation of a single fiber can now be given by the two angles θ and ϕ or as a vector p given in Equation 2.11.

In Figure 2.4, the embedded fiber is loaded along its axis, which is the ideal case for the load introduction and strengthening effect. This effect is significantly reduced as soon as the load is rotated by the angles θ or ϕ [53].
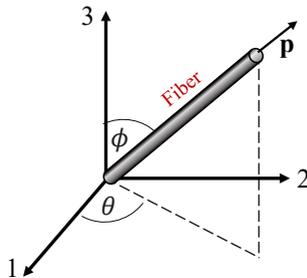
Figure 2.8: A single fiber in the Cartesian coordinate system whose orientation is defined by the angles θ and ϕ and the unit vector p.

Since Dico-FRPs consist of a large number of fibers (up to 10000 per cm^3), the description of the angle of each fiber is a enormous task. Therefore, there are also statistical quantities for the fiber orientation, which describe the entire orientation of the fibers [54, 55, 47]. The simplest case to make such descriptions is the case of planar orientation, where all fibers lie in the 1-2 plane. This is a good approximation for compression molded FRPs having long fibers relative to the thickness of the component [54]. Thus, in planar

orientation $\phi = 90°$ all orientations can be described with a single angle θ, which is restrictet between $-90°<\theta \leq 90°$. For the fiber orientation vector $\boldsymbol{p}$ as defined in Equation 2.11 it results, that $p_3 = 0$. This means that you can now describe the orientation of the fiber with p_1 and p_2, where $p_1 + p_2 = 1$ must be valid.

$$\boldsymbol{p} = \begin{bmatrix} p_1 \\ p_2 \\ p_3 \end{bmatrix} = \begin{bmatrix} \sin\phi\cos\theta \\ \sin\phi\sin\theta \\ \cos\phi \end{bmatrix} \tag{2.11}$$

The fiber orientation of a sum of fibers can be plotted as a histogram against the angle θ. These histograms will be required later as orientation information for the Halpin-Tsai method (cf. 2.1.4.1).

A histogram shows a discrete approximation of a probability function of the orientations. This function is described in the planar state as $\Psi_\theta(\theta)$, for the three dimensional state as $\Psi(\theta, \phi)$ or $\Psi(\boldsymbol{p})$ and is commonly referred to as the orientation distribution function.

The use of vectors to describe the entire orientation presents certain difficulties. For instance, if a symmetric distribution function is employed, averaging the vectors will invariably yield a zero result. Consequently, each vector is multiplied by itself using the dyadic product, which generates the second-order orientation tensor $\boldsymbol{pp}$. [56, 54].

$$\boldsymbol{p} \otimes \boldsymbol{p} = \begin{bmatrix} p_1p_1 & p_1p_2 & p_1p_3 \\ p_2p_1 & p_2p_2 & p_2p_3 \\ p_3p_1 & p_3p_2 & p_3p_3 \end{bmatrix} \tag{2.12}$$

In order to describe the orientation of a number N of fibers in a vector, it is possible to calculate the average of the individual orientation tensors of the fibers.

$$\boldsymbol{A} = \langle \boldsymbol{p} \rangle = \sum_{k=1}^{N} (\boldsymbol{p})_k \quad \text{or} \quad A_{ij} = \sum_{k=1}^{N} (p_i p_j)_k \tag{2.13}$$

To illustrate the three basic types of fiber orientation of a Dico FRP, Figure 2.9 shows generated microstructures for a fiber volume content of 5% with (a) randomly oriented fibers, (b) random in plane fiber orientation, and (c) an unidirectional fiber orientation with all fibers oriented in the 1 direction. In addition, the corresponding fiber orientation tensors are given for each case. Depending on the homogenization technique employed, effective mechanical

$$\boldsymbol{A} = \begin{pmatrix} 1/3 & 0 & 0 \\ 0 & 1/3 & 0 \\ 0 & 0 & 1/3 \end{pmatrix} \qquad \boldsymbol{A} = \begin{pmatrix} 1/2 & 0 & 0 \\ 0 & 1/2 & 0 \\ 0 & 0 & 0 \end{pmatrix} \qquad \boldsymbol{A} = \begin{pmatrix} 1 & 0 & 0 \\ 0 & 0 & 0 \\ 0 & 0 & 0 \end{pmatrix}$$
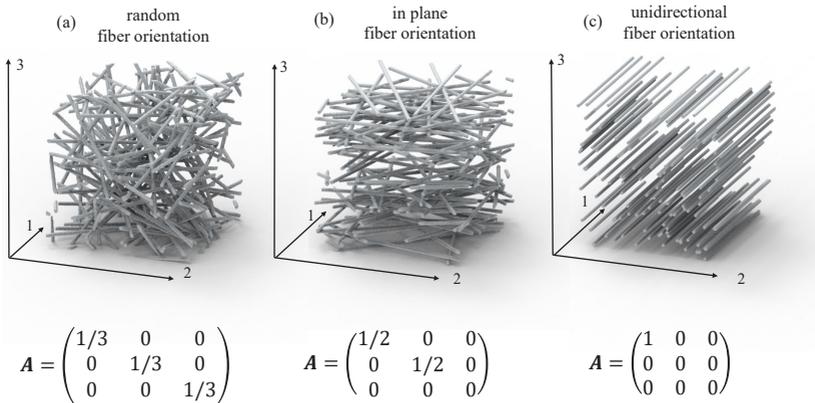
Figure 2.9: Illustration of generated microstructures with corresponding FOT for a fiber volume content of 5% with (a) randomly oriented fibers, (b) random in plane fiber orientation, and (c) an unidirectional fiber orientation with all fibers oriented in the 1 direction.

properties can be evaluated using orientation tensors, histograms, or distribution functions. Certain methods, such as Mori-Tanaka, necessitate a fourth-order fiber orientation tensor, which can be derived from the second-order orientation tensor through closure approximations. However, the resulting tensor varies significantly depending on the closure approximations used [57, 58, 59]. Hence, it is more advantageous to directly determine fourth-order fiber orientation tensors through experimental means. This can be achieved, for instance, via μCT evaluation [54, 60].

2.1.4 Modeling approaches of FRTPs

Only one selected modeling method is discussed in this chapter. An overview of other in-depth methods with detailed descriptions can be found in [25, 39].

Mortazavian et al. showed that with experimentally determined fiber length and orientation distributions, orientation dependent mechanical properties of a Dico-FRP can be well predicted using Halpin-Tsai and Classical Laminate Theory, which are described in the following [61] .

2.1.4.1 Halpin-Tsai homogenization

A simple modeling approach for the effective properties of a composite is the Halpin-Tsai method, a purely scalar and a semi-empirical method according [62]. In its original form, the model is used to predict the effective, elastic stiffness properties of UD-Dico-FRP with a uniform fiber length and is therefore only valid for these. According to Fu et al. [39] based on Halpin [62, 63] and Tsai[64], the equations in the Halpin-Tsai model are given with

$$E_{11} = \frac{1 + 2(l/d)\eta_L c_f}{1 - \eta_L c_f} E_m, \tag{2.14}$$

$$E_{22} = \frac{1 + 2\eta_T c_f}{1 - \eta_T c_f} E_m, \tag{2.15}$$

$$\nu_{12} = \nu_f c_f + \nu_m c_m, \tag{2.16}$$

$$\nu_{21} = \frac{E_{22}}{E_{11}} \nu_{12}, \tag{2.17}$$

$$G_{12} = \frac{1 + \eta_G c_f}{1 - \eta_G c_f} G_m, \tag{2.18}$$

where

$$\eta_{\mathrm{L}} = \frac{E_{\mathrm{f}}/E_{\mathrm{m}} - 1}{E_{\mathrm{f}}/E_{\mathrm{m}} + 2(l/d)}, \tag{2.19}$$

$$\eta_{\mathrm{T}} = \frac{E_{\mathrm{f}}/E_{\mathrm{m}} - 1}{E_{\mathrm{f}}/E_{\mathrm{m}} + 2}, \tag{2.20}$$

$$\eta_{\mathrm{G}} = \frac{G_{\mathrm{f}}/G_{\mathrm{m}} - 1}{G_{\mathrm{f}}/G_{\mathrm{m}} + 1}. \tag{2.21}$$

Equation (2.14) shows that the longitudinal modulus of elasticity of a UD-Dico-FRP depends in addition to the fiber volume fraction and the fiber modulus to matrix ratio also on the fiber aspect ratio a. For Dico-FRP with a high aspect ratio, the longitudinal modulus of elasticity approaches a limit (cf. Figure 2.6 in Section 2.1.3.2) corresponding to that of a UD-Co-FRP, which in turn is determined by the RoM (cf. Equation (2.3)) [39].

Thus, the modulus of elasticity of UD-Co-FRPs and UD-Dico-FRPs can be predicted with this method. By calculating the components of the stiffness matrix Q_{ij} and using the constants from Equation 2.1.4.1, an effective planar stress-strain relation can be constructed for an UD-FRP with aligned principal fiber and stress directions [65]:

$$\begin{bmatrix} \sigma_1 \\ \sigma_2 \\ \tau_{12} \end{bmatrix} = \underbrace{\begin{pmatrix} Q_{11} & Q_{12} & Q_{16} \\ Q_{12} & Q_{22} & Q_{26} \\ Q_{16} & Q_{26} & Q_{66} \end{pmatrix}}_{=Q_{ij}} \begin{bmatrix} \varepsilon_1 \\ \varepsilon_2 \\ \gamma_{12} \end{bmatrix}, \tag{2.22}$$

The components of Q_{ij} are given with [65]:

$$Q_{11} = \frac{E_{11}}{1 - \nu_{12}\nu_{21}}, \tag{2.23}$$

$$Q_{12} = \nu_{21}Q_{11}, \tag{2.24}$$

$$Q_{16} = 0, \tag{2.25}$$

$$Q_{22} = \frac{E_{22}}{1 - \nu_{12}\nu_{21}}, \tag{2.26}$$

$$Q_{26} = 0, \tag{2.27}$$

$$Q_{66} = G_{12}. \tag{2.28}$$

With the theory of linear elasticity [66], the stress-strain relation in any off-axis system rotated around the third principal axis is expressed as

$$
\begin{bmatrix} \sigma_1' \\ \sigma_2' \\ \tau_{12}' \end{bmatrix} = \underbrace{\begin{pmatrix} Q_{11}' & Q_{12}' & Q_{16}' \\ Q_{12}' & Q_{22}' & Q_{26}' \\ Q_{16}' & Q_{26}' & Q_{66}' \end{pmatrix}}_{=Q_{ij}'} \begin{bmatrix} \varepsilon_1' \\ \varepsilon_2' \\ \gamma_{12}' \end{bmatrix}, \tag{2.29}
$$

with the transformed stiffness components [65]:

$$
\begin{bmatrix} Q_{11}' \\ Q_{22}' \\ Q_{12}' \\ Q_{66}' \\ Q_{16}' \\ Q_{26}' \end{bmatrix} = \begin{pmatrix} c^4 & s^4 & 2c^2s^2 & 4c^2s^2 \\ s^4 & c^4 & 2c^2s^2 & 4c^2s^2 \\ c^2s^2 & c^2s^2 & c^4 + s^4 & -4c^2s^2 \\ c^2s^2 & c^2s^2 & -2c^2s^2 & (c^2 - s^2)^2 \\ c^3s & -cs^3 & cs^3 - c^3s & 2(cs^3 - c^3s) \\ cs^3 & -c^3s & c^3s - cs^3 & 2(c^3s - cs^3) \end{pmatrix} \begin{bmatrix} Q_{11} \\ Q_{22} \\ Q_{12} \\ Q_{66} \end{bmatrix}, \tag{2.30}
$$

where $c = \cos\theta$ and $s = \sin\theta$.

In a comparative analysis of various stiffness predictions for unidirectional short fiber composites, Tucker et al. demonstrated that the Halpin-Tsai method tends to slightly underestimate the stiffness in the E_{11} direction [67]. Similar results could also be shown by Huang et al. [68]. Therefore, there are some more physical approaches and extensions for the calculation of E_{11} in the literature [69].

2.1.4.2 Shear-lag modified Halpin-Tsai model

Since the classical Halpin-Tsai model is a semi-empirical model, there are some attempts to obtain a more physical approach to the stiffness in the fiber direction E_{11}. For this purpose Fu et al. integrated the Cox shear-lag model from Section 2.1.3.1 into the classical Halpin-Tsai model [65] . A more detailed derivation is given in Fu et al. [39] and results are found in Fu et al. [65]:

$$E_{11} = E_{\mathrm{f}} c_{\mathrm{f}} \left(1 - \frac{\tanh(\xi l/2)}{\xi l/2} \right) + E_{\mathrm{m}}(1 - c_{\mathrm{f}}) \tag{2.31}$$

.

The shear lag parameter ξ is given by:

$$\xi = \sqrt{\frac{2G_{\mathrm{m}}}{r_{\mathrm{f}}^2 E_{\mathrm{f}} \ln\left(R/r_{\mathrm{f}}\right)}} \tag{2.32}$$

A hexagonal fiber packing gives

$$\ln\left(\frac{2R}{r_{\mathrm{f}}}\right) = \frac{1}{2} \ln\left(\frac{2\pi}{\sqrt{3}c_{\mathrm{f}}}\right), \tag{2.33}$$

whereas a square fiber packing results in

$$\ln\left(\frac{2R}{r_{\mathrm{f}}}\right) = \frac{1}{2} \ln\left(\frac{\pi}{c_{\mathrm{f}}}\right). \tag{2.34}$$

For the application of the shear-lag modified Halpin-Tsai, it is now only necessary to substitute Equation 2.14 by 2.31.

As previously stated, both, the classic Halpin-Tsai and the shear-lag modified Halpin-Tsai model, are applicable only to UD-FRP with a specific fiber length. While the average value of a fiber length distribution can be employed, it is uncertain whether the mechanical properties will be accurately mapped. Consequently, further steps or simplifications are necessary to apply these methods to Dico-FRP, which are presented in Figure 2.10 (a-d) in a step-by-step manner.

The first step is to simplify the complex orientation to a planar orientation (cf. Fig. 2.10 (a-b)). Owing to the condition of planar fiber orientation, this
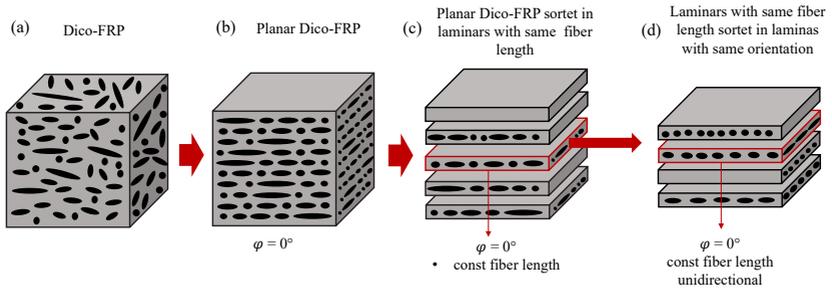
Figure 2.10: Schematic representation of a laminate model of a Dico-FRP showing: (a) the actual Dico-FRP structure, (b) a simplified planar representation of the Dico-FRP, (c) the planar Dico-FRP represented as a composite of laminates with uniform fiber lengths, and (d) each laminate represented as a stacked sequence of layers with identical fiber lengths and orientations according to [70].

is primarily applicable for Dico-FRP with planar fiber orientation distributions (FOD) [26, 39]. However, Fu and Lauke demonstrated that the modulus of elasticity in the planar plane of the Dico-FRP for the case of a spatial FOD is equivalent to that of a planar orientation distribution $\Psi(\theta)$, when $\Psi(\theta)$ is identical for both cases and independent of the FOD $\Psi(\phi)$. In other words, that the modulus of elasticity of Dico-FRPs depends only on the angle θ that the fibers form with the direction in which the modulus of elasticity of Dico-FRPs is to be evaluated. Consequently, the necessary simplifications are applicable

for plate structures whose in-plane properties are to be determined [35, 71]. As this applies to most Dico-FRP components, this offers an acceptable simplification. Owing to the existing variations in fiber lengths and orientations, additional transformations are required. First, the planar-Dico FRP is segmented into individual laminates characterized by fibers of uniform length, shown in Figure 2.10 (c). These laminates still contain fibers with different orientations, and thus a subsequent segmentation is performed to create laminates with unidirectional orientation shown in Figure 2.10 (d) [72]. The direction-dependent stiffness of these laminas only containing fibers with same fiber and same fiber orientation can now be calculated using the described Halpin-Tsai methods [70].

This approach is adaptable to Dico-FRP configurations with multiple types of reinforcing fibers. Therefore the Dico-FRP is segmented not only into laminates of same fiber length and orientation, but also into laminates of the same fiber type. For illustrative purposes, this is depicted in Figure 2.11.
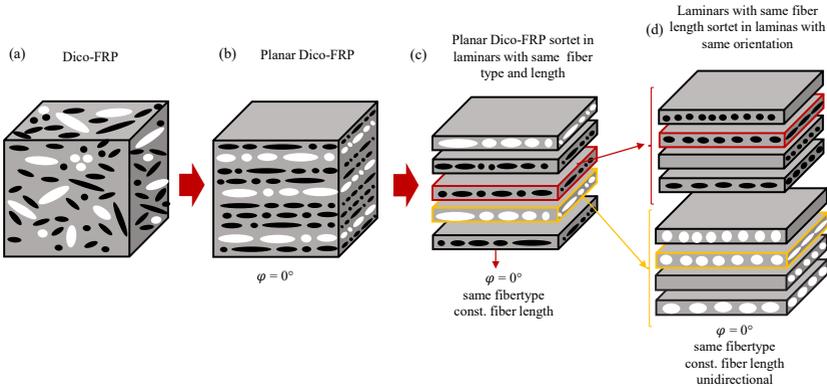
Figure 2.11: Schematic representation of a laminate model of a Dico-FRP showing: (a) the actual Dico-FRP structure, (b) a simplified planar representation of the Dico-FRP, (c) the planar Dico-FRP represented as a composite of laminates with same fiber type and uniform fiber lengths, and (d) each laminate represented as a stacked sequence of layers with same fiber type, identical fiber lengths and orientations according to [70].

In order to be able to recalculate to the overall stiffness of the planar simplified Dico-FRP (Fig. 2.10 (b) and Fig. 2.11 (b)), certain assumptions must be made. The Classic Laminate Theory (CLT) is an appropriate framework for this, as it allows homogenization of properties of individual laminae to be combined to form an overall laminate [26].

2.1.4.3 Classical Laminate Theory

The CLT is a form of laminate theory and is a theory that applies to thin laminates, i.e. the thickness is significantly smaller than the length and width, and makes the following assumptions [73]:

- a perfect laminate is assumed, i.e. there is perfect bonding between the individual layers,
- the laminate is undamaged and shows no flaws such as delamination, porosity, fiber curl, etc,
- it is assumed that there is uniform stress not only in the individual layers of the laminate, but also in the laminate as a whole,
- the laminate conforms to Kirchhoff's assumptions for bending of thin plates, wherein a line normal to the mid-plane remains straight and perpendicular to the mid-plane,
- the thickness of the laminate does not change during the entire deformation,

The validity of the CLT could be confirmed for different Co-FRP laminates for different load cases such as bending or torsion in comparison to experimental data [74, 75]. Nevertheless, it has been demonstrated in numerous studies that this method can be employed for Dico-FRP under tensile load, exhibiting a high degree of correlation with the experimentally determined stiffness values [76, 77, 70, 39, 78, 79]. Trauth et al. were able to accurately predict the flexural strength of a hybrid Co and Dico-FRP using an alanytic approach based on CLT and the observed failure evolution[80].

2.2 Influence of temperature and water on the mechanical properties of thermoplastics

This section describes the temperature-dependent effects in thermoplastics. In addition, special emphasis is placed on the influence of absorbed water in polyamides and the associated transistion mechanisms. Thermoplastics are polymers that are not cross-linked up to their decomposition temperature. Consequently, they undergo several thermal transitions when heated from very low temperatures up to decomposition.

2.2.1 Thermal transitions in thermoplastics

The thermal transitions in thermoplastics can be described, among other things, by the changes in free volume. Free volume is defined as the space a molecule has for internal movement and is related to the viscoelasticity, solvent penetration, and the effective mechanical properties of a polymer. Changes in free volume can therefore be measured as a change in volume of the polymer, as heat absorption or release associated with that change, as a loss of stiffness, or as a change in relaxation time [81, 82, 83].

2.2.1.1 Thermal transitions of the storage modulus

For a better visualization of the effects, it is suitable to look at the course of the storage modulus over the temperature which is schematically plotted for a thermoplastic with different softening phases in Figure 2.12. In order to proceed through the individual softening mechanisms step-by-step, commence at low temperatures, as indicated by the arrow in the Figure 2.12 on the left. If the temperature is increased from the low temperatures at which the molecules are highly compressed, the material expands, the free volume increases, and local

bonding movements such as bending, stretching, and to a certain extent, side chain movements become possible. As a result, a drop in the storage modulus can be observed in a small area (cf. Fig. 2.12 (6)-(5)). This transition temperature is also known as the gamma transition (T_γ) and often shows interactions with absorbed water [81, 84].
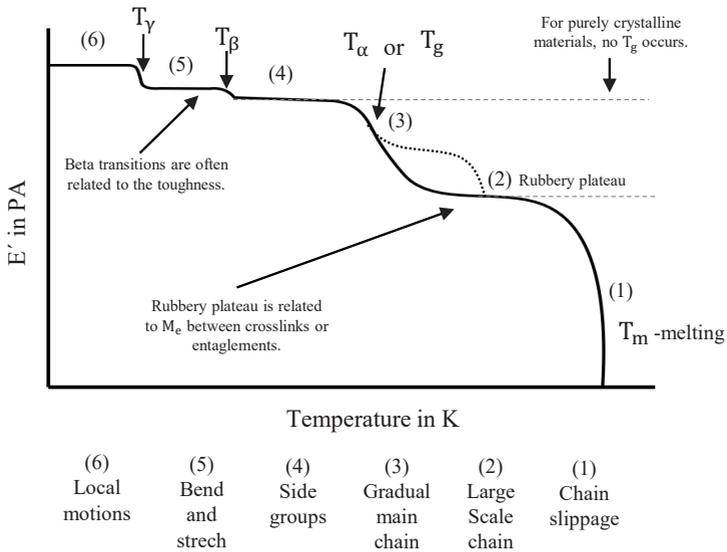
Figure 2.12: Schematic representation based on a semi-crystalline polyamide of the storage modulus E´ over temperature curve of a semi-crystalline thermoplastic divided into six regions that corresponds to: (6) local motions, (5) bond bending and stretching, (4) movements in the side chain or adjacent atoms in the main chain, (3) the region of the Tg (2) coordinated movements in the amorphous portion of the chain, (1) and the melting region according to [81].

If the temperature and thus the free volume continue to rise, all side chains and localized groups of four to eight backbone atoms gain sufficient space to move. This is visible in a drop in the storage modulus in a small area, shown in Figure 2.12 (5)-(4) and is referred to as the beta transition (T_β). This effect is generally equated with material toughness. If we now heat the material further, we reach the glass transition (T_g) or the alpha transition (T_α), at which the chains in the amorphous regions begin to coordinate large-scale movements. This again leads to a drop in the storage modulus, shown in Figure 2.12 (4)-(3). During the T_g transition, the polymer changes from a hard glassy to a rubbery state and represents an important transition for many polymers, as the physical properties drastically change. It is important to note, that the glass transition only occurs in materials with amorphous components and cannot be observed in 100 % crystalline materials. Nevertheless, the characteristics of the amorphous phase can vary, exerting a direct impact on the glass transition. Parodi et al. illustrated in the case of PA6 that two distinct amorphous phases exist—one rigid and the other mobile—whose ratio can alter the value of T_g [85]. Experimentally, T_g can be determined in a variety of ways, and it can also be defined using different ways in individual experimental methods. For example, in Dynamic Mechanical Analysis (DMA), there are at least five possibilities. This means that T_g can vary by up to 25° depending on the method. It is therefore advisable to consider T_g as a range. [81, 86].

The subsequent temperature range above T_g and below the melting temperature (T_m) is referred to as the rubber plateau (cf. Fig. 2.12 (2)). The dimensions and viscosity of this plateau depend on the molecular weight (M_e) of the material and the degree of crystallization. Further heating will reach T_m, where a final drop in the storage modulus can be observed (cf. Fig. 2.12 (1)). The melting point is the point at which the free volume has increased so much that the chains can slide against each other and the material flows. In the molten state, flowability again depends on the molecular weight of the polymer [81, 84]. Because thermoplastics are viscoelastic materials, in addition to the storage modulus E' or the elastic component , they also have a loss modulus E'' or damping component that is also temperature dependent. This rises to a maximum at T_g

and then falls, and is therefore often used as a definition of T_g. Another widely used definition of T_g is the peak of the loss factor $\tan \delta$, which is the ratio of E'' and E' [81]. This definition for determining T_g is also specified in ASTM E1640-23 [87].

In addition to the temperature dependence, E' and E'' also have a time dependency. Between the time and temperature dependence, the relaxation mechanisms can be converted into each other by means of the time temperature superposition (TTS). This is equally applicable for characterization in the frequency range, for example by DMA, as well as in the time range, for example by creep or relaxation tests. As a result, material data determined in a limited frequency range at different temperatures can be transferred to an extended frequency range that goes beyond the experimentally defined limits of frequency and time [88]. In addition to storage and loss modulus, other material parameters exhibit temperature-dependent behavior including the Poisson's ratio [89, 90].

2.2.1.2 Thermal transitions of poisson's ratio

In terms of material mechanics, the Poisson's ratio ν is defined as a negative fraction between transverse strain ϵ_t and longitudinal strain ϵ_l under uniaxial loading and is given in Equation 2.35. Like modulus, Poisson's ratio is a measure of the elastic or viscoelastic behavior of a material. As such, it relates to, for example, the modulus of elasticity with the shear modulus or the compression modulus of isotropic materials [90].

$$\nu_{21} = -\frac{\epsilon_t}{\epsilon_l} = -\frac{\epsilon_2}{\epsilon_1} \tag{2.35}$$

The Poisson's ratio of thermoplastics is not a constant value, but is fundamentally dependent on the test conditions and the structural and processing parameters of the material. The real values of thermoplastics are between about 0.3 and 0.5. In general, ν tends towards 0.5 with decreasing stiffness and increasing temperature. Liquids, including thermoplastic melts, are at this upper

limit which means volume conservation and thus complete incompressibility. Figure 2.13 shows the course of ν over temperature for typical thermoplastics. The change in Poisson's ratio with temperature does not follow a general trend; rather, there is considerable variation in the curves for different thermoplastics. The individual curves of can be recognized, which reach 0.5 at the melting or flow temperature [90, 89]. Similar to E' and E'', ν also shows a frequency dependency. For example, it was shown that with short-term strain, ν decreases with increasing strain rate [91, 92]. In general, no application of TTS to ν is known up to date.
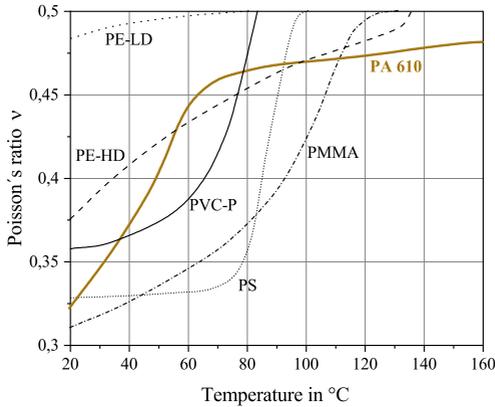
Figure 2.13: Poisson's ratio of some thermoplastics as a function of temperature adapted from [89].

2.2.2   Moisture dependence of thermoplastics

Certain thermoplastics exhibit hygroscopic behavior, resulting in water absorption and subsequent effects on mechanical properties. Since the investigations in this work are limited to PA6 as a matrix material, the water absorption of PAs will be considered exclusively in the following.

2.2.2.1 Influence of water on polyamides

A very comprehensive literature review on the effects of water on polyamides is given in Venoor et al. [93].

In general, when PAs are exposed to a humid environment bipolar water molecules diffuse in the PA and form a complex with the hydrogen bonds between two neighboring bipolar amide groups. It is known that water diffuses mainly into the amorphous regions between the crystalline domains. The water molecules increase the distance between the molecular chains, weakening the secondary bonds and thus acting as a plasticizer, while at the same time influencing the glass transition temperature. Water molecules continue to diffuse into the polyamide until saturation is reached, whereby the degree of saturation depends on the relative humidity, the degree of crystallinity, the temperature and the number of hydrogen bonds of a polyamide [94, 95, 93, 96, 97, 98].

The transition of the amorphous phase of PA6 from a glassy to a rubbery state due to water absorption can cause a significant decrease in the glass transition temperature, sometimes as much as 60-70 K [99]. Initially, the prediction of these temperature changes was based on methods developed by Kelley and Bueche [100] and Reimschuessel [101]. However, it is important not only to consider the effect of moisture on thermomechanical properties, but also to understand the underlying mechanisms. Consequently, many researchers have focused on studying and modeling the diffusion processes responsible for these changes [102, 103].

The most straightforward transport model that describes the diffusion of water in polyamide is the Fickian diffusion model [104]. For most polymers, the material-dependent diffusion coefficient D and the saturation mass $M_w(\infty)$ can be used to solve Fick's second law in one dimension, which is given in Equation 2.36 according to [94] with the thickness of the samples h in mm and the time t in s.

$$\frac{M_w(t)}{M_w(\infty)} = 1 - \frac{8}{\pi^2} \sum \frac{1}{(2i+1)^2} \exp(-\frac{D(2i+1)^2\pi^2 t}{h^2}) \qquad (2.36)$$

The percentage by weight of the water $M_w(t)$ dissolved in the polymer is defined by

$$M_w(t) = \frac{M(t) - M_0}{M_0} \cdot 100. \qquad (2.37)$$

The diffusion coefficient can be calculated according Equation 2.38 from the initial linear part of the sorption curve, for which the $\frac{M(t)}{M_\infty} \leq 0.5$ applies [104, 105, 106, 93]

$$D = \frac{\pi}{16} \cdot \frac{h^2}{t} (\frac{M(t)}{M_\infty})^2. \qquad (2.38)$$

In some studies it could be shown that deviations from Fickian water diffusion in polyamides are present, which is due to an increase in diffusivity during water absorption by the already absorbed water [107]. To describe this non-Fickian water diffusion, some extended models have been developed, which can be found in [94, 108, 109, 110, 111].

2.2.3 Influence of temperature and moisture on fiber-reinforced polyamides

The addition of reinforcing fibers can help to partially compensate for the degradation of mechanical properties of polyamides caused by elevated temperature or absorbed moisture. Again, this depends on the type of fiber, its length, and its orientation. However, there is still a significant effect on the overall properties of the composite. Since the matrix, as can be seen from the models in Section 2.1.4.1, is largely responsible for the effective mechanical properties of the composite, this is not surprising [112, 95].

The Fickian model is also frequently used for water absorption in composite materials. Since for composite materials the water absorption should also be related to the matrix material, Equation 2.37 must be adjusted with:

$$M_w(t) = \frac{(M(t) - M_\mathrm{f})(M_0 - M_\mathrm{f})}{M_0 - M_\mathrm{f}} \qquad (2.39)$$

The diffusion behavior of water in polyamides is also influenced by the presence of fibers, their orientation and the interface between fiber and matrix. These influences on the absorption behavior of polyamides has also been studied in multiple works and was partially converted into models [95, 113, 107, 94, 114, 115, 116].

Most reinforcing fibers itselfs such as CF are hardly or not at all affected by moisture. However, in the case of FRP, the interface forms between the fibers and the matrix, which is essentially responsible for load transfer and depends on the interface adhesion. This in turn is reduced by the absorption of water in PA6 [117].

Hassan et al. performed DMA analyses and found that moisture absorption also affects the T_g of short glass fiber-reinforced polyamide 6.6, causing them to decrease. The incorporation of glass fibers into polyamide 6.6 resulted in a significant increase in tensile modulus and strength, but with a decrease in elongation at break. Exposure to varying environmental conditions, from dry to humid, caused a decrease in both strength and modulus, while increasing the elongation at break [118].

Chaichanwong et al. conducted a study to investigate the effect of moisture absorption on the mechanical properties of short glass fiber/polyamide composites with varying weight percentages (0 wt% to 30 wt%). Their results showed a significant decrease in yield strength, tensile strength, and flexural strength for all specimens upon moisture absorption followed by stabilization. In addition, Young's modulus decreased during initial moisture absorption and remained reduced after saturation [119].

Since the absorbed moisture, as already mentioned, leads to a shift in the glass transition temperature, there are approaches in FRP to describe the mechanical behavior as a function of the distance to the glass transition temperature. Launay et al. deal with this in a temperature-humidity equivalence principle, in which the distance between temperature and water dependent glass transition temperature describes the sensitivity of the behavior to both temperature and relative humidity on the effective mechanical properties [120].

2.3 Long fiber-reinforced thermoplastics

2.3.1 General aspects

Long fiber-reinforced thermoplastics (LFT) are a composite material consisting of a thermoplastic matrix and "long" reinforcing fibers [121, 122]. To the author's knowledge, the most common definition of the term "long" in this context is that the critical fiber length L_{crit} (see Section 2.1.3.1) must be exceeded. Since LFT often have a fiber length distribution, there is some leeway in the definition as to which statistical metric (e.g. median, mean, ...) is used. Depending on which value is used, the same material can therefore be reinforced with long fibers or short fibers [122]. In addition, there are other definitions according to which a fiber is called long if it exceeds the length of 1 mm [54]. In others, however, the area of long fibers only begins from a length of 2 mm [121]. Since according to this definitions neither the fiber type, (i.e. its diameter and aspect ratio) or the interfacial shear strength is considered, this definition seems to be imprecise.

Due to the longer fibers, LTFs are characterized by higher mechanical properties (cf. Fig. 2.6) compared to short-fiber thermoplastics (SFT), while still being easy to process and offering high cycle times [122, 123]. A further advantage is that a large number of matrix and fiber combinations can be processed. LFTs can thereby be processed in different ways. In the first instance, a distinction is made between two types of semi-finished products. The first type is the

so-called granulated-LFT (G-LFT), which consists of a rod-shaped granulate, 12.5 mm or 25 mm long, with fibers over the entire length. These semi-finished products can be purchased ready to use, but must be melted down again in an extruder for on-site processing. The shear stresses in the extruder cause the fibers to shorten so that the original fiber length is not achieved in the finished component [18, 124]. The fiber in the final component of G-LFT often has a length of 1 mm-2 mm [7].

The second variant is the so-called inline compounding (ILC) or LFT direct compounding process (LFT-D), which does not require any semi-finished products at all. With LFT-D, the component is manufactured directly from the raw materials (fiber, polymer and additives) [124]. Basically, both types can be processed by injection molding or compression molding. Since this work deals exclusively with compression molded composites, these will be described in the following (cf. Sec. 2.3.3).

2.3.2 LFT-Direct Inline compounding (LFT-D-ILC) process

Systems with so-called Inline compounding (ILC) are a special form of the LFT-D process. Generally, these consist of two twin screw extruders (TSE) and is shown schematically in Figure 2.14. The first TSE serves a compounding process that involves mixing and plasticizing the matrix material (polymer and additives), which is then transferred to the second TSE through an open film die. The matrix material is thus compounded in line. Continuous fiber rovings are fed directly into the second TSE at the same position where the matrix material flows into it. The rovings are then shortened by the shear forces to form bundles, which are cut and separated into individual filaments and then homogenized with the matrix over the processing length of the second TSE [124, 125, 126].

Glass fibers were initially utilized as reinforcing fibers in the LFT-D process due to their cost-effectiveness, often being less expensive than the matrix material. This ensured a mechanical improvement with a simultaneous reduction
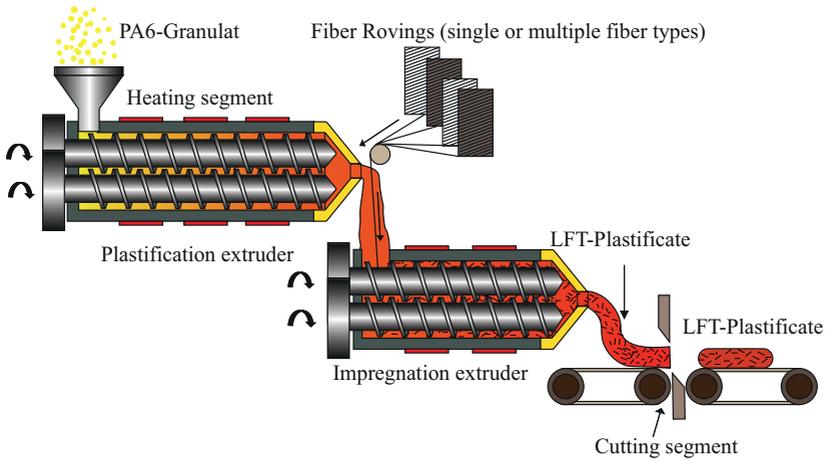
Figure 2.14: Schematic drawing of the long-fiber-reinforced-thermoplastic direct Inline compound-ing process (LFT-D-ILC) with two co-rotating twin-screw extruders (TSE) connected in series. The first for plasticising and adding the polymer matrix and the second impregnating TSE, in which the fiber rovings are broken up, split up and impregnated with the matrix according to Scheuring et al. [127].

in costs. Following the introduction of stricter regulations regarding emissions, particularly in the automotive sector, the focus shifted towards reducing weight and increasing financial flexibility. This has led to an increase in demand for Dico-FRP with CF as reinforcement in recent years [9, 10]. A significant po-tential for structural component applications was demonstrated for thermoset based Dico-CFRP by combining both excellent mechanical properties and a complex formability [10].

These advantages are also obtained when using a thermoplastic matrix for Dico-CFRP, which additionally offers a solution for high-cycle production and recyclability [128, 129, 10]. In a comparison between PA6, PA6.6, PC, HDPE and PE, Roh et al. observed the highest interfacial shear strenghth for PA6 and CF and also achieved the best fiber dispersion [130].

2.3.3 Compression molding of LFT

Compression molding is a process in Dico-FRP processing in which a usually preheated molding compound (the so-called initial charge cf. Sec. 2.3) is charged into an open, heated mold cavity. This process enables the production of high-strength objects with complex geometries in combination with a short cycle time and high production rate [131, 132, 125].

Unlike injection molding, this process gives the fibers extended potential to retain their length due to the limited shear rate in the cavity. Since the quality of the final product is significantly dependent on the condition of the fibers within the component, this results in significantly improved mechanical properties [131, 125].

In addition, an adjustable strand nozzle and an open mold allow a flow-optimized initial charge to be placed in a flow-optimized position in the mold. This allows larger parts with final wall thicknesses of 1.5 mm to be produced, resulting in a significant weight reduction compared to injection molding [125].

As schematically shown in Figure 2.15 the initial charge can cover either only part (Fig. 2.15 (b), (c)) of the mold or the entire mold (Fig. 2.15 (a)). With the partial cover, the insertion position and also the percentage of the mold that is covered at the beginning can be varied. This has a direct influence on the flow path and thus also on the subsequent fiber orientation in the finished part (cf. Sec. 2.3.4). In order to determine the position and the percentage with which a mold filling can be achieved, the flowability of the initial charge must be taken into account. The flowability ability of the initial charge depends essentially on the fiber volume content. Thus, in the case of complex geometries with ribs and beads, complete mold filling cannot be guaranteed at high FVC with partial cover.

Another effect that occurs in the compression molding of LFT with complex geometries is the so-called fiber seperation. This occurs in the case of strong geometric changes such as ribs. During the compression molding process, the long reinforcing fibers at the rib entry are subject to increasing fiber-fiber interaction caused by changes in flow velocity, cross-sectional constriction and fiber alignment during compression molding. This increased interaction due to
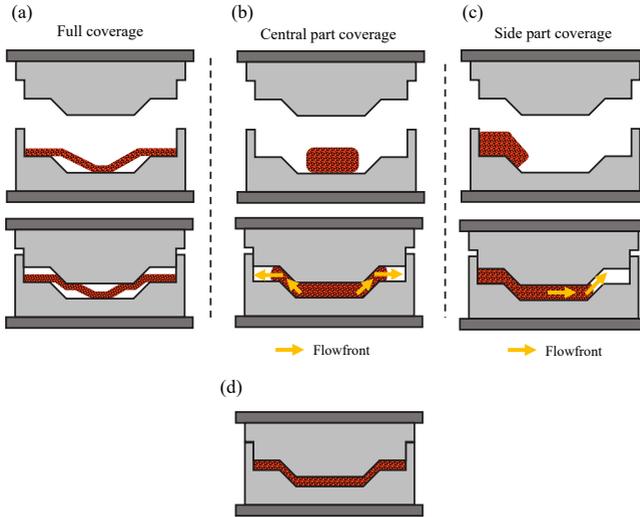
Figure 2.15: Schematic representation of LFT compression mold with an initial charge from the LFT-D process with (a) full coverage, (b) central part coverage and (c) side part coverage with the respective development of the flow front and (d) the finished pressed component.

the restricted cross-section results in the accumulation of fibers at the rib entry, creating a fiber jam that prevents the fibers from penetrating into the upper rib area, resulting in a lower fiber content in the rib tips [133]. However, this effect depends strongly on the orientation of the rib to the flow front. Kuhn et al. showed that in logintudinal ribs a strong fiber jam occurs at the rib entry, whereas this is much less pronounced in perpendicular ribs. However, in both cases, significantly lower fiber volume contents were detected in the rib tips [133].

2.3.4   Influence of flow on the fiber orientation

During compression molding, a variety of deformation types and flow phenomena can occur, which essentially depend on the rheological properties of the

material, the mold geometry, the geometry and position of the initial charge and the processing conditions such as mold temperature, preheating temperature, surface condition of the mold and closing speed of the mold [134].

These phenomena have a direct influence on the development of the fiber structure, since Dico fibers embedded in a molten thermoplastic matrix undergo rotation and displacement as a result of the deformation mass caused by the molding process. Internal shear and tensile stresses lead to the alignment of the fibers resulting in anisotropic properties in the formed Dico-FRP part.[25, 7, 135]

This interaction can be described by Jeffrey's Equation and is based on two rules [54]:

- Shearing flows align fibers in the flow direction
- Stretching flows align fibers in the stretching direction.

The process-related alignment of Dico fibers has been investigated in detail in numerous experimental and numerical studies. Most studies are concerned with injection molding and focus mainly on the pattern of fiber alignment that occurs due to the fountain flow effect and the related speed and shear profile. Usually these results in a shell-core structure, which means, that the fibers are mainly oriented in the flow direction on the walls of the mold, where shear stress is highest; inside, they remain orthogonal to the flow direction [136, 137, 25, 138].

Both the fountain flow and the shell core effect are essentially due to the high flow velocities and the associated shear forces. In LFT compression molding, however, the shell-core effect is different. As the fibers in the edge areas of the initial charge are oriented in the extrusion direction during extrusion, and this area is the first to freeze during compression molding, the fibers in this shell or skin area remain in exactly this configuration and are therefore no longer affected by the flow [139].

In the inner or core of the samples, the fibers orient themselves along the flow path in the direction of the flow front until a homogeneous orientation is achieved. Simon et al. were able to demonstrate this using compression molding samples in the sliding plate rheometer [140]. During compression

molding, the flow can be classified as either lubricated squeeze flow, where the material slides on the mold surface, or non-lubricated squeeze flow, where the material remains stationary on the mold surface. The presence of one of these two types of flow leads to a different course of flow speed and shear [54].

In addition, the initial charge from which the flow develops has a complex fiber structure, which in turn is reflected in the flow behavior. Song et al. showed, that fore the initial orientation of the fibers in the initial charge has a considerable effect on the evolution of the fiber orientation during molding [131]. The influence of fiber orientation on mechanical properties has already been investigated for both compression molding and injection molding. In the following Section, however, the focus is on the mechanical properties of LFT-D-ILC with compression molding.

2.3.4.1 Fiber orientation in LFT-D-ILC compression molding

To consider the evolution of fiber orientation during compression molding, it is easiest to first consider a 2D plate geometry. In this case, compression molding can be simplified to two parallel plates moving towards each other. This restricts the flow direction to the ordinate and the flow can be treated as a two-dimensional element, since the thickness of the molded part is much smaller than the width and length [141, 142, 143].

Bondy et al. were able to show that for a square plate tool with a side insert, there is a significant difference in tensile modulus and tensile strength between samples taken from the flow area at 0° and 90° orientation to the flow direction. He was able to show that higher fiber volume contents are accompanied by a significant increase in the modulus of elasticity in the 0° orientation, while hardly any increase can be seen in the 90° orientation. He achieved the highest values for PA6 reinforced with 25 vol. % CF with 20.79 GPa in 0° and 5.71 GPa in 90° orientation. An interesting observation was made, that tensile stiffness and strength as well as flexural stiffness were consistently higher in the

+45° direction compared to the -45° direction. The tensile modulus was 20% higher, the tensile strength 10% higher and the flexural modulus 8% higher in the +45° orientation. As a result, the technical elongation at break in uniaxial tensile tests was on average 18% lower in the +45° direction [144]. This effect has already been observed in previous studies and can probably be explained by the fact that the fibers are not oriented in the direction of flow, but that there is a deflection of the 0° orientation. To the best of the author's knowledge, a deflection from the 0° orientation was shown for the first time by Tröster using circular specimen in the tensile test for GF-PP-LFT out of the LFT-D-ILC process with side insert [145].

Radtke employed the same methodology of circular specimens to ascertain the anisotropy in side-inserted GF-PP-LFT plates and reached a comparable conclusion. According to Radke, the uneven filling of the mold due to the anisotropy of the initial charge is responsible for the shifted fiber orientation. Filling of the mold begins at the back, i.e. in the last part of the initial charge extracted from the TSE, resulting in a shifted flow front, which in turn leads to a skewed fiber orientation. [146]

Exactly this effect was shown by Fliegener for a GF-PA6-LFT with the same side insert using μCT-determined fiber orientation tensors. The maximum of the distribution function does not occur at 0° to the flow front, but is shifted by about 10° [147]. According to Radtke, the reason for this is the temperature difference of approximately 10 K - 30 K between the beginning and end of the initial charge, as it cools slightly more at the end that is discharged first. This temperature gradient results in a viscosity variation within the initial charge, which in turn leads to a slightly rotated orientation of the flow front relative to the mold edges [146].

2.3.5   Influence of Bundles

Since in the LFT-D process the fibers are processed directly from rovings and are broken into bundles in the first step, this can lead to the fact that at high FVC individual bundles do not disintegrate over the process distance. Generally the term "bundling" refers to the condition in which the fiber bundles are not completely disintegrate during the melting process, which often results in a reduction of the mechanical properties [148, 25, 149].

Thomason made the bundles responsible for the fact that both tensile strength and impact strength decrease at very high FVCs (cf. Fig. 2.6). [122, 50]

Bondy et al. were able to show on PA6-CF LTF-D under tension tension fatigue, that bundles of poorly impregnated fibers were found on many fracture surfaces of specimens with fatigue properties at the lower fatigue limit. This is attributed to voids forming at the end of the bundle or to local stress increases around the bundles [150].

In addition to the FVC, the fiber length is another important factor in many processes that can lead to increased bundling. Therefore, especially in the second TSE of the LFT-D-ILC process, there is a conflict of objectives between the most gentle treatment possible to obtain longer fibers and a high energy input to ensure good dissolution of the bundles and impregnation of the fibers.

Ranganathan et al. were able to show that the application of higher shear forces due to a higher screw speed in the LFT-D process leads to better dispersion of the fibers, as expected, and at the same time to greater fiber shortening. Overall, this still results in better mechanical properties [151]. This is confirmed by the mechanical tests carried out by Rohan et al. on PA6 CF produced at different screw speeds. They were able to show that the mechanical properties decrease with lower screw speeds and more bundles occur. However, material inhomogeneity in the form of fiber bundles was observed at all screw speeds [152].

2.3.6 Failure mechanics in Dico-FRP

The fracture of composites is primarily characterized by the initiation and propagation of cracks and the deformation behavior of the matrix. In-depth summaries of the fracture mechanisms in Dico-FRP can be found in [153, 154, 155, 7, 156]. The general mechanisms during failure are characterized by:

- Debonding of fibers
- Fiber sliding
- Delamination
- Pullout
- Fiber break
- Brittle or ductile matrix failure

Usually, these phenomena occur simultaneously, but with varying intensity. Especially the matrix failure is strongly dependent on the test environment (load case, temperature and moisture content) and the fiber orientation in the composite [154, 7]. In general, failure at the micro level can be divided into five successive stages, which are illustrated in Figure 2.16.

In the initial stage, interfacial microfailure begins at the fiber tips due to tensile stress concentration in the surrounding matrix. This microfailure leads to the separation of the matrix from the fiber tips. At low strain, cracking initiates primarily at the ends of the longest fibers oriented in the direction of strain. As strain increases, crack initiation shifts more to the ends of the shorter and more disoriented fibers [156, 157].

In the second stage, micro-fracture propagation occurs along the interfaces of the fiber sides, accompanied by a concentration of shear stress within the matrix along these sides. If the matrix-fiber interaction is weak, failure can occur in the interface itself, leaving little matrix residue on the fiber surface. Once the shear deformation reaches a critical value, micro-fracture propagates from the fiber tips along their sides.
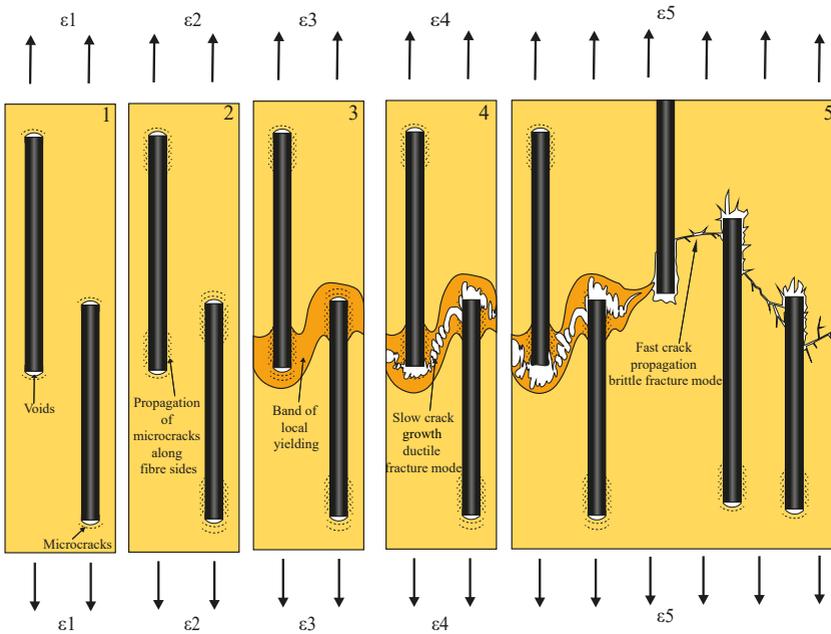
Figure 2.16: Model of microfailure process of Dico-FRP separated into 5 steps with **1** occurrence of microcracks and void at fiber ends, **2** propagation of microcracks along fiber sides, **3** occurrence of band of local yielding, **4** slow crack growth leaving ductile fracture mode **5** fast crack propagation leaving brittle fracture mode with $\varepsilon_1 < \varepsilon_2 < \varepsilon_3 < \varepsilon_4 < \varepsilon_5$ according to [156].

Subsequently, in the third stage, a band of plastic deformation occurs in the matrix induced by the micro-fractures surrounding the fibers. This results in a localized stress concentration within the matrix region. The plastic band then propagates along the micro flaws at the fiber sides and tips [158, 156, 7, 157].

In the fourth stage, the process is characterized by crack opening and the subsequent phenomenon of slow crack propagation. When the deformation limit of the matrix within the deformation band is reached, crack initiation begins. This crack then gradually propagates through the band, establishing links between the micro-fractures along the fiber sides and tips. During the

complex process of slow crack propagation, the fibers experience extraction from the matrix, which precedes the advancement of the crack tip [158, 156, 153].

Upon reaching a critical size, the subsequent catastrophic crack propagation unfolds in a brittle manner within the composite. This represents the fifth stage and is the peak of micro-failure, where a significant proportion of the fibers are often detached from the matrix due to the previous structural damage along the fiber surfaces (cf. Fig. 2.16 1-2). This can be recognized by a step-like surface on the fracture surfaces. For more brittle matrix materials, the fourth stage is omitted and the crack opening coincides directly with the fifth stage [158, 156].
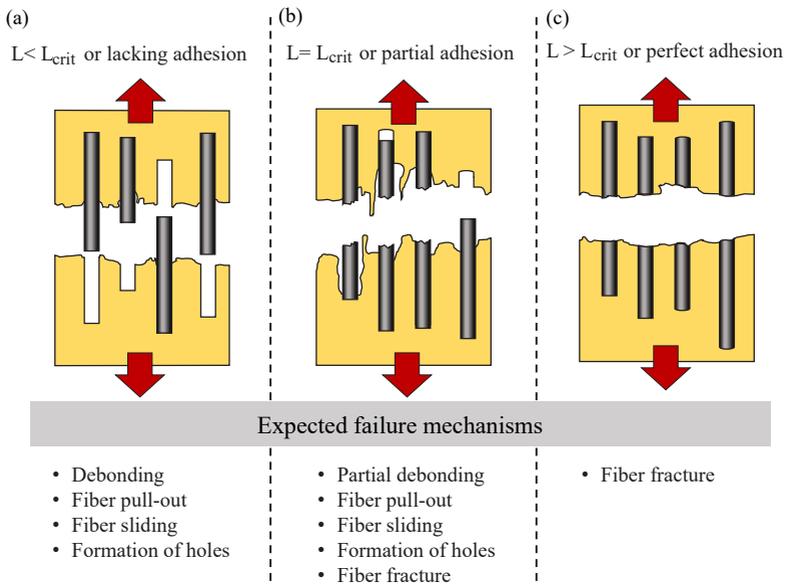
Figure 2.17: Schematic illustration of the appearance of different failure characteristics of a UD-Dico-FRP loaded in the fiber direction as a function of fiber length with respect to L_{crit} (cf. Sec. 2.1.3.1) or adhesion according to [154, 7].

In general the mechanisms governing the fast brittle crack propagation and fracture depend on the fiber length, the fiber orientation, and the quality of the interface.

In cases where the fiber orientation is parallel to the load direction, failure modes such as fiber-matrix debonding, pull-out, fiber slippage, and/or fiber fracture can be induced. Conversely, when the fiber orientation is perpendicular to the load direction, interface separation between fibers occurs, accompanied by crack propagation along the interface or within the matrix [7]. Figure 2.17 shows the different crack propagation mechanisms for an aligned Dico-FRP as the function of fiber length with respect to L_{crit} or adhesion when loaded in the direction of the fibers (0°). In Figure 2.18 the same is shown for when loaded transversal to the direction of fiber (90°).
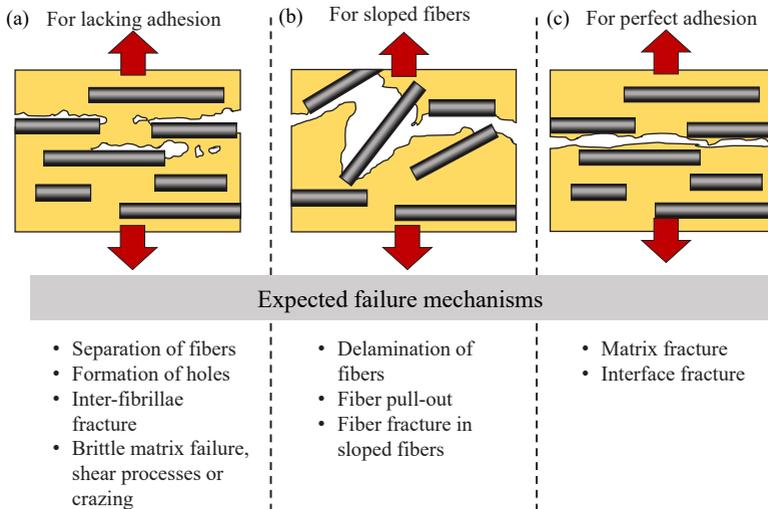
Figure 2.18: Illustration of the appearance of different failure characteristics of a UD-Dico-FRP loaded 90° to the fiber direction adhesion according to [154, 7].

As shown in the previous chapter, Dico-FRP is often characterized by a complex fiber orientation distribution and rarelyexists in completely aligned states. Therefore, in real DicoFRPs, a mixture of crack propagation mechanisms shown in Figure 2.17 and Figure 2.18 occur.

When different fibers are incorporated in the composite, the fracture mechanisms become more complicated. Using both, CF and GF as a reinforcement in one composite, Li et al. showed that the interfacial debonding under increasing loads occurs primarily at the CF ends. As the applied stress continues to increase, cracks propagate as described above along the length of the CF and into the adjacent matrix, but in the presence of GF, these cracks are "bridged," increasing the loading capacity of the CF in the hybrid composites and resulting in a positive synergistic effect on their strength[159].

2.4 Thermoplastic Co-FRP (Co-FRTP)

In the case of UD-FRTP, only the tapes used in this work and their further processing into semi-finished products are discussed.

2.4.1 Unidirectional fiber-reinforced tapes

Unidirectional fiber-reinforced tapes, also known as UD tapes, are a promising alternative to woven fiber-reinforced organic sheets because the fibers can be oriented in any desired load direction without featuring an undulation. This opens up the possibility of producing component-specific products with minimal material waste [160, 161]. For the production of such tapes, fibers are impregnated directly from rovings with a thermoplastic matrix. For impregnation of such thin fiber layers, the combination of a calender and an extruder with a film die is very effective, especially when used with thermal post-spreading equipment as shown in Figure 2.19 [162].
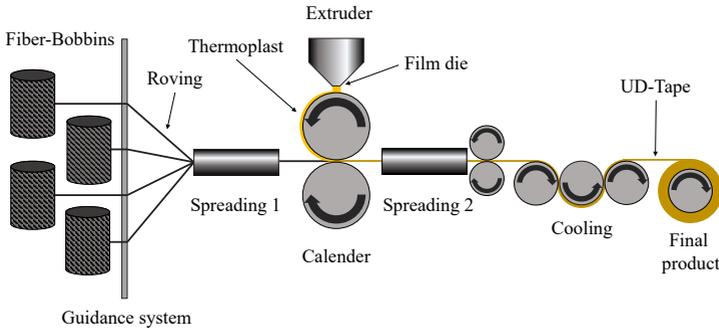
Figure 2.19: Schematic diagram of a production line for thermoplastic UD tapes in accordance with [162].

However, UD tapes are only a semi-finished product and are usually processed into larger structures or used as a reinforcing element. These variants are discussed below.

2.4.2 Two-dimensional preforms

UD tapes can be laid side by side to create two dimensional geometries and stacked on top of each other in various orientations to create structural components or reinforcing elements. The layered structure can be adapted to the respective loads by placing the layers in different orientations [161]. This offers several advantages over woven organo sheets. For example, there is no longer a dependence on organo sheets with predefined layers, but they can be produced individually. Figure 2.20 shows a comparison of a 2D preform made from organosheets and tapes of different width.

In the example shown in the Figure 2.20, halving the tape width in this case also means halving the cutting waste. However, the time required to lay down the tapes also increases significantly, since more than twice as many tapes have to be laid down. This again leads to a trade-off between cycle time and resource efficiency, which must be coordinated with the other process steps [161]. The
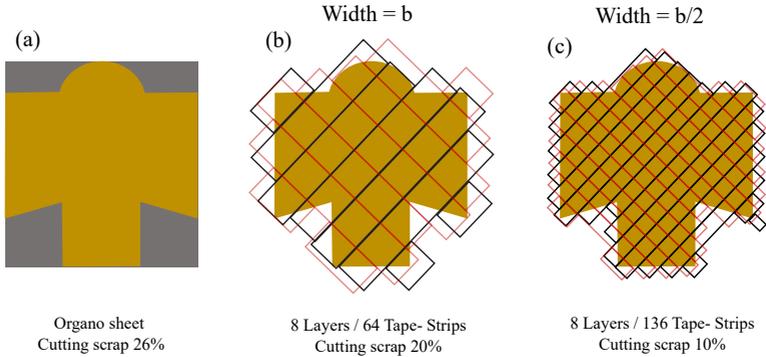
Figure 2.20: Schematic representation of the production of a two-dimensional preform on the basis of a woven organosheet and by the use of UD-tapes with different widths including the comparison of the cutting scrap based on investigations of [161].

mechanical behavior of such materials can be determined by the description of Co-FRPs in Section 2.1.2 or by the Halpin-Tsai method with infinite long fibers in Section 2.1.4.1 and the application of classical laminate theory in Section 2.1.4.3.

2.5 Continuous-discontinuous-LFT composites

Continuous-discontinuous-fiber-reinforced plastics (CoDico-FRP) represent a new class of composite materials. As they consist of two different material classes, Co-FRP and Dico-FRP materials, CoDico-FRP can be described as hybrids. The motivation for such material classes is to combine the partially opposing advantages of Co-FRP and Dico-FRP (cf. Fig 2.1), for example to combine complex geometries with high specific material properties [5, 80, 163]. A schematic representation of which properties can be combined in CoDico-FRPS according to Böhlke et al. is given in Figure 2.21 [5].
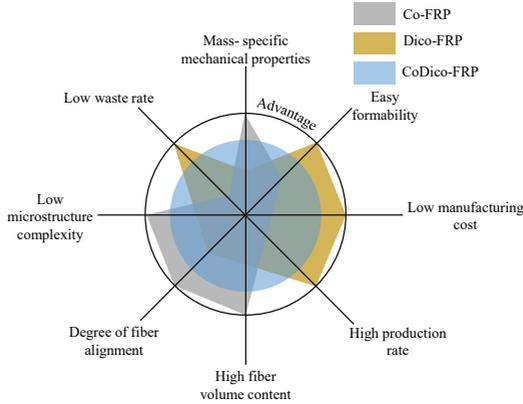
Figure 2.21: Schematic comparison of the advantages and disadvantages of Co-, Dico- and CoDico-FRP in accordance to Böhlke et al. [5].

However, in order to be able to discuss the different effects of such hybrids in more detail, it is first necessary to take a fundamental look at the concept of hybrids.

2.5.1 General aspects of hybrid materials

Hybrids are basically defined by the fact that they consist of two or more different materials which, when combined, have properties that they could not provide individually, or, in other words to combine two or more materials to obtain materials with specific properties that cannot be covered by the known materials. A good illustration of this is given by the Ashby diagrams, where two material properties are plotted on their axes and different materials are placed as data points in the diagram. For example, if you look at the modulus of elasticity versus density plot as shown in Figure 2.22, you will see that there are gaps, or holes, in the upper left corner and the lower right corner. These are holes that need to be filled by the hybrid materials [164, 165, 166, 13]. At this point, it is reasonable to raise the objection that the composites discussed so far, consisting

of both fiber and matrix material, could also be classified as hybrids. However, because they behave similarly to a homogeneous material and their properties are predominantly determined by the average of the two components, they can be considered a single class of material [13, 19].
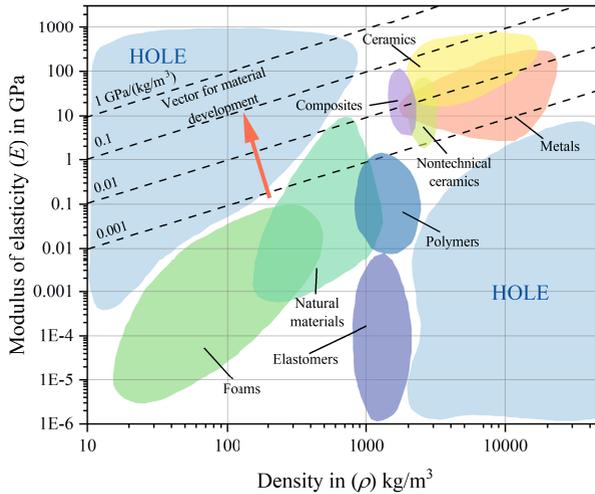
Figure 2.22: The modulus over density space with marked areas of common engineering materials, accompanied by gaps that indicate potential avenues for the development of novel materials according to Ashby [13].

However, an exception is made for special composites, such as those fabricated from two distinct reinforcing fibers within a single matrix system. In such cases, the term "hybrid composites" is employed [167]. This definition will be used consistently throughout the remainder of this work. Hybrid composites can be further categorized based on the degree of the dispersion of the individual fiber types, which is shown sorted by increasing dispersion in Figure 2.23 [168, 169, 170]. Thereby Figure 2.23 (a) shows a low level of dispersion characterized by distinct layers for each fiber type, which can be improved by

increasing the number of layers or reducing their thickness, as shown in Figure 2.23 (b). Alternatively, dispersion can be improved by hybridization at the fiber bundle level, as shown in Figure 2.23 (c) and reaches the optimal dispersion, when the different fiber types are randomly distributed Figure 2.23 (d) [170].
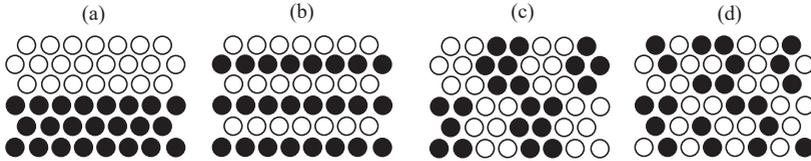
Figure 2.23: Various hybrid composite configurations with different degrees of dispersion: (a) two layers, (b) alternating layers, (c) bundle dispersion, and (d) completely random dispersion according to Swolfs et al. [170].

2.5.2 Effects of hybridization

Figure 2.24 shows two types of materials labeled as M1 and M2 in a diagram with properties P1 and P2, where high values of P1 and P2 are desirable. Mixing these materials creates several possibilities. The Figure illustrates four typical scenarios that represent different hybrid classes. Depending on the shape and combination of materials, one of the following options may be observed [165].

In the "best-of-both" scenario, bulk and surface properties are combined, e.g. for galvanized steel. For the mixed scenario, the effective properties correspond to the arithmetic mean of the properties of the components. For some hybrids, however, weaker properties may dominate, resulting in a value below the mixing rule. In the "least of both" scenario, a component is designed to fail prematurely, e.g. a wax-metal hybrid as a temperature-dependent trigger for sprinkler systems [165, 13, 19].
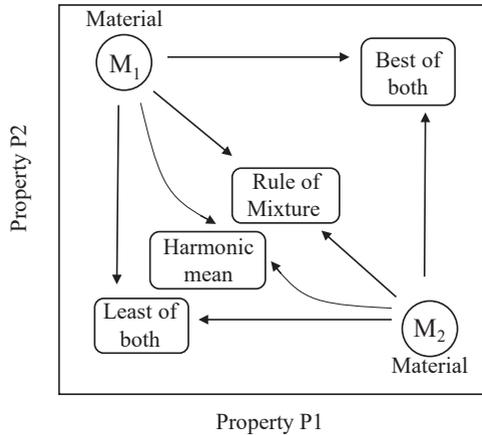
Figure 2.24: Potential effective characteristics of hybrid materials arising from the attributes of their individual components [165, 13].

Swolfs et al. outlines two main approaches to define the hybridization effect, as illustrated in Fig. 2.25 [170]. In Figure 2.25a), the hybridization effect is expressed as the deviation of a specific property from that of the individual components. Swolf et al. highlight the elongation at fracture as particularly noteworthy, as fibers from one component can exhibit considerably greater elongation in the hybrid configuration compared to a monofiber composite [170].

This effect can be interpreted positively or negatively depending on which component serves as the reference point. In Fig. 2.25b), the hybridization effect is assessed by comparing it to the RoM, as defined in Eq. 2.3, where the hybrid's properties are calculated as a weighted sum of its constituent components. A positive effect indicates an improvement over the RoM, while a negative effect signifies a deviation from it [170].
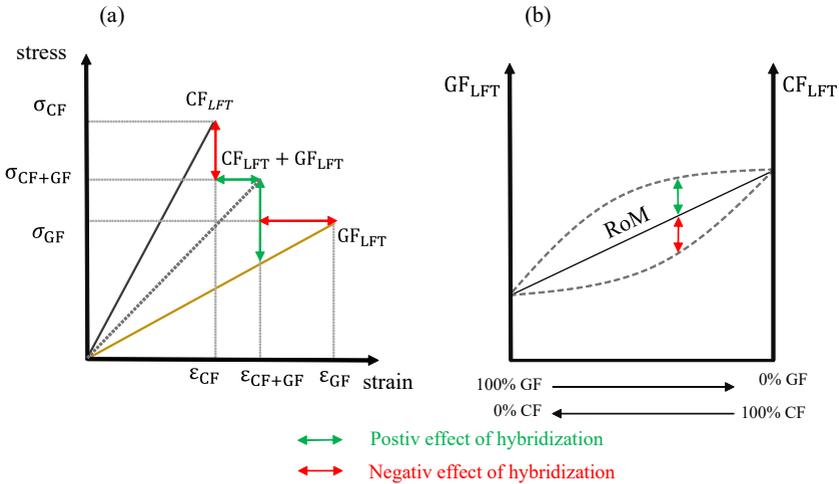
Figure 2.25: Definition of the hybridization effect according to Swolfs et al. with a) deviation of a distinct property of the hybrid with respect to one of the components and b) deviation from the "Rule of Mixture" (RoM) in positive or negative direction [170].

2.5.3 Existing concepts of hybrid or mixed fiber composites

Combinations of several fiber types in a hybrid composite were first investigated with continuous fibers and a thermoset matrix system, where no positive hybridization effect according to definition (b) in Fig.2.25 could be determined with respect to tensile modulus. The behavior of materials in this scenario adheres to the Rule of Mixtures (RoM) [167, 171]. Kretsis et al. validated this observation, demonstrating that for hybrid laminates based on epoxy, both compressive and flexural strength fall below the RoM [169].

Conversely, more encouraging outcomes emerged with fiber type combinations in discontinuous fiber-reinforced thermoplastics [172, 173, 39]. Fu and Lauke et al. identified a positive hybridization effect in the tensile ultimate strength and elongation at break of a (CF+GF) short fiber-reinforced polypropylene composite, while tensile modulus behaved in accordance with the RoM [172].

The positive hybridization effect in terms of elongation at break can be explained as follows. Cracks that form at the ends of the carbon fibers do not lead to failure of the hybrid composites because the glass fibers act as crack arrestors [172], which could be confirmed by Li et al. [174]. Additionally, Fu and Mai et al. demonstrated positive hybridization in fracture toughness for a similar hybrid [173]. Given the early interaction of fiber types in the LFT-D process and the utilization of properties from both fibers due to relatively long fiber lengths, hybrid LFT-D composites exhibit substantial potential. Fu et al. were able to show that glass and carbon fiber rovings introduced into a polymer melt via a twin-screw extruder, lead to longer carbon fibers and shorter glass fibers compared to single-fiber composites [173]. As mechanical characterization is time-consuming, adequately describing material parameters such as hybrid material stiffness through homogenization approaches is particularly intriguing. Yan et al. achieved promising outcomes for short GF+CF-reinforced PP using the two-step shear lag modified Halpin-Tsai method based on the classical laminate theory as described in 2.1.4 [70].

2.5.4 Existing concepts of CoDico-FRP

There are already several examples in the literature of the hybridization of Co-FRP and Dico-FRP to CoDico-FRP on a thermoplastic basis. Thereby overmolding is a prevalent technique in the production of thermoplastic CoDico-FRP, offering a seamless integration without the need for adhesive application. In the overmolding process, Co-FRTP eg. preconsolidated tapes are placed at selected positions in the mold and then overmolded with Dico-FRTPs eg. LFTs. This overmolding process offers a number of significant advantages, including the synergy of the LFT and Co-FRTP components, targeted local reinforcement only in the required areas, cost-efficient production compared to conventional semi-finished products such as GMT and GMTex, the ability to substitute rib and lattice structures, improved damage tolerance, increased crash resistance while reducing weight, and the promotion of recyclability [175, 176].

Overmoulding can be implemented in different processes, whereby the majority of studies deal with the injection molding process [177, 176]. However, there are some basic procedures that can also be applied to compression moulding.

Gusti et al. were able to demonstrate, that the temperature plays the main role in forming a good interface between the Co-FRTP and Dico-FRTP. They demonstrated that increasing the melt temperature and holding pressure increases weld strength by facilitating intimate contact between the two polymers and promoting interdiffusion of macromolecules [178]. As the preheated composite material cools down quickly in the ambient air or in the cooler mold, a fast handling system is of great importance. If the temperature after inserting the organic sheet into the injection mold is not high enough, additional heating is unavoidable.[177]

Akkerman et al. were able to confirm this but also showed that at higher interfacial temperatures, the Co phase was strongly deformed due to deconsolidation and the flow of the injected resin in the transverse direction to the fiber orientation of the Co-FRP, resulting in a mesostructure that differs markedly from the prepared orientation. [179]

A similar observation that there should be a certain stability in the Co phase was already made by Tanake et al. They hybridized carbon/PA6 LFT with a Co-FRP in an injection molding process. It was found that the optimum interfacial strength of 19.2 MPa was achieved at a mold temperature of 190 °C. However, at these temperatures, the Co-FRP was pressed into ribbed structures, so the highest mechanical strength of the entire component was not achieved [180].

Overmolding by injection molding has been successfully implemented in application-oriented prototypes. For example, Joo et al. developed a prototype front bumper using CoDico based on LFT and demonstrated its feasibility. In addition, they also emphasized that high flow rate and high injection pressure increase bond strength by facilitating improved interfacial diffusion, with injection pressure emerging as the most influential factor [6].

According to the knowledge of the author, the first studies on CoDico-FRTP produced by compression molding GF-PP-LFT over the Co-GF-PP were conducted by Thattaiparthasarathy et al. They compared pure rib geometries from LFT with flat hybrid samples from CoDico-FRTP and were able to show a higher reinforcement effect by the hybrids [181].

In contrast to traditional methods, the SMiLE project introduced an innovative approach known as the "local advanced tailored D-LFT process", which combines LFTs and Co-FRTPs. In this process, LFTs are strategically used in specific regions to reinforce the Co-FRTP structure and prevent buckling. As a result, wall thickness can be reduced and the overall weight of the final product can be reduced [182].

Behrens et al. investigated the interactions in a combined process of draping flat continuous semi-finished products and overpressing them with flowable GMT compounds in a flat form with partial layout of the GMT. Undesired fiber displacements occur in UD-fabrics depending on the orientation of the flow front to the fiber orientation. This effect is insignificant for fabrics and laminates with different fiber layer orientations, but must be taken into account for overmolding unidirectional fabrics [183].

Alkwar et al. overmolded GF-PP Tape strips in a [0/90] stacking sequence that were locally placed into the mold with GF-LFT-PP with 40 wt. %. The mechanical properties of pure 3.6 mm thick LFT- specimens are compared with those of 3.6 mm thick hybrids containing (a) 1.2 mm and (b) 1.8 mm cross-ply tape strings. An increase in flexural strength for variant (a) of 65 % and for (b) of 77 % with a simultaneous increase in flexural strength of (a) 119 % and (b) 143 % was determined. In all tests, the Co phase was positioned on the tension side. The fracture patterns in variant (a) showed that the tape was fully utilized. This led to fracture in the tape and then further crack development in the LFT, while delamination was also seen in variant (b). This is due to the fact that the interface is in the neutral axis and therefore exposed to a higher shear zone.

An increase of the hybrid in absorbed energy of 273 % on average was also achieved under impact [175].

2.6 Scientific questions

As noted earlier, numerous studies have explored concepts for manufacturing and designing hybrid composites and continuous-discontinuous FRP composites using a thermoplastic matrix material. Experimental analyses conducted by different researchers underscore the favorable mechanical properties and potential of this hybrid approach. In order to gain a comprehensive understanding of hybridization to CoDico, it is essential to grasp the interrelationships between the process, structure, and properties of the Dico material from the LFT-D-ILC process holistically. It is of paramount importance to ascertain whether employing multiple fiber types in a Dico material yields favorable hybridization effects. Such inquiry could shed light on the potential for recycling, streamline the separation process based solely on matrix material, and eliminate a sorting step. This comprehensive understanding of Dico materials facilitates further exploration into how hybridization to CoDico influences material behavior even under environmental conditions like temperature and humidity.

Microstructure and process-induced anisotropy of discontinuous LFT with different fiber compositions

To gain a full understanding of the LFT-D-ILC process, it is imperative to first understand the process-structure-property relationships of pure discontinuous LFT. This includes understanding the compression molding step and its impact on the final fiber orientation and distribution, as discussed in Section 2.3.3. In addition, studying the microstructure with respect to fiber dispersion behavior and evaluating whether fiber blends provide synergistic effects during impregnation in the extruder are critical areas of interest. Consequently, it should be possible to deduce the influence of these microstructural factors

on the effective direction-dependent mechanical properties. The following questions arise:

- How can the characteristic microstructure of monofiber or mixed fiber reinforced LFT-D-ILC composites be described? Does it resemble the microstructure of conventional LFT material with typical features such as fiber bundling and shell-core effect?
- Can mixed fiber LFT achieve specific mechanical properties that are superior to those attainable with monofiber LFT?
- How do processing parameters, in particular an extended flow path, influence the anisotropy of mechanical properties?
- Are there discernible differences between the region initially covered with material and the region where only flowed material is present in the mold?
- Can the mechanical properties be predicted from microstructural observations using established homogenization techniques?
- Can the fracture behavior of LFT be described by the failure mechanisms for Dico-FRP outlined in Section 2.3.6?

Characterising the effects of hybridization and assessing failure mechanisms in hybrid continuous-discontinuous carbon fiber LFT

Trauth [80] developed appropriate evaluation methods for continuous-discontinuous SMC composites to assess the effect of hybridization. Nonetheless, the applicability of these methods to continuous-discontinuous LFT composites remains uncertain.

- Which component dominates the mechanical performance in a certain load case?
- Which component dominates the damage evolution and critical failure?
- Can the hybrid be described as the sum of its parts, or are there synergies?
- How do different areas of Dico phase affect the behavior of the hybrid?

Characterization and evaluation of the effects of hybridization on the temperature and humidity-dependent behavior of hybrid continuous-discontinuous carbon fiber LFT

Thermally induced transitions in thermoplastics have already been discussed in detail in Section 2.2.1 . Of particular interest are the effects of these transitions on discontinuous LFT, continuous tape fabrics, and continuous-discontinuous LFT to evaluate the hybridization effect in a wider range of applications. Since the absorbed moisture also has an influence on the transition mechanisms, it is also important to understand, which effects occur in the matrix material and how they are transferred to the composites and the hybrid. This leads to the following questions:

- How do the marix transition mechanisms affect the mechanical behavior of the composites and hybrids studied?
- How does the anisotropy of the mechanical properties behave with increased temperature and moisture load?
- Can established homogenization methods be used to predict composite behavior based on temperature-dependent matrix properties and previous microstructural studies?
- Does the load case influence the transistion mechanisms in the matrix, composites and the hybrid?

3 Materials and specimen geometries

3.1 Materials and manufacturing

The materials studied in this work is polyamide 6 (Technyl®star provided by DOMO Chemicals Gmbh in Leuna, Germany) in unreinforced form and with various fiber reinforcements. The fibers in the materials are either discontinuous (Dico), continuous (Co) or a combination of both (CoDico). The Dico materials are LFTs (Dico-LFT) produced on a LFT-D-ILC machine with subsequent compression molding. A total of three materials with different fiber compositions were examined for the Dico phase investigations. One with pure CF (CF_{LFT}), one with pure GF (GF_{LFT}) and one with a mixture of equal amounts of CF and GF ($CF + GF_{LFT}$). The CF that were used were always "PX3505015W-61" (ZOLTEK) with a tex number of 3750 and the GF always "StarRov ® 895 2400" (Johns Manville) with a tex number of 2400. According to their respective data sheets, both types of fibers are well-suited for use with polyamides. For the Co and CoDico-LFT, only CF was used as reinforcement fiber for both phases. Prefabricated UD tapes (TECHNYL®LITE) were used as semi-finished products for the Co-phase. These were also provided by DOMO Chemicals GmbH in Leuna, Germany. It is important to mention here that the fibers and matrix of the UD tapes correspond to the types mentioned above.

3.1.1 Manufacturing of PA6 plates

Owing to the low viscosity of the molten polymer, it was not possible to produce unreinforced PA6 sheets using compression molding, since the transfer of the initial charge to the press is done manually and requires a certain minimum viscosity. Therefore, these sheets were produced at Fraunhofer ICT in Pfinztal, Germany, by injection molding on an "Engel DUO CombiM 700" (ENGEL AUSTRIA GmbH) out of PA6 granulates in a mold with a strip gate and dimensions 180 mm × 180 mm × 3 mm according to the injection moulding advice provided by DOMO.

3.1.2 Manufacturing of LFT plates (Dico-LFT)

The LFT-D plates were manufactured at Fraunhofer ICT in Pfinztal, Germany, using the LFT-D-ILC machine from Dieffenbacher GmbH Maschinen- und An-lagenbau, Eppingen, Germany, shown schematically in Figure 2.14, consisting of two Leistritz twin-screw extruders (TSE) and a Dieffenbacher press. The first TSE, a Leistritz ZSE 40HP GL/32D with 55 kW power, was utilized to plasti-cize the PA6 pellets and homogenize them with additives which were provided in the form of a masterbatch. The second TSE, a Leistritz ZSE 40 GL/14.5D with 27 kW power, was employed to combine the plasticized PA6 and the fibers, subsequently facilitating mixing via shear forces within the extruder. The screw geometries for both TSEs are described in detail in [126]. All materials were produced with a consistent polymer flow rate of 25 kg/h and a targeted fiber volume content of 25%. The sheets with a plagued thickness of 3 mm were pressed by using the Dieffenbacher press (type DYL 630/500) equipped with a polished steel plunging edge tool measuring 400 mm × 400 mm and applying a maximum pressure of 200 bar on the filled sheet. A side insert position was selected to ensure the formation of a flow front during the pressing process for mold filling. The pressing process with lateral insertion position is shown schematically in Figure 3.1 (a) to Figure 3.1 (d). The finished sheet can be divided into two areas: the charge area and the flow area, as illustrated in Figure

3.1 (e). It is important to note that this is a conservative estimation, as the initial charge only occupies approximately a quarter of the mold. However, this is made to ensure that the phenomena caused by the flow process are completed in the flow area and are present over the entire gauge length of the samples to be cut later. Additionally, different orientations with respect to the direction of the developing flow front are defined as shown in Figure 3.1 (e), serving as reference points for subsequent orientation-dependent characterization and homogenization [127].
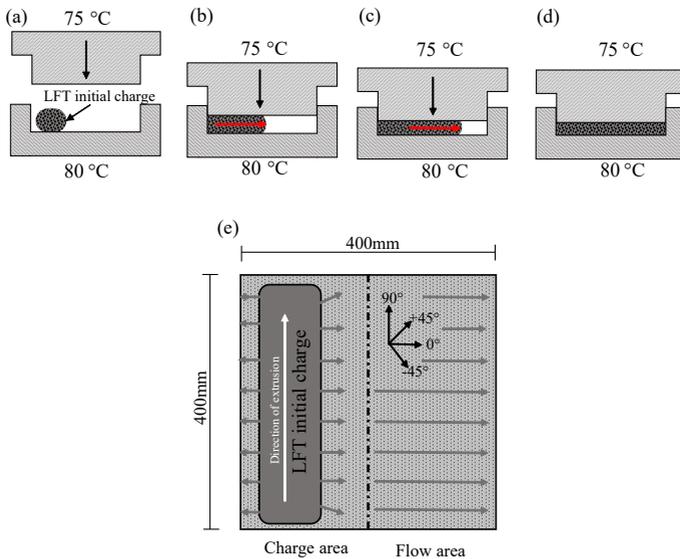
Figure 3.1: (a-d) Compression molding process with side insert area of the initial charge and flow path, (e) position of the initial charge, division of the finished plate into charge and flow area and definition of the orientation relative to the flow path from Scheuring et al. [127].

Special attention should be paid to this definition of orientations, as it is used as the basis for the orientation-dependent characterization in the following. All orientation-dependent results are presented in such a way that 0° orientation is defined from left to right (i.e., in the horizontal plane), and angular deviations are described as positive upward and negative downward.

3.1.3 Manufacturing of Co plates

To ensure subsequent recyclability both, the matrix and the fibers in the Co and Dico layers are identical. Specifically, 100 mm wide and 0.13 mm thick unidirectional tapes of TECHNYL LITE, supplied by DOMO Chemicals GmbH in Leuna, Germany, were used to fabricate the Co plates. These plates were fabricated with the necessary layups for characterization or subsequent reinforcement of the LFT plates. Initially UD tape layups are produced by using a Fiberforge provided by Dieffenbacher GmbH Maschinen- und Anlagenbau in Eppingen, Germany. Figure 3.2 shows the individual process steps. The first layer consists of seven 100 mm wide and 700 mm long tapes that are placed next to each other (cf. Figure 3.2(a)). In order to ensure an overlap, the second layer was offset by half a width, i.e. 50 mm, on the first layer in the same orientation. To ensure complete coverage of the first layer, it is therefore necessary to cover the second layer with one more tape, resulting in a total dimension of 700 × 800 mm, (cf. Figure 3.2(b)).
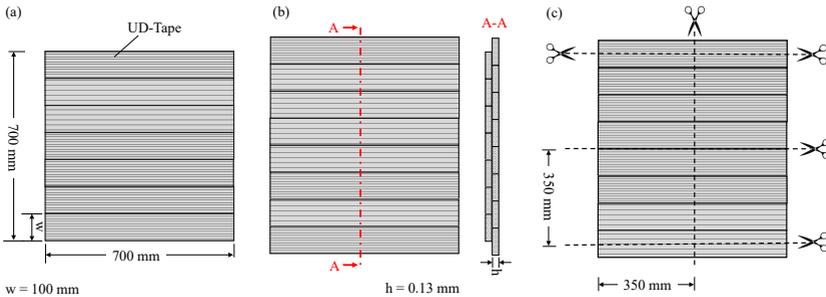
Figure 3.2: Process steps of manufacturing of the Co plates with: (a) laying the first layer out of seven 100 mm wide and 700 mm long UD tapes (b) second layer of eight UD tapes in the same orientation offset by half a width, i.e. 50 mm, and (c) cutting the consolidated layup into four 350 mm × 350 mm plates.

The tapes are loosely positioned on top of each other and only locally welded at a small spot to fix the positioning of the tapes. For further processing it is

important to consolidate the layup. This step occurs between Figure 3.2 (b) and Figure 3.2 (c) and is accomplished in a two-step procedure. First, the tapes are heated to 280°C in a contact oven manufactured by WICKERT Maschinenbau GmbH, Landau in der Pfalz, Germany. Subsequently they are subjected to consolidation at 80 °C and 20 bar of pressure between two metal plates in a Dieffenbacher DYL 630/500 hydraulic press. After the consolidation, the Co plates are cut into pieces measuring 350 mm $\times$ 350 mm, suitable for the subsequent Co-molding process described in the following as shown in Figure 3.2(c).

3.1.4 LFT overmoulded Co plate (CoDico-LFT)

For the manufacturing of the CoDico-LFT on plate level, a special process adaptation was developed. Since the unidirectional reinforcement on one side of the plates causes warping after cooling, a kind of sandwich layer structure was chosen in which both sides of the plate are reinforced with Co layers. This ensured that it was possible to prepare the test specimens at a later date without them deviating from the standard due to deformations. The Co plates produced as explained above were cut smaller than the mold, as contact with the mold wall was to be avoided in order to prevent wrinkling which would lead to poor interface qualities and a complex microstructure. The individual steps of the co-molding process are shown schematically in the Figure 3.3 (a) to Figure 3.3(g). The first step is to place two of the Co plates from section 3.1.3 each on a PTFE foil with the dimension of 390 mm $\times$ 390 mm to leave a margin for later manual handling (cf. Fig. 3.3) (a)).

The UD sheets are then preheated to 280 °C in a contact oven from WICKERT Maschinenbau GmbH, Landau in der Pfalz, Germany. For this purpose, another layer of PTFE foil is placed on top of the Co plates to ensure that the Co plates do not adhere to heated surface of the contact oven as shown in Figure 3.3) (b). This second PFTE foil is removed from the Co plates after the entire structure has been removed from the oven after a heating time of 30 seconds. However,
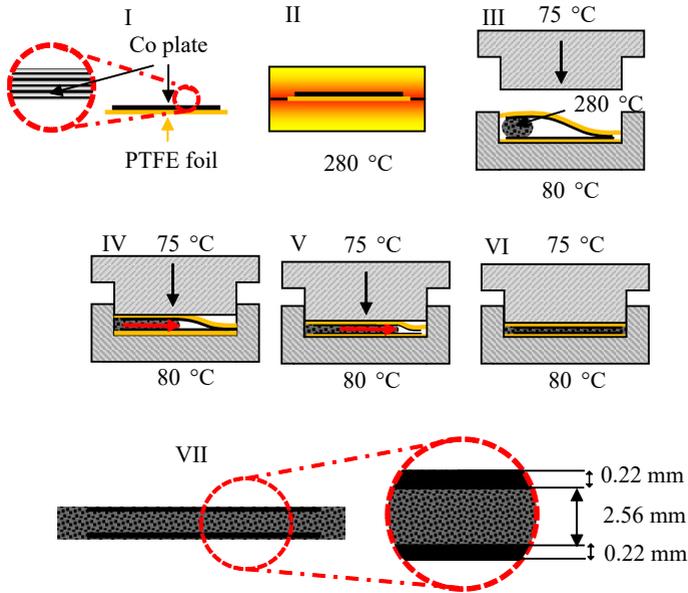
Figure 3.3: Compression molding process with side insert and flow path, which divides the plate into charge and flow area with different orientations.

the bottom layer is retained, since PTFE foil is crucial for the subsequent processing steps, as it stabilizes the otherwise unstable unidirectional Co plates while maintaining their fiber orientation.

The next step is then to strategically place the heated layups with the PTFE foil and the initial charge in the mold as shown in Figure 3.3) (c). This process step is carried out manually by two people. Initially, the first person positions the initial hot co-layup within the mold, aligning the fiber orientation from left to right. The Initial charge, is then carefully positioned from the second person onto the first Co plate in the same position as in the production of the Dico-LFT sown in Figure 3.1(a). Subsequently, the second Co plate is layered again by the first person on top of the initial charge, in such a way, that the PTFE foil is again between the mold and the Co plate, i.e. there is direct contact between Co plate and the initial charge.

For a deeper understanding of the loading sequences, the individual steps are illustrated in Figure 3.4 with pictures from the real process.
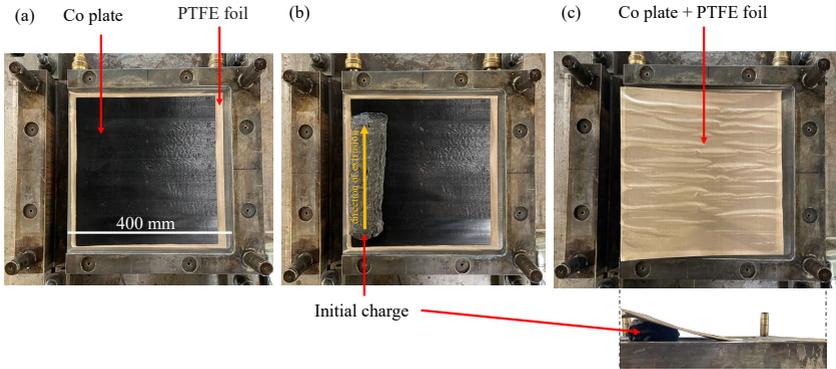
Figure 3.4: The individual steps of loading the mold with from Figure 3.3 step III with (a) placement of the first co-layups on PTFE foil into the mold with fiber orientation from left to right, (b) placement of the initial charge on the left side into the mold with extrusion direction from bottom to top and (c) placement of the second co-layups with PFTE film.

Since the temperature plays a major role in the quality of the interface that is formed during co-molding, the coordination of time to avoid cooling of the individual parts during the co-molding phase is crucial. Therefore, simultaneous to the heating process of the Co plates, a PA6 CF LFT-D-ILC initial charge, is produced in the same way as already explained in Section 3.1.2. The process times are adapted to each other so that the hot Co plate and the initial charge are available at the same time. As mentioned earlier, the PTFE foil is mainly a handling aid, but since it is placed between the mold and the fabric, it also acts as an insulator between the 280 °C heated Co plate and the 80 °C hot mold.

The co-molding process shown in Figure 3.1 (d) to Figure 3.1 (f) is executed with a fast press closing profile, moving at a speed of 30 mm/s to minimize

cooling of all constituents. The flow front develops as a result of closing and spreads between the two Co plates and ensures that they remain at the edge of the finished plates in the already mentioned sandwich structure. At the beginning of the pressing process, the only places where the two Co plates are held in position are the contact points with the initial charge and the contact points with the mold. Therefore, in the flow area, there may well be slight shifts of the Co layups to the orientation that was selected when they were placed into the mold. The CoDico-LFT plates were produced with a plagued total thickness of 3 mm, and the molding is carried out at a pressure of 200 bar for a duration of 35 seconds. This meticulous process ensures the creation of CoDico-FRTP with the desired properties and structural integrity. Figure 3.3 (g) shows the individual proportions of Co and Dico-LFT of the finished in total 3 mm thick plates.

3.2   Specimen preparation and geometry

For each test, a specific sample geometry was used, based on the standards for the respective test. However, in certain cases, adjustments to the standardized specimen were necessary to emphasize the desired effects. To ensure consistent analysis of the hybridization effect and to minimize the effect of specimen geometry, a uniform specimen geometry was adopted for Dico-LFT, Co, and CoDico-LFT in each test. Owing to the inherent variations in dimensions during plate fabrication and subsequent sample preparation, all samples were dimensional measured according to DIN EN ISO 16012 [184] prior to testing. The measured values were then used for subsequent specimen evaluation.

3.2.1   Water-jet cutting

Specimens were cut from the pressed plates in an iCUTwater smart of the company imes-icore GmbH in Eiterfeld, Germany with a pressure of 1500 bar, a cutting speed of 300 mm/min and a flow rate of 250 g/min of cutting sand

Classic Cut 120 garnet provided by GMA Garnet Pty Ltd. in Perth, Australia. The manufacturer's specifications indicate a positioning accuracy of 80 µm/m and a repeatability of under 40 µm/m. To ensure that the position of the initial cut does not affect subsequent mechanical characterization, it was consistently chosen within the clamping area for all specimens. Additionally, a tangential cut with a 5 mm distance was selected. These cutting parameters yielded satisfactory results and dimensions for all Dico-LFT. Given the increased risk of delamination between the Co and Dico phase inherent in the CoDico-LFT, a tangential initial cut with a 15 mm distance was chosen. Despite potential delamination, sufficiently accurate sample dimensions could still be maintained.

3.2.2 Specimen geometries

3.2.2.1 Microstructure investigations

Micrographs were taken from 12 × 12 mm samples taken from the pressed plates along the center line from the charge and flow area for all material types (cf. Fig. 3.5 (a)). Since only micrographs with flow direction and expected fiber orientation were taken from the plane, the dimensions of 12 mm × h prove to be sufficient to get a comprehensive impression of the microstructure.

For the determination of key microstructural parameters, including FMC, the resulting calculated FVC, FLD, and FOD, larger 25 mm × 25 mm samples were selected. These dimensions provide a substantial volume for adequate statistics, based on a study by Blarr et al. on the sensitivity of sample size to microstructure values [185]. Three samples were taken from both the charge and flow area, and an additional three samples at the boundary between the two areas. The exact sampling location is shown in the Figure 4.1. The selection of this sampling position aims to enable the mapping of any alterations in the microstructure as a function of the flow path.
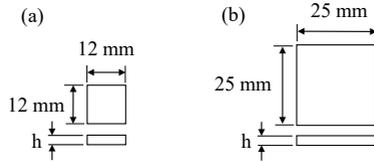
Figure 3.5: Sample geometries for the microstructure examinations with h as plate thickness which is nominally 3 mm (a) for the microsections and (b) for the µCT examinations, the fiber content measurements and the fiber length measurements.

3.2.2.2 Tensile Test

Since in this work not only the direction-dependent mechanical properties of both continuous and discontinuous LFT materials are to be investigated in the tensile test, but also the hybridization effect, a uniform specimen geometry was chosen for all material states and types. Since dog bone specimens can be problematic with unidirectional materials, leading to longitudinal cracks in the radius, a rectangular geometry was chosen. Trauth's research showed that both, the scatter and the results for dog bone and rectangular specimens in Dico-FRP are very similar [186]. Therefore, the 200 × 15 mm specimen shown in Fig. 3.6 was chosen as the tensile specimen for Dico-LFT, Co and CoDico-LFT. The specimens were clamped with a free gauge length of 100 mm. The entire gauge length was sprayed with a pattern for DIC. However, an area component of approximately 70 mm × 10 mm was chosen for the evaluation of the tensile modulus of elasticity to avoid edge effects on the one hand and the influence of the clamping on the other hand. Three virtual extensometers were placed in the gauge area in the X and Y directions, whose mean value and the mean of the strain of the entire gauge area were used to determine the elastic tensile modulus according DIN-EN ISO 527-4 [187].

200 mm
100 mm
15 mm
h
70 mm x 10 mm
Gauge section for determining the modulus with DIC
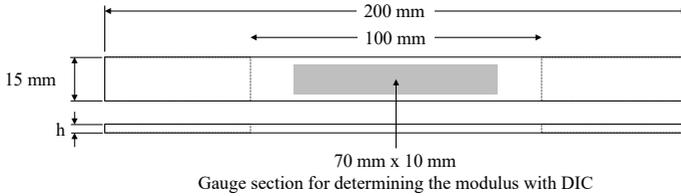
Figure 3.6: Geometry of a tensile specimen without end taps made of Dico-LFT with the dimensions 200 mm × 15 mm × h as plate thickness which is nominally 3 mm, the free test length of 100 mm and the gauge section with 70 mm× 10 mm for determining the elastic modulus using DIC.

It was not necessary to use end taps for the Dico-LFT as there was sufficient failure in the gauge length. For the Co and CoDico-LFT materials, the specimen were provided with end taps in the clamping area to ensure uniform load application. As a result, a sufficient number of specimens failed in the gauge length.

200 mm
100 mm
15 mm
h
70 mm x 10 mm
Gauge section for determining the modulus with DIC
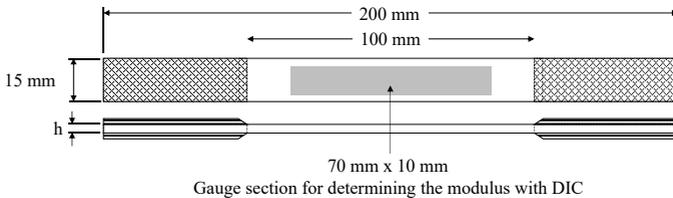
Figure 3.7: Geometry of a tensile specimen with end taps made of Co and CoDico-LFT with the dimensions 200 mm × 15 mm × h as plate thickness which is nominally 3 mm, the free test length of 100 mm and the gauge section with 70 mm× 10 mm for determining the elastic modulus using DIC.

3.2.2.3 Bending Load

Since the main focus of the bending tests is also on determining the hybridization effect, a uniform specimen geometry was also selected for all materials. In accordance with the standard DIN EN ISO 14125,2011 [188] rectangular specimens illustrated in Figure 3.8 with a width of 15 mm and a length of 100 mm

were used for the bending test. As the pure Co samples were only available in a maximum thickness of 0.5 mm, bending tests on the pure Co material were not carried out.
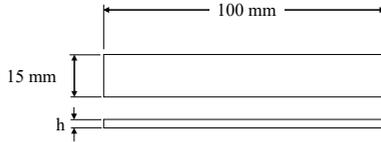
Figure 3.8: Geometry of a bending specimen made of PA6, Dico-LFT and CoDico-LFT with the dimensions 100 mm × 15 mm × h as plate thickness which is nominally 3 mm.

3.2.2.4 DMA

For the tensile DMA tests, the same specimen width was used as for the tensile test. However, the 160 mm specimens were shorter than the tensile test specimens. The clamping on both sides was again 50 mm, resulting in a free specimen length of 60 mm. This is due to the fact that the DMA is designed to run at the highest possible frequencies. This is only possible with small strains, so the free length was reduced. Since the stiffness of the DMA was determined from the crosshead travel and the previously determined machine stiffness, end taps were not used for all material types. The geometry in the Figure 3.9 is therefore valid for all material classes. For the DMA tests under bending load, the same specimens as for the quasi static bending tests, shown in Figure 3.8 were used for all materials.
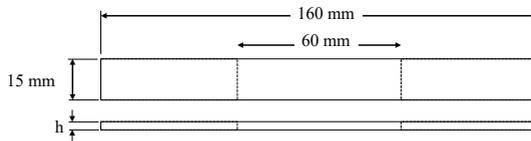
Figure 3.9: Geometry of a DMA specimen under tensile load made of Co, Dico-LFT and CoDico-LFT with the dimensions 160 mm × 15 mm × h as plate thickness which is nominally 3 mm and the free test length of 60 mm.

3.2.3 Conditioning procedure

After cutting, the samples were dried in a vacuum oven at 50 °C for at least 240 h. After this period, regular weighing showed no further weight loss. The samples were then hermetically sealed and additionally stored in a dessicator with silica gel to ensure that no moisture was absorbed during storage. This condition is examined and characterized in more detail in this work and is defined as "dry". If a special conditioning was carried out, the conditioning was always started from the "dry" state. The samples were weighted dry so that the amount of water absorbed could be quantified later by re-weighing.

In this work, another state is examined in more detail: the saturation state after storage in distilled water. Since conditioning at room temperature takes several months to reach saturation, accelerated conditioning at 50 °C was chosen. Regular weighing showed that no further weight increase could be observed after a storage period of one week. This was therefore assumed to be the saturation state. To prevent the conditioned samples from drying out, the samples were stored in distilled water at room temperature after conditioning. Further weighing prior to the experiments confirmed that the saturation state was already reached after storage at 50 °C. This condition is referred to below as "wet".

As these two conditioning states represent the two extreme values, a further conditioning state was also investigated in order to analyze the effect in unreinforced PA6. For this purpose, the samples were conditioned in a Vötsch climatic chamber at 70 °C and 80 %rH. No increase in weight could be determined after a period of time. However, a time of 240 h was also selected here. This condition is referred to below as "moist". The samples were clamped directly from the climate chamber into the testing machine to prevent them from drying out. A summary of the individual conditioning state and the weight fraction of absorbed water relative to the matrix fraction within the material at the saturation state according to Equation 2.37 and Equation 2.39 is shown in Table 3.1.

Conditioning state	Procedure	Saturation state in wt% of water in matrix material
dry	240 h in 50 °C vacuum atmosphere	0
moist	240 h in 70 °C wet air with 80 %rH	5
wet	240 h in 50 °C distilled water	8.2

Table 3.1: Conditioning states, along with their respective procedures, and the weight fraction of absorbed water relative to the matrix fraction within the material according to Equation 2.37 and Equation 2.39.

4 Experimental procedures

This chapter outlines the individual experimental methods, their implementation, and the calculation of the effective material properties.

4.1 Microstucture investigations

This section describes the experimental procedures and the analyses used in this study to analyze the microstructure and describe characteristics such as FVC, FLD and FOD.

4.1.1 Fiber volume content (FVC)

Fiber content measurements were performed at the Fiber Institute Bremen (FIBRE) in Bremen, Germany. The matrix of nine samples per material type with a dimension of 25 mm $\times$ 25 mm was exposed to sulfuric acid. Previously, the samples were dried and weighted to obtain the mass of the composite. Wet chemical removal of the matrix was chosen because preliminary tests in a TGA showed that ashing of the matrix without incinerating part of the carbon fibers could not always be guaranteed. This could be due to a poor nitrogen atmosphere. Valid results were obtained for the pure GF_{LFT} with the TGA as the GF showed no sensitivity to ashing . However, in order to use a uniform method for all materials investigated in this work also the fibers of pure GF_{LFT} samples were exposed using this method. However, the GF_{LFT} is a special case, as the TGA also provided valid results here and are therefore used for a

Material	Densitiy ρ in g/cm^3	Source
CF	1.8	[189]
GF	2.5	[190]
PA6	1.14	[191]

Table 4.1: Density of the base materials utilized taken from the respective data sheet of the manufacturer.

later comparison. After the matrix was dissolved, the remaining fibers were weighed again and thus the mass weight was determined according to Equation (2.2). The densities from the data sheet for the PA6 and the respective fiber density were then used to determine the fiber volume content to Equation (2.1). The values used are also given in Table 4.1.

All samples were previously scanned in the μCT to enable fiber orientation measurements and to attribute variations in fiber volume content to possible fiber bundles. In order to visualize possible flow effects on fiber length and fiber content, three samples each were taken from the charge area, from the boundary between the charge and flow area, and from the flow area. The exact sampling locations are shown in Fig. 4.1.

4.1.2 Fiber length distribution (FLD)

The fiber length distribution analysis was performed on the exposed fibers with FiberShape from Innovative Sintering Technologies AG at FIBRE in Bremen, Germany. Operating at a resolution of 5400 dpi, particles and fibers as small as 7 μm can be distinctly identified. FibreShape and its variants successfully demonstrated that the method provides identical results across laboratories with appropriate documentation [192]. Owing to the impracticality of measuring every exposed fiber, a representative sample was extracted from each of the nine specimens per material type for measurement.
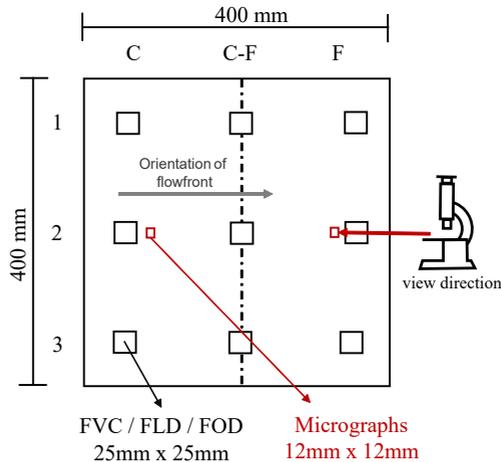
Figure 4.1: Representative size, position and labelling of the fiber content- (FVC), fiber length-(FLD) and fiber orientation- (FOD) specimen in a plate. "C" denotes a specimen out of charge area, "F" denotes a specimen out of flow area and "C-F" labels the intermediate zone. "1", "2" and "3" signify the position concerning the y-axis from Scheuring et al. [127]

4.1.3 Micrographs

For the micrographs, 12 mm ×12 mm specimen were prepared from the charge and flow area, respectively shown in Fig.4.1. All micrographs were taken with the 0° orientation, i.e. the flow front, pointing out of the image plane as shown in Fig. 4.1. Three samples were embedded in a cylindrical mold with VariCem. After curing, the grinding was carried out in increments starting with a grain size of 320, then 600, then 1000 and finally 2500 (grain sizes are specified according to DIN 69176). Each embedded mold had a contact force of 10 N. The grinding wheel rotated at 200 rpm and the sample holders rotated in the opposite direction at 60 rpm. Each step was ground for 2 minutes. After these steps the samples were then polished, again step by step with polishing paste with a grain size of 6 µm for 3 min, then 3 µm for 2 min, then 1 µm for 1,5 min. For all polishing steps, gamma polishing discs were used, which are softer and thus prevent the fibers from "tearing out". After each polishing step, the samples were cleaned in an ultrasonic bath to ensure that no coarse-grained paste affected

the next step. In all polishing steps the polishing wheel rotates at 130 rpm and the sample holder rotates at 60 rpm in the same direction. The light microscopic images were taken by using the Axiovert 200 MAT digital inverted microscope from Carl Zeiss AG, with multiple images being stitched together directly in the software. The microsections of the samples containing carbon fibers did not require post-processing, as the carbon fibers are easily distinguishable from the matrix material due to their strong reflection. Conversely, with glass fibers, which possess similar translucent properties to the matrix material, partial post-processing of the images was necessary to facilitate fiber identification. Only the contrast and brightness have been changed.

4.1.4 X-ray computed tomography

For the µCT microstructure analysis of the LFT materials, nine specimens per material system, whose specific positions and labels are already shown in Figure 4.1 were used. Characteristic structures of the Co plates were optically identified and used to investigate the pure Co phase. The selected sites, identifiable from pre-existing tensile samples, were scanned for further analysis. All specimens were scanned using an YXLON-CT precision µCT system from Yxlon International CT GmbH in Hattingen, Germany. This system features a µm-focused X-ray transmission tube with a tungsten target and a PerkinElmer Y.XRD1620 high-resolution flat-panel detector with 2048 pixels × 2048 pixels. Each material was subjected to individual scan parameters, which are listed in the table 4.2. The projections were reconstructed into a 3D volume using the Feldkamp cone-beam algorithm [193].

Table 4.2: Scan parameters for the different material types according to Scheuring et al. [127].

Parameter	CF$_{LFT}$ and CF+GF$_{LFT}$	GF$_{LFT}$	Co
Voltage in kV	110	125	120
Current in mA	0.13	0.12	0.12
Voxel size in µm	17.39	19.17	13.61
Line binning parameter	2	2	2
Number of projections	2220	2100	3000
Exposure/Integration time in ms	800	1000	1000

4.1.5 Fiber orientation determination

The fiber orientation was determined according to the method of Scheuring et al. [127]. Only the basic procedure is described here; for a more detailed explanation and further evaluation methods, please refer to the original paper by Scheuring et al.[127].

The fiber orientation determination based on the reconstructed µCT data was performed with a C++ code implemented by Pinter et al. [60] by the structure tensor based method creating a vector-valued image with the orientations per voxel. The tensor resulting from the dyadic product of the gradient in each voxel is then computed to the second-order fiber orientation tensor by summing the element-wise products of two image channels across all voxels of each specimen. Following this, the orientation tensor is normalized by its trace. After converting the matrix data to point data, the angles θ, restricted to the range 0° to 180° (i.e., 0 to π) due to the symmetric nature of the distribution beyond this interval, are derived using the four-quadrant inverse tangent. The θ data are then segmented into $n_{centers} = 20$ bins, each spanning an interval arc length of $n_i \in [i \cdot \pi/20, (i + 1) \cdot \pi/20)$, where $i = x \in \mathbb{N}_0 : x < 20$. The frequency of occurrence of angles falling within each bin is then tallied, resulting in a discrete fiber orientation histogram [127].

4.2 Mechanical characterization

4.2.1 Quasistatic tests

4.2.1.1 Tensile tests

Tensile tests were performed according to DIN EN ISO 527-4 2020 [194] and ASTM D3039 [195] on a Zwick Roell Universal testing machine equipped with a 20 kN load cell, hydraulic clamping jaws and a commercially available digital image correlation system (GOM-Aramis 4M Adjustable, containing two 4MP Teledyne Dalsa cameras with 50 mm Schneider Kreuznach objectives) to record strain. The samples were pre-painted white, followed by applying a black speckled pattern over the entire gauge length. The recording frequency was 5 Hz. From all materials (CF_{LFT}, GF_{LFT}, $CF + GF_{LFT}$ and CoDico-LFT), for both areas (charge area, flow area) and for each orientation (0°, ±11.25°, ±22.5°, ±45°, 90°), at least five valid samples, that failed in the valid gauge length, were considered for further evaluation. A strain range of 0.05 % to 0.25 % was considered for the evaluation of modulus of elasticity and Poisson's ratio. The calculation was performed using the least squares method in accordance with ASTM E111-17 [196]. In order to use corresponding matrix properties for modeling, tensile tests were performed on samples of injection molded unreinforced PA6 using the same dimensions. Since the PA6 is assumed to be an isotropic material, however, no direction-dependent investigations were carried out here. For all specimens tensile modulus of elasticity E, tensile strength σ_m, elongation at break ε_b and Poisson's ratio ν_{12} were determined.

4.2.1.2 Bending tests

To test a larger volume, the bending tests were carried out as four-point bending based on DIN EN ISO 14125 [188] on a ZwickRoell universal testing machine with a 2.5 kN load cell. The preference for 4-point bending over 3-point bending is due to the advantage of eliminating shear forces within the material volume

between the two central supports. The lower supports had a distance of 81 mm and the upper supports a distance of 27 mm. Deflection was measured using an extensometer in the middle of the samples. Specimens with orientations of 0°, ±11,25°, ±22,5, ±45° and 90° each from the charge and flow area were tested. Flexural modulus was determined between 0.05 % and 0.25 % strain. Each orientation was tested with a minimum of eight specimens. A test was considered invalid if specimens fractured at the jaw level. A minimum of five valid specimens was considered sufficient to consider the series usable.

4.2.2 Dynamic mechanical analysis

In order to be able to test a representative volume element of discontinuous fiber-reinforced plastics, large speciment are required and thus also higher forces during the test. Since the load capacity of standard test equipment for performing a dynamic mechanical analysis (DMA) is limited, in this work an Instron E3000 ElectroPulsTM with a nominal force of 3 kN and a load cell capacity of 5 kN was used. The machine was equipped with a temperature chamber of Instron with with liquid nitrogen cooling and a temperature range of -100 °C to 350 °C. Figure 4.2 shows the set-up for the tensile load test. The test specimens were clamped in the clamping jaws with four screws each, which were tightened to 12 Nm, whereby a constant measuring length of 60 mm was maintained. To protect the load cell from overheating during the test, a water cooling system was used to ensure accurate force measurement.

Since the elongation of the specimen was measured by recording the movement of the crosshead the tests were carried out, with including the machine stiffness. These were determined by a steel sample with known stiffness and subsequently included in loss and storage modulus schematically shown in Fig 4.3. The steel specimen was also run at all tested frequencies at similar forces to see if the measurements were affected by natural frequencies of the testing machine. No influence could be determined up to the highest frequency of 5.623 Hz tested in this work. The relationship between the stiffness of the test frame (E_{frame}) and
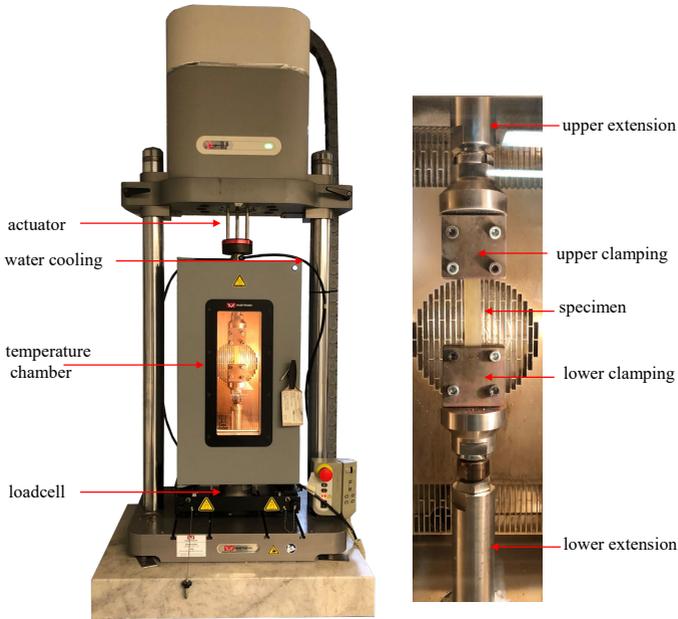
Figure 4.2: Instron E3000 ElectroPulsTM equipped with a temperature chamber of Instron and the set-up for testing under tensile load.

the stiffness of the specimen (E_{specimen}) was considered as a friction circuit, so the adjustment can be described with the total measured stiffness E_{total} by Eq.4.1.

$$E_{\mathrm{specimen}} = \frac{E_{\mathrm{total}} \cdot E_{\mathrm{frame}}}{E_{\mathrm{frame}} - E_{\mathrm{total}}} = E^* \tag{4.1}$$

The determined machine stiffness, which is used for further calculations, is 18.35 kN/mm which shows a good agreement with the determined value of Sessner, who used the same setup for his tests and determined a stiffness of the test frame of 17.2 kN/mm [88].

All experiments were performed as combined temperature and frequency sweeps were the temperature was varied with 10 K steps. In the range around T_{g}, which was taken from the data sheet (60 °C), smaller temperature increment
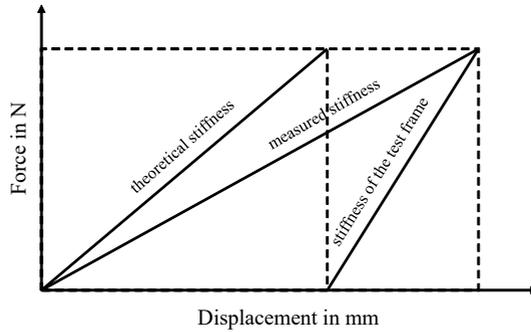
Figure 4.3: Schematic representation for calculation of the test frame stiffness.

of 5 °C were selected, to achieve a finer resolution there. For the tests in the wet state, the approximate position of T_g was determined by a preliminary test and the test program was adapted in such a way that the temperature was increased in 5 K steps in the area around T_g. The test direction was selected from low to high temperature. After reaching the initial temperature, with an absolute preload of 5 N and a waiting time of 1800 s, the first cycle was started. Each cycle consisted of an absolute average strain phase followed by testing at different frequencies. The frequency steps were performed from 0.1 Hz to 5.623 Hz, with 4 steps selected per decade. For each frequency, the number of load cycles was selected so that the load occurred for one minute at each frequency. As start-up effects occur during a frequency change, the first 25 % of the cycle is excluded from the evaluation. For the remaining cycles, all DMA characteristic values were determined and then the mean value of the last 75 % was calculated. Once the new temperature was reached, the sample was held at 5N for 600 s to ensure that the entire sample had reached ambient temperature. This cyclic process continued until the final temperature was attained.
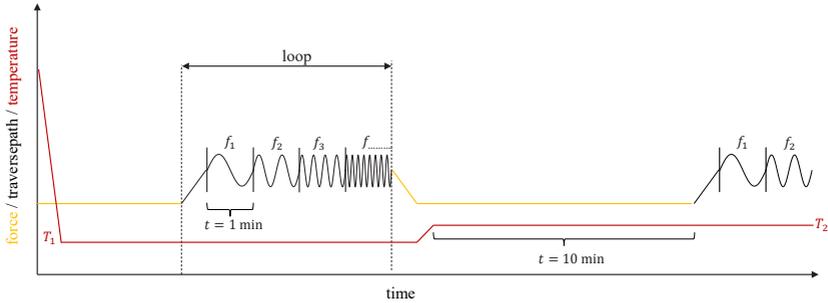
Figure 4.4: Test procedure DMA under tension with temperature and frequency sweeps.

The energy method stored in the WaveMatrix testing software was used to calculate the loss and storage modulus. In this method ratio of the areas of the hysteresis loop and an ellipse bounded by the force and displacement amplitudes of the hysteresis loop is used and calculated according to the formula 4.2.

$$\delta = \arcsin \frac{\text{energy}}{\pi \cdot \frac{\text{traversepath}}{2} \cdot \frac{\text{forcerange}}{2}}, \tag{4.2}$$

with the energy equal to the area enclosed by the hysteresis loop (integral of the force over the displacement) shown in figure 4.5. For the calculation of the storage modulus E', the complex elastic modulus or dynamic modulus E^*, which is the ratio of stress to strain range (see Fig. 4.5), is multiplied by the cosine of the loss angle.

The tests were carried out under tensile loading and under three-point bending in accordance to DIN EN ISO 6721-1 [197] and ASTM D4065-20[198].
The experiments under tensile loading were strain-controlled with a strain ratio of $R = 0.3$. To avoid falsification of the stiffness measurement, all specimens were tested without end taps. In this way, the influence of the adhesive layer of the end taps can be neglected.
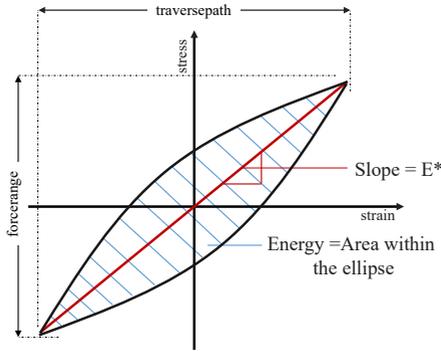
Figure 4.5: Hysteresis loop with elliptical surface as energy for calculating the loss angle with the energy method.

The bending were carried out on selected samples under three-point bending with a support distance of 62 mm. Since only small forces were required for the bending tests, the influence of the frame stiffness was not taken into account here. The cross head travel was used as the displacement measurement, since this proved to be sufficiently accurate in a comparable setup compared with a laser extensometer shown by Trauth et al. [199]. The notation and abbreviations for all further evaluations of the DMA results are given in table 4.3

Table 4.3: Symbols for the results of the DMA examinations and the application of the principle of time temperature superposition.

T_{g}	Glass transition temperature
T	Temperature
E^*	Complex modulus $E^* = E'(1 + i\tan\delta) = E' + iE''$
E'	Storage modulus $E' = E^* \cdot \cos\delta$
E'_{norm}	normalized Storage modulus $E'_{\mathrm{norm}} = E'/E'_{0\mathrm{C}}$
E''	Loss modulus
$\tan\delta$	Damping factor E''/E'

4.3 Fracture surface analysis

The fracture surfaces of selected samples were examined in a Zeiss Leo Gemini 1530 scanning electron microscope (SEM) at an acceleration voltage of 6 kV, and images were captured using an Inlens detector sensitive to secondary electrons. The fracture surfaces were sawn off at a sufficient distance from the surface and then attached to a specimen holder with conductive tape. A conductive connection was created between the sample holder and the fracture surface with a thin line using conductive lacquer. The prepared specimen holder was then coated with a thin layer of gold for approximately 20 s in a argon gas low pressure atmosphere using the Cressington Sputter Coater 108auto from Cressington Scientific Instruments. No subsequent image processing was carried out for the images presented in this work.

5 Experimental results and discussion

The results are consistently denoted with a color-coded system, as depicted in Figure 5.1. This systematic application of colors serves to effectively distinguish between various material classes and positions. In some cases, the microstructure parameters for the LFT materials were averaged over the entire plate. In this case, a mixed tone was selected from the two areas. For the representation of the mechanical characteristics of the LFT materials and the CoDico-LFT, the charge area is shown as a circle and the flow area as a triangle for additional differentiation of the positions.
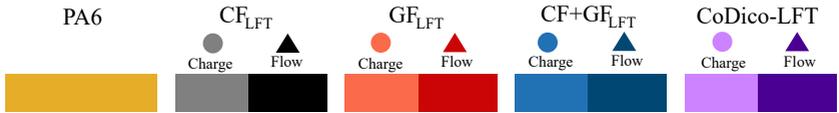
Figure 5.1: Color-coded symbol system to identify each material and extraction position.

5.1 Microstructure

5.1.1 Fiber mass content / Fiber volume content

Figure 5.2 shows the results of the fiber mass content (FMC) studies using wet chemical removal of the matrix for (a) CF_{LFT}, (b) GF_{LFT} and (c) $CF + GF_{LFT}$. Significant differences in FMC were found in certain samples, which is typical for LFT materials. This effect occurred in all materials tested. The specimen with particularly high FMC could be attributed to the presence of fiber bundles based on the analysis of the µCT data.
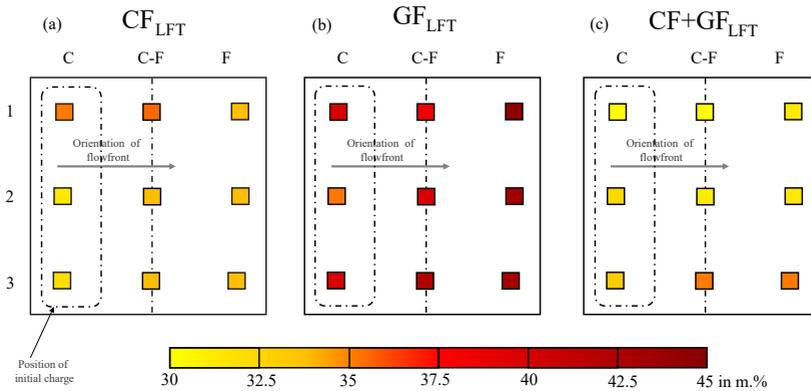
Figure 5.2: Fiber weight content of (a) CF_{LFT} plaques and (b) GF_{LFT} and (c) $CF + GF_{LFT}$ obtained by wet chemical re movement.

The results of CF_{LFT} and $CF + GF_{LFT}$ do not show a recognizable orderly distribution of the higher FMC, but appear to be largely randomly distributed. In contrast, an increase in FMC from charge to flow area can be seen across the entire plate of GF_{LFT}. The GF seems to be strongly influenced and carried along by the polymer flow, leading to a gradient in fiber content. This gradient manifests as lower fiber content in the charge area, slightly higher between the charge and flow areas, and reaching its peak in the flow area at all three extraction

positions. Since only one sheet was examined here, this observation may also be due to random effects, and confirmation of the effect would have to be carried out using other sheets. For this purpose, the preliminary examinations by TGA can be used at this point to confirm this effect, since no ashing effects occurred in the GF of GF_{LFT}, as mentioned previously in Section 4.1.1. The results of the TGA study are therefore shown in Figure 5.3. It can be seen that a higher FMC in the flow range can also be determined for GF_{LFT} here.
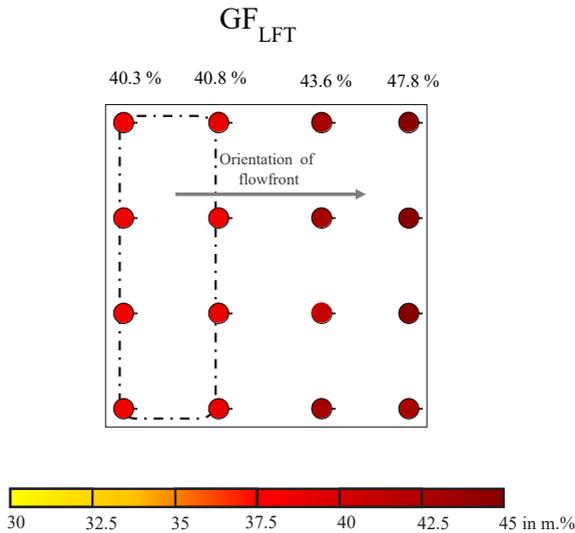
Figure 5.3: TGA-Results of GF-LFT

For a more precise understanding, Table 5.1 shows the experimentally determined FMC and the resulting calculated fiber volume content (FVC) for all material types, with the help of the density information of the fibers and the matrix given in Table 4.1. The results are categorized into the three extraction areas and presented as averages over all three specimen. In particular, materials with only one type of fiber (CF_{LFT} and GF_{LFT}) show an effective achievement of the target volume percentages of 25 %. However, for CF_{LFT} the average

FVC was slightly lower by 1.5 % and for GF_{LFT} it was lower by 0.34 %. This indicates a reliable adjustment of the desired volume content of the individual fibers. In contrast, the hybrid material has a significantly underestimated fiber volume content of about 20 %. When evaluating mechanical properties, the lower volume fraction in the hybrid must be carefully considered.

Table 5.1: Results of fiber weight content and of fiber volume content from wet chemical removement and resulting fiber length distribution from Scheuring et al. [127].

Material Region	w_f in %	v_f in %	L_p in mm	L_n in mm	Median in mm
CF_{LFT} (C)	32.90	23.6	5.9	1.45	0.50
CF_{LFT} (C-F)	33.89	24.4	7.57	1.45	0.50
CF_{LFT} (F)	31.84	22.7	5.68	1.77	0.77
CF_{LFT} (Average)	32.88	23.5	6.38	1.55	0.54
GF_{LFT} (C)	37.96	22.8	5.38	1.45	0.62
GF_{LFT} (C-F)	42.08	24.89	5.40	1.13	0.49
GF_{LFT} (F)	43.91	26.3	3.93	0.97	0.52
GF_{LFT} (Average)	41.31	24.66	4.90	1.18	0.53
$CF + GF_{LFT}$ (C)	31.31	19.37	7.97	1.71	0.56
$CF + GF_{LFT}$ (C-F)	31.67	19.59	6.83	1.85	0.79
$CF + GF_{LFT}$ (F)	32.70	20.23	7.24	2.09	0.75
$CF + GF_{LFT}$ (Average)	31.89	19.73	13.6	1.86	0.68

For materials containing CF, a comprehensive analysis indicates that the different extraction areas have no discernible influence on the FMC, which points to a homogeneous distribution of the FMC across the entire plate. Therefore, the average value is used as a representative value for the entire plate and is used for subsequent homogenization. In GF_{LFT}, a difference between the individual areas as discussed before can be seen, but this is not particularly pronounced,

so that a general mean value is also used here for further homogenization. This ensures that a uniform method can be guaranteed.

5.1.2 Fiber length distribution

The fiber length measurements for each material, categorized into three extraction areas, are detailed in Table 5.1. This table encompasses the number average value (L_{n}), weight average value (L_{p}), and the median of the fiber length. The data within the table underscore notable distinctions in fiber length between the two monofiber materials. Specifically, CF exhibits a significantly lower susceptibility to fiber breakage during the extrusion process compared to GF, resulting in longer lengths in the final parts. Moreover, an extended average fiber length is evident in the hybrid material compared to both monofiber materials. In general, there is no noticeable influence of the sampling positions. For example, one area of each material examined shows slightly longer fibers, but this is a different area in each case. Since only a part of the exposed fibers per specimen could be examined in the fiber length analysis, the pre-propagation for the FLD analysis has a further influence. It is therefore likely that the deviations are statistical scatter. To be able to compare the fiber length distributions, the FLD is therefore considered to be homogeneous over the entire plate.

Figure 5.4 depicts the fiber length distribution graphs for the overall average of all specimens of $\mathrm{CF_{LFT}}$ (a), $\mathrm{GF_{LFT}}$ (b), and $\mathrm{CF + GF_{LFT}}$ (c). The histogram illustrates fibers categorized with a width of 75 µm. Each graph includes the exact number of measured fibers and characteristic values from the accompanying table. Additionally, the critical fiber length L_{crit}, calculated as per Eq. 2.8 with values provided in section 3.1.2, is marked by a black vertical line at 0.16 mm for CF and a red vertical line at 0.50 mm for GF. Even if individual fibers with a length of up to 25 mm could be measured in all materials, the histogram is cut off at 7 mm, since over 90 % of the measured fibers are located in this area. However, all measured fibers were considered for calculating the statistical values.
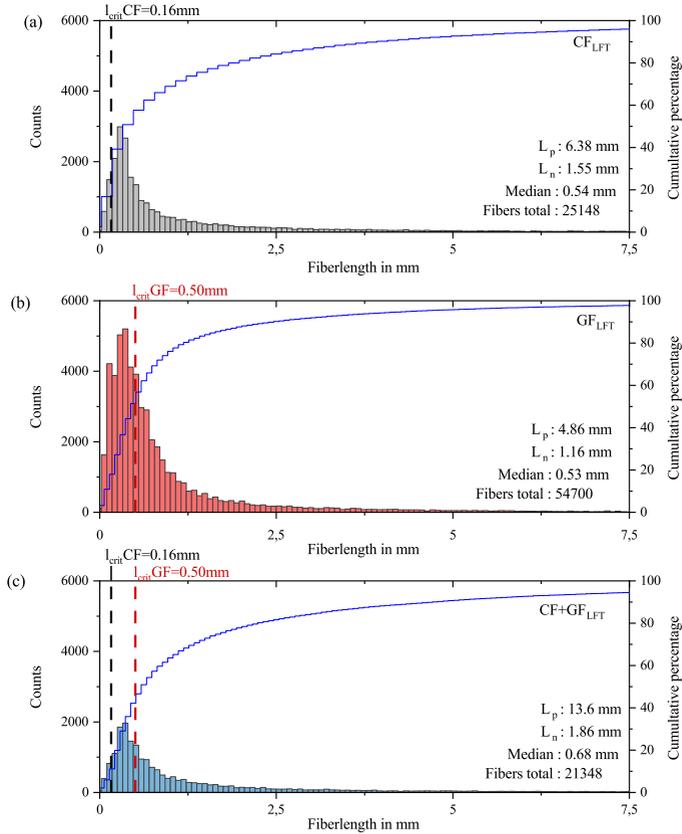
Figure 5.4: Fiber length distribution of all 9 specimens together divided into categories with a width of 75 µm, the critical fiber length according to Eq. 2.8 and the statistical moments for (a) CF_{LFT}, (b) GF_{LFT} and (c) $CF + GF_{LFT}$ according to Scheuring et al. [127].

Upon initial observation, the distribution curves for all three materials exhibit a similar appearance, with a substantial proportion of fibers falling within the 0 mm - 1.25 mm range. When considering L_{crit} in the monofiber materials, an evident observation emerges: approximately 80 % of CF fibers exceed L_{crit}, whereas for GF, only about half (approximately 50 %) surpass L_{crit}. Unfortunately, individual fiber lengths in the hybrid could not be determined; thus, only

the combined spectrum is considered for the hybrid. For a separate fiber length measurement, the CF could be ashed in an additional process step to measure only the GF length again.

5.1.3 Microstructural differences between charge and flow area

To analyze the microstructural differences between charge and flow area, microsections of the individual areas are considered below. In Figure 5.5 (a) therefore shows the division of the plate into charge and flow area and schematically the fiber orientation in the initial charge. Additionally in Figure 5.5 micrographs over the entire high of (b) CF_{LFT}, (c) GF_{LFT} and (d) $CF + GF_{LFT}$ from both charge an flow area are shown. In all micrographs, the viewing plane is perpendicular to the flow front or in other words the flow orientation points out of the plane. This does not apply to the schematic representation of the initial charge in Figure 5.5 (a), which is shown in the A-A sectional plane. The charge area of all three materials in Figure 5.5 (b), (c) and (d), shows the presence of two distinct regions across the cross section. A notable abundance of fibers is observed at the top and bottom edges of the plate where the fibers are cut into a highly elongated ellipse. This is indicating an orientation perpendicular to the flow direction. This is most noticeable in the CF_{LFT} and $CF + GF_{LFT}$, where both fiber types are cut as elongated ellipses in the edge area. Conversely, in Figure 5.5(c), the GF_{LFT} shows fewer fibers cut at the edge, which gives the impression that there are fewer fibers in the edge area. These edge effects are typical for compression molded LFT-D are commonly referred to as shells. The central area within the charge zone, referred to as the core, forms a significant portion of the microstructure. Within the core, all three materials have predominantly cut fibers that form short ellipses or circles. This pattern suggests that the fibers in the core are oriented in the direction of flow. Upon examination of the micrographs, it becomes evident that the edge regions of CF_{LFT} exhibit considerably higher fiber concentrations than GF_{LFT}. This observation, however, may be misleading due to the significantly reduced probability of encountering
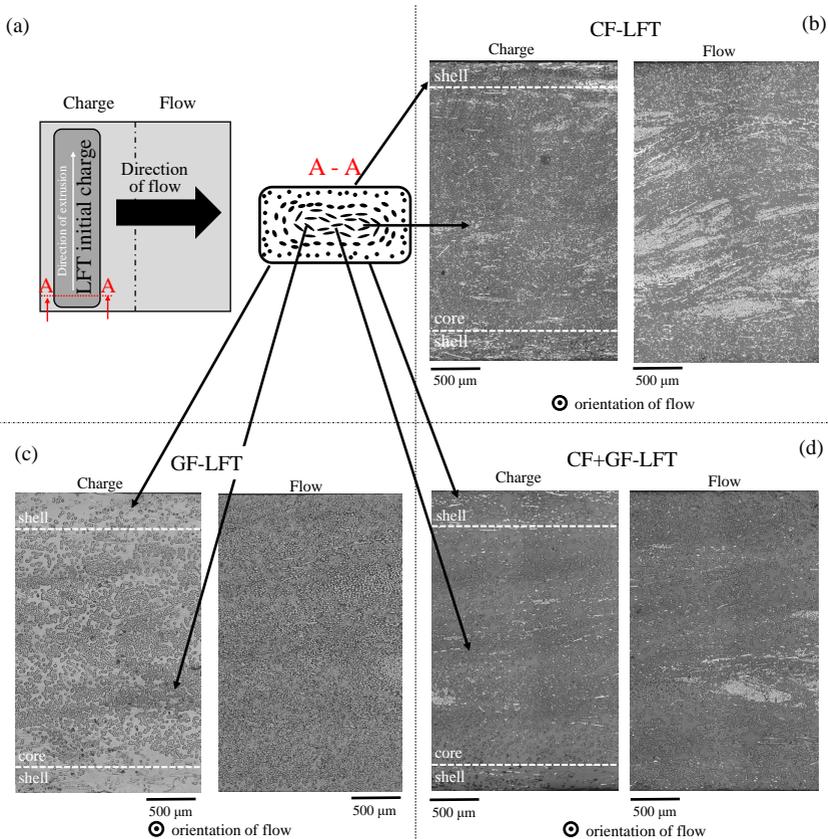
Figure 5.5: (a) Division of the plate into charge and flow areas, along with a schematic representation of fiber orientation in the initial charge. Micrographs of (b) CF_{LFT}, (c) GF_{LFT}, and (d) $CF + GF_{LFT}$ from both charge and flow areas with the viewing plane perpendicular to the flow front according to Scheuring et al. [127].

a fiber with an orientation approaching 90°. When considered alongside the comparatively lower number of fibers in the GF_{LFT}, the probability of cutting a 90° GF is significantly lower. Nevertheless, the zone of influence in CF_{LFT} appears to be more limited, resulting in a less uniform orientation. In addition, in $CF+GF_{LFT}$, GF seems to be mainly concentrated in the peripheral areas.

5.1.4 Fiber dispersion and bundeling

Since the separation and impregnation of the fibers only take place in the process through the second TSE, it is of particular interest how the fiber dispersion and impregnation looks in the final component. Figure 5.6 therefore shows micrographs of a $12\,\text{mm} \times 12\,\text{mm}$ specimen for the three Dico-LFT materials ((a) CF_{LFT}, (b)GF_{LFT} and (c) $CF + GF_{LFT}$) from the flow area.

The microstructures of the CF_{LFT} (Figure 5.6 (a)) and GF_{LFT} (Figure 5.6 (b)) thereby show clear differences. In most cases, the GF are largely surrounded by matrix and well distributed, except a few clusters that indicate an agglomeration of fibers to a so-called bundle. When the GF occurs in bundles, they are bundles with a manageable number of fibers, each of which appears to be well-impregnated. In essence, the portion of each individual fiber's circumference within the bundle that appears impregnated with the matrix outweighs the portion in contact with other fibers. In general, none of the micrographs of the GF_{LFT} examined showed any instances of completely unimpregnated GF.

In contrast, the CF in CF_{LFT} (cf. Fig. 5.6 (a)) also show good impregnation in areas with few fibers, but more often occur in bundles. Within these bundles, the number of fibers is significantly higher than in the GF_{LFT}, which in some cases leads to insufficient impregnation. A more detailed examination of the bundle in Figure 5.6 (a), which is only partially impregnated, reveals that the fibers become increasingly dense from the outside to the inside. They reach a point where they are so tightly packed that they are difficult to separate. Going further inside the bundles, there is another part where the fibers are less densely packed again, but are surrounded by black instead of the gray of the matrix and therefore surrounded by air. In some cases, black areas can also be seen inside such bundles, indicating that there is no more material there. These are areas in which unimpregnated fibers were present. These are partially torn out during the grinding process, so that the fibers in this area appear less densely packed, or the black areas appear. These unimpregnated areas inside the CF bundles were only visible in a few micrographs. However, large bundles with a large
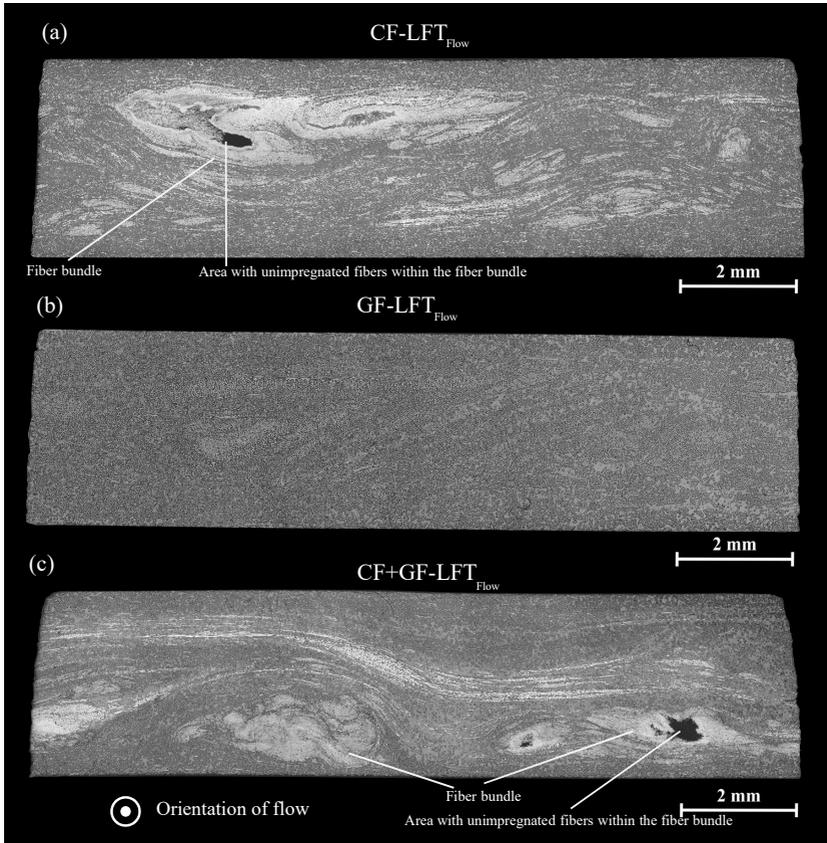
Figure 5.6: Micrographs with a representative microstructure of flow area of (a) CF_{LFT}, (b) GF_{LFT} and (c) the $CF + GF_{LFT}$ with high amount of CF-Bundles according to Scheuring et al. [127].

number of fibers were visible in each of the micrographs of CF_{LFT}, but often appear to be well impregnated.

When looking in Figure 5.6 (c) at the micrographs of the mixed fiber reinforced material $CF + GF_{LFT}$, it is primarily noticeable that no particularly good mixing of the fiber types could be achieved. The micrograph shows predominantly large areas where the fibers are still present in clusters of their fiber type. It is

noticeable that bundle formation is again more pronounced in the CF. The bundles behave similarly to the mono-fiber materials, i.e. only well-impregnated GF bundles were observed in all hybrid micrographs, while the CFs occur in both well-impregnated and partially unimpregnated bundles from which the fibers are partially torn out.

What is also noticeable in all of the micrographs examined, regardless of the material type, is that the bundles are always located in the center of the section and never at the edge of the specimen. This impression was also confirmed by the CT scans. This reinforces the validity of the impression given by the micrographs since a volume of 25 mm $\times$ 25 mm $\times$ 3 mm can be examined in the CT examinations. Both studies together gives the impression that the edge areas of all specimens have a lower fiber volume content. The $CF + GF_{LFT}$ micrographs also give the impression that in the edge areas of the specimen mainly GF are visible. This would indicate a different behavior of the fibers during the pressing process, probably due to the diameter or length of the fibers.

Upon examination of the micrographs of the charge area in Figure 5.7, it becomes evident that there are notable differences. For instance, there are significantly fewer bundles in the micrograph of the CF_{LFT} in the charge area (cf. Fig 5.7 (a)). This was generally observed in all of the CF_{LFT} micrographs of the charge area. Despite the lack of bundles, a high number of fibers can be observed in both areas. This is in contrast to the micrographs of GF_{LFT}, where it also appears that there are significantly fewer fibers in the charge area. However, the number of GF bundles is similar to that in the flow area. Additionally the shell-core effect is also noticeable in the images of the entire microsection, as the fibers at the edge are oriented 90° to the flow direction. This reduces the probability of cutting the fibers at the edge, resulting that it seems as if there are fewer fibers in the edge areas of m GF_{LFT}. However, there also appears to be a less dense fiber content in the interior.
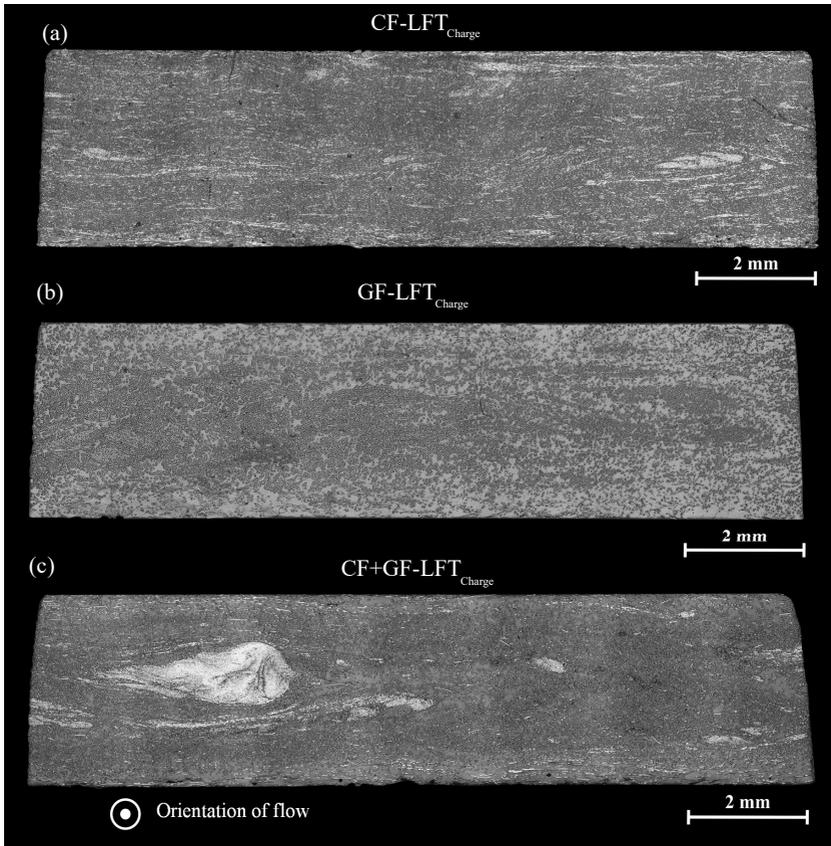
Figure 5.7: Micrographs with a representative microstructure of charge area of (a) CF_{LFT}, (b) GF_{LFT} and (c) the $CF + GF_{LFT}$.

Figure 5.8 shows the μCT examinations from both the charge and the flow area of all three materials. Since the CT images are volumetric images, only a slice from the center of each volume was selected for visualization, preserving all important details included. Figure 5.8 (a) shows a slight difference between the matrix and the fibers. This is because CF and PA6 have a very similar density ($\rho_{PA6} = 1.14\,\mathrm{g/cm^3}$ and $\rho_{CF} = 1.8\,\mathrm{g/cm^3}$) and therefore show only a slight difference in gray value in the μCT analysis. In addition, mainly bundles are

visible as individual fibers cannot be separated with the resolution of the µCT due to their small diameter. In the flow area of Figure 5.8 (a), a bundle with a dark spot can be seen on the left side. This is a bundle with an unimpregnated interior as shown earlier in the Figure 5.6 (a). It is evident that the dry component is situated within the bundle and is encased by an impregnated portion. This shows that the effects already explained with micrograph of CF_{LFT} in Figure 5.6 are effects that also occur in the volume.
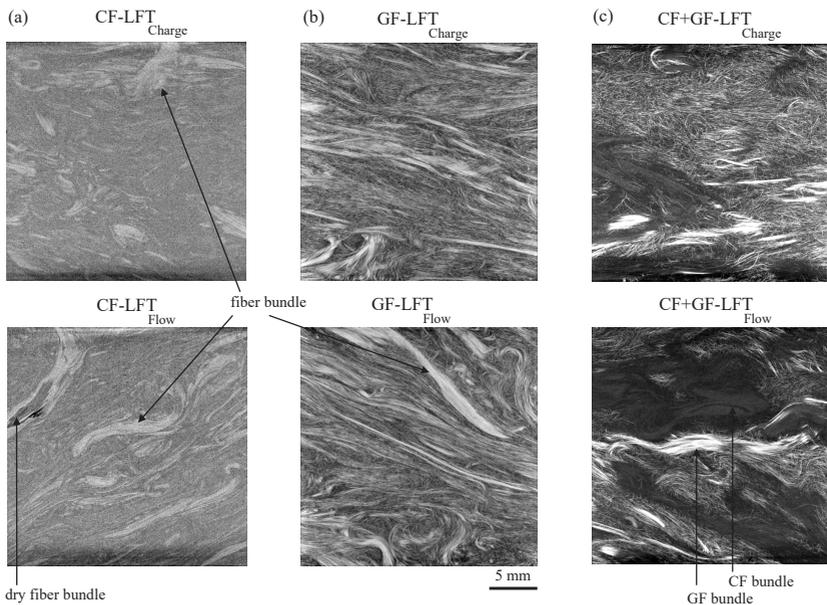
Figure 5.8: µCT scans with a representative microstructure of the center of the specimen of charge area and flow area of (a) CF_{LFT}, (b) GF_{LFT} and (c) the $CF + GF_{LFT}$.

Figure 5.8 (b) shows sample scans of the GF-LFT from the charge and flow area. The difference between GF and matrix is visible. This is due to the significant difference in density between GF and PA6 ($\rho_{PA6} = 1.14\,\mathrm{g/cm^3}$ and $\rho_{GF} = 2.5\,\mathrm{g/cm^3}$), which allows the fiber and matrix to be separated. The bundles are also clearly visible, but the individual fibers can also be seen between

them. In the $\mathrm{CF} + \mathrm{GF}_{\mathrm{LFT}}$ in Figure 5.8 (c), the GF are again clearly visible as bundles and as individual fibers, while the CF are again only distinguished from the black matrix by a slightly lighter shade of gray. The assumption from Figure 5.6 (c) that the fiber types are not well mixed is again confirmed. It can be seen that GF and CF are also present in clusters in the volume. In the material types that contain CF, the impression was confirmed that bundles occur more frequently in the flow area. No major difference could be detected with pure GF material. A crucial aspect observed in all the examined materials is the curvature of fibers, which deviate from straight lines, appearing predominantly curved. This curvature is evident not only in bundle structures but also in individual fibers, as notably visible based on the GF. This emphasizes the importance of volumetric fiber orientation analysis utilizing µCT data, enabling the inclusion of curvatures in the orientation assessment.

5.1.5 Fiber orientation distribution

The fiber orientations presented here were determined from the µCT-Data. All evaluation of the raw data from the CT, such as free-cutting, post-processing and determination of fiber orientation, was carried out by Juliane Blarr. The results of the orientation tensors are presented here to be able to use the homogenization methods in the following.

Figure 5.9 shows the proportions of fiber orientation in '11' '22' and '33' direction through the thickness of (a) $\mathrm{CF}_{\mathrm{LFT}}$ and (b) $\mathrm{GF}_{\mathrm{LFT}}$ of one sample each from the charge area and the flow area. As previously defined, the 11 direction represents the component in the flow direction, the 22 direction represents the orientation 90° to it in the plane, and the 33 direction represents the component along the plate through-thickness direction. The first thing that stands out is that the '33' component is very low in all samples and never exceeds 0.03. This means that the fiber orientation can be simplified to a planar orientation as described in Figure 2.9 (b) without a great loss of information.

Resulting from this, it simplifies the further handling of the fiber orientation information. Due to the planar orientation, the portion of angle ϕ can be neglected and the FOD can now be described by a single angle θ resp. the orientation function Ψ_θ.
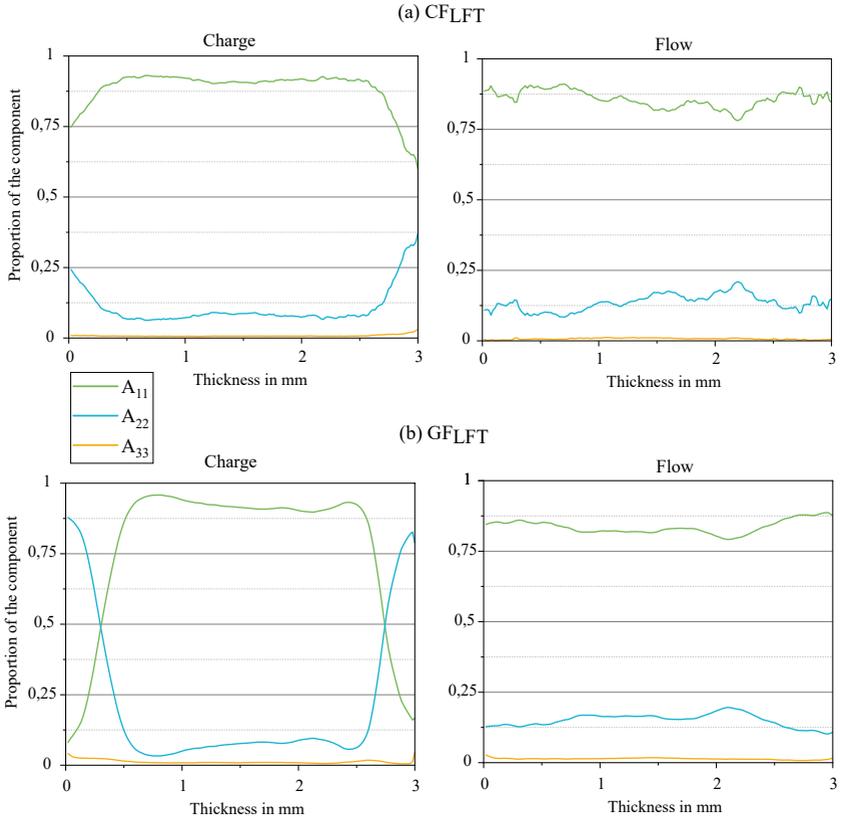
Figure 5.9: Proportions of fiber orientation across the thickness divided into the '11', '22' and '33' components for (a) CF-LFT and (b) GF-LFT for charge and flow area.

There is also a notable difference in the orientation distribution through the thickness between the charge and flow areas in both materials. In the charge area, starting from the center and moving towards the edges of the sheet, there is a significant increase in the 22 orientation, while the 11 orientation decreases. This area has a thickness of approx. 0.5 mm on each side for both materials, but is much more pronounced in the GF_{LFT} than in the CF_{LFT}. In the flow area, the values of 11 and 22 components are largely constant over the whole thickness, and, as already mentioned, no skin effect can be observed. The 11 component is in the range of 0.8, indicating a strong orientation of the fibers in the flow area. This strong alignment can also be observed to the same extent inside the samples from the charge area in the range of approx. 0.5 mm -2.5 mm in both materials examined.

By reducing the fiber orientation to a to planar orientation, it can now be described by a single angle and the distribution can be divided into discrete categories and displayed as a histogram. Since the values for FVC and FLD were already averaged over the entire plate, the same procedure is used here, regardless of the shell effect in the samples of the charge area. Figure 5.10 therefore shows the histograms of the orientation assumed to be planar, averaged over all 9 samples and divided into categories of 9° for (a) CF_{LFT}, (b) GF_{LFT} and (c) $\text{CF} + \text{GF}_{\text{LFT}}$. For $\text{CF} + \text{GF}_{\text{LFT}}$, the orientations are shown separately for CF and GF.

When looking at the histograms in Figure 5.10, it is noticeable that the maximum is always at the positive grade numbers. For CF_{LFT} and GF_{LFT} in the range of 0° - 9° and for $\text{CF} + \text{GF}_{\text{LFT}}$ in the range of 0° - 18°. This shows that the fiber orientation is slightly offset from 0°, which means that either the fibers are not aligned exactly in the flow direction or that a skewed flow front is created according to which the fibers are aligned. The histograms of the two mono-fiber materials show very similar curves. As mentioned above, the maximum peak is found between 0° and 9°, where more than 20 % of the fibers are located. After that, the values flatten out in both directions, with significantly more fibers in the 9° to 18° range than in the 0° to -9° range.
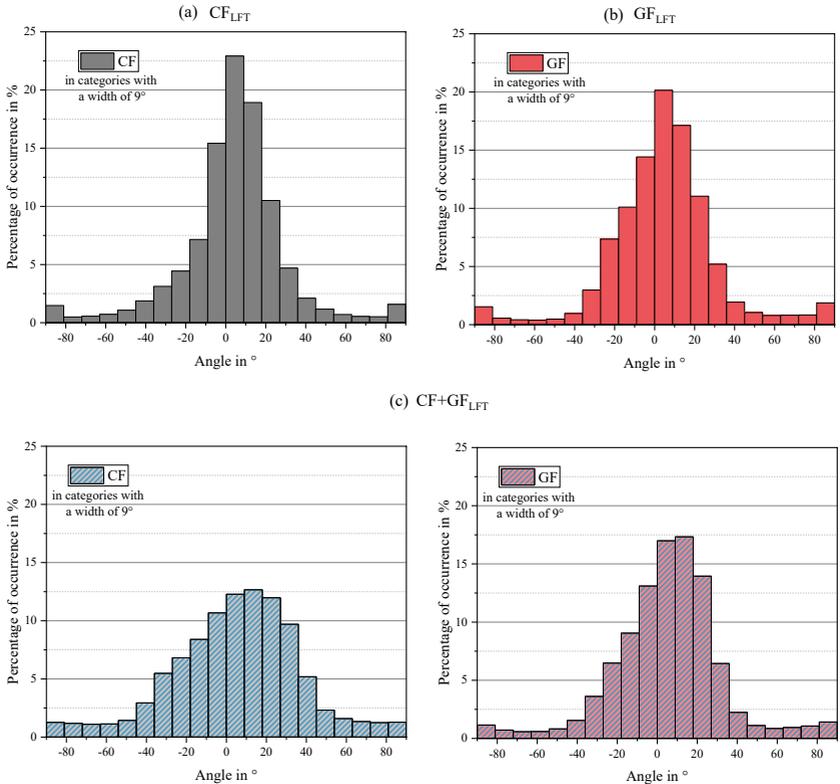
Figure 5.10: Histogram of the planar fiber orientation of (a) CF_{LFT} , (b) GF_{LFT} and (c) $CF + GF_{LFT}$ separated in CF and GF based on µCT measurements according to Scheuring et al. [127].

The curve values continue to flatten out until they flatten to a kind of plateau in the range of 46° to values of less than 1 %. The slight deflection in the category from -90° to -81° or from 81°-90° is due to the shell structure in the charge area.

5.1.6 Microstructural characteristics of the Co phase

To analyze the Co phase, Co tensile specimens cut from the Co plates were scanned at representative locations in the μCT. The orientation in which the tapes were laid, i.e. in which the planned fiber orientation also lies, is shown horizontally from left to right. Figure 5.11 shows μCT scans of representative characteristic positions of different Co samples with increasing degrees of deviation from the targeted unidirectional alignment from (a) to (d). Figure 5.11 (a) shows an orientation of the fibers with only minimal deviations in the form of small waves. In Figure 5.11 (b), small black spots can be seen in the lower right area, indicating pores. Around these pores, larger deviations from the fiber orientation can be seen in the form of waves. This phenomenon is more pronounced in Figure 5.11 (c), where large deviations from the fiber orientation already lead to large pore formations. Figure 5.11 (d) shows particularly strong deviations and a very large number of pores on the examined area.

It can be seen here how the undulation of individual fiber strands, partly upwards and partly downwards, can be identified as the cause of the pore formation. The structures shown in Figure 5.11 were found on every Co-Plate. No particular locations were found where the "waviness" was more prevalent; the distribution appears to be random. All of the structures shown were also generally present in the tensile specimens over the 100 mm gauge length.

5.1.7 Interface of continous-discontinous LFT

Figure 5.12 shows micrographs of the CoDico-LFT from the charge area in Figure 5.12 (a) and the flow area inFigure 5.12 (b). As in the images above, the flow direction is again out of the image plane, which means that fibers with this orientation are cut as a circle.

In both sections, the Co phase is clearly visible at the top and bottom of the sample due to the many white dots representing individual fibers. It can also be seen that the fibers in the Co phase appear as small bundles, which are most
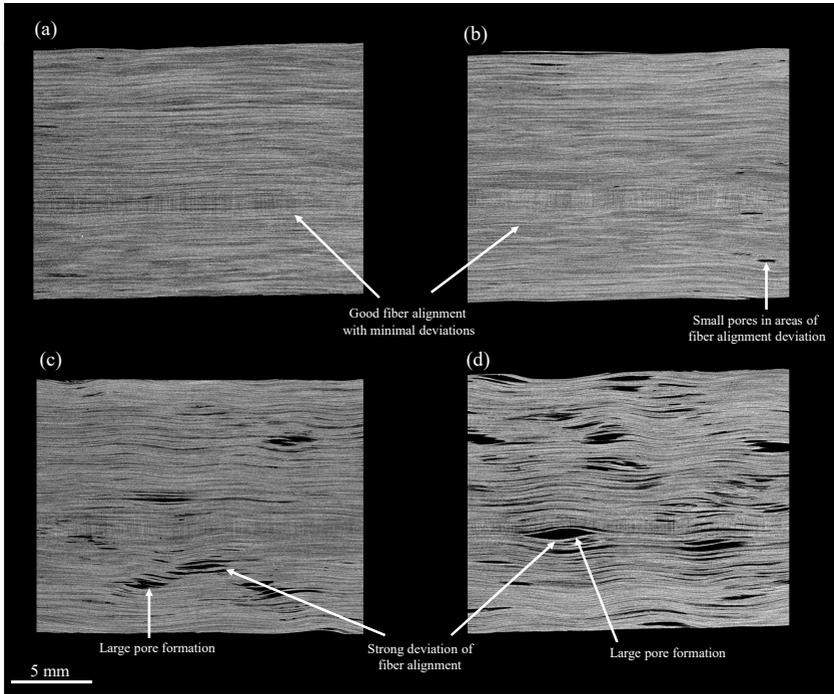
Figure 5.11: µCT scans of representative characteristic positions of different Co samples with increasing degree of deviation from the targeted unidirectional alignment with (a) good fiber alignment with minimal deviations (b) with small pores in areas of small fiber alignment deviation (c) and (d) with strong deviation of fiber alignment as large pore formation.

likely artifacts of the rovings from which the Co phase is made. Furthermore, the small horizontal black line clearly in the Co phase shows that this is a two-layer Co phase. Upon examination of the scale, it becomes evident that the Co phase exhibits a thickness of approximately 0.25 mm. It is noteworthy that the Co phase does not exhibit a uniform thickness, with the presence of thinner regions. This phenomenon is likely attributed to the potential presence of minor gaps between individual tapes during the laying and consolidation process.

103
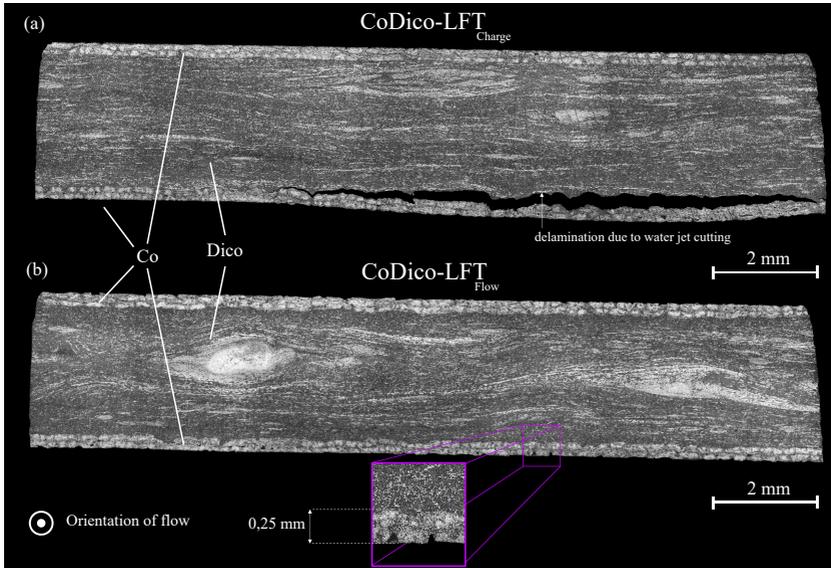
Figure 5.12: Micrographs with a representative microstructure of CoDico-LFT from (a) charge area and (b) flow area with the orientation flow pointing ou of the plane.

In addition, the two micrographs confirm the impression from the micrographs of the pure Dico-LFT materials in Figure 5.7 and Figure 5.6 that CF bundles are increasingly found in the flow area. The micrograph of the charge area in the Figure also shows a point where the Co phase separates from the Dico phase. This is a delamination that often occurs during water jet cutting of small CoDico-LFT samples from the charge area and indicates a poor interface in this area. It is noticeable that the Dico phase in the charge area has formed exactly the contour of the Co phase.

5.1.8 Discussion

Fiber content distributions   As illustrated by the fiber content measurements presented in Figures 2.7 and Table 5.1, the desired fiber content for the monofiber materials could be met with a high degree of accuracy, whereas there was a notable discrepancy for the $CF+GF_{LFT}$. The discrepancy in the results can be attributed to the manner in which the manufacturing process is calculated. The calculation table takes into account the rotational speed in the second TSE, the number of rovings, the tex number of these, and the polymer flow introduced from the first TSE. However, it only relates one fiber type to the polymer flow at a time, which can lead to an error in the in-situ calculation of the $CF+GF_{LFT}$. The lower volume fraction in the hybrid requires careful consideration when evaluating mechanical properties.

The increase in w_f the flow path observed with GF_{LFT} is consistent with the literature and can be well explained, especially for compression molding. During the molding process, the fibers suspended in the polymer melt migrate in accordance with the local shear rates. As this increases along the flow path during compression molding, w_f also increases along the flow path [54].

Fiber length distribution in LFT   In all three LFT materials under consideration, the characteristic shape of the fiber length distribution curve in Figure 5.4 aligns with expectations for fiber-polymer masses processed through an extrusion procedure described by Sharma et al. [200]. The typical distribution curve for LFTs, which peaks at shorter fiber lengths and extends toward longer fibers, is evident across all three materials. This characteristic fiber length distribution has been corroborated by numerous previous studies on LFT-D-ILC materials [201, 48, 200, 202].

The longer fiber lengths observed in the CF_{LFT} compared to the fiber lengths in the GF_{LFT} (cf. Tabel 5.1) can be ascribed to the inherent characteristics of CF rovings, which feature a higher tex number, lower density, and smaller fiber diameter, culminating in a higher fiber count per roving (50k) compared

to the GF rovings (approx. 4.5k). Consequently, this makes individual fiber separation more challenging and diminishes fiber breakage in the impregnation extruder, which in turn results in the longer fiber lengths observed in CF_{LFT}.

The extended fiber lengths observed in the hybrid compared to both monofiber materials (cf. Tabel 5.1) hints at a potential synergistic interaction between different fiber types within the impregnation TSE, leading to reduced damage and consequently longer fibers in the final parts. Nevertheless, it is crucial to note that the reduced fiber volume in the hybrid material may be a contributing factor to the observed reduction in fiber shortening. A lower fiber content leads to less fiber-fiber interaction and thus to fewer fiber breaks. However, previous studies have indicated that a positive synergy effect in the impregnation extruder and therefore longer fibers can be achieved with a mixture of carbon fiber and glass fiber even with the same fiber volume than in the monofiber materials. A similar study by Shao Yun and Lauke, in which they used a similar process to impregnate GF and CF directly from rovings with polypropylene at various ratios, with total volume content of 25 % showed comparable results [172]. They were able to show that as the relative volume fraction of CF increases and the relative volume fraction of GF decreases, the average lengths of both GF and CF decrease. This suggests that the GF-CF interaction causes more damage to the GF than the GF-GF interaction. Similarly, the same fiber interaction causes less damage to the CF compared to the CF-CF interaction [203, 172].

Given the longer average length of fibers in the hybrid, which even surpasses that of CF_{LFT}, and the significantly higher number of CF due to their smaller diameter compared to the GF, it is reasonable to assume that the majority of fibers in the hybrid also exceed L_{crit}. Despite the relatively short average fiber lengths of all materials, the classification as LFT remains, since in all cases a large proportion of the fibers exceed L_{crit} and so does the statistical moments L_p, L_n and even the median in all cases.

Microstructural differences between charge and flow area   The presence of the shell layer, observed in the charge area with fibers oriented 90° to the direction of flow as depicted in Figure 5.5, is confirmed by orientation analyses over the thickness, as shown in Figure 5.9. This analysis allows a clear separation between the shell and core layers and thus clearly delineates the area of influence. These shell core effect is typical for compression molded LFT-D-ILC materials and can be attributed to the retention of extrusion process results in the shell layer with a fiber orientation of 90° to the flow front. This phenomenon can be elucidated by considering the initial fiber orientation in the initial charge (cf. Figure 5.5 (a)). The structure has an outer shell in which the fibers are oriented in the direction of extrusion.

The fiber orientation phenomena discussed in section 2.3.4 result from the shearing action between the fixed wall and the moving extrudate in the nozzle of the TSE. Inside of the initial charge, the fibers tend to orient more perpendicular to the direction of extrusion. In particular, the artifacts of the two screws in a TSE are visible, creating a swirl effect around which the fibers appear to be wrapped. For a comprehensive analysis of fiber orientation in the initial charge, refer to the research conducted by McLeod et al. [201] and Schreyer et al. [204].

When the initial charge is now placed in the 80 °C heated mould and the molding process is initiated, the outer layer cools below the flow temperature on contact with the mold surface, effectively solidifying it. This sequence results in the formation of the shell structure with the fiber orientation orthogonal to the flow in the charge area. As pressing continues, the still-liquid interior of the initial charge is displaced to the sides. The outer shell then cracks along the sides and folds both up and down, allowing the inner portion to flow into the mold as the pressing motion continues.

Examination of the flow regions in Figure 5.5 reveals that the fibers in all three materials are oriented in the flow direction throughout the whole cross section. The flow motion of the inner part aligns the fibers in the charge area in the direction of flow. In particular, the absence of shell structure artifacts in the flow area, where only flowing material is present, serves to support the hypothesis mentioned before. This structure is typical for compression molded LFTs, which is why a distinction is made between the different areas in studies [147, 144, 205, 126, 206].

Fiber dispersion and bundeling   The greater tendency of CF to remain in bundles observed in the micrographs shown in Figure 5.6 and Figure 5.7 and the µCT images shown in Figure 5.8 may be due to the higher tex number, the smaller diameter and the associated higher fiber count within the rovings. As mentioned in the previous discussion about the fiber length distribution, the fibers in the roving or bundles will be mutually shortened, resulting in lower dispersion and, in some cases, poor impregnation. Since CF is processed in fiber-rich rovings (50k), it can be assumed that the dissolution of the CF rovings and the impregnation of the fibers require more time and effort than for GF rovings (approx. 4.5k). Therefore, in the 2nd TSE, higher energy input into the polymer matrix blend would have to be added either by additional mixing elements or a longer screw path.Nevertheless, in addition to enhanced dispersion, this also results in augmented fiber shortening, which presents a conflict of objectives at this juncture.

The exclusive localization of the bundles within the inner volume of the plate can be attributed to the stress distribution within the flowing fiber-polymer mass during compression molding. In the inner part of the flow area, only low shear stresses occur due to the low-speed gradient in the middle of the component, which means that the long fibers, especially the fiber bundles, are found in the core area of the formed parts. This agrees with the observations of Truckenmüller and Fritz who were able to observe bundle formations primarily

in the interior of injection molded slabs [207]. Another reason could be that the bundles are primarily formed by fiber rovings that wrap around the screw and thus protect each other from degradation, e.g. fiber breakage. Since the portion of the initial charge where the screw artifacts are visible contributes to the mold filling in the interior and even more so in the flow area of the plate, this explains why the bundles are more prevalent in the interior and flow areas.

Fiber orientation distribution The planar orientation observed Figure 5.9 for all three LFT materials in agreement with the literature for compression molded LFT plates with a low ratio of height to width or length [35, 143, 141]. The shell-core effect, characteristic of compression-molded LFT-D materials and previously attributed to artifact structures of the initial charge, is also clearly visible in the fiber orientation analysis across the thickness in Figure 5.9 of the charge area. This enables a precise quantification of the area of influence. In the GF_{LFT}, a significantly greater proportion of fibers oriented at 90° was observed in the shell. This observation aligns with the cross-section analysis, which revealed that most of the fibers were cut in an elliptical shape and that a smaller number of fibers were visible in the shell of the GF_{LFT}. Consequently, it is likely that most fibers are oriented at 90°, and as previously noted, these fibers are less prone to being cut. The proportion of 90° oriented fibers is highest at the edge, were the surface layer of the initial charge shows direct solidification immediately after contact with the mold.

In the range of 0 to 0.5 mm from the edge of the sheet, however, a gradient of fiber orientation in the direction of flow can be observed, which indicates an increasing orientation of the fibers in the direction of flow. It can be assumed that these layers freeze during further cooling in the molding process before the fibers are fully aligned. In contrast, a strong alignment in the direction of flow can be seen in the inner part of the charge area (0.5 mm - 2.5 mm) and over the entire thickness in the flow area. Since during the molding, the hot material from the inside of the initial charge freezes immediately on contact with the mold surface, it can be assumed that this is a non-lubricated squeeze flow [54].

This would result in a velocity distribution shown in Figure 5.13 which in turn result in a velocity gradient across the height of the flow front, with the gradient being highest at the walls of the mold.
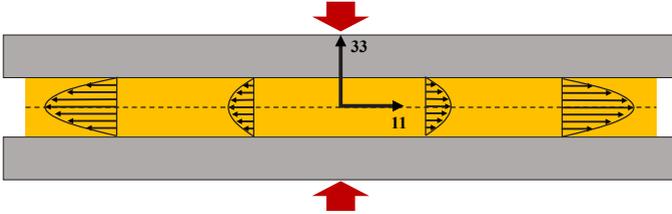
Figure 5.13: Horizontal velocity distribution $v1_{(11,33)}$ for non-lubricated squeeze flow according to [54].

This is where shear forces align the fibers in the direction of flow. Toward the center of the sheet, the gradient continues to decrease so that there is little shear. However, in the region where shear is zero, the highest strain rate in the direction of flow occurs in the material. This phenomenon, as previously discussed, also causes the fibers to align in the direction of flow. Between the two extremes at the wall and in the center, there is a mixture of the two mechanisms and a transition from one to the other. From the results in Figure 5.9, it can be seen that this leads to a uniform alignment of the fiber in the flow direction over the entire height in the flow area.

The combination of micrographs and µCT images proved to be suitable for the precise analysis of the bundles and the fiber orientation. The micrographs can be used to identify individual fibers in CF_{LFT} due to the high resolution of the images and the strong contrast provided by the reflective CF. By combining this with the µCT images, these findings can be extrapolated to a larger volume, and fiber curvatures can be visualized. These fiber curvatures also show the need for a fiber orientation determination via the µCT data where these can at least be included in the orientation determination. In general, all fiber types show a strong orientation in the flow direction during compression molding with a constant deviation from the anticipated direction. This could also be shown

for a similar process guidance by Fliegener et al. and is probably due to the initial charge [147]. This is discussed in detail later in the thesis. All in all this results in a very complex microstructure, which must either be described by a representative volume element (RVE) or must be simplified for further applications. It should be noted that the complexities of the microstructure are largely lost in simplifications such as statistical averaging.

Microstructural characteristics of the Co phase   The wave-like orientation deviations observed in the μCT images in Figure 5.11 are most likely caused by a step in the consolidation process. One possible explanation is, that these waves arise during the heating phase. UD-FRTPs exhibit an anisotropic thermal expansion behavior, characterized by two different coefficients of thermal expansion (CTE). In the fiber direction, the CTE is constrained by the mechanical properties of the fibers, resulting in lower values. Conversely, perpendicular to the fibers, the CTE is primarily influenced by the polymer matrix, leading to higher values due to the limited confinement by the fibers. This anisotropy can induce significant thermal stresses within the matrix [208]. The heating in the contact oven of the $700\,\text{mm} \times 700\,\text{mm}$ sheets may not be uniform. Heated areas expand while the surrounding cooler areas restrict this expansion, resulting in the formation of waves within the plane to accommodate the expansion. A further possible explanation is that with uneven cooling, the same principle applies in reverse, leading to the orientation deviations. However, it is also possible that the deviation is due to the deposition process in the Fiberforge. In the Fiberforge, the laid tapes are welded together locally at small points with an ultrasonic probe. This local fixation can lead to pre-tensioning or deformation in the tapes during further handling or transportation in the contact furnace, which degrades during heating and leads to local orientation deviations.

In general the microstructure within the Co phase becomes much more complex due to the local deviations from the intended fiber orientation, ranging from minimal waviness to significant pore formation. Simplification to a uniformly oriented material could potentially lead to a misperception of the material.

In addition, the presence of pores leads to non-uniform fiber content, which introduces further variation.

Interface of continous-discontinous LFT   The disparate delamination behavior observed in the charge and flow areas during waterjet cutting, as illustrated in Figure 5.12, can be attributed to variations in interface quality. It can be inferred that the flow area exhibits favorable interface quality, whereas the charge area displays inferior interface quality. Nevertheless, it has been demonstrated that the Dico phase can still adhere to the complete contour of the Co phase. This suggests that the Dico phase was still warm enough to deform, but not warm enough to form a good interface. This could be because the initial charge cools at the edge after extrusion and is therefore unable to form a good interface. The delamination occurred on the side facing up during the water jet, i.e., the side where the water jet cuts through the Co and then the Dico-LFT. However, delamination occurred regardless of which side of the sheet was facing up. Therefore, no process-related difference between the top and bottom interfaces could be detected during sample preparation. Delamination in the flow area was never observed with waterjet cutting. This can be attributed to the fact that only hot material from the inside of the plastificate enters the flow area and overflows the Co phase. This appears to be hot enough to form a good interface.

All in all, the hybridization of CoDico-LFT has no significant influence on the microstructure of the individual components. These behave essentially as if they were present as a single phase. The differences in interface quality in the individual areas is discussed in detail later in the thesis.

5.2 Tensile test

The investigations of the direction-dependent mechanical properties under tension were carried out both for the different LFTs and for the CoDico-LFT exclusively on samples in "dry" conditions as explained in section 3.2.3.

5.2.1 Tensile properties of LFT

5.2.1.1 Modulus of elasticity and strength

The polar diagrams in Figure 5.14 illustrate the orientation dependent results of the tensile modulus of elasticity (a) and tensile strength (b) for all materials, for both the charge area and the flow area. This is presented as a function of the angle relative to the flow direction, as illustrated in Figure 3.1 (e). Each data point, derived from at least five valid specimens, represents an orientation at 0°, ±11.25°, ±22.5°, ±45°, or 90° and is presented as a mean with standard deviation. To enhance visual comprehension, linear connections were incorporated between data points of the same categories.

Looking at the flow area results for all three material combinations, the 0° orientation to the flow path shows the most significant strengthening effect of the fibers in terms of tensile modulus and tensile strength. Conversely, the 90° orientation shows the least reinforcement effect of the fibers in terms of tensile modulus of elasticity and tensile strength. While the tensile modulus of elasticity remains relatively stable at small angles away from 0° (+11.25°), a significant decrease is observed at larger angles (+22.5°). At an angle of +45°, there is another significant and more pronounced reduction. The characteristic values at +45° are very similar to those at 90°, which are the minimum values.

The plots also show a noticeable asymmetry relative to the 0°-180° orientation line, with a consistent rotation toward positive degrees (upward) observed for all three materials, evident in both tensile modulus and tensile strength. Notably, the tensile modulus of elasticity and the strength values at +11.25° and +22.5°

(a)   Tensile modulus of elasticity
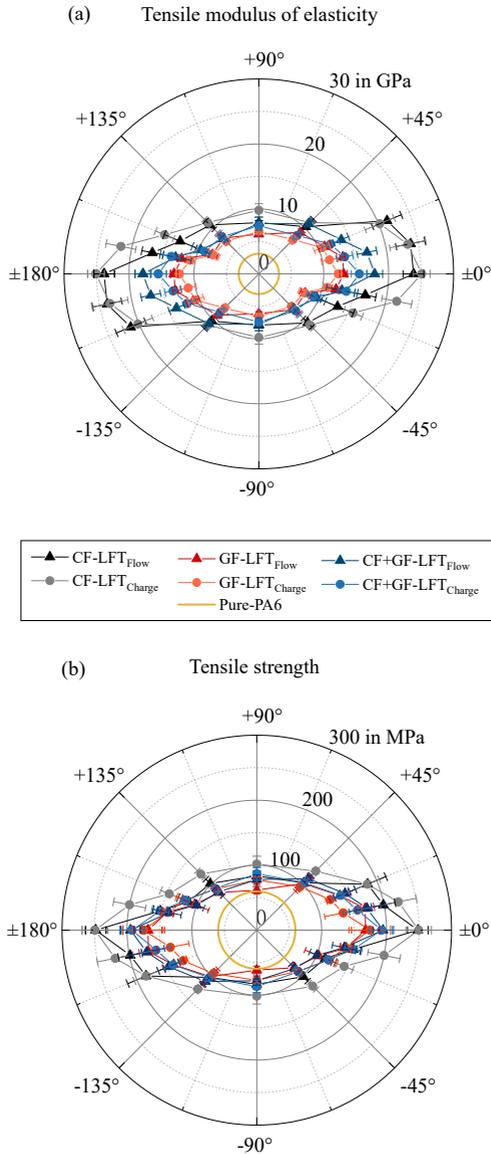
(b)   Tensile strength

Figure 5.14: Polar diagram of (a) tensile modulus of elasticity and (b) tensile strength of the three different LFT-Materials in different orientation to the flow direction separated by charge and flow area according to Scheuring et al. [127].

surpass those at -11.25° and -22.5°. This is particularly significant at CF_{LFT}, which shows the most pronounced reinforcing effect due to its high modulus and strength. While the values of the tensile modulus of elasticity at 0° (23.83 GPa) and +11.25° (23.82 GPa) are almost identical, there is a decrease of about 30 % between 0° and -11.25° (16.71 GPa). This suggests that the primary fiber orientation during the molding process occurs between 0° and +11.25°. This is in line with the results of the fiber orientation studies from section 4.1 in Figure 5.10 (a) where the peak, i.e. most of the number of fibers in this orientation is found between 0° and 9° (cf. Fig. 5.10). A similar trend is evident in the other two materials: both the GF_{LFT} and the $CF + GF_{LFT}$ exhibit identical tensile modulus values at 0° and +11.25°, with a marked decline observed when transitioning from 0° to -11.25°.

It is also noticeable that for the CF_{LFT} the charge area in 0° orientation has the same modulus of elasticity and tensile strength with a similar scattering range as the flow area. For other orientations, the mean value of the charge area is often even higher than that of the flow area. For GF_{LFT} the maximum values are also very close to each other. This is also true for the other orientations, where the values for the charge area if they differ, are slightly below those for the flow area. For $CF + GF_{LFT}$ there is a clear difference between the two regions in the maximum values of the modulus of elasticity. The charge area is significantly below the flow area for 0°, +11.25°, and +22.5°. For the tensile strength, the values are again very close.

Additionally, the previously mentioned asymmetry of the mechanical properties concerning the 0°-180° line in the flow area is also observable in the charge area for all three materials. However, this asymmetry is less pronounced in this area and there is a decline between 0° and +11.25°, even if this is smaller than the decline from 0° to -11.25°. The contrast between the decline to +22.5° and to -22.5° is more distinct, unmistakably indicating the upward shift in all three materials, even within the charge area.

In order to show the experimental results from the tensile test in more detail, each test is shown as a measuring point in the tensile strength versus tensile modulus of elasticity diagram in one diagram per material. For CF_{LFT} in Fig. 5.15, for GF_{LFT} in Fig.5.16 and $CF + GF_{LFT}$ in Fig. 5.17. Once more,
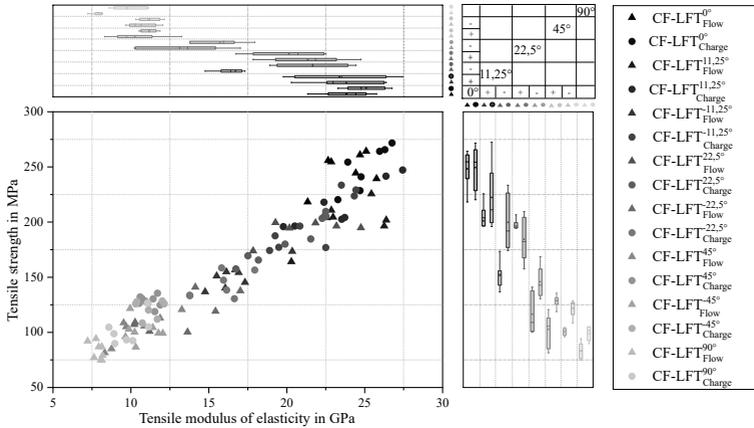
Figure 5.15: Tensile strength over tensile modulus of elasticity of CF_{LFT} separated by the triangle symbol in Flow and by the dot symbol in Charge area. The individual orientations are symbolized by the different brightness gradients, where dark indicates the 0° and the bright the 90° orientation according to Scheuring et al. [127]

samples extracted from the charge area are depicted as points, while those from the flow area are represented by triangles. To differentiate between individual orientations, distinct colors are assigned to each orientation. The 0° orientation features a fully saturated color tone, progressively brightening with increasing angle deviation (both in the positive and negative directions). Additionally, boxplots for tensile strength and tensile modulus of elasticity are positioned at the periphery. This side-by-side arrangement of box plots effectively highlights the disparities between the + and - orientations, particularly noticeable at smaller angles (±11.25° and ±22.5°). The scattering areas hardly overlap, so a significant effect can be assumed for all materials.
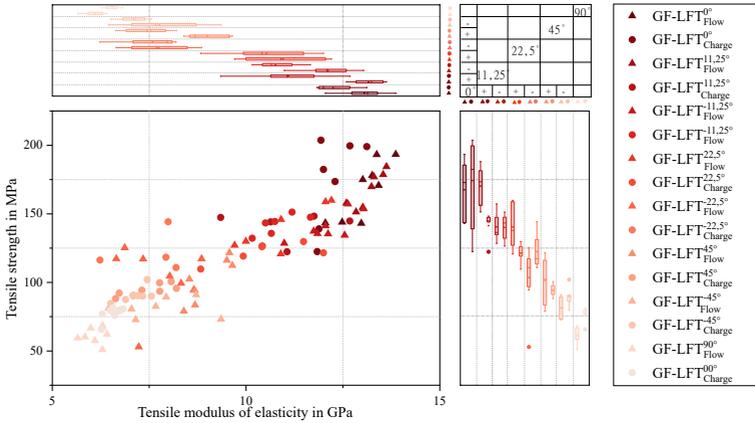
Figure 5.16: Tensile strength over tensile modulus of elasticity of GF_{LFT} separated by the triangle symbol in Flow and by the dot symbol in Charge area. The individual orientations are symbolized by the different brightness gradients, where dark indicates the 0° and the bright the 90° orientation according to Scheuring et al. [127]

In the context of CF_{LFT} (cf. Fig. 5.15), a distinct observation emerges: notably higher strengths and modulus are evident in the charge range at -11.25° and -22.5° compared to the flow range. This suggests, particularly in CF_{LFT}, the development of an upwardly rotated fiber orientation over a specific flow path. In the case of GF_{LFT} (cf. Fig. 5.16), such a difference in strength is not apparent, only manifesting in modulus at -11.25°. Remarkably, these effects are entirely absent in $CF + GF_{LFT}$ (cf. Fig. 5.17). In the case of GF_{LFT}, a notable observation is the significantly higher modulus at 0° and ±11.25° in the flow region compared to the charge area, while the strength remains very similar. This pattern could be attributed to the findings in section 5.1.1, which indicate a significantly higher fiber content in the flow region which in turn leads to the higher modulus. Analyzing all orientations from both regions in the tensile strength versus elastic modulus plot gives the impression of a linear correlation of values for all three materials with some scatter.

117
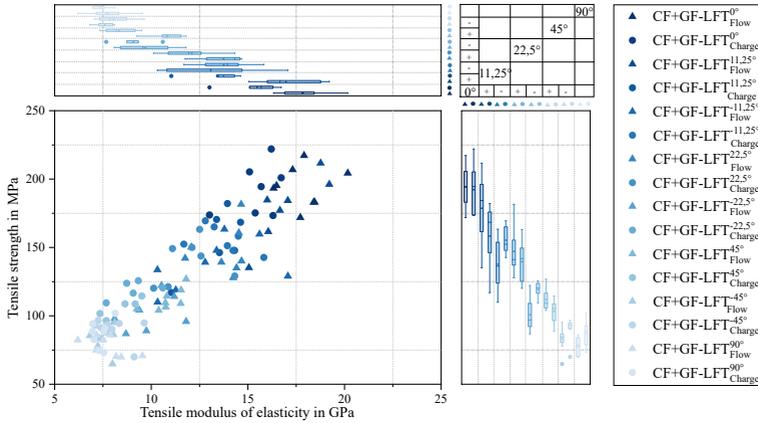
Figure 5.17: Tensile strength over tensile modulus of elasticity of $CF + GF_{LFT}$ separated by the triangle symbol in Flow and by the dot symbol in Charge area. The individual orientations are symbolized by the different brightness gradients, where dark indicates the 0° and the bright the 90° orientation according to Scheuring et al. [127]

5.2.1.2 Analytical modeling of LFT using the shear-lag modified Halpin-Tsai method

The homogenization results were generated by using the shear-lag modified Halpin Tsai method explained in 2.1.4.1 implemented in the open source Python package HomoPy [209] with a more detailed description in [127]. FVC was used as the mean value for the entire plate shown in table 5.1. For the FLD, the median was used from the same table. The histogram from chapter 5.1.5 averaged for a whole plate were used as orientation information and included in the modeling with the general laminate theory.

The polar diagrams in Figure 5.18 depict the results of modeling of the tensile modulus of elasticity in comparison with experimentally determined data for (a) CF_{LFT}, (b) GF_{LFT}, and (c) $CF + GF_{LFT}$. Observation of the orientation of the modulus bodies in the polar plot, specifically the positioning of the maximum and minimum values, reveals a distinct lack of symmetry to the 0° - 180° axis in both the model and experimental data. Instead, they show a drift towards positive angles. Notably, this drift is consistently well matched with the
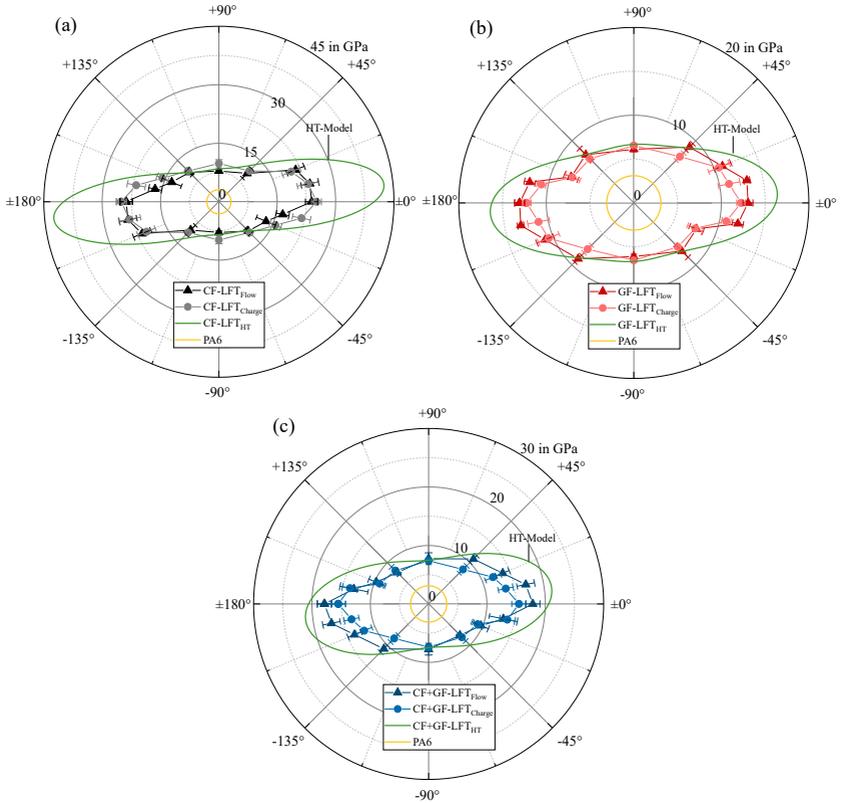
Figure 5.18: The results of modeling, using the shear lag modified Halpin-Tsai and classical lami-
nate theory, rely on experimentally derived values for FVC, FLD and FOD (cf. Sec.
4.1). These results are represented in polar plots alongside the experimental data,
specifically for (a) CF_{LFT}, (b) GF_{LFT}, and (c) $CF + GF_{LFT}$, facilitating a com-
prehensive comparison according to Scheuring et al. [127]

experimental data across all three materials. Upon examination of the absolute
values of both the model and experimental data, a notable trend emerges: values
at 90° orientation and angular deviations of ±45° are relatively accurate across
all three materials. In contrast, the predicted modulus in the orientation where
the maximum value can be found (8°-11°) consistently exceeds the experimental
results for all three materials, with CF_{LFT} (cf. Fig. 5.18 (a)) exhibiting the

119

most substantial overestimation, almost doubling the experimental values. For all three materials, the experimental data fall within the range predicted by the model and do not exceed the model's values, except for the 90° samples from the CF_{LFT} and the $CF + GF_{LFT}$ from the charge area, which lies outside this range and the $\pm45°$ from the GF_{LFT} where the scattering band lies outside.

5.2.1.3 Effect of hybridization of mixed fiber LFT

The hybridization effect is then analyzed based on the definitions provided in Figure 2.25 to determine whether the synergies are positive or negative. As shown in Figure 5.14, the most pronounced effect of fiber reinforcement on both modulus and strength is observed in the orientation range from 0° to +11.25°. Owing to the different properties of the fibers, the most significant deviation among the three materials is observed within this interval. Therefore, samples from this orientation range are particularly well suited for meaningful comparisons and evaluation of hybridization effects. Since the 0° orientation is consistent with the expected direction of flow, samples oriented at 0° were selected for comparison. In addition, since there are no pronounced shell structures in the flow region, selecting samples from this region ensures a fair and relevant comparison. Figure 5.19 shows the stress-strain curves for all validly tested samples with 0° orientation from the flow area, providing a comprehensive overview. The use of a colored background in the Figure effectively illustrates the scatter range and improves visual clarity.

At first glance, it's clear that the colored areas show significant scatter in the test results. Notably, there is no overlap between the individual areas. Looking at the curves, it's clear that the $CF+GF_{LFT}$ curves consistently fall between those of the two single fiber reinforced materials. This observation highlights a notable difference between the materials, especially at 0° orientation. The positive hybridization effect, as defined in Figure 2.25 (a), based on the average of the specimen types within each material system, is illustrated in Figure 5.19 by the green arrows. Compared to GF_{LFT}, the hybrid shows a significant 16 %
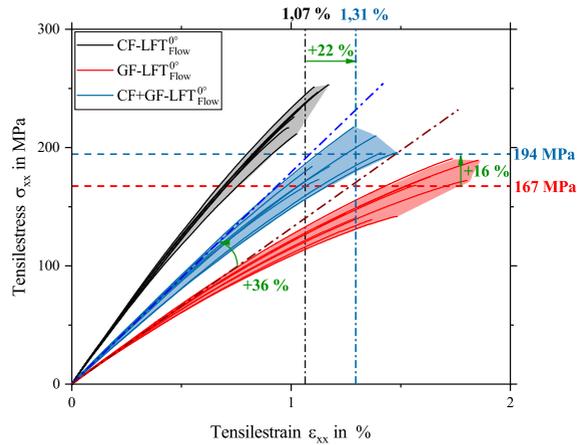
Figure 5.19: Positive effect of hybridization on the example of specimen from the flow area in 0° orientation to the flow front, were the highest reinforcement effect of the fibers could be observed according to Scheuring et al. [127]

increase in tensile strength and a remarkable 36 % increase in tensile modulus. This is accompanied by a 22% increase in elongation at break compared to the CF_{LFT}.

In the same way as in Figure 5.19 the negative hybridization effect, as defined in Figure 2.25 (a), based on the average of the specimen types within each material system, is illustrated in Figure 5.20 by the red arrows. With regard to the CF_{LFT}, this results in a significant reduction in tensile strength of 22% with a simultaneous reduction in tensile modulus of 25%. This is accompanied by a reduction in elongation at break of 19% in relation to the GF_{LFT}
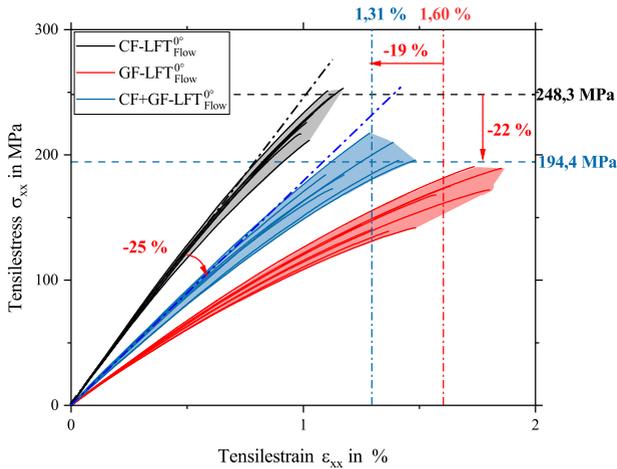
Figure 5.20: Negative effect of hybridization on the example of specimen from the flow area in 0° orientation to the flow front, were the highest reinforcement effect of the fibers could be observed.

5.2.1.4 Failure behavior of LFT under tensile load using the example of CF$_{LFT}$

For a comprehensive examination of the damage behavior of the different areas in CF$_{LFT}$, Figure 5.21 presents stress-strain curves for representative specimens with a 0° orientation from both the charge and flow area. In addition, the DIC images taken at certain points of the experiment, marked in the stress-strain diagram, provide a visual representation of the progressive damage evolution. Upon examination of the stress-strain curves, it becomes evident that following an initial linear slope (origin to a), there is a steady decline of the slope in both the charge and flow area (a-c) until the specimen finally reaches failure (d). In the course of both samples, no anomalies are observed and show the expected course for Dico-FRTPs. Examining the DIC images, both scenarios at point b reveal the emergence of local strain maxima at the surface that correlates with stress maxima within the specimen. These maxima propagate to point
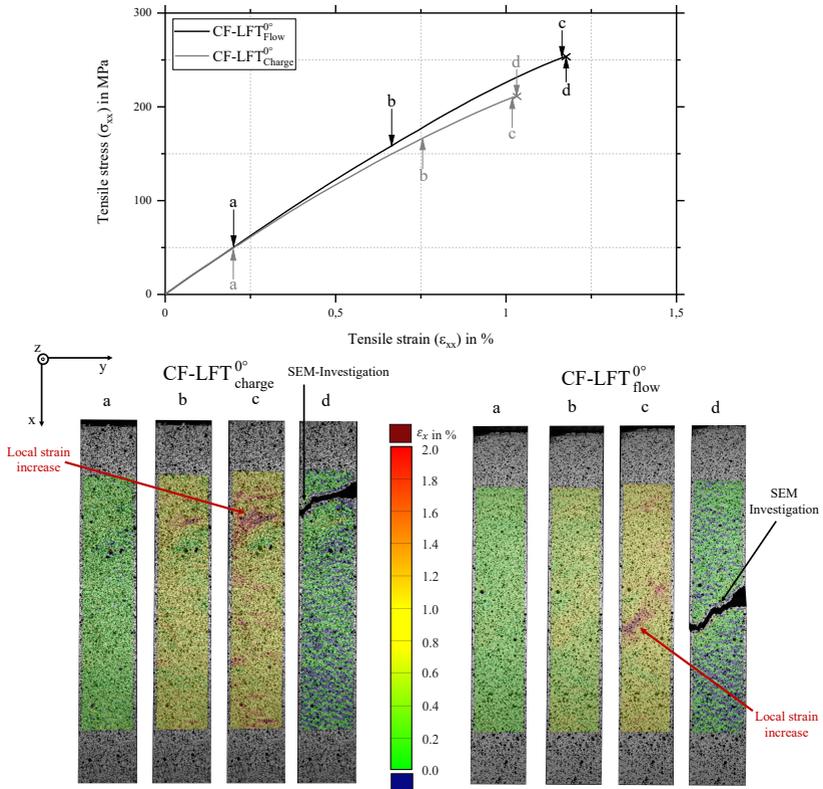
Figure 5.21: Stress-strain curves for representative Dico-LFT 0° specimen from the charge and flow area, along with corresponding DIC images at selected points to visually illustrate the progressive damage development.

c, notably extending over a significant portion of the width of the specimen. Notably, in addition to the primary strain intensity observed in the charge area, there are distinct local increases scattered throughout the sample, all consistently oriented at 90°. Conversely, in the flow area sample, in addition to the strain intensity, there is a uniform strain distribution throughout the sample. The fracture of the specimen is shown at point d, with the crack orientation following the previous strain maxima, deviating from the 90° orientation in

both cases. Thus, in both areas, the early detectable main strain and thus stress increases initiate the ultimate failure of the specimens.

To investigate the underlying causes of these strain increases, Figure 5.22 presents SEM fracture surface images of the 0° CF_{LFT} sample from the charge area, as shown in Figure 5.21. These images provide detailed views of the specific location where the strain increase begins and ultimately leads to fracture, observed at various magnifications.
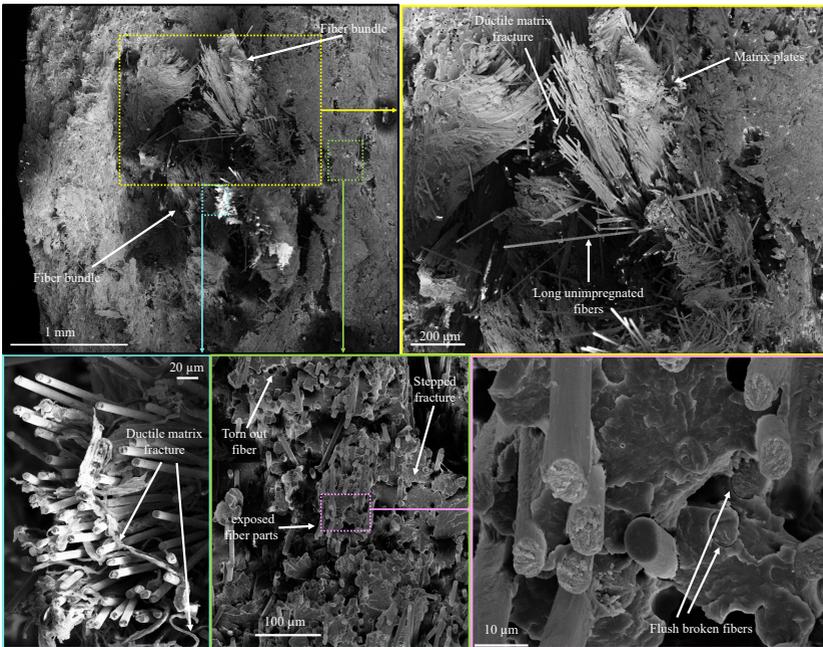
Figure 5.22: SEM fracture surface image of the 0°-CF_{LFT} specimen from Figure 5.21 of the charge area at the point of the strain increase leading to fracture marked in Figure 5.21 at various magnifications.

At the lowest magnification level, a fiber bundle can be seen that consists of long fibers surrounded by strong indentations. Given that this bundle is situated

within the fracture surface at the point where the strain increase occurs, it is reasonable to infer that this bundle is responsible for the observed strain escalation. A further indication of this assumption is ductile deformed matrix residues, which can be recognized in the turquoise detail. Together with the fracture mechanics principles from section 2.3.6, this suggests that crack initiation has taken place here (cf. Fig.2.16). In the yellow detail, such ductile deformed matrix residues can also be seen and additionally "matrix plates" at one bundle edge, which suggest that the bundle end was there. This would suggest that the bundle acts as a macroscopic inclusion at the end of which the damage-causing stress increases occurs, which in turn would also lead to the observed strain increase.

The remaining fracture surface around the bundle shows a structure, highlighted in the green and magenta details, characteristic of aligned Dico-FRP and consistent with the mechanisms elucidated in section 2.3.6 (cf. Fig. 2.17). While short free fiber ends are observed, their lengths are significantly shorter than the determined fiber length. Therefore, it is reasonable to infer that these are either torn fiber ends or fragments of broken fibers partially pulled out of the matrix. In addition, holes resulting from torn fibers are also visible. The fracture surface has a distinct step-like morphology due to intermittent interaction with different fiber ends. Closer inspection, particularly in the red detail, reveals that individual fibers are fractured flush with the fracture surface. Of particular note are the contrasting appearances of the visible fiber ends on the fracture surface. It appears that both broken and torn fibers are visible, contributing to this varied texture. In addition, subtle matrix elements are observed on the fiber flanks, suggesting a strong interface between the fibers and the matrix material.

Figure 5.23 shows SEM fracture surface images of the $0°$ CF_{LFT} specimen from the flow area, shown in the same schematic framework as Figure 5.22. This analysis zooms in on the exact location identified in Figure 5.21 where strain increase occurs. At this point, a fiber bundle is visible, but its composition is markedly different from that observed in the charge area. Specifically,

fewer fibers are exposed within this bundle and its overall structure appears more cohesive. Upon closer inspection of the green detail, matrix plates can be seen next to some exposed fibers at the edge of the bundle, indicating the end of the bundle. This observation is supported by the details shown in yellow detail. On the bundle side, both the yellow and magenta details show a distinct structure compared to the previous regions. The surface of the bundle appears to be coated with matrix material, although this may be due to ductile failure of the matrix, as indicated by certain surface features. As mentioned earlier, ductile failure implies that crack initiation occurred at this particular location.

Figure 5.23: SEM pictures of the fracture surface of the $0°$ CF_{LFT} flow specimen from Figure 5.21 at the point of local strain increase marked in Figure 5.21 in different magnifications.

On the remaining fracture surface, a few more, albeit smaller, bundles were visible, but no ductile structure could be found around them. The remaining fracture surface behaved in the same way as the details from the charge area. Only at the edge of the sample was a clear distinction between the charge and flow zone possible. Images of these edge structures are shown in the Figure 5.24.

(a) CF-LFT$_{\text{Charge}}^{0°}$

(b) CF-LFT$_{\text{Flow}}^{0°}$
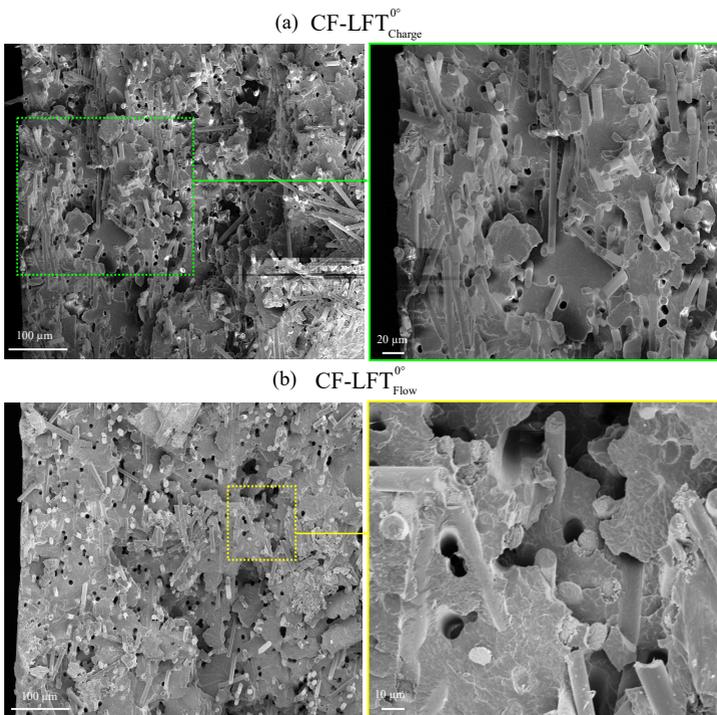
Figure 5.24: SEM pictures of the edge area of the fracture surface of the 0° CF$_{\text{LFT}}$ specimen from (a) the charge area and (b) the flow area in different magnifications.

127

It can be seen that the usual fracture behavior can be seen in the interior of the two images. Upon examination of the edge of the fracture surface, it becomes evident that a significant number of 90° oriented fibers are visible in the charge area, while the structure of the interior continues to the edge in the flow area.

5.2.2 Tensile properties of CoDico-LFT

5.2.2.1 Modulus of elasticity and strength

The polar plots in Figure 5.25 show orientation-dependent results for (a) the tensile modulus of elasticity and (b) the tensile strength of CoDico-LFT, using the same scheme as in Figure 5.14 for the various LFT-materials.

Since the Dico phase in CoDico-LFT was realized by CF_{LFT}, the results of CF_{LFT} from Figure 5.14, here referred to as Dico-LFT, are included for comparative analysis. The influence of the Co phase on the directional dependence of both tensile modulus of elasticity and tensile strength is particularly evident. The decrease in modulus from the maximum at 0° to the minimum at 90° within the flow area is more pronounced in CoDico-LFT, registering 82 % compared to the 67 % observed with the pure Dico phase in the flow area. In the 90° orientation, the values of CoDico-LFT are almost indistinguishable between the charge and flow regions, closely matching the values of the Dico phase observed in the flow region. However, it is noteworthy that in the 90° orientation, the strength of the Dico phase in the charge and flow area is slightly higher than that of CoDico-LFT.

In general, curves of the tensile modulus of elasticity in the charge and flow area in CoDico-LFT show considerable similarity, while the curves of the tensile strength show distinct differences between the two areas. In the flow range, the drop in strength from 0° to +11.25° is significant but small (-19 %), while at -11.25° the values are in a similar range (-3 %). In contrast, the drop in the charge area was significantly more pronounced. For example, from 0°

(a)   Tensile modulus of elasticity
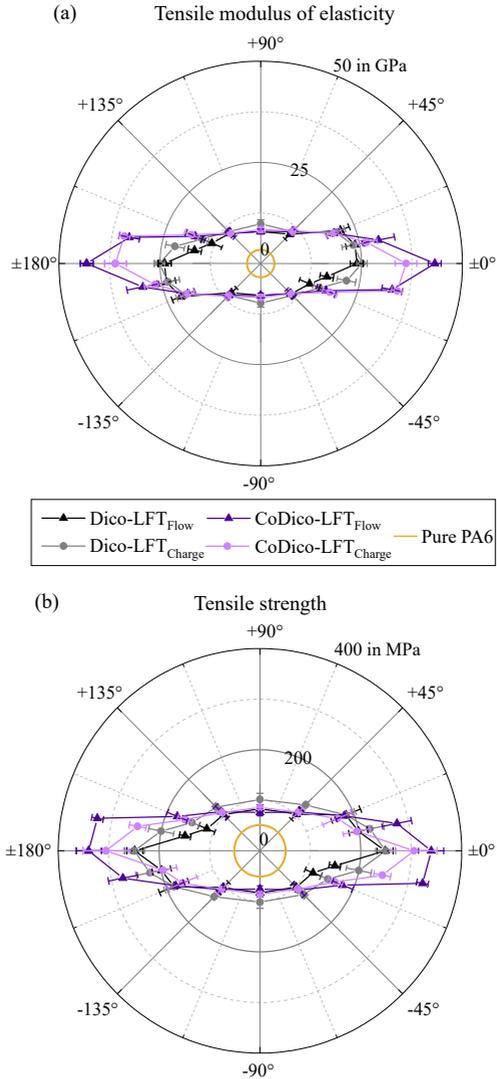
(b)   Tensile strength

Figure 5.25: Polar diagram of (a) tensile modulus of elasticity and (b) tensile strength of the CoDico-LFT and Dico-LFT (CF_{LFT}) in different orientation to the flow direction separated by charge and flow area.

to +11.25° the drop is again about 20 % but from 0° to -11.25° the drop is about 36 %. Consequently, the structural strength profile exhibits a pronounced sharpness in the charge area, contrasting with a comparatively blunt appearance in the flow area. In other words, the unidirectional Co phase exerts a strengthening influence in the flow region over a wider angular range.

5.2.2.2 Failure behavior of CoDico-LFT under tensile load

To examine the damage behavior of CoDico-LFT in more detail, Figure 5.26 shows stress-strain curves for representative CoDico-LFT 0° specimens from both, the charge and the flow area. The accompanying DIC images at selected points provide a visual representation of the damage evolution. Notably and already shown in Figure 5.25, the flow area exhibits significantly stiffer behavior and shows a higher tensile strength. Upon closer inspection, the stress-strain curve in the flow area (a-e) appears linear, in contrast to a sudden force drop and deformation jump in the charge area (b-c), followed by a subsequent force increase (c-d) leading to fracture (e). Inspection of the associated DIC images reveals a small surface fracture between points b and c in the charge area. Further analysis shows an additional small dip in the curve between c and d, resulting in a additional surface fracture at the edge. After the fracture at point e, an explosive propagation of damage development is observed, resulting in delamination of the Co layer over the entire clamp length. This simultaneous deflection is indicative of the typical failure behavior of unidirectional Co layers.

Closer examination of the DIC images in the flow area reveals a homogeneous strain from point a to b that extends over the entire sample. However, starting at point (c), there are localized strain increases at two distinct points. It is noteworthy that one of these strain increases propagates more strongly (d) and leads to fracture of the specimen (e), with the final crack coinciding with the locations of the two initial strain increases.
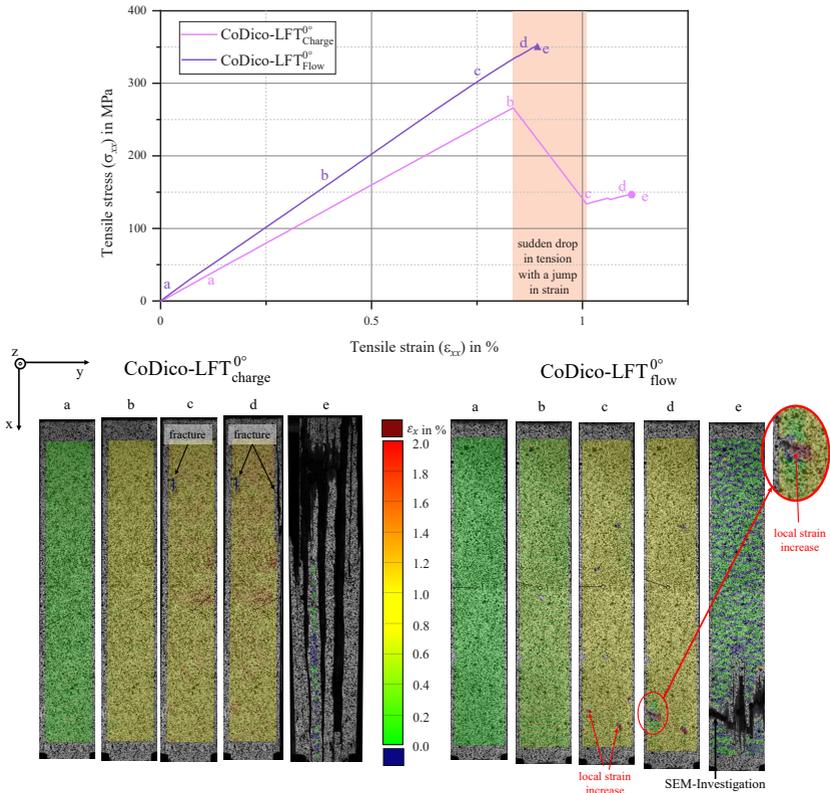
Figure 5.26: Stress-strain curves for representative CoDico-LFT 0° speciment from the charge and flow area, along with corresponding DIC images at selected points to visually illustrate the progressive damage development.

In contrast to the charge area, the interface between Co and Dico-LFT remains intact over a significant portion of the specimen length. Only in the vicinity of the final crack do localized delaminations and more pronounced longitudinal cracks in the Co phase appear.

131

Since the poor interface quality between Co in Dico-LFT is a problem that can be solved by process optimization, the damage behavior in the charge area is not analyzed in depth here. Therefore to analyze the failure behavior under the condition of a good interface quality in a more in-depth investigation, the fracture surface of the 0° sample from the flow area from Figure 5.26 at the point with the local strain increase (cf. Fig. 5.26), shown in the Figure 5.27 at various magnifications.
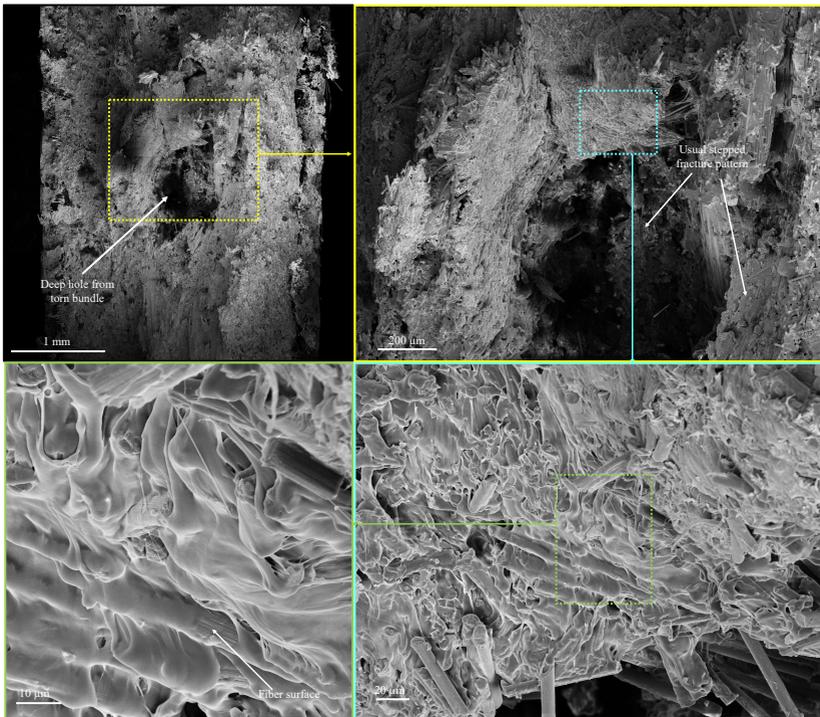
Figure 5.27: SEM pictures of the fracture surface of the 0° CoDico-LFT specimen from Figure 5.26 at the point of local strain increase marked in Figure 5.26 in different magnifications from the flow area

At the lowest magnification, a notable deepening can be seen in the center of the Dico phase, likely due to a torn out fiber bundle. A closer look at the flanks of this deepening reveals fibers that appear to have been overflown by the matrix, with instances of non-impregnated fiber segments. This area is distinctly different from other stepped broken regions on the fracture surface and seems to be the impregnation boundary of an internally unimpregnated bundle. The unimpregnated side is torn away during specimen failure so only the area reveals, to which the matrix was able to penetrate during the impregnation in the second TSE. The presence of such bundle evidence on the fracture surface of the CoDico-LFT suggests that the stress overload induced by these bundles also contributed to the failure of the CoDico-LFT specimen.

Examination of the periphery of the fracture surface, particularly in the flow area with an unusual interface, reveals two notable effects, which are illustrated in Figure 5.28. Figure 5.28 (a) shows an area where the interface between Co and Dico-LFT remains intact after fracture, and the crack manifests in a similar plane in both phases. Holes resulting from torn fibers and free fiber ends are observed in both areas. Due to the significantly more densely packed and therefore larger number of fibers, it can be clearly seen that the Co phase has a significantly higher FVC. In the Dico phase, the characteristic stepped fracture behavior is evident, which also extends into the Co phase. Figure 5.28 (b) shows a section where the Co phase detached during fracture, revealing a visible Co fragment no longer attached to the Dico-LFT. Despite this detachment, the interface quality is still discernible as Dico-LFT residues remain on the Co phase, indicating that delamination did not occur directly at the interface. However, the fracture surfaces of each phase show no deviation from those shown in Figure 5.28 (a).

The consideration of the 0° orientation is a special feature here, since the Co phase also assumes a supporting function in the charge area due to the uniaxial stress state. Consequently, it becomes interesting to examine the variations in fracture behavior when subjected to small angular deviations. To investigate this further, the fracture behavior of CoDico-LFT specimens with an orientation of 11.25° was examined.

133
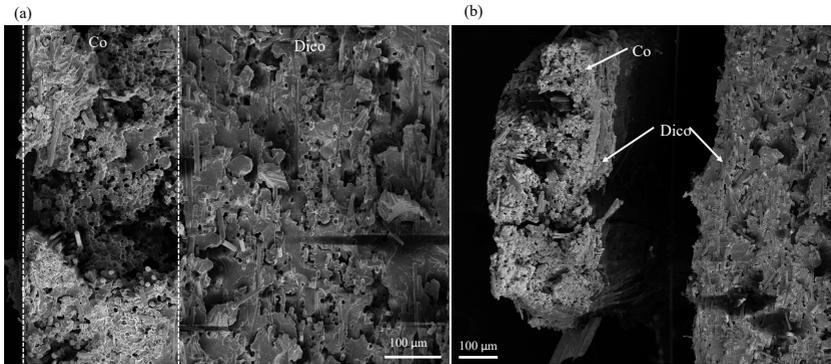
Figure 5.28: SEM pictures of fracture surface regions of a 0° CoDico-LFT specimen from the flow area, featuring (a) an intact interface between Co and Dico-LFT, or (b) delamination of the Co phase with small remnants of Dico-LFT.

The stress-strain curves of a selected specimen from the charge and from the flow area are shown in Figure 5.29. The accompanying DIC images at selected points provide a visual representation of the damage evolution from the charge area shown in Figure 5.31 and from the flow area shown in Figure 5.30.
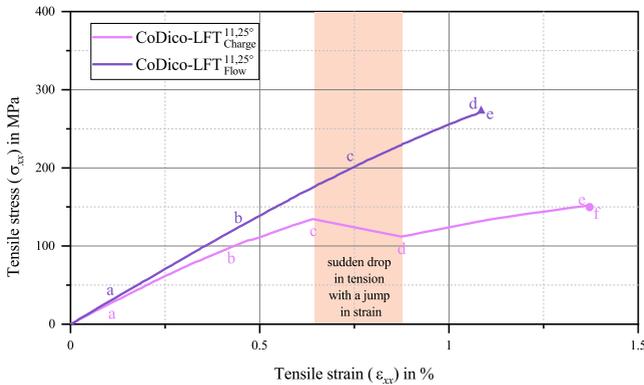
Figure 5.29: Stress-strain curves of a representative CoDico-LFT sample from the charge and the flow area with an 11.25° orientation.

In the initial investigation of the failure with a good interface utilizing the sample from the flow area depicted in Figure 5.30, it can be observed that from point (b), analogous to the 0° orientation, a localized increase in stress occurs, which propagates in the lower part of the sample. This escalation intensifies in (c), resulting in a localized stress increase in the edge region of the specimen. The elongated stress increase corresponds to the fiber orientation of the Co phase. In (d), this stress increase propagates downward along the fiber orientation of the Co phase. The absence of the surface component at the upper edge surfaces in (d) indicates the initiation of a crack in the Co phase.
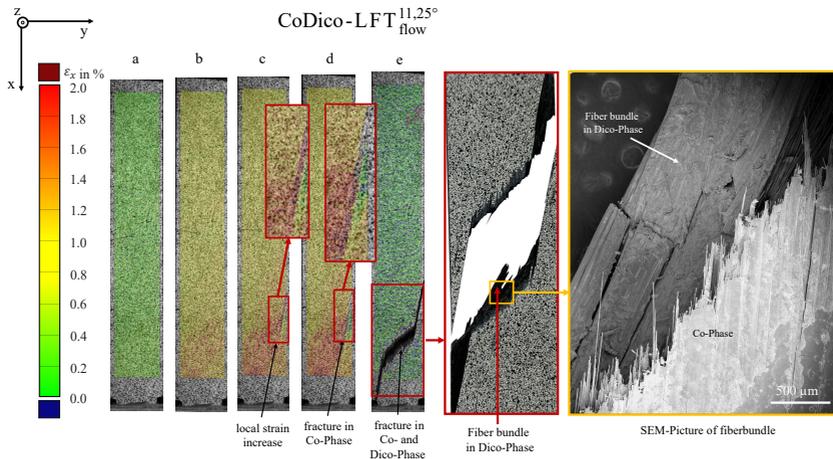
Figure 5.30: DIC images of the 11.25° specimen from the flow area from Figure 5.29 at selected points to visually illustrate the progressive damage development. A corresponding photo of the final crack and an SEM image of a fiber bundle in the fracture plane is also provided for reference.

The fracture of the specimen is shown in (e), revealing a crack in the Co phase corresponding to the stress increase described earlier. Since this is consistent with the fiber orientation mentioned earlier, a detectable matrix failure occurs purely within the Co phase at this point. However, in the center

of the specimen, the crack deviates from this orientation and exhibits a more transverse propagation. Consequently, fiber breakage occurs in the Co phase within this region. This is again an indication of a good interface in the flow area since the load between Co and Dico-LFT is sufficient to carry in fibers with a deflection of 11.25° after sufficient load to break. At the opposite edge of the specimen, the crack again develops in the Co phase along the fiber orientation. To validate the effect of the favorable interface, it is necessary to examine the failure behavior of a representative sample from the charge area, as shown in Figure 5.31.
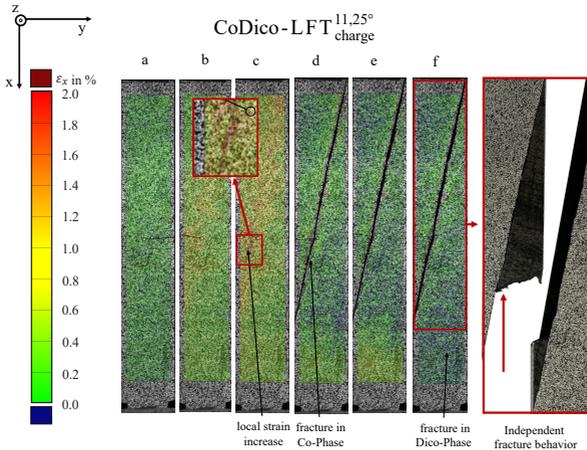
Figure 5.31: DIC images of the 11.25° specimen from the charge area from Figure 5.29 at selected points to visually illustrate the progressive damage development. Additionally, a corresponding photo of the final crack is provided for reference.

Similar to the flow area, an initial strain increase is observed (a-b), which culminates prematurely in a local strain increase in (c). At this point (d), the Co phase undergoes cracking accompanied by extensive delamination over a significant portion of the sample. It is noteworthy that the crack in the Co phase propagates directly along the fiber orientation, indicating matrix failure

exclusively in this region. Delamination is recognizable when the Co phase no longer exhibits positive elongation, although the sample is still under load, i.e. the Dico phase exhibits positive elongation. The delamination extends significantly over the specimen, except in the lower part where a slight positive strain is still evident, facilitating load transfer between the intact Dico phase and the Co phase. In (e), only the Dico phase is loaded until it fails in (f). It is important to note that the cracks in the Dico and Co phases have different orientations and occur independently. As expected, the two Co phases are observed to move in parallel due to the fiber orientation of the Co phase. Interestingly, they also move at nearly the same height. Furthermore, the strain exaggeration leading to failure is particularly concentrated at the intersection of the Co and Dico cracks, where a frayed structure indicates the presence of a bundle. This suggests that the Dico phase bundles also appear to trigger the critical failure in the charge area of the CoDico-LFT.

5.2.2.3 Effect of hybridization of CoDico-LFT

Due to the different damage behavior triggered by the poor interface in the charge area, the effect of hybridization is only evaluated in the flow area. This selective approach is warranted, as the improvement of the interface in the charge area can be achieved by process adjustments. As with the evaluation of the effect of hybridization of the pure Dico-LFT materials, only samples in 0° orientation are considered, as the strongest reinforcement effect of the Co layers could be observed in this orientation. Therefore, the clearest hybridization effect can be evaluated in this orientation and the potential of CoDico-LFT can be illustrated.

Figure 5.32 (a) shows the stress-strain curves of the specimens with a 0° orientation for the flow area of CoDico-LFT in comparison with curves of the Dico-LFT (CF$_{LFT}$). The mean values of CoDico-LFT and Dico-LFT for elongation at break and tensile strength are given on the abscissa and ordinate. For purposes of comparison, additional curves of the pure Co phase, also in 0° orientation, are given in Figure 5.32 (b).
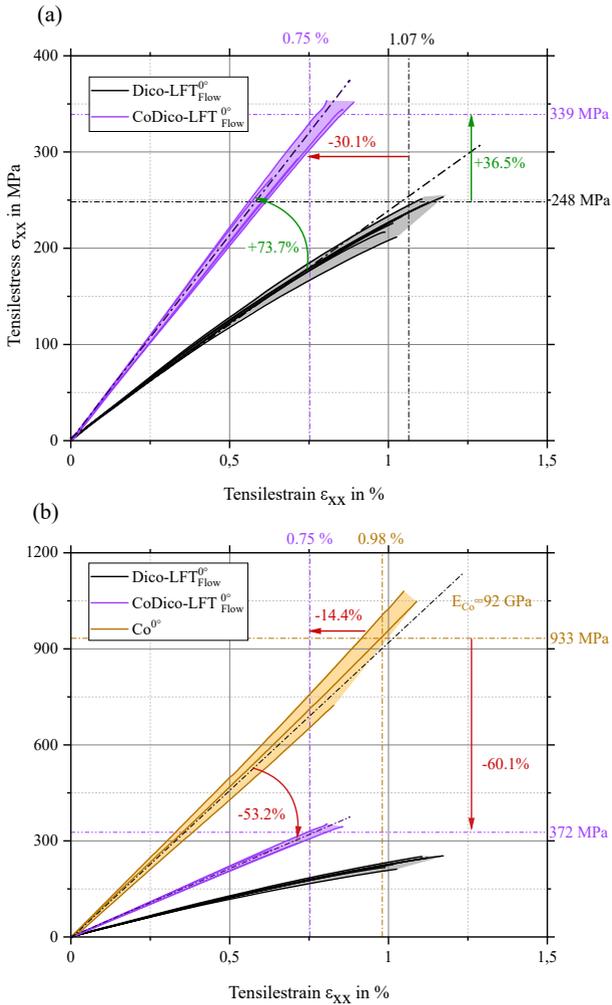
Figure 5.32: Effect of hybridization of CoDico-LFT under tensile load in comparison to CF-LFT on the example of specimen from the flow area in 0° orientation to the flow front, where the highest fiber reinforcement effect was observed in both the Dico and Co phases.

Here, the mean values are marked on the abscissa and ordinate too. As the very thin Co phase specimen showed a high degree of scattering and many of the samples failed invalidly, only the curves of three samples are shown here. The mean values therefore have no statistical validation and should only serve as a reference point. In the same schematic as already shown in Figure 2.25 the mechanical properties of CoDico-LFT in relation to those of the Dico-LFT in Figure 5.32 (a) or of those of Co in Figure 5.32 (b) are indicated by the red and green arrows for better comparison.

First of all, it is noticeable that there is no overlap between the individual scattering ranges of the different materials. Further there is a significant increase in tensile modulus of +74 % and an increase in tensile strength of 32 % in comparison to the Dico-LFT. This effect is similar to the hybridization effect observed with the mixed fiber LFT. Hybridization with a Co phase also results in a more pronounced stiffening than strengthening effect. However, these improvements are accompanied by a significant decrease in elongation at break of 30 % compared to the Dico-LFT. A comparison of the characteristic values of the CoDico-LFT with those of the pure Co phase reveals that they are, as anticipated, significantly lower for tensile strength and tensile modulus. Unexpected is the fact that the elongation at break in CoDico-LFT is also significantly lower than in the pure Co phase.

5.2.3 Discussion

5.2.3.1 Tensile properties of LFT

Modulus of elasticity and strength   A notable observation from the results of the direction-dependent tensile tests in Figure 5.14 is, that all three materials tested showed a deviation of approximately $+9°$ to $+11°$ from the expected symmetry axis, both in terms of tensile modulus of elasticity and tensile strength. This effect can be found in the literature, as mentioned in the section 2.3.4.1, for compression molded LFT-D-ILC materials, and seems to be typical

for this process [144, 147, 145, 146, 126]. Since the drift reverses direction when the initial charge is rotated 180°, this indicates that the effect is due to the initial charge itself. This observation underscores the importance of the orientation of the initial charge in influencing the drift direction. Possible causes for this phenomenon are explored in more detail in Section 6.1, where various contributing factors are analyzed to understand the underlying mechanisms.

A comparison with the literature is essential in order to be able to classify the values determined here. In the case of CF-LFT based on PA6 in the LFT-D process, only one reference by Rohan et al. provides data with a simular carbon fiber mass content of 35 % and differentiating between the flow and charge range while characterizing the 0° and 90° orientations separately. Comparable strength values were observed for both the 0° orientation (approximately 200 MPa in the charge and 230 MPa in the flow area) and the 90° orientation (approximately 120 MPa in the charge and 80 MPa in the flow area). Likewise, similar tensile modulus values were recorded for the 0° orientation (approximately 22 GPa in the charge and 25 GPa in the flow area) and the 90° orientation (approximately 10.5 GPa in the charge and 8 GPa in the flow area)[152]. As with the materials investigated in this work, this results in a stronger anisotropy of the characteristic values in the flow area, where a more uniform fiber orientation is assumed due to the longer flow path. Another reason for the lower anisotropy in the charge area could be the shell structures with fibers oriented 90°, as mentioned in Section 4.1. These structures reduce the effective mechanical properties in the 0° orientation and increase them in the 90° orientation, thereby contributing to the lower anisotropy. The tensile modulus and tensile strength for materials featuring lower fiber content notably fall below those determined in the flow direction in this work. In the case of PA6 reinforced with 24 wt.% CF, the tensile strength stands at only 145.9 MPa and the tensile modulus at 13.2 GPa [210]. For PA6 with 18 wt.% CF, the tensile strength diminishes to 110 MPa and the modulus to 6.46 GPa [211].

The results of all tested samples, plotted in the tensile strength versus tensile modulus of elasticity diagramm in Figures 5.15, 5.16, and 5.17, indicate a linear relationship between these properties for all three materials. To verify this observation, a linear regression was performed on the tensile strength versus tensile modulus plot for all specimens tested, regardless of specimen area and orientation. The results of this regression are shown in Figure 5.33. To emphasize the distinction between material classes, all data points are shown as squares, each corresponding to the specific material color.
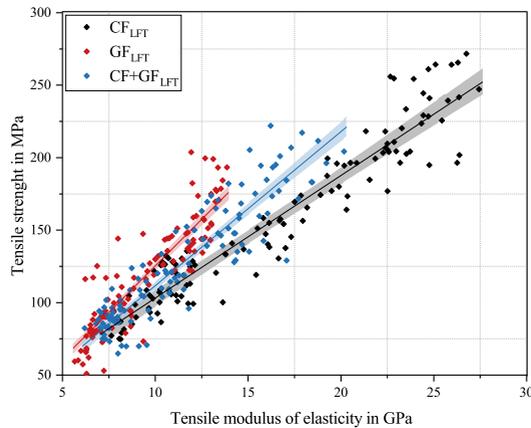
Figure 5.33: Linear regression in tensile strength versus elastic modulus diagram between all tensile tests independent of orientation and position of CF_{LFT}, GF_{LFT} and $CF + GF_{LFT}$ according to Scheuring et al. [127].

The GF_{LFT} regression line has the highest slope, indicating the lowest strength-to-stiffness ratio, while the CF_{LFT} regression line has the lowest slope, representing the highest ratio. The values of the regression line of $CF + GF_{LFT}$ lie fairly in the middle between these two regression lines. This emphasizes that the inclusion of CF in the LFT process primarily provides a significant increase in modulus, making it suitable for stiff components. This observation

is consistent with the inherent properties of CF, where its higher modulus, especially when oriented close to the main fiber direction, naturally results in a more pronounced stiffening effect, which influences the slope. The regression line of the hybrid falls between the two monofiber materials, as expected given the equal composition of the two fibers. It can be inferred that blends with a higher percentage of GF or CF would shift the regression line more in the GF_{LFT} or CF_{LFT} direction, respectively.

Analytical modeling of LFT using the shear-lag modified Halpin-Tsai method   The homogenization results from the Figure 5.18 showed an exact alignment of the principal symmetry axis of the modulus curve for all three materials, indicating a match in the positions of the maximum and minimum stiffness values. The fact that the model's orientation dependence is derived solely from the orientation information from the histograms in section 5.1.5, leads to the conclusion that the fiber orientation determination via µCT is valid regardless of the fiber type.

Further in the 90° and ±45° orientations, a precise agreement between the absolute values of the model and the experiment is evident for all three materials, whereas significant deviations occur in the 0° and the ±11,25° orientation. This observation, when correlated with orientation information from section 2.1.3.3, indicates that the 90° and ±45° orientations involve the least fiber alignment, leading to the smallest reinforcement effect due to the fibers. Therefore, the modulus is notably influenced by the properties of the matrix. Consistent modulus values in this direction suggest a reliable approximation for the modulus of the matrix material. At 0° and 11.25°, the most pronounced fiber alignment is observed, along with the largest disparity between experimental and model data. Two plausible explanations are considered. First, the experimental measurements may not accurately reflect the actual values in the material, possibly underestimating them. However, given the sensitivity of the employed methods, this seems unlikely to account for such a significant deviation. A more probable explanation is that the homogenization procedure overlooks fiber interactions and assumes a uniform distribution of perfectly bonded uncurved fibers.

Therefore one potential explanation for the overestimation observed across all materials could be attributed to fiber curvatures. While these are considered in the µCT orientation analysis, the model represents orientation using uncurved fibers. This idealized representation is the optimum case for load introduction, may lead to an overestimation of the modulus. However, incorporating curved fibers into the model is not feasible with the current framework. Another contributing factor could be the uneven distribution of fibers or bundling, as previously discussed in Section 5.1, which is particularly prominent within the CF_{LFT}. It can be assumed that fiber bundles may have a diminished reinforcing effect due to weaker fiber-matrix bonding, resembling the case of dry fibers that do not contribute to overall composite reinforcement. In addition, increased fiber interactions within bundles may further reduce the reinforcement effect. This has already been observed in other studies for Dico-FRPs in which fiber bundling has occurred [212, 67]. Given the fact that the overestimation is most pronounced in CF_{LFT}, and that it is also the material that shows the most bundles with even partial dry spots, supports this hypothesis. In addition, the overestimation is notably lower for the other materials. This aligns with the earlier assumption, supported by microstructure investigations that indicated a significantly reduced tendency to form bundles in the case of GF_{LFT} and $CF + GF_{LFT}$. Therefore, a plausible explanation for the discrepancy could be that the effective fiber volume content, which represents the fraction of fibers actively contributing to load transfer, is significantly lower than the experimentally determined fiber content.

Another explanation is, that the fibers within the bundles protect themselves from shortening during the extrusion and pressing processes. As a result, the fibers in the bundles are significantly longer than those that are well dispersed. This implies that the elongated fibers have a limited contribution to load transfer, which may lead to an overestimation of the effective fiber length and thus also of the effective aspect ratio based on the experimentally determined values. Since bundles were found in the CT images of all nine samples used for fiber length measurements, it can be assumed that they are also reflected in the

measurements [213]. This approach has been employed in existing literature sources for LFTs as a means to achieve alignment between experimental data and the model for LFTs with high fiber content [148, 50]. An in-depth investigation of the effects of fiber length distribution on the elasto-plastic behavior of short fiber composites was developed by Mentges et al. using an extended micromechanical orientation averaging model [214].

The current homogenization procedure do not inherently address these effects. Therefore, adjusting the measured fiber volume content and aspect ratio to an effective value that considers these effects could potentially align predicted and experimental results. It is reasonable to assume that an optimal representation of reality is obtained when both values are adjusted. To measure the effect of an adjustment, it is advisable to change only one parameter at a time in the subsequent analysis. Since the results of the model differs the most from the experimentally determined data in CF_{LFT}, which also represents the Dico phase in the later CoDico-LFT, it will be considered in more detail below.

Figure 5.34 illustrates the results of a Halpin-Tsai model adjusted in two different ways to the experimental data to the value of $0°$. In Figure 5.34 (a), only the fiber length was reduced from 0.54 mm to 0.17 mm, representing a reduction of 68.5 %. The shear-lag modified H-T model incorporating the fiber length adjustment is denoted below as "l_f adj. H-T". Meanwhile, in Figure 5.34 (b), only the fiber volume was reduced from 23.5 vol.% to 15 vol.%, representing a reduction, of 36.2 %.

The shear-lag modified H-T model incorporating the fiber volume content adjustment is denoted below as "vol_f adj. H-T". For comparison, the experimental data from the flow region is shown as usual, with the scattering region shown in gray for reference. It can be seen that the setting of both adjustments, adapted to the value in the $0°$ orientation, also gives good results in the other orientations.
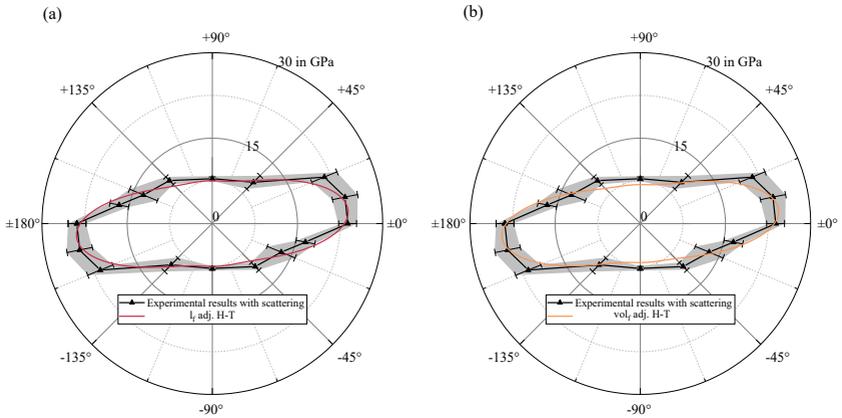
Figure 5.34: Adjustment of the shear-lag modified Halpin-Tsai model for CF_{LFT} to the experimental data of the tensile modulus of elasticity with (a) adjustment of the fiber length "l_f adj. H-T" (b) adjustment of the fiber volume content "vol_f adj. H-T".

It is noteworthy that the volume reduction induces a more pronounced decrease of the values in the 90° orientation compared to the length reduction. Consequently, the vol_f adj. H-T variant extends beyond the scattering range from -45° to -90°.

Effect of hybridization of mixed fiber LFT The results of the hybridization effect analysis from Figure 2.25 are consistent with the findings of Fu and Lauke et al. where a hybrid with equal amounts of CF and GF showed a 33 % increase in tensile modulus compared to a pure GF composite [172]. There are also examples in the literature of more substantial effects, as shown by Wollan, who reported a remarkable 106 % increase of tensile modulus in a hybrid of equal parts CF and GF compared to a pure GF composite, both based on PA6 [215]. It is worth noting that the production process uses pre-impregnated pellets containing both fiber types, ensuring effective fiber impregnation [215]. This supports the hypothesis that CF in the investigated hybrid as in the CF_{LFT} may not reach its full potential due to its bundled occurrence.

The notable 22% increase in elongation at break compared to CF_{LFT}, as observed in Figure 2.25, aligns with findings documented in the literature can be explained by this. Previous research has shown that interfacial shear stress peaks at the fiber end [153]. Considering the higher modulus of carbon fibers compared to glass fibers, it can be inferred that stress transfer theory predicts higher peaks at the tips of carbon fibers. The initiation of the first crack is likely to occur at these points [172, 174, 153, 158, 216].

These CF-derived cracks propagate through the matrix until they encounter a GF, which acts as a bridge and prevents immediate failure. Ultimate failure occurs when these cracks merge with those forming at the end of the GF [172, 77]. Schematic representations of this micro-failure process for CF+GF-Dico materials can be found in Fu and Lauke et al. [172] and Li et al. [174]. This underscores the mechanical synergy of the $CF+GF_{LFT}$, which combines the beneficial properties of both materials. Owing to the different properties of the fibers, including density and cost, the multi fiber material induces changes in specific mechanical properties. For a comprehensive comparison, table 5.2 provides an overview of the performance of $CF+GF_{LFT}$ relative to the base configurations of CF_{LFT} and GF_{LFT}. The table highlights promising combinations of mixed fiber LFTs for various optimization goals.

The introduction of CF into GF_{LFT} results in a significant 52 % improvement in weight specific modulus. Conversely, the addition of GF to CF_{LFT} results in a small increase in both price and CO_2 specific modulus. Importantly, the hybrid investigated in this study positions itself between GF_{LFT} and CF_{LFT} in the presented table, demonstrating its ability to expand the design space between these two configurations.

Table 5.3 shows the experimental results for the hybrid and the prediction using the RoM defined in Eq. 2.3. Owing to the significantly lower fiber volume content of the hybrid compared to the two monofiber materials, an additional adjusted RoM is used.

Table 5.2: Mechanical characteristics and production values of $CF + GF_{LFT}$ in comparison to GF_{LFT} and CF_{LFT} from Scheuring et al. [127].

Parameter	$CF + GF_{LFT}$ / GF_{LFT}	$CF + GF_{LFT}$ / CF_{LFT}
Tensile strength in 0°	116 %	78 %
Tensile Modulus in 0°	138 %	75 %
Elongation at break in 0°	81 %	122 %
Weight	91 %	104 %
Price primary Fibers	177 %	64 %
CO_2 primary Fibers	162 %	69 %
Modulus per weight	152 %	72 %
Modulus per price	78 %	117 %
Modulus per CO_2	85 %	109 %

This adjustment accounts for the lower fiber volume content of approx. 20 % in the hybrid by incorporating an additional amount of pure matrix. This results in a combination of 40 % each of GF_{LFT} and CF_{LFT}, along with an additional 20 % of pure matrix (PA6): $E_{hybrid} = 0.4 \cdot E_{GF-LFT} + 0.4 \cdot E_{CF-LFT} + 0.2 \cdot E_{PA6}$. The results based on the adjusted RoM are also shown in the table 5.3. It's worth noting that the experimentally determined values deviate slightly below the RoM. Specifically, the hybrid misses the RoM by only 7 % for σ_m and by only 3 % for $E_{tensile}$. Especially for $E_{tensile}$, the RoM shows a robust correlation considering the variability of the measured values. However, according to definition b) (cf. Figure 2.25), there is no observable positive hybridization effect.

In contrast, for σ_m, the hybrid outperforms the adjusted Rule of Mixtures (RoM) by 8 %, placing it exactly between the two estimates. Notably, for $E_{tensile}$, the hybrid outperforms the adjusted RoM by a substantial 16 %, underscoring that hybridization has a more pronounced effect on modulus than on strength.

Table 5.3: Rule of Mixture of 0° Flow Specimen from Scheuring et al. [127]

Parameter	RoM	adj. RoM	Exp.
σ_m in MPa	207.85	180	194.4
$E_{tensile}$ in GPa	18.4	15.43	17.9

Using the adjusted RoM as a benchmark, the hybrid exhibits a positive hybridization effect according to definition b) (cf. Figure 2.25). Considering both definitions of hybridization effects, it can be concluded that there is a positive effect according to definition a) (cf. Figure 2.25). However, according to definition b) (cf. Figure 2.25), the determination of a positive effect depends on whether the conventional RoM or the adjusted RoM is considered.

Failure behaviour of LFT under tensile load using the example of CF$_{LFT}$ Basically, the DIC images and the associated fracture surface analyses in the SEM showed that local strain increases and the resulting stress increase at the in the surrounding area of bundles can be held responsible for damage initiation. The bundles act as a geometrically diffuse macroscopic enclosure around which the stress and strain increases are distributed. This is consistent with results in the literature. Bondy et al. were able to show that bundles, and especially unimpregnated bundles, could be an initiator of damage, as they were observed in almost all fracture surfaces of CF-PA66-LFT-D materials subjected to fatigue loading [150].

While as shown in Figure 5.24 a single initial and then damage-critical strain increase can be seen in the flow area, in the charge area, next to a strain increase responsible for the critical failure, several, albeit less intense, strain increases can be seen distributed over the specimen surface. A plausible explanation for this phenomenon could be attributed to the presence of 90° oriented fibers on the surface of the sample, as detailed in section 5.1.3. These fibers on the surface can cause an increase in strain between fiber-rich areas. Since these are directly on the surface where the strains are also detected, this could lead to

the distributed weaker increases. This again shows the influence of the artifact structure from the extrusion process of the original charge, which freezes and remains in the charge area. However, these weaker strain and stress increases do not appear to have any influence on the failure mechanisms, as the crack development is clearly caused by bundle structures from the volume. But they are responsible for the higher modulus and strength in the 90° orientation in the charge area.

5.2.3.2 Tensile properties of CoDico-LFT

Modulus of elasticity and strength   As shown in Figure 5.25 in the 90° orientation, the tensile strength of the Dico-LFT in the charge and flow area is slightly greater than that of CoDico-LFT. This phenomenon can be attributed to the orientation of fibers within the Co phase. In a 90° specimen, none of the fibers in the Co phase are aligned with the load direction; rather, they are positioned orthogonally. In contrast, within the Dico phase, a limited portion of fibers align with the load direction due to the inherent distribution of fiber orientations. The lower volume content of the Dico phase within CoDico-LFT consequently leads to reduced strength in the structure. As illustrated in Figure 5.25, the unidirectional Co phase within the flow area exerts a reinforcing influence over a broader angular range than in the charge area. The reason for this can be explained by the different interface quality in the two areas. As described in section 5.1.7, the interface in the charge area is of significantly lower quality, probably because the outer layer of the initial charge has cooled down too much for optimal bonding. The specimens are fully clamped in the tensile test, which ensures that the load is introduced into the specimen via shear stress over the clamping pressure in the jaws. Furthermore, at lower strains, the deformation difference between Co and Dico-LFT is minimal, which results in both phases being loaded, thus yielding very similar modulus in both areas. Strength at 0° is also comparable because the Co and Dico phases are loaded independently, even after delamination. In the case of small angular deviations, this load application in the Co phase is still present after delamination, but

since the fibers in the co phase no longer extend over the entire gauge length, this leads to intermediate fiber breakage (cf. Figure 5.31) and thus to a lower strength, which partially corresponds to that of Dico-LFT, as can be seen at +11.25° in Firgure 5.25.

As expected, the reinforcing effect of the Co phase in CoDico-LFT manifests itself primarily in the orientation of the Co phase itself and in slight angular deviations from it. This underscores the potential for targeted use of Co phase reinforcements in Dico-LFT structures, allowing for resource-efficient applications tailored to specific loads. The fabrication methodology used in this study proves effective in demonstrating the potential of such materials under tensile loading conditions. In addition, the handling of PTFE-Films proves to be highly suitable for prototype development.

Failure behavior and Effect of hybridization in CoDico-LFT   Upon initial observation, the hybridization effect at CoDico-LFT in 0° orientation appears to align with expectations. In terms of tensile modulus and tensile strength, CoDico-LFT exhibits characteristics between those of Co and Dico-LFT. It was anticipated that, similar to the mixed fiber LFTs, the elongation at break would fall between the individual components. However, as illustrated in Figure 5.32, this is below that of both Co and Dico-LFT.

The fracture mechanics analysis clearly demonstrate that the negative properties of the bundles in the Dico phase adversely impact the fracture behavior of CoDico-LFT in the flow area. The combination of DIC images and fracture surface analysis, as shown in Figure 5.26 and Figure 5.27, reveals that strain increases indicating critical failure are localized at points where bundles can be found in the Dico phase. As already mentioned, these bundles are the origin of a local stress and strain increase in the Dico phase. Due to the good interface quality between the Co and Dico phases in the flow region, these strain increases are transferred to the Co phase, resulting in local stain increases in the Co phase detectable in the DIC images. The local strains in the Co phase exceed the elongation at break, resulting in a fracture that propagates to the Dico phase

and ultimately leads to the complete failure of the specimen. It is noteworthy that the macroscopic strain of the entire sample remains below the elongation at break of both individual components. The inhomogeneities of the Dico phase therefore mean that the properties of the Co phase can only be partially utilized in the hybrid. As the hybrid is therefore below the individual components, this can be regarded as a negative effect of hybridization no matter which material is chosen as the reference.

Therefore, the importance of a good dispersion of the fibers in the Dico phase is emphasized once again to fully utilize the properties of the Co phase in the hybrid. However, this relates to the strength. Concerning modulus, the full potential of the Co phase could be exploited since this is determined at small strains and thus before the occurrence of a local strain increase. However, this only applies on condition that a suitable interface is guaranteed, as in the flow area.

Since a simplified strain equilibrium can be assumed in both phases in the tensile test, the RoM can also be used here to predict the effective mechanical properties of the hybrid. It should be noted, however, that the RoM tends to overestimate the CoDico-LFT in the case of tensile strength due to the differing elongation at break. Nevertheless, in order to provide a reference point for the evaluation of the effect of hybridization according to definition b), it is still considered here. The volume fractions determined in Section 5.1.7 are used for this purpose and the results are given in table 5.4.

Table 5.4: Rule of Mixture on CoDico-LFT 0° Flow Specimen

Parameter	RoM	Exp.
σ_m in MPa	362	339
$E_{tensile}$ in GPa	35	43

It is noticeable that the strength is only slightly overestimated by the RoM with a deviation of approx. 7 % while the modulus is clearly underestimated with a deviation of 18 %. One possible explanations for this is, that the experimentally determined modulus of the Co phase is significantly underestimated. For example, small angular deviations during specimen preparation or clamping can lead to a significantly lower modulus in the sample. In the CoDico-LFT, load bearing is significantly improved even at small angular offsets due to its good interface. This is evidenced by the significant difference in modulus observed between specimens with an orientation of 11.25° from the charge and flow area. Consequently, it is plausible that the CoDico-LFT system exhibits reduced sensitivity to small angular variations, resulting in higher modulus or an underestimation of modulus by the RoM. In addition, it is also possible that local deviations from the preferred alignment of the fibers, as shown in section 5.1.6, reduce the overall modulus in the Co phase. Since the areas where waviness occurs sometimes extend across the entire width of the sample, the properties of the fibers can only be exploited to a limited extent at these points. In the hybrid, it is now possible that the movements are restricted by the hybridization at this point and therefore the Co phase has a higher stiffening effect in the composite. It is also possible that the clamping concept results in different expansions in the different phases. Since the strains were only measured at the surface of the Co phase DIC, this could lead to an overestimation of the modulus of the hybrid.

5.3 Bending tests

The investigations of the direction-dependent mechanical properties under bending were carried out both for the different LFT Materials and the CoDico-LFT exclusively on specimens in "dry" conditions as explained in section 3.2.3. No bending tests were carried out on the pure Co phase.

5.3.1 Flexural properties of LFT

The polar plots in Figure 5.35 show the orientation dependent results of the flexural modulus of elasticity in Figure 5.35 (a) and flexural strength in Figure 5.35 (b) of the LFT materials in the same schematic as the results of the tensile tests in section 5.2. A distinction is made between the charge and the flow area and the results are presented as the mean value with standard deviation from at least 5 samples for the orientations 0°, ±11.25°, ±22.5°, ±45°, and 90°. For better understanding, the points are connected linearly. Figure 5.35 (a) illustrates the flexural modulus, which exhibits notable similarities to the tensile modulus. However, there are also discernible differences. In particular, the fibers exhibit the most pronounced stiffening effect between the flow direction (0°) and +22.5°. Again, the consistent elevation of the modulus at +11.25° and +22.5° relative to their counterparts at -11.25° and -22.5° is noteworthy for all three materials. This represents a curve of the flexural modulus that deviates from the expected symmetry along the 0°-180° axis. This was previously observed in tensile tests and is discussed in greater detail in section 6.1. It is noteworthy that, for all three materials, the flexural modulus in the flow direction and for smaller angle deviations in the positive direction is significantly higher in the flow area compared to the charge area. The difference thereby is smallest with the CF_{LFT}, and much more pronounced with the GF_{LFT} and $CF+GF_{LFT}$. Furthermore, it is evident that while in the charge area of GF_{LFT} and $CF+GF_{LFT}$, the flexural modulus of a 0° sample is remarkably similar, in the flow area significant discrepancies can be observed. The 90° orientation specimens exhibit a contrasting behavior. All three materials have a higher
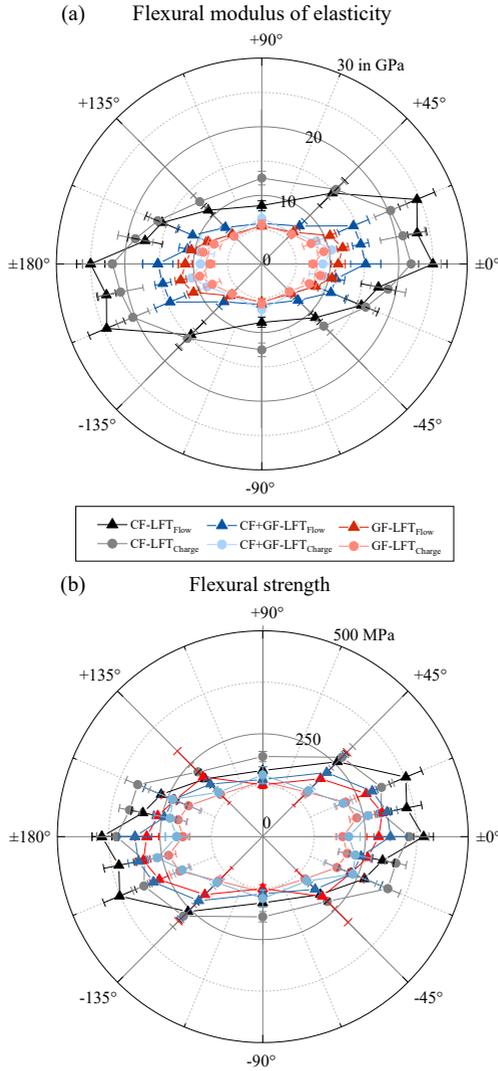
Figure 5.35: Polar diagram of (a) flexural modulus of elasticity and (b) flexural strength of the three different LFT Materials in different orientation to the flow direction separated by charge and flow area.

flexural modulus in the charge area compared to the flow area. For GF_{LFT} and $CF+CF_{LFT}$, the differences are minimal and not statistically significant. However, for CF_{LFT}, a significantly higher flexural modulus is observed at 90° in the charge area. Looking at the flexural strength in Figure 5.35 (b), it is again noticeable that the stiffening effect of the fibers exceeds the strengthening effect, even under flexural loading. This means that the difference in strength between CF_{LFT} (which contains the stiffest and strongest fibers) and the other two materials is much smaller than the difference in modulus. However, it is again noticeable that the charge area has a lower strength in the 0° direction and a higher strength in the 90° orientation than the flow area which is consistent with the considerations of the flexural modulus.

5.3.2 Flexural properties of CoDico-LFT

Modulus of elasticity and strength   The polar plots in Figure 5.36 show the orientation dependent results of Figure 5.36 (a) the flexural modulus of elasticity and Figure 5.36 (b) flexural strength of the CoDico-LFT in the same way as in Figure 5.35. Since the Dico phase in CoDico-LFT corresponds to the CF_{LFT}, the results of the CF_{LFT} from Figure 5.35, here referred to as Dico-LFT, are shown again for comparative analysis. An initial analysis of the flexural modulus of elasticity reveals consistent values across various orientations for the charge and the flow area of the CoDico-LFT, with a notable exception at -11.25°. As in the tensile tests, the CoDico-LFT also demonstrates under flexural loading in 0° direction a significantly higher modulus of 49 GPa compared to Dico-LFT with 22 GPa in the charge area and 25 GPa in the flow area. This results in a significantly more pronounced stiffening effect by the Co phase of approx. 122 % and 96 % in the flexural modulus. The stiffening effect is also observed over a wider range, with the effect still discernible up to deviations of ±22.5°. In the ±45° orientation, the flexural modulus for CoDico-LFT and Dico-LFT are found to be highly similar, although there are discernible

(a)   Flexural modulus of elasticity

(b)   Flexural strength
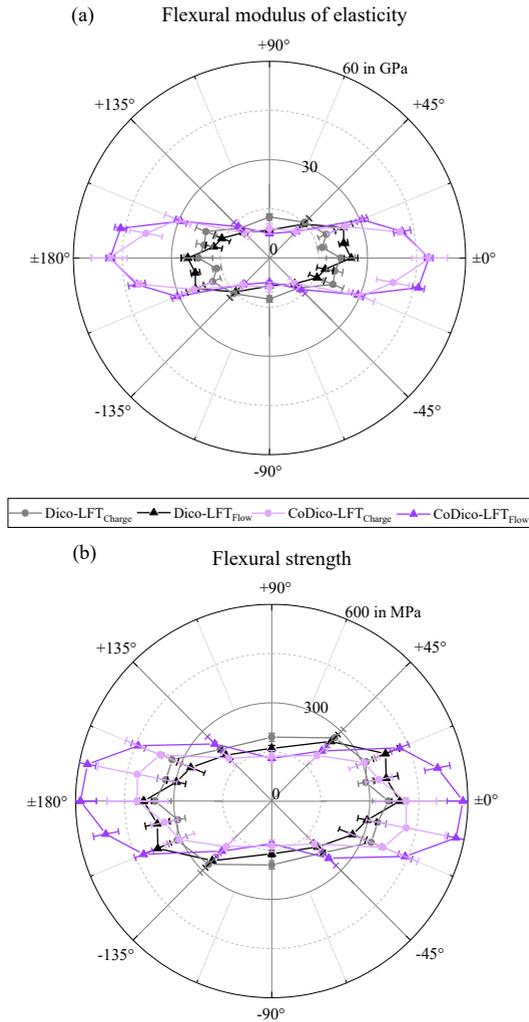
Figure 5.36: Polar diagram of (a) flexural modulus of elasticity and (b) flexural strength of Dico-LFT and CoDico-LFT in different orientation to the flow direction separated by charge and flow area.

differences in the 90° orientation. In this orientation, CoDico-LFT and Dico-LFT exhibit identical modulus values in the flow area, yet Dico-LFT exhibits a markedly higher modulus value in the charge area. Due to the greater difference between 0° and 90° orientation in the CoDico-LFT, this results in a significantly stronger directional dependence of the flexural modulus of elasticity than of the pure Dico-LFT. It is also noticeable that in comparison with the Dico-LFT the flexural modulus of elasticity of the CoDico-LFT is almost symmetrical to the 0°- 180° axis. This is a illustrates the influence of the Co phase, which reinforces the symmetry to this axis by aligning it in the 0° orientation.

Upon examination of the flexural strength, it becomes evident that there is a discernible distinction between the charge and flow area of the CoDico-LFT. While in the flow area, similar to the flexural modulus, the flexural strength is significantly higher than the Dico-LFT in the 0° orientation and angular deviations up to ±22.5°, the charge area shows a similar flexural strength as the Dico-LFT in these orientations. Furthermore it is noticeable that the flexural strength in the charge area shows a considerable scatter in the 0° orientations and small angular deviations from this. In the ±45° orientation, both areas of the CoDico-LFT exhibit comparable flexural strength to that of the Dico-LFT. However, in the 90° orientation, the values of the CoDico-LFT are distinctly lower than those of the Dico-LFT across both areas.

5.3.2.1 Failure behavior of CoDico-LFT under flexural loading

In order to identify the underlying cause of the discrepancy between similar flexural modulus but significantly different flexural strengths in the two areas of the CoDico-LFT material, it is useful to look at failure behavior. Figure 5.37 shows representative stress-deformation curves for 0° specimens from the charge and the flow area. The first thing to notice is that both curves start with the same slope from the origin. The area in which the flexural modulus is determined according to DIN EN ISO 14125 is highlighted in gray. As can be seen, this area is within the range that has the same slope and therefore the same flexural modulus is determined for both areas, as already shown in Figure

5.36. As the curve progresses, there is a rapid drop in stress in the course of the charge area at point A in Figure 5.37, while the curve continues to rise with the same gradient in the flow area. After the drop in the curve of the charge area, the curve rises with a much smaller slope until another drop in stress occurs at point B in Figure 5.37. The curve then rises again, but at a slower rate, until fracture or break occurs.
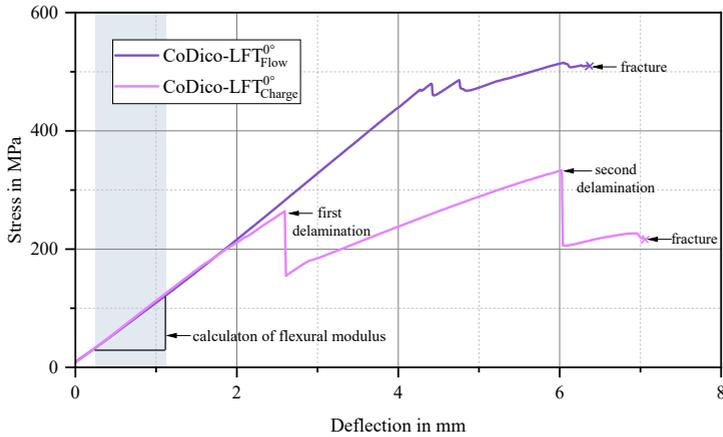
Figure 5.37: Representative stress-deformation curve of the 0° CoDico-LFT specimen from the charge and flow area, with the points A and B specifically marked, illustrates the rapid stress drop observed in the curve of the charge area.

In order to comprehend the mechanisms underlying the rapid stress reduction observed at points a and b, it is necessary to examine the images of the specimen at these points in the test. These images are presented in Figure 5.38. Figure 5.38 (a) shows that delamination occurs between the two supports at the top of the sample, i.e. at the point where compressive stresses act on the Co phase.

The second drop, as illustrated in Figure 5.38 (b), demonstrates the delamination spreading on the upper surface of the specimen. The delamination from Figure 5.38 (a) thereby progresses from the upper supports to the point at the specimen's top where the load is applied through the lower supports on the opposite side

of the specimen. In the region where the sample overlaps the lower supports, the interface remains intact. This phenomenon is characterized by a rapid drop-off followed by a reduction in modulus, which is reflected in a flatter curve. The lower layer, which is subjected to tensile stress at the bottom of the specimen, also exhibits delamination in a post-mortem analysis. However, this was challenging to discern during the experiment, as the Co phase remained under tension due to the compression on the outer supports and the coating under tension. It is likely that it also contributed to the load transfer over the entire test period.
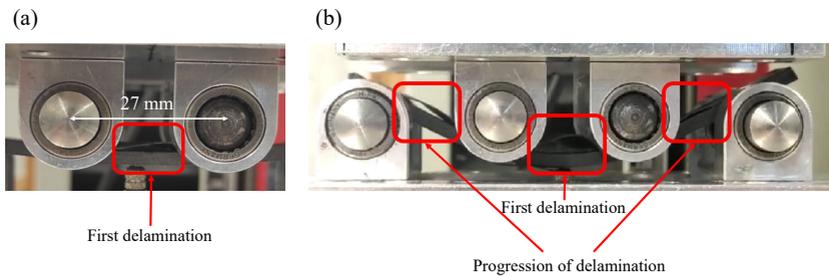
Figure 5.38: Images of the failure progression of the 0° CoDico-LFT sample from the charge area in Figure 5.37 at the points of the sudden drop in stress.

A comparison of the curve from the flow area in Figure 5.37 with the curve of the charge area reveals that the curve from the flow area rises linearly over a significantly longer deformation range. However, from a certain point onwards, the former also shows points at which the stress suddenly drops. However, this drop is much less pronounced than in the charge area. At the same time as this drop in stress occur, noise was noticed during the test. Visual inspection of the samples revealed small "waves" on top of the specimen in the Co phase, where the Co phase was minimally separated from the Dico phase. However, this cannot be compared with delamination in the charge area, but looks more like a buckling of the Co phase. Furthermore, fractured samples revealed that the fracture in the Co phase on the side under tension did not proceed in a straight line. Instead, the Co phase partially failed at different positions.

159

5.3.2.2 Effect of hybridization of CoDico-LFT

As previously stated, the suboptimal interface can be rectified through process engineering. Consequently, the impact of hybridization is considered to be solely under flexural load within the flow area. For this purpose, the curves of all valid tested 0° specimens from the flow area of Dico-LFT and CoDico-LFT are shown in Figure 5.39. The mechanical properties of CoDico-LFT in relation to those of the Dico-LFT are indicated by the red and green arrows for better comparison. In addition, the scattering areas are highlighted in color.
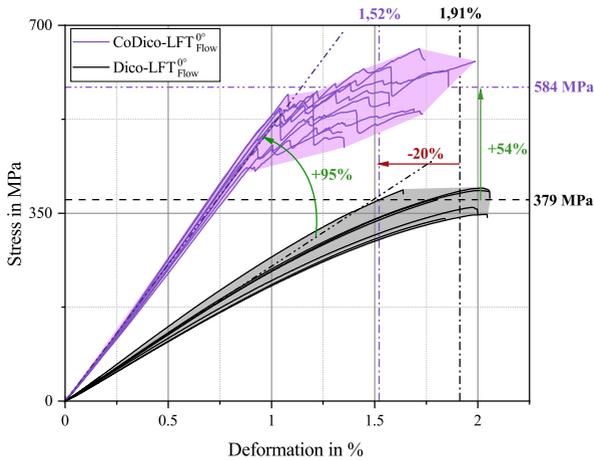
Figure 5.39: Effect of hybridization of CoDico-LFT under bending load in comparison to CF-LFT on the example of specimen from the flow area in 0° orientation to the flow front, where the highest fiber reinforcement effect was observed in both the Dico and Co phases.

The first thing to note is that there is a significant increase in flexural modulus and flexural strength. However, the increase is significantly higher than in the tensile tests in each case. CoDico-LFT shows a 95 % higher flexural modulus and a 54 % higher bending strength. This is associated with a 20% reduction

in fracture deformation. In addition, the curves for all specimens show that in the CoDico-LFT there is no continuous line at higher deformations and stresses. Instead, all tested specimens show small, sudden stress drops, as in the representative specimen from the flow area in Figure 5.37. In contrast, the Dico-LFT curves display a continuous increase in stress and deformation until the final fracture.

5.3.3 Discussion

5.3.3.1 Flexural properties of LFT

As shown in Figure 5.35, for all three LFT materials, the flexural modulus in the flow direction and with smaller angular deviations in the positive direction is significantly higher in the flow area than in the charge area. This phenomenon can be attributed to the differing microstructures of the two areas. In particular, the shell structures present in the charge area, in which the fibers are aligned perpendicular (90°) to the direction of flow, contribute to this effect. Since there is no homogeneous stress distribution over the height of the specimen under bending load, the edge areas experience the highest elongation and thus also the highest stress. Consequently, these areas have a more than proportional effect on the determination of the modulus. Figure 5.40 (a) provides a schematic illustration of flexural loading in comparison to tensile loading, accompanied by stress distribution curves and a depiction of the microstructures present in the charge and flow area for a 0° specimen and in Figure 5.40 (b) for a 90° specimen. It can be observed that in a 0° sample of the charge area, the point of maximum elongation occurs at the point where the fibers are orthogonal to the load direction, resulting in a minimal stiffening effect. Consequently, the outer layer exhibits a matrix-dominant behavior. In contrast, in the flow area, the fibers in a 0° specimen are aligned in the load direction up to the edge, which allows the fiber properties to be exploited at the point of maximum elongation. This results in the observed differences in modulus.
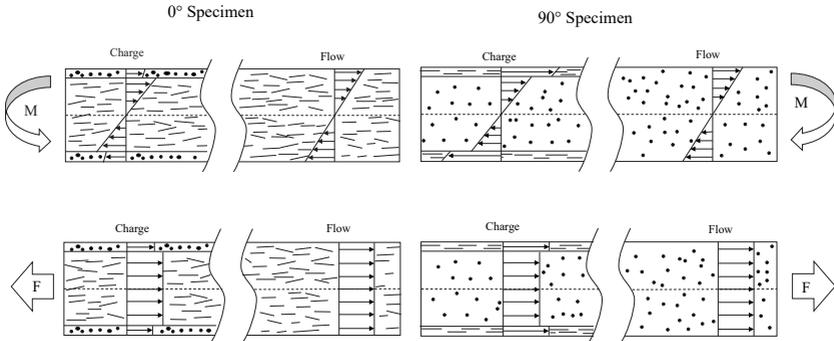
Figure 5.40: Schematic stress distribution in 0°- and 90°-oriented LFT specimens from the charge area and the flow area under tensile and bending loads

As shown in Figure 5.35 the difference thereby is smallest with the CF_{LFT}, and much more pronounced with the GF_{LFT} and $CF+GF_{LFT}$. This observation is consistent with the findings from the micrographs presented in section 5.1.3, which show the least pronounced shell structure for CF_{LFT}. Therefore, the influence here is also the least recognizable. It has also been shown that the flexural modulus of a 0° specimen is remarkably similar in the charge area of GF_{LFT} and $CF+GF_{LFT}$, but there are significant differences in the flow area. The microsections demonstrate that the shell structure is similarly pronounced in $CF+GF_{LFT}$ and GF_{LFT}, with the GF_{LFT} exhibiting a significantly reduced number of fibers. In both cases, a strong orientation of the fibers towards the edge can be observed in the flow area, where a mixture of well-impregnated fibers of both fiber types can be found in the $CF+GF_{LFT}$. The well-aligned and well-impregnated CF are presumably responsible for the different modulus in the flow area between GF_{LFT} and $CF+GF_{LFT}$.

In the 90° oriented specimen, a parity in modulus between the charge and flow areas is evident for GF_{LFT}. In contrast, $CF+GF_{LFT}$ and CF_{LFT} exhibit a conspicuous enlargement in modulus within the charge area compared to the flow area. This observation appears to corroborate the preceding assumption that there are markedly fewer fibers in the shell structures of GF_{LFT}. Consequently,

162

the beneficial impact of the fibers in the surface layer aligned in the load direction in a 90° oriented sample is not discernible. In contrast, with CF+GF$_{\text{LFT}}$, where more fibers are already visible, a distinction can be observed with 90° oriented samples in the charge and flow areas. This phenomenon is most evident in CF$_{\text{LFT}}$, where the microsections appear to indicate that a comparable number of fibers are present in the shell structure. As illustrated in Figure 5.35 (b), the charge area exhibits lower flexural strength in the 0° direction and higher flexural strength in the 90° direction compared to the flow area, mirroring the trend observed for the flexural modulus. Again, this is due to the stress distribution across the thickness shown in Figure 5.40 which is responsible for that in the boundary layers in the charge area, which have a 90° rotated orientation, higher stresses can be withstood for 90° samples and lower stresses for 0° samples before fracture occurs.

This influence of the artifact structures of the initial charge is already known from the literature and sometimes leads to even greater differences between charge and flow area under bending load [126]. Given that the greatest stresses are concentrated on the surface of the sample and that the bundles, which were the source of the critical failure under tensile load, are located within the sample, there is no correlation between the bundles and the initiation of failure under flexural loading.

5.3.3.2 Flexural properties of CoDico-LFT

The rapid stress drop observed at point a in Figure 5.41 during the bending tests of the 0° CoDico-LFT specimens from the charge area can be attributed to the delamination of the Co layer from the Dico layer between the inner supports. This delamination causes the Co layer to lose its ability to absorb any force, resulting in a sharp decline in the load-bearing capacity of the structure. Consequently, the Co layer on the upper side is no longer able to contribute to load bearing in this area, leading to a reduction in the material's modulus and a subsequent decrease in the gradient of the curve. A similar effect is observed after the second delamination at point b in Figure 5.41, which occurs between

the inner and outer supports. This delamination further prevents the Co phase in this section of the specimen from participating in load bearing, resulting in an additional reduction in the gradient of the curve.

The slight stress drops that can be observed in the flow area shortly before failure can be explained by a different mechanism. As described in Section 5.3, it was observed that the failure in the Co phase did often not form a straight line on the bottom side of the specimen. This indicates that, due to the in Section 5.1 identified inhomogeneities in the Co phase, parts of the Co phase fail before the overall structure fails. Further it is assumed that the formation of the waves observed on the top of the specimen between the inner supports or the local premature failure on the downside are responsible for the small dips in the curve observed in the flow area in Figure 5.37. The elongation at break of both areas differs only slightly.

In summary, similar to the tensile test, a poor interface can be responsible for poor material performance in the charge area due to early delamination. Under flexural stress, the effect of weakening is even greater. This underlines the relevance of the process adaptations to achieve a good interface over the entire structure, which is discussed in more detail later in Section 6.2. The potential of CoDico-LFT sandwich structures and the benefits of hybridization compared to the individual components are evident in the flow area, where a strong interface is present, as illustrated in Figure 5.32. Compared to the tensile test, a significantly higher reinforcement effect can be seen over a wider orientation range.

This may be another explanation for the more pronounced hybridization effect in addition to the inhomogeneous stress state. While the stress increases continuously from the neutral line outward in materials that are homogeneous across the thickness, such as PA6 and LFT, there is a jump in stress in inhomogeneous materials such as CoDico-LFT. To illustrate, the comparison with samples under tensile load is shown schematically in the Figure 5.41. This illustrates that the hybridization of Dico-LFT with Co in a sandwich structure is particularly advantageous for the load case of bending, as the highly rigid Co layers are

located at the point of greatest elongation and thus make a high contribution to load transfer. This effect has already been successfully demonstrated for CoDico-FRPs based on SMC by Trauth and Bartkowiak [80, 217].
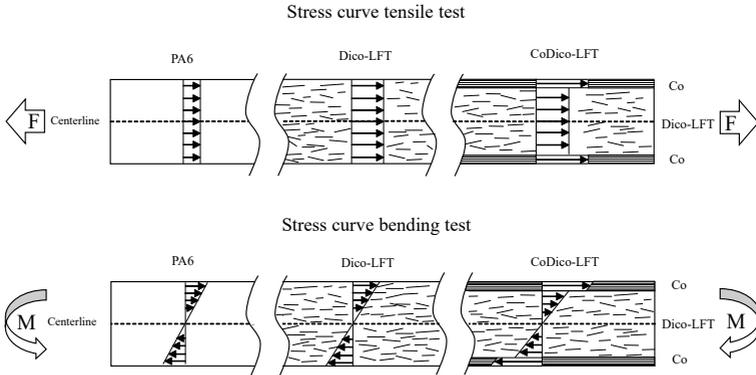
Figure 5.41: Stressdistribution in unreinforced PA6, Dico-LFT and CoDico-LFT (a) under tensile load and (b) under bending load

The marked increase in stiffening and hardening is accompanied by a significantly smaller reduction in elongation at break compared to the tensile test. This reduction is mainly because the edge phase, which experiences the maximum elongation during bending, contains the Co phase with lower elongation at break. The smaller reduction observed is probably due to the bundling within the volume of the Dico phase, which does not induce significant strain jumps in the Co phase, as could be observed in the tensile tests. The micrographs in Section 5.1 show that these bundles are typically located in the center of the Co phase. In the uniaxial tensile test, this results in an increase in strain or stress propagation from the bulk to the surface Dico phase.

However, in the bending tests with varying stress across the thickness, the point of low stress or strain is in the center of the specimen, which again means that the bundles do not affect the damage behavior of the edge layers. This suggests that the stress distribution in the Co phase remains more uniform during bending, preventing local stress peaks and premature failure.

5.4 Dynamic mechanical analysis

5.4.1 Temperature-induced transition mechanism under tensile load

5.4.1.1 Temperature-induced transition in PA6 in dry state

To illustrate the general procedure and the definition of some characteristic values, the representative course of E', E'' an tan δ for unreinforced PA6 in the dry state are shown as a function of temperature and frequency in Figure 5.42. As already mentioned, PA6 is assumed to be homogeneously isotropic,
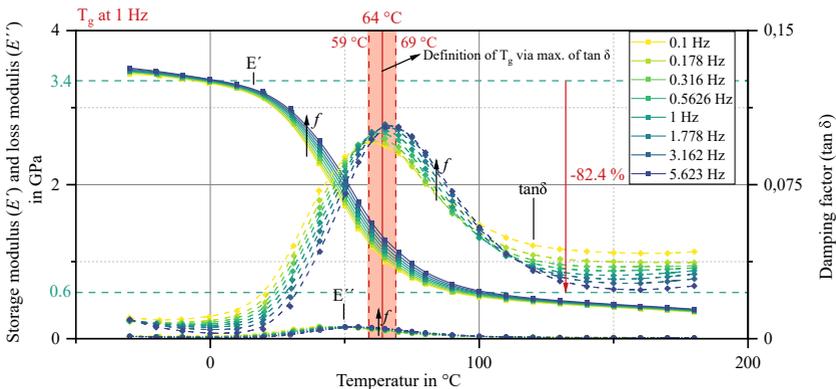
Figure 5.42: Representative evolution of storage modulus (E'), loss modulus (E'') and damping factor (tan δ) of PA6 in the dry state as a function of temperature and frequency with definition of the frequency-dependent glass transition temperature (T_g) as the maximum of tan δ.

this course applies to all orientations. The red area depicts the range of the frequency-dependent T_g. This is defined in all subsequent analyses by the peak of tan δ. The range is delimited by the minimum frequency at 0.1 Hz with 59 °C and by the highest frequency at 5,623 Hz with 69 °C. The peaks of tan δ and thus also the T_g of the frequencies in between are located in this range in

ascending order. This illustrates the frequency-dependent softening behavior. Since a discrete value is useful for the later comparison of the different material classes; thus, T_g at 1Hz, which in the case of dry PA6 is 64 °C is also provided. Unless otherwise stated, the peak of tan δ at 1 Hz will be used to determine T_g for all materials in the rest of the work. The temperature range corresponding to T_g or the main softening range is also visible course of E' on the basis of the area in which there is a more significant drop can be observed. However, this drop extends over a much larger temperature range.

An almost linear decrease of E' is observed from -30 °C to 10 °C, until the decrease gradient increases significantly at 20 °C and above. In the temperature range of 40 °C to 60 °C, the rate of decrease reaches its maximum and then decreases continuously up to approximately 90 °C, before returning to a sort of linearity from approximately 100 °C until the end of the test at 180 °C. To quantify the main softening range drop, it is useful to consider the drop from 0 °C to 100 °C, as this encompasses all the effects of the main softening range on E'. For unreinforced PA6, a significant decrease in storage modulus is observed, dropping from 3.4 GPa to 0.6 GPa, a reduction of 82.4 %. The course of the E'' is only very weakly pronounced in this scaling. However, it can be seen that in the range in which the storage modulus falls, the loss modulus rises and begins to fall again after a maximum at approx. 50 °C - 55 °C.

5.4.1.2 Temperature-induced transition in Co, Dico-LFT, and CoDico-LFT under tensile load in a dry state in 0°

The results of section 5.2 indicates that the 0° orientation is associated with the greatest fiber reinforcing effect. In order to determine the influence of the fibers on the temperature-dependent behavior, it is useful to first examine fiber-reinforced samples with a 0° orientation, since the strongest contrasts between the materials are to be expected here. Figure 5.43 shows therefore the curves of E' for unreinforced PA6 and 0° oriented specimens of Dico-LFT, CoDico-LFT, and Co under tensile loading in the dry state. The legend color-codes

the different test frequencies, with squares representing the actual measured values connected by a B-spline. To facilitate relative comparisons, the values for E' at 1 Hz and temperatures of 0 °C and 100 °C are plotted on the right ordinate. Upon examination of the T_g of Dico-LFT, it is observed that it is 3 °C lower (61 °C) than that of unreinforced PA6 (64 °C). However, this is within the typical range of scatter, indicating that the addition of Dico fibers has no significant effect on T_g.
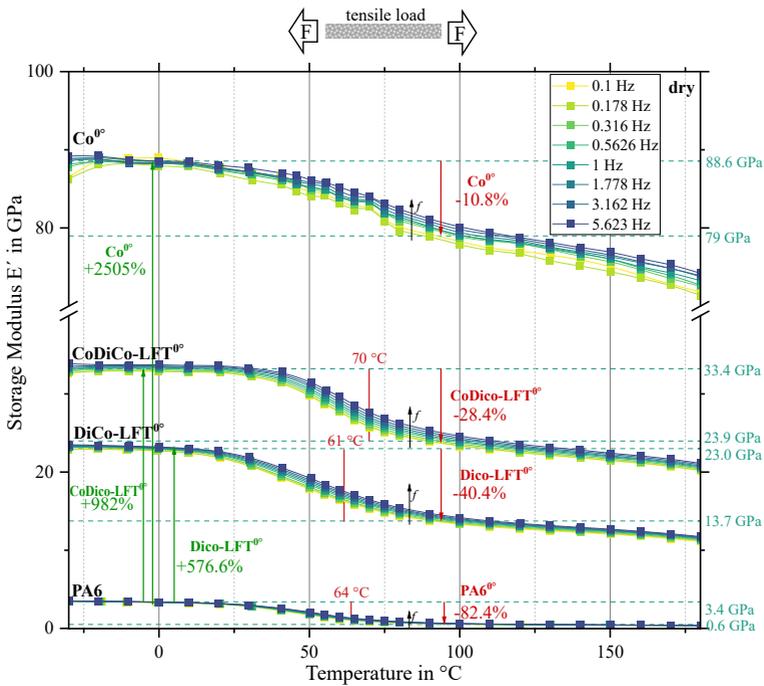
Figure 5.43: Representative evolution of the storage modulus (E') from the tensile DMA measurements of PA6 and Dico-LFT CoDico-LFT and Co in 0° direction in dry conditions in the range from -30 °C to 180 °C, with the exact values at 0 °C and 100 °C for the test frequency 1Hz at the right ordinate. The red arrows indicate the percentage drop in E' over the 100 °C range. The green arrows indicate the percentage increase in E' between the material classes at 0 °C. The vertical red lines describes the glass transition temperature (T_g) at 1 Hz defined by the peak of tan δ.

A further examination of the T_g of CoDico-LFT at 70 °C reveals a more pronounced disparity of 6 °C to PA6 and 9 °C to Dico-LFT. Figure 5.43 does not show a Tg for the Co material. This is due to the fact that the tan δ does not have a local maximum for the Co, but instead increases steadily up to the maximum temperature of 180°C. Consequently, it is not possible to determine the Tg of the Co material with absolute certainty.

Upon initial examination of the Dico-LFT data, it becomes evident that there has been a notable increase of 576.6 % at 0 °C to 23 GPa. This value falls within the scatter band of the quasi-static values presented in Section 5.2. In addition, the relative temperature sensitivity is significantly reduced. While PA6 shows an 82.4 % decrease in E' from 0 °C to 100 °C, Dico-LFT shows only a 40.4 % decrease.

A similar phenomenon can be observed in the CoDico-LFT curve, where the value of E' increases and the temperature sensitivity decreases further. The CoDico-LFT shows an increase in E' of 982 % compared to unreinforced PA6 at 0 °C, while at the same time , the decrease between 0 °C and 100 °C is only 28.4 %. As expected, the greatest reinforcement effect can be observed in 0° orientation with the Co, with a 2505 % increase in storage modulus compared to PA6. In particular, the temperature sensitivity is also significantly reduced, with only a 10 % decrease in E' between 0 °C and 100 °C.

5.4.1.3 Temperature-induced transition in Co, Dico-LFT, and CoDico-LFT under tensile load in a dry state in 90°

In order to consider the other extreme case, the temperature-dependent properties of the specimens oriented at 90° are examined in more detail. As the quasi-static results in section 5.2 show, the reinforcement effect of the fibers is expected to be minimal in this orientation. For this purpose, the results of E' from specimens of PA6, Dico-LFT, CoDico-LFT and Co in a 90° orientation are shown in Figure 5.44 in the same schematic as in Figure 5.43.
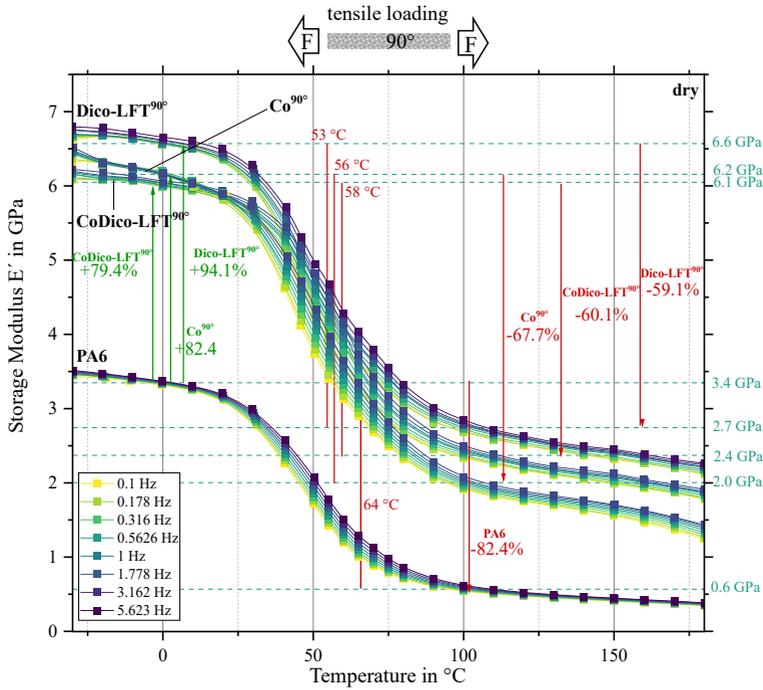
Figure 5.44: Results of the storage modulus E' from the tensile DMA measurements of PA6, Dico-LFT, Co and CoDico-LFT in 90° direction in dry conditions in the range from -30 °C to 180 °C, with the exact values at 0 °C and 100 °C for the test frequency 1Hz at the right ordinate. The red arrows indicate the percentage drop in E' over the 100 °C range. The green arrows indicate the percentage increase in E' between the material classes at 0 °C. The vertical red lines describe the glass transition temperature (T_g) at 1 Hz defined by the peak of tan δ.

Since PA6 is assumed to be isotropic, the same graph is shown as for the samples with 0° orientation. A preliminary examination of the values of T_g reveals that they are significantly closer together for Dico-LFT (53 °C) and CoDico-LFT (58 °C). In addition, a local maximum in the tan δ and thus a concrete T_g could also be determined for Co in 90° orientation (56 °C), which lies between that of Co and Dico-LFT. However, when these T_g values are compared with those of unreinforced PA6, it is evident that they are significantly lower in each case.

Furthermore, the T_g value is also significantly lower for all materials when compared to the 0° oriented specimen.

In all three fiber-reinforced materials a reinforcing effect of the fibers can be observed even in the 90° orientation. For example, at 0 °C there is a relative increase in E' of 94.1 % for Dico-LFT, 79.4 % for CoDico-LFT and 82.4 % for Co compared to unreinforced PA6. Similarly, a decrease in temperature sensitivity can be seen for all three materials. Dico-LFT and CoDico-LFT show a decrease of 59.1 % and 60.1 % respectively between 0 °C and 100 °C, while the decrease for Co is significantly higher at 67.07 %. For all materials, the usual frequency dependence can be seen, i.e. higher E' can be determined at higher test frequencies over the entire temperature range. The biggest influence of frequency can again be seen in the main softening range around T_g.

5.4.1.4 Comparison of relative storage modulus in 0° and 90° orientation

In order to highlite the influence of the fiber orientation in the individual materials, the curve of E' measured at a test frequency of 1 Hz and normalized to the value at 0 °C, is plotted against the temperature for unreinforced PA6, as well as for Dico-LFT, Co and CoDico-LFT. The results are presented for both, specimens with a 0° orientation in Figure 5.45(a) and specimens with a 90° orientation in Figure.5.45(b). In the case of the 0° orientation, it is notable that the temperature-dependent softening differs significantly between the materials. While the unreinforced PA6 exhibits the greatest softening, the other materials, sorted by fiber volume content and length distribution, each exhibit less softening. While the main softening region of Dico-LFT and CoDico-LFT is recognizable by a region with a stronger drop, this is only very slightly visible for Co. When the curves are examined in the 90° orientation, the main softening region is recognizable for all materials. It is also notable that Co exhibits the strongest softening of the composites, in contrast to the 0° oriented samples.
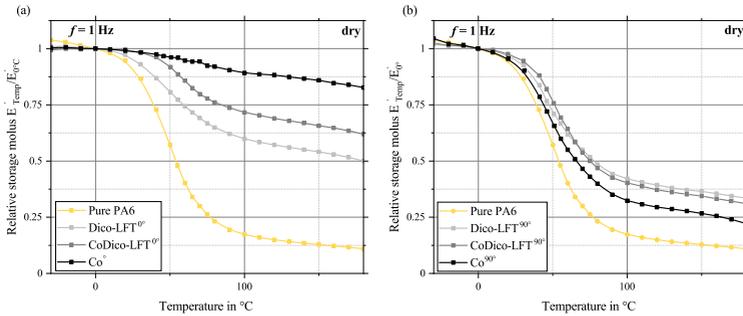
Figure 5.45: Storage modulus E' at a test frequency of 1 Hz normalized to the value at 0 °C as a function of temperature of unreinforced PA6 and Dico-LFT Co and CoDico-LFT with (a) specimen with 0° and (b) specimen with 90° orientation.

This illustrates the strong influence of fiber orientation. It can therefore be concluded that the reduction in temperature sensitivity is essentially dependent on the fiber content, length and orientation. In summary, lower temperature sensitivity can be achieved by increasing fiber content, increasing fiber length, or fiber orientation in load direction.

5.4.2 Analytical modeling approaches of temperature-dependent storage modulus under tensile load

5.4.2.1 Analytical modeling approaches of Dico-LFT

To check whether the shear-lag modified Halpin-Tsai model adapted to the quasi-static tests can also reproduce the behavior of the Dico-FRP over the investigated temperature range, the l_f adj. H-T and the vol_f adj. H-T from Section 5.2.3.1 will also taken into account. The objective is to ascertain the influence of each correction on the temperature dependence of the storage modulus. Since all initial parameters, with the exception of modulus and Poisson's ratio of the matrix, are assumed to remain constant with respect to temperature, only these

variables need to be integrated into the model based on temperature variations. As the frequency dependence of the materials is not a factor in this comparison, this analysis is confined to a frequency of 1 Hz. Thereby, the modulus of the matrix is extracted from the storage modulus curve of PA6 at 1 Hz, as illustrated in Figure 5.42. The temperature-dependent Poisson's ratio for PA6 is derived from the existing literature [89]. First, the behavior of a 0° specimen is examined. For this purpose, the curve of the storage modulus at 1 Hz from the experimental data and the curve of both adjusted models with the temperature-dependent matrix properties are shown in Figure 5.46 (a). The curve of the l_f adj. H-T is depicted by the red line, while the curve of the vol_f adj. H-T is represented by the orange line. It is important to note that the fitted methods refer to the quasi-static data of Section 5.2.
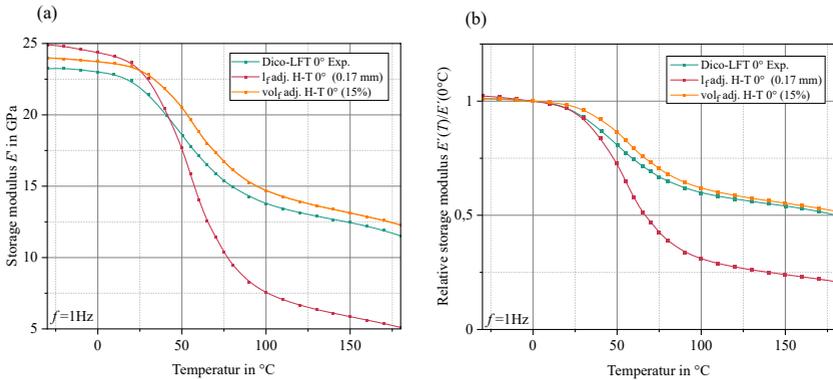
Figure 5.46: Comparison of the temperature-dependent storage modulus E' of the fiber volume and fiber length adjusted shear-lag modified Halpin-Tsai model with the experimental data for a Dico-LFT 0° sample (a) in absolute values and (b) in relative values.

As the mean value of the quasi-static results of the tensile modulus of elasticity is higher than the storage modulus, it is not surprising, that the curves of both, in the temperature range from -30 °C up to about 30 °C, are above the experimentally determined E' of the Dico-LFT. It is evident, that the volume-corrected H-T model is closer to the experimental curve and remains above it

permanently. Conversely, the length-reduced model shows a more pronounced decrease and intersects the experimental curve. To enable a better comparison of the individual curves, it is useful at this point to consider the relative curves normalized to the storage modulus at 0 °C shown in Figure 5.46 (b). This corroborates the impression derived from the absolute values. The curve of the vol$_f$ adj. H-T is an apt match for the experimental data and offers a reasonably accurate prediction of the temperature sensitivity of E'. In contrast, the l$_f$ adj. H-T significantly overestimates the decrease.

5.4.2.2 Analytical modeling approaches of Co

The following section presents an attempt to model the temperature-dependent behavior of the storage modulus from the Co phase by using the shear-lag modified Halpin-Tsai method. The case of a UD-Co-FRTP simplifies the model, as only a single laminate with a very large aspect ratio needs to be calculated, thus eliminating the necessity to utilize laminate theory. Given that the clamping length of the DMA was 60 mm (cf. Sec. 4), a fiber length of 60 mm was assumed. The fiber volume content of 48 vol.% was extracted from the datasheet. As with the modeling of the Dico-LFT, the temperature-dependent parameters of the matrix (E' and ν) are employed here.

Figure 5.47 illustrates the results of the modeling for Co, demonstrating the direction-dependent course of E' over the temperature range from -30 °C to 180 °C.

Firstly, it is evident that the directional dependence of Co is pronounced throughout the entire temperature range. Moreover, it is noteworthy that the temperature-dependent reduction reaches its minimum when aligned at 0°, progressively increasing with angular deviations from 0°, peaking at ±90°. The model tends to overestimate the absolute values of E' at 0° orientation by 23 % (108.8 GPa vs. 88.6 GPa) and at 90° orientation by 90 % (11.8 GPa vs. 6.2 GPa).
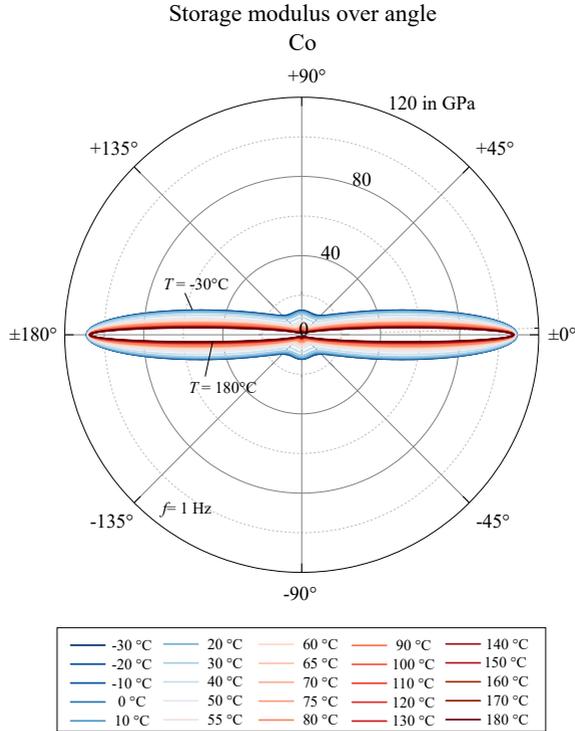
Figure 5.47: Results of modeling the temperature-dependent storage modulus E' of Co using the shear-lag modified Halpin-Tsai as a function of angle shown in the polar plot.

A comprehensive analysis and evaluation of the model will be conducted by examining the relative temperature drop for both 0° and 90° orientations, as illustrated in Figure 5.48. This clearly demonstrates the model's significant underestimation of the temperature drop at 0° orientation and its notable over-estimation at 90° orientation. Specifically, the model predicts a mere 1.3 % drop over the 100 K range at 0° orientation, in contrast to the experimental determination of 10.8 %. Conversely, in the 90° orientation, the model anticipates an 81 % drop, while the experiment measures a more moderate 67.7 %.
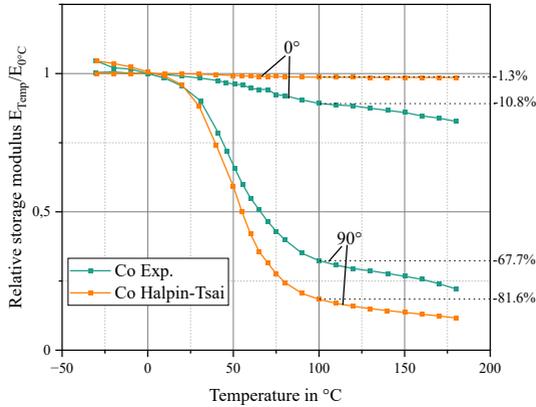
Figure 5.48: Comparison of the temperature-dependent relative storage modulus E' normalized to 0 °C of the sample in 0° orientation and in 90° orientation in comparison with the results of the shear-lag modified Halpin-Tsai for Co materials.

5.4.2.3 Analytical modeling approaches of CoDico-LFT

Following the identification of minor discrepancies in the modeling of Co and Dico-LFT, an attempt is made to replicate the temperature-dependent behavior of CoDico-LFT based on the experimental data obtained from both Co and Dico-LFT. Using the volumetric proportions determined in Section 5.1.7, the curve of E' of CoDico-LFT can be constructed from the experimental data of the Co and Dico phases using the RoM.

The curves modeled in this way for all investigated frequencies are shown in Figure 5.49 as absolute values compared to the experimental data of CoDico-LFT for both (a) the 0° and (b) the 90° orientation. Upon examination of the 0° orientation in Figure 5.49(a), it becomes evident that the absolute drop from 0 °C to 100 °C is sufficiently accurate. Additionally, the curve in the primary softening range displays a remarkable similarity. However, a significantly earlier onset of the main softening range is observed in the modeled curve. Given the predominantly linear decline of the Co phase, it can be reasonably assumed that this decline can be attributed to the Dico phase.

176
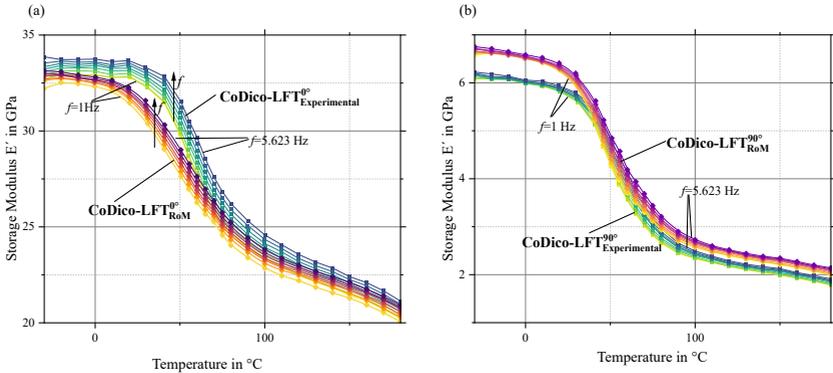
Figure 5.49: Comparison of storage modulus versus temperature using RoM based on experimental data of Co and Dico-LFT to predict CoDico-LFT and experimentally determined CoDico-LFT for (a) 0° specimens and (b) 90° specimens.

The earlier decline can therefore be attributed to the lower glass transition temperature of the Dico phase, which significantly influences a significant portion of the modeled curve. The observed decline in the experimental curves occurs at a later point in temperature, which can be used to infer that the Co phase shifts the softening processes in the Dico phase to higher temperatures. Although this effect is relatively minor, it can be regarded as a beneficial hybridization effect, as the hybrid is more efficient than the sum of the two individual components.

A comparison of the 90° orientation trajectory reveals that the experimental curve of CoDico-LFT is highly correlated with the modeled curve using the RoM, demonstrating remarkable accuracy. While the modeled curve exhibits slightly higher overall values, this outcome is not unexpected given the nature of absolute values. Notably, the main softening range is identical, with both the beginning and end of the softening occurring within the same temperature range. This further underlines the effectiveness of the ROM in providing a reliable approximation in the 90° orientation. Upon examination of the frequency dependence of CoDico-LFT in both directions, it becomes evident that there are clear differences. However, it is noteworthy that the RoM reflects this difference in both cases. Consequently, the frequency dependence appears to be direction-dependent and results from the sum of both components.

5.4.3 Temperature-induced transition mechanism of Co, Dico-LFT and CoDico-LFT in the dry state under bending load

The results of the DMA tests under three-point bending are presented below, using the same methodology as for the tensile tests. Since the Co was available in a maximum thickness of approximately 0.8 mm, the Co was not tested under this load case. Figure 5.50 shows the curves of E' for PA6 and 0° oriented specimens of Dico-LFT and CoDico-LFT in the dry state under bending load. The legend color-codes the different test frequencies, with squares representing the actual measured values connected by a B-spline. To facilitate relative comparisons, the values for E' at the test frequency of 1 Hz and temperatures of 0 °C and 100 °C are again marked on the right ordinate.

It is noteworthy that there does not appear to be any load case dependence of the glass transition temperature for PA6. This is only minimally shifted at 65 °C. However, this does not apply to Dico-LFT and CoDico-LFT, for which a load case dependency of T_g appears. The discrepancy between the T_g determined under tensile load and the T_g of Dico-LFT (76 °C) is somewhat surprising. The T_g of Dico-LFT is approximately 15 °C above the T_g determined under tensile load. In contrast, the T_g of CoDico-LFT (64 °C) is approximately 5 °C below the T_g determined under tensile load.

Looking at the absolute values of E' at 0 °C for unreinforced PA6 and Dico-LFT in the 0° orientation, it can be seen that they slightly exceed the values observed under tensile loading for both materials (PA6 = 3.6 GPa and Dico-LFT = 24.8 GPa). This also applies to the relative increase in E' of Dico-LFT to PA6 at 0 °C of +588.9 %, which is slightly higher in comparison with the results under tensile load. However, these values fall within a range where material scattering can be expected. An examination of the behavior of CoDico-LFT at 0 °C reveals a markedly augmented effect resulting from the additional Co layers, which exceeds the effect observed under tensile stress (+1166.6 % under bending vs. +882.4 % under tensile load).
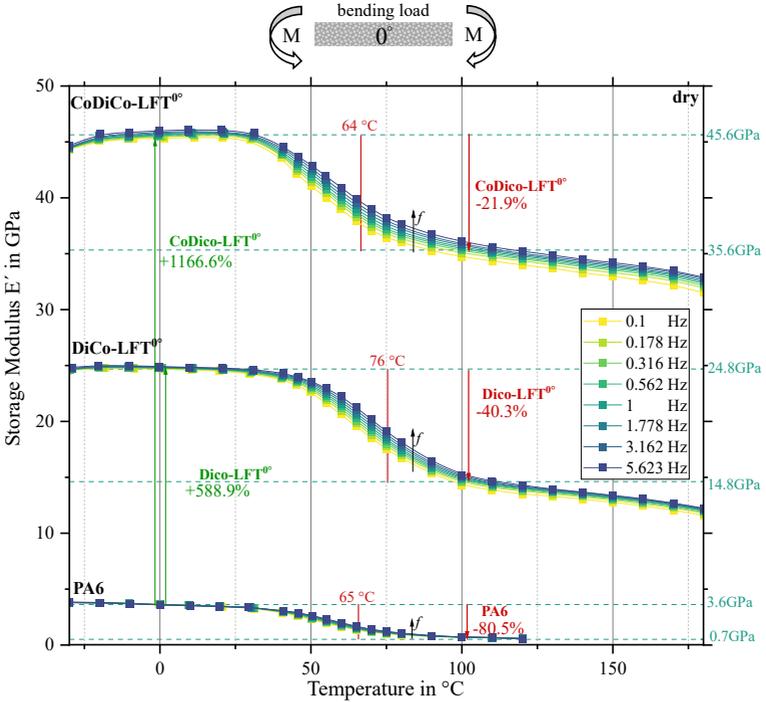
Figure 5.50: Results of the storage modulus E' from DMA measurements under bending load of PA6, Dico-LFT and CoDico-LFT in 0° direction in the dry state in the range from -30 °C to 180 °C, with the exact values at 0 °C and 100 °C for the test frequency 1 Hz at the right ordinate. The red arrows indicate the percentage drop in E' over the 100°C range fron 0 °C to 100 °C. The green arrows indicate the percentage increase in E' between the material classes at 0 °C. The vertical red lines describe the glass transition temperature (T_g) at 1 Hz defined by the peak of tan δ.

This observation is further corroborated by examining the relative reduction of both materials between 0°C and 100°C. PA6 experiences a loss of approximately 80.5%, whereas Dico-LFT shows a reduction of 40.3%, aligning with the relative decrease under tensile loading. For CoDico-LFT, the relative reduction in E' between 0°C and 100°C is significantly less pronounced than under tensile stress, with a decline of only 21.9%.

5.4.4 Influence of moisture in PA6 under tensile load

The Figure 5.51 shows a representative evolution of (a) tan δ and (b) $E´$ of PA6 in the dry state, in the moist state with 5 wt % absorbed water and the wet state with 8.2 wt % absorbed water as a function of temperature and frequency. These curves illustrate a typical effect of absorbed water on the mechanical properties of PA6. As described in the previous section, the frequency-dependent T_g can be determined from the peak of the tan δ curve. This is shown again for all three conditioning states in Figure 5.51 (a) at the limits at 0.1 Hz and at 5.623 Hz by the red dashed, with the clamped range marked with a bright red area for extra clarity. Moreover, the T_g at 1 Hz is presented as a discrete value. It is evident that the glass transition temperature T_g for PA6 with absorbed water exhibits a discernible shift towards lower temperatures. To illustrate, if T_g at 1 Hz is taken as a reference, T_g shifts by 66 °C for the moist state and by 80 °C for the completely saturated wet state.

Looking at the curve of tan δ after the local peak, it is noticeable that in the two humid states at higher temperatures around 100 °C there is a further small increase in tan δ, while the curve appears almost horizontal in the dry state. Upon closer examination of the corresponding curve of $E´$ in Figure 5.51 (b), it becomes evident that the main deviation range has also shifted with T_g, in line with the curve of tan δ. However, it is also noticeable that the progression of the individual stages is very different. The curves show clear differences in the values below the main softening range. To compensate for the horizontal shift, it is necessary to compare the values of the storage modulus at a test frequency of 1 Hz and a temperature of T_g -70 K. The values for this are given on the right axis of the diagram in Figure 5.51 (b) for dry at 0 °C, for the moist state at -70 °C and for the wet state at -80 °C. A comparison of the values reveals that the moist state exhibits a 50 % higher storage modulus than the dry PA6, as indicated by the green arrows. Similarly, the wet state displays a 70 % higher storage modulus than the dry PA6.
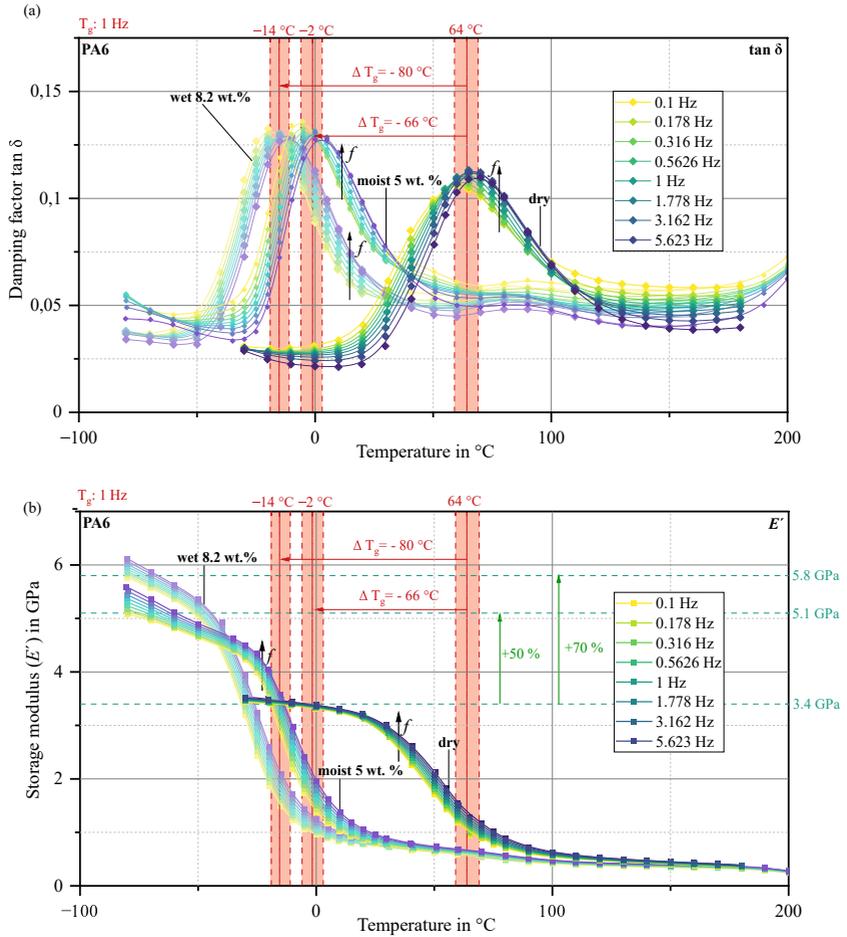
Figure 5.51: Representative evolution of (a) damping factor (tan δ) and (b) storage modulus (E') of PA6 n the dry state as well as in two conditioned states, i.e. the moist state with 5 wt% absorbed water and the wet state with 8.2 wt% absorbed water, as a function of temperature and frequency with definition of the frequency-dependent T_g as the maximum of tan δ represented by the red area additionally with red line the discrete value at 1 Hz. The red arrows show the shift of T_g and the green arrows show the percentage increase E' at T_g-60 K

Upon examination of the relative stiffening in relation to the amount of absorbed water, it becomes evident, that at 5 wt. % an increase of 10 % per wt. % of absorbed water is observed, while at saturation it is 8.5 % per wt. % of absorbed water. This suggests that there is no linear relationship between absorbed water and stiffening. For a more precise analysis of the correlation, the space between saturation and the dry state should be covered with further samples in the future.

5.4.5 Influence of moisture in Co, Dico-LFT and CoDico-LFT under tensile load

To investigate the effects of altered matrix behavior on the properties of composites and hybrid materials Figure 5.52 shows the curves of E' for unreinforced PA6 and 0° oriented specimens of Dico-LFT, CoDico-LFT and Co under tensile loading in the wet state. Given that the wet and dry states represent the two extreme values, situated at opposite ends of the spectrum, it is possible to assess the full impact of absorbed water on different materials by considering this particular conditioning states. The legend color-codes the different test frequencies, with squares representing the actual measured values connected by a B-spline. To facilitate relative comparisons, the values for E' at 1 Hz and temperatures of -70 °C and 30 °C are plotted on the right ordinate.

Upon examination of the T_g values for the three materials, it becomes evident that the T_g range is remarkably consistent. The lowest T_g value is observed in PA6, at -14 °C, while the T_g values for Dico-LFT and CoDico-LFT are slightly higher, at -10 °C and -9 °C, respectively. Once more, no local maximum of $\tan \delta$ could be identified for Co, thus precluding the determination of a specific value for T_g. Nevertheless, the area where the main softening effect can be localized is in the Co, is similar to the range observed in the other materials based on an analysis of the course of E'. The analysis of the materials allows the conclusion that the matrix dominance on T_g is confirmed, and that the influence of the fibers on the position of T_g can be classified as low, at least under the influence of water.
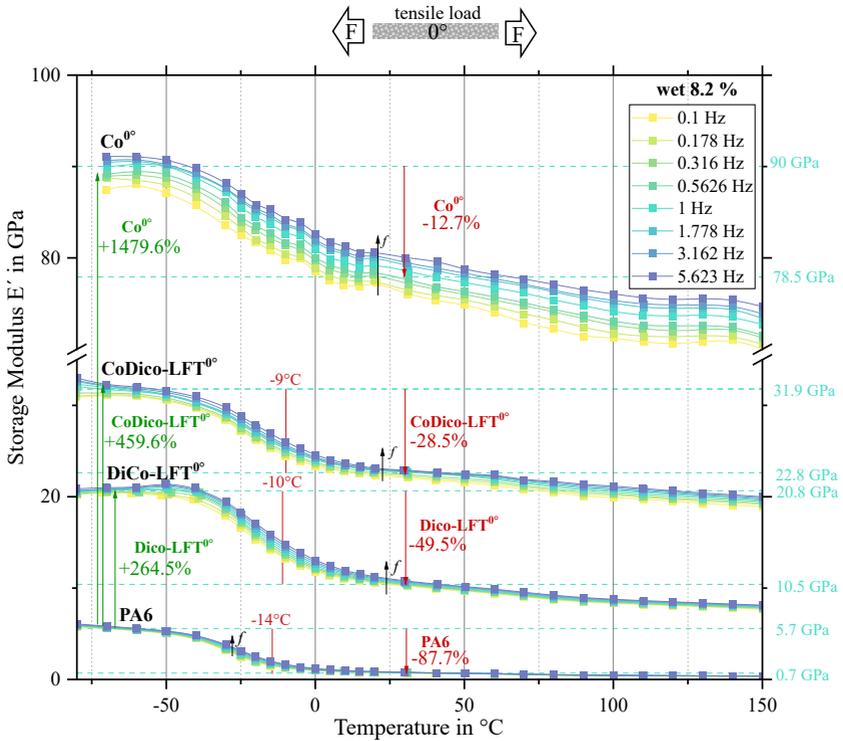
Figure 5.52: Results of the storage modulus E' from the tensile DMA measurements under tensile load of PA6, Dico-LFT, Co and CoDico-LFT in 0° direction in wet condition (8.2 wt. % Water in Matrix) in the range from -80 °C to 150 °C, with the exact values at -70 °C and 30 °C for the test frequency 1Hz at the right ordinate. The red arrows indicate the percentage drop in E' over the 100 °C range. The green arrows indicate the percentage increase in E' between the material classes at -70 °C. The vertical red lines describe the glass transition temperature (T_g) at 1 Hz defined by the peak of tan δ.

Upon examination of the relative stiffening effect of the fibers at -70 °C, it becomes evident that this is significantly diminished for all three materials in comparison to the stiffening effect observed in the dry state. This phenomenon can be observed for Dico-LFT at 264 %, CoDico-LFT at 459.6 % and Co at 1479.6 %. The relative stiffening effect of the fibers is therefore over 50 % lower than in the dry state for Dico-LFT and CoDico-LFT. When examining

the absolute values, it can be observed that these are very similar for all three materials in both the wet and dry states. Consequently, the stiffer matrix at low temperatures does not result in stiffer composite materials or hybrids.

Upon examination of the relative decline in E' between -70 °C and 30 °C, it becomes evident that this is more pronounced for all materials except CoDico-LFT than the comparable decline from 0 °C to 100 °C in the dry state. The underlying cause for PA6 is readily apparent. As the stiffening effect of water is only present at low temperatures, it is no longer present above T_g. This becomes evident when one compares the stiffness of PA6 in the dry state with 0.6 GPa at 100 °C and the wet state with 0.7 GPa at 30 °C, which exhibit similar values. Consequently, the relative drop is more pronounced in unreinforced PA6. A comparative analysis of the relative drop in Dico-LFT in the same temperature ranges between the to states reveals a significantly more pronounced drop of 49.5 % in the wet state compared to 40.4 % in the dry state.

5.4.6 Discussion

5.4.6.1 Temperature-induced transition mechanism under tensile load

Temperature-induced transition in PA6 in dry state   In the DMA tests of unreinforced PA6 in Figure 5.42, a pronounced softening of 82.4% was observed in the curve of E' over the temperature range from 0 °C to 100 °C. The most significant decline thereby occurred in the region of T_g. This significant softening within the primary softening range indicates a significant presence of amorphous regions, as the softening effect in the region of T_g predominantly affects these regions [81]. Furthermore this is a typical relative drop for dry PA6; Kehrer et al. also found a drop of approx. 80 % between 0 and 100 °C for a commercial PA6 [103].

Temperature-induced transition in Co, Dico-LFT, and CoDico-LFT under tensile load in a dry state in 0° The slightly reduced glass transition temperature observed in Figure 5.43 in the 0° Dico-LFT samples, compared to unreinforced PA6, contrasts with the expected increase in T_g. Typically, the restriction on polymer chain mobility imposed by the fibers would lead to an increase in T_g [218, 199]. However, the slight decrease in T_g is consistent with other observations in literature: For example, Karsli et al. found no discernible trend of T_g in short carbon fiber-reinforced PA6 in the range of 0-20 wt%. They were only able to detect fluctuations of about $3\,°C$ via DMA and DSC measurements [219]. This is consistent with the experiments by An et al. who also found no change in T_g for LFT made of PA6 and CF at fiber contents from 0 to 18 wt.%. [211] Liang et. al, on the other hand, observed a continuous decrease in T_g with the addition of CF in PA6, however, they could only observe a difference of $2\,°C$ from 0 to 20 wt.% CF, which casts doubt on the significance of this observation [220]. However, the fact that Liu et al. were also able to detect a continuous decrease in T_g of a similar magnitude for GF/PA6 LFT and Vishaei et al. the same fore CF/PP could again speak in favor of this [221, 222].

The observed disparity in Tg for CoDico-LFT, as depicted in Figure 5.43, reveals a difference of 6°C in comparison to PA6 and 9°C in comparison to Dico-LFT. The observed effect on T_g could be due to the increased FVC, fiber length or uniform orientation, which thus cause a restriction of chain mobility through the fibers, as explained by Chukov et al. [218]. This impression is further strengthened when considering the properties of the pure Co phase, where no discrete T_g could be detected. Similar observations were also made by Stokes Griffin et al.. They were able to show that UD-Co-tapes with a high degree of consolidation, i.e. high fiber content, does not exhibit T_g in the orientation of the fibers using DMA [223]. Thus in the CoDico-LFT, the softening of the Dico phase seems to be hindered by the properties of the Co phase, which leads to the increased T_g.

As illustrated in Figure 5.43, the incorporation of fiber into the Dico-LFT results in a notable stiffening effect (+576.6%), accompanied by a concurrent reduction in temperature sensitivity from 0 °C to 100 °C from 82.4% for unreinforced PA6 to 40.4%. These two observations show a good agreement with the results of An et al. [211]. In their study, the comparison of E' with a distance of 100K was only possible at higher temperatures from 30 °C to 130 °C. The curves for unreinforced PA6 show a drop of approx. 70 % and for CF-PA6 LFT with 18 wt. % fibers a drop of only 41 %. This means that the relative reduction in temperature sensitivity is slightly lower, but it is also an LFT with a lower fiber content. The lower fiber content is also responsible for the fact that the increase in E' from PA6 to Dico-LFT at 30 °C is only 364 % [211].

As illustrated in Figure 5.43, the CoDico-LFT exhibits a 982% increase in E' relative to unreinforced PA6 at 0°C, while concurrently, the decline between 0°C and 100°C is only 28.4%. Nikoforooz et al. conducted a similar investigation focusing on unidirectional composites utilizing PA. The study examined the thermal properties of unidirectional PA6/GF laminates across a temperature range of 23 °C to 100 °C. They observed a notable 14.4 % decrease in modulus across this span of 77 °C [224]. This underscores the positive impact of hybridization, enabling a wider range of material applications with improved modulus and reduced temperature sensitivity indicating a positive hybridization effect.

In all materials, there is an observable frequency-dependent trend in E'. Specifically, E' consistently exhibits higher values at elevated frequencies.This frequency dependency is due to the visco-elastic behavior of the polymer matrix, which also affects the mechanical behavior of the composite [221].

Temperature-induced transition in Co, Dico-LFT, and CoDico-LFT under tensile load in a dry state in 90°   As shown in Figure 5.44, the T_g of the 90° specimens of Co, Dico-LFT, and CoDico-LFT is significantly lower than that of both the unreinforced PA6 and the 0° specimens of each material.This is in agreement with the literature. Wolfrum et al. studied the effect of fiber orientation on T_g. Their results showed that FRPs with fibers oriented at 90° have a reduced T_g compared to those with fibers oriented at 0° [225]. Nevertheless, this does not explain why T_g is significantly lower than that of unreinforced PA6. One potential explanation for this phenomenon is the presence of additives in all composite materials, with a concentration of approximately 4 % added to all samples. In contrast, a significantly lower proportion of additives was incorporated into the unreinforced PA6 produced by injection molding. The higher additive content in the composites could, in turn, result in a reduction in T_g. This effect may only be observable at all 90° orientations, as the matrix properties are dominant in this orientation due to the fiber orientation. In the 0° samples on the other hand, this effect is probably compensated by the added fiber, which are mainly or completely oriented in the load direction. This can lead to the restriction of the chain movements described by Chukov et al., which in turn leads to a T_g in a similar range. [218]

Upon examination of the curves of E' in Figure 5.44 from Dico-LFT, CoDico-LFT, and Co, it becomes evident that the curves are in close proximity to one another and exhibit considerable overlap in numerous regions. This directly confirms the matrix dominant behavior, as the type of reinforcement does not affect the mechanical properties in 90° orientation. The higher fiber content of Co and CoDico-LFT does not seem to have too much influence either.

This is probably due to the fact that in Co all the fibers are oriented orthogonally to the load direction, whereas in Dico-LFT and CoDico-LFT a certain proportion of the fibers are also oriented in the load direction or at small angles to it. This means that even with a softening matrix, load can still be introduced into this fiber, which in turn has a stiffening effect even at higher temperatures. This has already been demonstrated with the 0° oriented specimens. For all

materials, the usual frequency dependence can be seen, i.e. higher E' can be determined at higher test frequencies over the entire temperature range. The biggest influence of frequency can again be seen in the main softening range around T_g.

5.4.6.2 Analytical modeling approaches of temperature-dependent storage modulus under tensile load

Analytical modeling approaches of Dico-LFT   As shown in Figure 5.46, the vol$_f$ adj. H-T curves agree well with the experimental data and provide a reasonably accurate prediction of the temperature sensitivity of E'. In contrast, the l_f adj. H-T significantly overestimates the decrease, which can be attributed primarily to the load introduction into the fiber based on the Cox shear-lag model. In the presence of a softening matrix, the critical fiber length exceeds the reduced fiber length at a certain point, preventing the full transfer of load into the fiber. This results in a more pronounced decline. In contrast, with the vol$_f$ adj. H-T variant, the load transfer into the fibers is still possible over the full range of the softer matrix. It can therefore be concluded that the elongated fibers are not only present in bundles, but that the determined fiber length is indeed accurate.

To accurately depict the absolute values of the storage modulus, it is possible to further reduce the fiber volume content. This adjustment yields a value of 14.5 vol.%, which precisely aligns with the E' value. The results for this are shown in Figure 5.53. The curves fit very well, but it appears that the curve from the model has been shifted slightly to the right. This discrepancy can be attributed to the difference in T_g. The model uses the values of unreinforced PA6, whose T_g is about 4 °C higher, to illustrate the temperature dependence. This indicates that the softening processes also occur 4 °C later, which explains the observed shift.
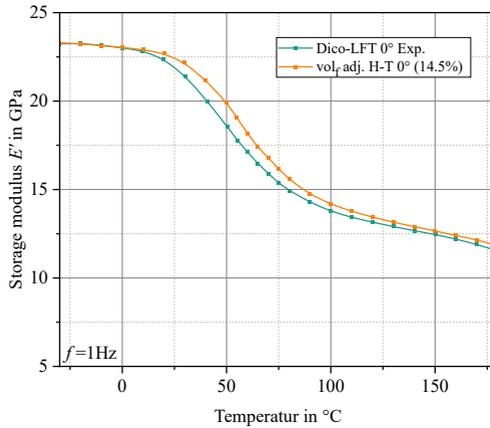
Figure 5.53: Comparison of the temperature-dependent storage modulus of the volume reduced shear-lag Halpin-Tsai model fitted with the experimental data for E' of a Dico-LFT 0° specimen at 0 °C in absolute values.

The favorable outcomes of the initial analysis have led to the utilization of the vol_f adj. H-T with a value of 14.5 % for further investigation. In order to consider the direction-dependent behavior, a curve of E' over the angle can now be generated for each temperature between -30 °C and 180 °C. The results are shown in a polar plot in Figure 5.54. As previously demonstrated, the temperature-dependent E' in the 0° orientation aligns closely with the experimental data. Having obtained the values of E' in 360°, it is now possible to utilize the experimentally determined curve of E' at 90° to assess the predictive capability of the E' in that orientation. For the purpose of illustration, Figure 5.55 depicts the experimental Dico-LFT 90° curve overlaid with the modeled values from Figure 5.54, with (a) the absolute and (b) the relative values. While the absolute values at 0 °C from both the model and the experiment exhibit excellent agreement, resulting no discernible difference between the relative and absolute curves, it is noteworthy that the model tends to overestimate the decline in the 90° orientation. Despite the experimental data in the Figure 5.55 indicating a 59 % reduction in E' between 0 °C and 100 °C, the model predicts a more substantial drop of 66.5 %.
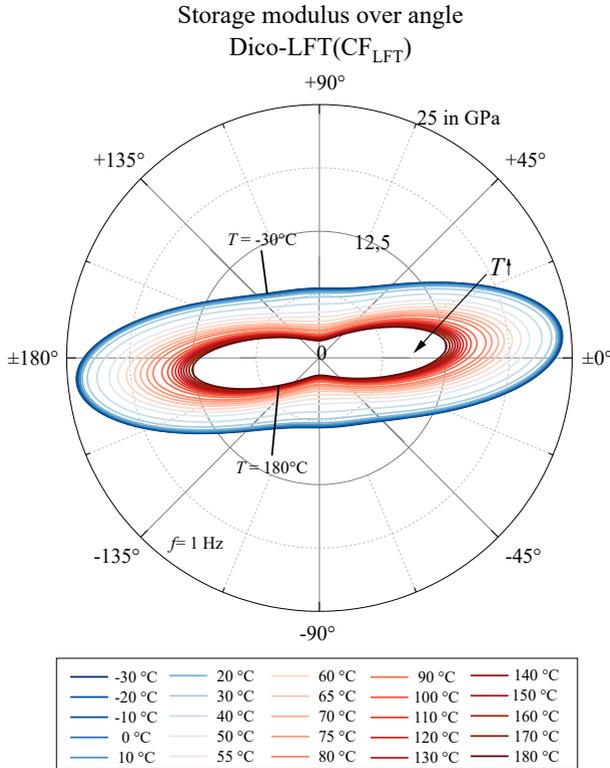
Figure 5.54: Results of modeling the temperature-dependent storage modulus E', using volume adjusted shear-lag modified Halpin-Tsai model, as a function of angle shown in the polar plot.

Analytical modeling approaches of Co   One potential explanation for the discrepancy between the modeled and experimentally determined curves of Co in 0° and 90° orientation, as illustrated in Figure 5.47, is the inadequate alignment of the fiber orientation with the intended 0° orientation. Small angular deviations as already mentioned in section 5.2.3.2, may occur during production, sample cutting, and alignment on the testing machine.
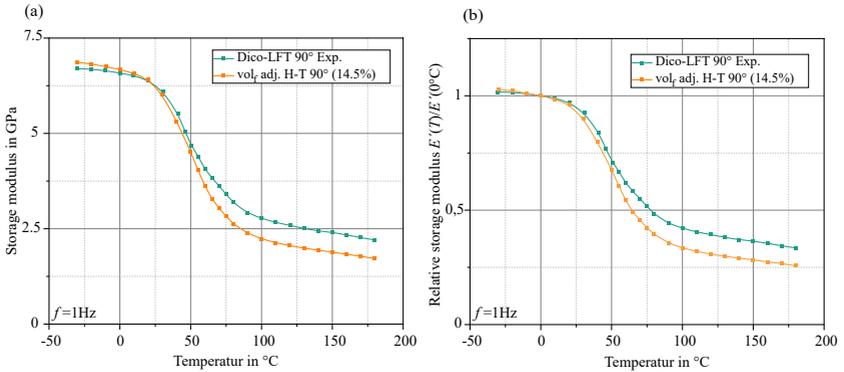
Figure 5.55: Comparison of the temperature dependent (a) absolute and (b) relative storage modulus, normalized to 0 °C, of the Dico-LFT sample in 90° orientation with the results of the shear-lag modified Halpin-Tsai from Figure 5.54 fitted to the 0° direction.

To further investigate this phenomenon, it is assumed that the tapes and fibers are perfectly aligned during manufacturing. This allows the examination of the influence of angular deviation during sample preparation or clamping in the testing machine on the curve of E'. This deviation could potentially yield results in the model that exhibit a similar relative drop between 0 °C and 100 °C, as observed in the experiment with a specimen oriented at 0°. The outcomes of this investigation are presented in Figure 5.56. The investigation revealed that the curves of a material with a deviation of 1.6° and 1.8° closely encapsulate the experimental curve for the Co. Notably, the experimental curve exhibits a distinctly earlier drop compared to all modeled curves. Beyond the temperature range of 65 °C, however, the experimental curve converges once again between the curves of 1.6° and 1.8°. Figure 5.54 demonstrates the considerable impact that even minor angular deviations can have on the temperature-dependent trajectory of E'. This phenomenon may provide a plausible explanation for the discrepancies observed between the experiment and the model in the 0° orientation. Conversely, at 90°, minor angular deviations do not exert a similarly significant influence.
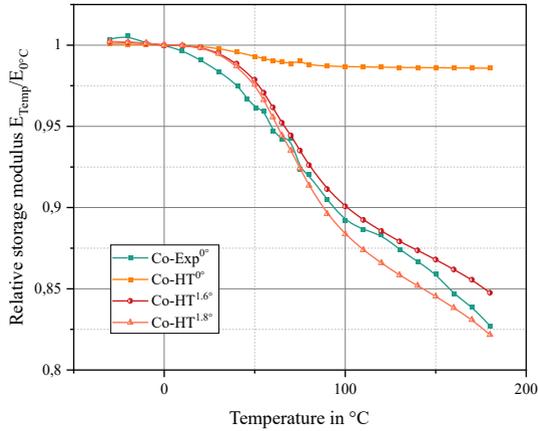
Figure 5.56: Temperature dependence of the relative storage modulus, normalized to 0 °C, for the Co sample at 0° compared to the results of the shear-lag modified Halpin-Tsai for Co materials at 0°, 1.6° and 1.8° to illustrate the influence of small angular deviations.

In particular, for the 90° orientation, the 81 % drop (compared to 82 % for unreinforced PA6) indicates that the model predicts a predominantly matrix-driven behavior. In the experimentally derived curve, however, there appearsto be an influence of the fibers leading to the observed lower drop in E'.

The assumption of an ideal alignment of tape and fiber, on which this study is based, has not yet been questioned. However, the results of the investigations in Section 5.1.6 indicate that local deviations in alignment occur during consolidation. Even at low temperatures, this leads to a reduced load application of the fiber, which in turn results in a lower modulus. In the range from 0° to 100°, the matrix modulus is significantly reduced, which could lead to larger strains in local deviation areas. This is another aspect that can be held responsible for the significantly stronger temperature dependence of E' compared to the experimental data. Since the influence of these areas cannot be quantified with the models used, no concrete statements are possible in this regard. To quantify the aforementioned influences, it would be possible to generate a series of different RVE's from the µCT data and subsequently employ FEM modeling with temperature-dependent matrix properties.

5.4.6.3 Temperature-induced transition mechanism of Co, Dico-LFT and CoDico-LFT in the dry state under bending load

As illustrated in Figure 5.50, T_g of Dico-LFT is approximately 15 °C higher than the T_g measured under tensile load. Conversely, the T_g of CoDico-LFT is about 5 °C lower than the T_g determined under tensile load. Given the distribution of stress across the cross-section from Figure 5.41, the opposite behavior would have been anticipated, since the Co layers for which no T_g could be determined are located at the points of highest stress in CoDico-LFT, and thus are disproportionately involved in the load transfer. One potential explanation for the elevated T_g in the Dico-LFT is the presence of bundles within the sample. When subjected to tension, these bundles result in local stress increases. Conversely, under bending, they exert minimal influence due to their proximity to the neutral position. In this scenario, the highest stresses are observed in areas where the fibers are more evenly distributed and impregnated, thereby exerting a stronger influence on T_g. According to this explanation, however, a higher T_g should also be determined in the CoDico-LFT than under tension. Consequently, it is questionable whether this is a suitable explanation. In a similar study, Wolfrum et al. found no influence on the mean Tg when comparing torsional and bending loads. However, both cases involved non-uniform load distributions [225].

As illustrated in Figure 5.50, the E' values at 0°C for unreinforced PA6 and Dico-LFT in the 0° orientation are slightly higher than those observed under tensile loading. As a result, the relative increase in E' of Dico-LFT over PA6 is slightly greater, although still within the expected range of material variation. This observation is further supported when considering the relative reduction of both materials between 0 °C and 100 °C. PA6 shows a loss of approximately 80.5 %, while Dico-LFT shows a loss of 40.3 %, which is consistent with the relative reduction under tensile loading. This consistency is well in line with the expected behavior of the materials, as neither shows any discernible variation with thickness. unreinforced PA6 is generally considered to be isotropic, and

the Dico-LFT material shows no thickness-related variance based on fiber orientation studies in the flow area. This, in turn, results in the stress distribution already depicted in Section 5.3 in Figure 5.41. Although microsections reveal the presence of bundles within volume of the Dico-LFT, this does not appear to have a noticeable effect on the thermo-mechanical behavior.

As shown in Figure 5.50, the CoDico-LFT in the 0° orientation at 0°C exhibits a significantly enhanced effect due to the additional Co layers, surpassing the effect observed under tensile loading. This finding is consistent with quasi-static results and can be attributed to the stress distribution during bending shown in Figure 5.41. The higher modulus of the edge layers results in a significantly higher load absorption by these layers than their volumetric fraction. This is in contrast to tensile stress, where only the volumetric fraction contributes to the absorption, making the reinforcing effect more pronounced in bending. Consequently, the relative reduction in E' between $0\,°C$ and $100\,°C$ is considerably less pronounced than under tensile stress, with a decline of only 21.9 %. This demonstrates the beneficial impact of hybridization on temperature sensitivity during bending, as the Co phase exerts a more pronounced effect in this regard.

5.4.6.4 Influence of moisture in PA6 under tensile load

As shown in Figure 5.51 on the basis of the different conditioning states, absorbed water in PA6 leads to a shift of T_g towards negative temperatures. This effect is known in the literature (cf. section 2.2.2.1) and describes the α softening of the amorphous phase. The dipolar water molecules diffuse to the dipolar amide groups and form hydrogen bonds with them. This results in a breakdown of the dipole-dipole bond between the chains and increases the distance between the macroscopic PA6 molecules in the amorphous phase [226]. Since the intermolecular forces responsible for chain cohesion in the amorphous region are distance dependent, they are reduced by the absorbed water [98]. This is similar to an increase in free volume, which in turn facilitates

the sliding motions of the macroscopic chains. As a result, the sliding of the chains, which defines T_g, takes place at lower temperatures. The loss factor curve in Figure 5.51 (a) is therefore shifted to lower temperatures. Looking at the relationship between the shift in T_g and the amount of water absorbed, it can be seen that there is no direct linear relationship. This observation is supported by Reimschüssel et al. who showed in the case of PA6 that the influence of the absorbed water is initially strong and gradually decreases until it reaches a saturation point and further absorption of water has no further influence on T_g [101]. In contrast, studies conducted by Avakian et al. indicate a linear correlation between absorbed water and the observed shift in T_g [227].

Upon closer examination of the curves of tan δ in Figure 5.51 , it becomes evident that the curves of the different conditioning states exhibit a high degree of similarity. This is evidenced by the nearly identical expression of the peak at T_g in relation to the value approximately 50 °C below T_g. Although, the curves of the two humid conditions seem to be slightly shifted upwards. This would imply that the loss factor and thus the relative damping component in the material increases slightly due to the absorbed water. It can also be seen that the width of the rise and fall in the humid samples is significantly narrower than in the dry PA6, which means that the transition mechanisms take place in a smaller temperature range. As shown in Figure 5.51 (a), at higher temperatures around 100°C, there is a noticeably small increase in the curve of tan δ for the two humid conditions, while the curve for the dry state remains almost horizontal. This is due to the fact that the DMA tests were performed in a temperature chamber without humidity control. This in turn means that the material starts to dry at higher temperatures and therefore a surface layer of dry material is already present when this temperature range is reached. This layer of dry material in turn softens in this temperature range and causes a further small increase in the tan δ curve. Therefore, no special attention should be paid to the results of the wet specimens at higher temperatures. At lower temperatures, however, the diffusion coefficient is so low that it can be assumed that hardly any drying has taken place and the determination of the T_g and thus the main softening range is valid.

As illustrated in Figure 5.51 (b), the E' curve shifts towards negative temperatures with T_g. However, it was identified that the course of the steps varies considerably, especially at values below the main deviation range. To compensate for this, a comparison of the storage modulus values at 1 Hz and T_g -70.K is useful. The determined values indicated a 50% higher storage modulus for the wet state and a 70% higher storage modulus for the wet state, in each case in comparison to dry PA6. These changes in the course of the storage modulus and tan δ are consistent with observations from the literature. Pramoda et al. were able to show both for wet PA6 the shift in T_g, i.e. the curve of tan d, and the stiffening effect at temperatures below the glass transition temperature [228]. While the shift of T_g is attributed to the plasticizing effect of the absorbed water, Pramoda et al. and Mano et al. attribute the stiffening effect at low temperatures to ice [229, 228].

A further analysis of the individual transition mechanisms depicted in Figure 2.12 reveals that below T_g and above T_β, movement is mainly possible in the side groups of the polymer chain. These side groups are groups that are located to the side of the main chain and are therefore located in exactly the same space as the absorbed water. As the free volume in the entire PA6 decreases at very low temperatures and there are now additional water molecules in this area, these restrict the movement of the side groups. This in turn leads to a significant increase in the storage modulus and can be referred as β stiffening. This aligns with the findings of Cartoff et al., who illustrated that absorbed water causes the β relaxation to shift toward lower temperatures, while the γ relaxation is minimally affected and shows only a slight shift toward lower temperatures [230]. In addition, their research highlighted that moisture increases the intensity of the β relaxation and decreases its activation energy, while also decreasing the peak height of the γ relaxation with negligible change in activation energy. This decrease in γ intensity, which Cartoff et al. termed an "antiplasticization" effect, is associated with increased modulus and decreased impact strength [230]. Park et al. describe a similar phenomenon in wet PA6 and observed that T_γ can no longer be differentiated since it appears to merge into the large and broad T_β transition, which is shifted to low temperatures by

the water. They attribute this to the fact that T_β is formed by intramolecular hydrogen bonding between water molecules or between water and amide groups in wet polyamides. The γ relaxation, is attributed to the inter- and intramolecular hydrogen bonds between amide groups [231].

5.4.6.5 Influence of moisture in Co, Dico-LFT and CoDico-LFT under tensile load

The lower T_g of PA6 in comparison to Dico-LFT and CoDico-LFT observed Figure 5.52 in may be attributed to the absence of additives, which enhances the influence of water. Nevertheless, the slightly elevated T_g observed in Co and Dico-LFT could also be attributed to the inhibitory effect of the fibers on chain mobility, as previously discussed in Section 5.4.1 . As illustrated in Figure 5.52, the decline in E' within the temperature range from -70 °C to 30 °C is more pronounced in the wet state than in the dry state from 0 °C to 100 °C for all materials except the CoDico-LFT.

This phenomenon is accompanied by a reduction in relative stiffness at T_g - 70 °C, which indicates that the load conduction into the fiber is reduced in the presence of water. One potential explanation for this phenomenon is the susceptibility of fiber sizing to water. The precise composition of the sizing is unknown, but it is known that the most common fiber sizings of CF and PA6 are particularly sensitive to moisture [232]. Tanaka et al. demonstrated in single fiber pull-out tests on CF and PA6 that interfacial shear strength is significantly reduced when water is absorbed. This appears to be reversible damage to the interface, as the interfacial shear strength regained its original strength when the samples were dried again [233].

According to the Equation 2.8, a reduction in interfacial shear strength leads to an increase in L_{crit}. It is therefore possible that when exposed to moisture, part of the fibers in the Dico-LFT no longer exceeds the L_{crit} and therefore are only partially involved in the load transfer. As a result, the higher modulus of the matrix at low temperatures does not lead to a higher modulus of the composite

materials. At temperatures above T_g, where the matrix modulus in the dry and wet states are highly comparable, a reduced modulus can be observed in the wet Dico-LFT.

This development cannot be used as an explanation for the greater drop in the Co of 12.7 %. However, it can be assumed that the strong angular dependence of the relative drop discussed in Section 5.4.2.2 is also a cause of the fluctuations in the test results. This phenomenon may also account for the nearly identical decline observed in the CoDico-LFT data for both wet and dry state.

6 Discussion

6.1 Structure and behavior of Dico-LFT materials at RT

Orientation deviations in LFT   Fiber orientation, as determined in Section 5.1, directly correlates with and is thereby confirmed by the material properties observed in the tensile test and the bending tests. No discernible differences were found in the orientation processes of the different fiber types or their combination during the flow phase. Any deviation in orientation from the expected flow direction can be attributed to inherent irregularities within the initial charge leading to an asymmetric mold filling, shown by the short shots in Figure 6.1. Filling of the mold begins at the young end of the initial charge (6.1 (c)) and gradually spreads over the entire height during the second stage (Fig. 6.1 (b)). This results in an inclined flow front that continues to propagate (Fig. 6.1 (e-f)) until the entire cavity is completely filled (Fig. 6.1(g)). The direction of propagation of the inclined flow front coincides with the final fiber orientation and is therefore considered to be its cause. By using different insertion positions, it was possible to prove that the cause lies in the initial charge. Two inhomogeneities that are present in the initial charge can be considered as triggers. The first explanation involves a temperature gradient, as depicted schematically in Figure 6.1, which results in a higher concentration of flowable material at the "young" end, thus accelerating flow initiation at this point. Another factor is a density gradient in the initial charge. This phenomenon is likely due to the presence of two swirls within the fibers at the points where the screws of the TSE were positioned as shown in Figure 5.5
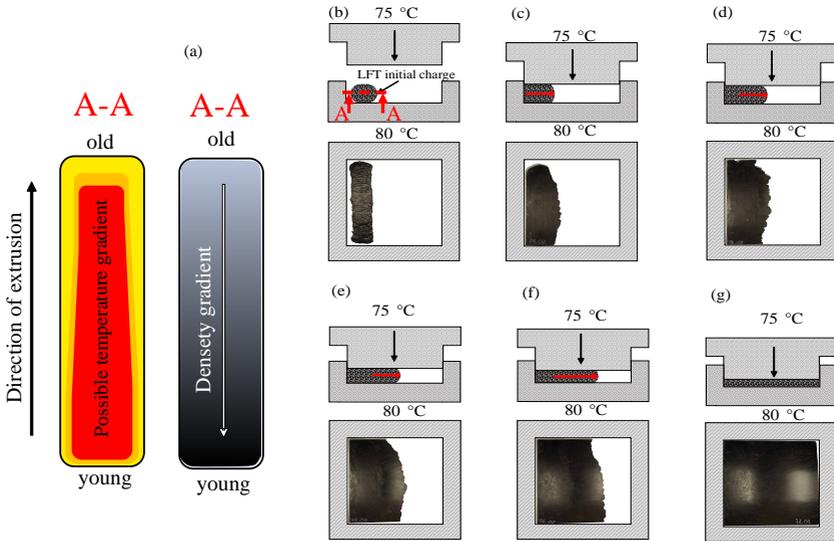
Figure 6.1: Mold filling study of the compression molding of CF$_{LFT}$ (a) a possible temperature distribution in the initial charge with young and old end (b) - (g) compression molding process with development of the flow front and mold filling according to Scheuring et al. [127].

(a). As the initial charge leaves the nozzle, the fibers attempt to relax from this position, resulting in an inflation of the initial charge. However, this process takes a certain amount of time, and thus, the effect is more pronounced at the old end than at the young end. Consequently, the mass is distributed in a manner that results in a greater concentration at the young end of the initial charge. This implies that the center of the volume is not coincident with the center of the mass. As a result, there is more material at the young end, which is forced to flow earlier. Both inhomogeneities are shown schematically in Figure 6.1 (a). At this point, integrating this influence into process simulation models would be beneficial, enabling the prediction of flow paths and associated fiber orientations even for complex geometries.

Effect of the bundles in the CF$_{\mathrm{LFT}}$ and CF+GF$_{\mathrm{LFT}}$ As expected, the use of CF in the LFT-D process shows significantly greater stiffening and strengthening compared to GF. The design leeway between the two material systems can also be exploited by hybridizing both fibre types. Of particular interest is the positive hybridization effect in relation to elongation at break. Since crack inhibition by the GF can be of great advantage, especially with fatigue loads. However, the tendency of CF to agglomerate in bundles means that the fiber properties are not fully exploited. This applies both to modulus, where the fibers are not involved in load transfer, and to strength, where bundles generate local stress peaks that lead to critical failure. Unimpregnated bundles are also disadvantageous for other types of stress, such as fatigue, as the dry part acts like a crack in the volume, from which the critical crack begins to grow, as Rhode-Tibitanzl was able to show [7]. Bondy was also able to show that bundles were observed in almost all fracture surfaces of CF-PA66-LFT-D materials subjected to fatigue loading [150].

In order to exploit the full potential, process adjustments should therefore be made to avoid bundles. A simple step that does not require any changes to the raw materials would be to change the screw design in the impregnating extruder and add further mixing elements. The same effect can also be achieved by using a longer screw, i.e. by extending the length of the impregnating extruder. This extends the dwell time of the material in the extruder and therefore the mixing time [234]. Although better mixing leads to a more pronounced fiber shortening, it often also results in higher mechanical properties [144, 235]. However, since a large fraction of the fibers are above l_{crit} at RT, the fibers are likely to exceed l_{crit} by a large fraction even at higher shear forces. Ranganathan et al. have already shown that shorter fibers with better impregnation result in better mechanical performance for viscous fiber-reinforced polypropylene [151]. Another way to improve mixing is to increase the screw speed. Rohan et al. were able to show that this also leads to an improvement in the mechanical properties despite increased fiber shortening [236]. Incorporating lower Tex rovings could provide additional benefits as the bundled fibers provide mutual protection against degradation and mixing [7]. The use of lower Tex

fiber rovings would result in smaller initial bundles after initial roving breakup, potentially minimizing these effects and improving impregnation capabilities. All in all, the dispersion of fibers remains an area of research that is not well understood and therefore requires further investigation [25].

6.2 Structure and behavior of CoDico-LFT at RT

Reason for the inadequate interface between Co and Dico-LFT in the charge area of CoDico-LFT The considerably worse mechanical properties, particularly tensile strength, in the charge area underscores the presence of a poor interface. This can be attributed to the low temperatures of both components leading to the poor interface. Interestingly, the interface is of sufficient quality in the flow area where the Co layer experiences prolonged cooling. This suggests that the temperature within the initial charge (approximately 280 °C) is sufficient to form a robust interface with an already cooled Co phase during overflow. Or in other words: A satisfactory interface can be achieved even with a cooler Co phase. This is important for overflow scenarios involving Co phases in Parts with complex geometries, where dimensional stability of the Co phase should be ensured during overmouding to avoid warping. Lower temperatures of the Co phase can provide this stability.

Another aspect to consider, as mentioned earlier, is the significant influence of pressure on interface formation. The initial path regulation of the press when closing results in a relatively low force being exerted on the initial charge at the start of the moulding process. This gradually increases until mold filling is complete, at which point it reaches its peak and the press switches to a force-controlled holding phase. In the flow area, the time between the hot material flowing out and the maximum pressure being reached is minimal. This ensures that both critical criteria for a robust interface are satisfactorily met. In contrast, in the charge area where partially cooled surfaces are stacked, there is a much

longer delay before maximum pressure is reached. As a result, neither criterion is adequately met in these areas.

Additionally, it's worth considering the possibility of PA6 degradation within the surface layer of the initial charge due to exposure to air, especially oxygen at elevated temperatures. Dong et al. demonstrated that thermo-oxidative degradation can occur at temperatures in the range of 120 °C - 170 °C [237]. An in-depth study of the termo-oxidative degradation in PA6 is given in [238]. This temperature is significantly exceeded by the initial charge exiting the extruder, a condition that is maintained within the heating tunnel. With an approximate duration of 1 min to complete an initial charge, there is ample time for degradation to occur. Since the degraded material is solely responsible for the interface formation in the insertion area, this degradation could further exacerbate the poor interface quality.

Process adaptation to improve the interface between Co and Dico-LFT in the charge area of CoDico-LFT   To optimize the process and achieve a robust interface, the easiest parameter to adjust would be the temperature, which is currently considered insufficient. The use of transport heaters for the initial charge and/or infrared heaters to heat the Co layer in the mold could solve this problem. A further potential solution is to heat both the Co and Dico layers on the surface using a tailored microwave antenna. The microwave antenna can be adjusted so that only the desired area is heated without contact. Given the efficient absorption of microwaves by CF and subsequent conversion to heat, rapid surface heating becomes feasible. This has already been extensively studied for the curing of thermoset CF composites with the aim of optimizing curing conditions [239, 240, 241, 242]. Lee et al. were able to show that microwave heating is particularly suitable for thin, unidirectional CFRP composites [239]. Li et al. have developed an indirect microwave heating medium for multidirectional laminates that exhibits very good heat generation. It consists of carbon with a fiber content of 50 vol.% and a fiber length of 5 mm and is very similar to a CF based Dico-FRP [243].

203

Microwaves therefore appear to be suitable a heating mechanism for both classes of material. Although this limitation may present obstacles for the aforementioned application, it offers a promising opportunity for addressing the specific issue of the poor interface in the charge area. Since only the surfaces of both parts need to be hot enough to form a good interface. This therefore provides an energy-efficient option. In addition, automated positioning by a robot would ensure worker safety during this process.

6.3   The influence of temperature and humidity on the mechanical properties of Co, Dico-LFT and CoDico-LFT

The directional dependence was also confirmed for the course of the temperature-dependent storage modulus. The transition mechanisms that are dominated by the matrix also affect the behavior of the composite materials and the hybrid system in the same temperature range. While the behavior of all three fiber-reinforced materials is very similar in the 90° orientation and is dominated by the matrix, considerable differences were found in the 0° orientation. The investigation has demonstrated that the temperature dependency can be significantly reduced by the fibers. The degree of alignment of the fibers in the load direction, the fiber volume content, and the fiber length are of paramount importance in this regard. High values of the respective category lead to a reduced temperature sensitivity of the storage modulus.

Furthermore, a comparison of the adjusted H-T models from Section 5.2.1.2 with the experimental data revealed the existence of two fundamental mechanisms. The volume-corrected model demonstrated the most satisfactory agreement with regard to the experimental data, while the fiber length-corrected

model predicts a more significantly reduction. In addition to the reduced modulus of the matrix, this can be attributed to the reduced interfacial shear strength τ_y between the matrix and fiber. Tannaka et al. demonstrated using single-fiber pull-out tests that τ_y decreases drastically under the influence of temperature. They were able to show that τ_y for PA6 and CF is approximately 44 MPa at 25 °C and 24 MPa at 80 °C. This corresponds to a reduction of 45 % over 55 K [244]. With Equation (2.8) for calculating L_{crit} it becomes clear, that this is almost nearly doubled as a result of the significant decline of τ_y. The fiber length of the l_f adj. H-T model only exceeds L_{crit} at room temperature, thus matching the values determined experimentally. However, at higher temperatures, the reduced length falls below L_{crit}, preventing complete load transfer into the fiber. This results in a more pronounced decrease in modulus than that observed experimentally. In contrast, L_{crit} is exceeded over the entire temperature range in the vol_f adj. H-T model. Given the relatively minor discrepancies between this model and the experiment, it can be reasonably inferred that the vol_f adj. H-T model more accurately reflects the material's characteristics. This is of particular interest as it allows to deduce what effect the bundling has on the behavior of the material.

These findings permit the derivation of some basic design recommendations for LFTs. In Section 6.1, it was recommended that better impregnation might be achieved by increasing the number of mixing elements, although this would result in a reduction in fiber length. This is of particular importance for LFTs at room temperature, as their fiber length is significantly longer than L_{crit}. For the use of LFT materials at higher temperatures, however, this proposal must be extended to include the temperature-dependent $L_{\mathrm{crit}}(T)$. Since it should be ensured that L_{crit} is exceeded at all times at the respective application temperature, significantly longer fibers are required here. This drastically reduces the scope for better dispersion at the expense of fiber length. Therefore, for use at elevated temperatures, more effective dispersion could be achieved by reducing the volume of the fibers and thus the fiber-fiber interaction in the second TSE. This should lead to the formation of longer but well-impregnated fibers. Since the temperature-dependent transition mechanisms in PA6 shift towards negative

values due to absorbed water, the temperature and absorbed water dependence $L_{\text{crit}}(T, w_{\text{water}})$ must be taken into account for use in real conditions in which water is absorbed.

Overall, the modeling of the Dico-LFT material with the vol$_\text{f}$ adj. H-T model has proven to be well suited, offering several advantages. For instance, a precise analysis of the matrix behavior and a detailed microstructure analysis can be used to map the temperature-dependent behavior, which is particularly helpful for the design of LFT components. Furthermore, the potential of hybridization has been sufficiently demonstrated. For instance, the CoDico-LFT exhibits a response to tensile load in accordance with the RoM, which, by definition, is not a positive hybridization effect. Nevertheless, the potential for local reinforcement at specific points can significantly reduce temperature sensitivity. As the hybrid under investigation is the simplest possible structure with only unidirectional Co-reinforcement, it can be expected that further positive effects will be observed with the use of multidirectional Co-reinforcements such as cross-ply or quasi-isotropic laminates. For example, flow direction-dependent properties in the LFT could be compensated for at certain points where isotropic behavior is required, e.g. for load application points. Given that the pure tensile load is a relatively abstract concept and serves as a useful simplification for the purpose of elucidating general mechanics, it would be beneficial to consider additional cases for a more comprehensive evaluation of the potential of CoDico-LFT. As with the quasi-static results, the hybridization effect at elevated temperatures is significantly more pronounced under flexural loading. Since flexural loading is significantly closer to the operational loads of structural applications this further substantiates the potential of such CoDico-LFT materials based on thermoplastic matrix materials.

The effects of water absorption on the transition mechanisms of PA6, which were clearly recognizable in the experimental investigations, are consistent with the effects described in the literature. Both the reinforcing effect of the fibers and the reduction in relative temperature sensitivity are lower in the wet state of the Dico-LFT than in the dry state. In contrast, CoDico-LFT demonstrated a similar reduction in sensitivity when compared to the dry state. This observation

206

suggests that three distinct advantages of hybridization in CoDico-LFT can be identified. For instance, local co-strengthening can simultaneously enhance the modulus and reduce the temperature and moisture sensitivity at the local level. In light of the fact that elevated temperatures and contact with water can rarely be ruled out in real-life operating conditions, it can be argued that the hybridization to CoDico-LFT enables the use of LFT materials in a wider range of real-life applications.

7 Conclusions and recommendations

The influence of different compositions of fibers on the directional effective mechanical properties of LFD-D-ILC compression molded plates was investigated under quasi-static loads. Based on microstructural investigations, it was possible to report on coincidences and deviations from an established modeling approach. The hybridization of LFT with Co plates was successfully demonstrated, and critical aspects to ensure a good interface were derived. The influence of different operating conditions on the different material types could be understood by means of DMA experiments. The findings of this research contribute to a more profound comprehension of CoDico-FRP based on a thermoplastic matrix material and illustrate the prospective benefits of such hybrid composites. This chapter presents the most important conclusions and recommendations derived from the findings presented in this thesis.

7.1 Conclusions

LFT-D-ILC with mixed fibers

- The impregnation behavior of GF and CF differs significantly in the LFT-D-ILC process. While the GF can be separated more effectively due to its lower fiber count therefore be impregnated well, some CF remain in bundles, some of which in their inner even unimpregnated. No interaction was observed when both fibers were used simultaneously.

- The simultaneous use of GF and CF in the LFT-D-ILC process opens up the design space between the materials in which only one type of fiber is used. This makes it possible to achieve specific mechanical properties, such as cost-specific stiffness, which cannot be achieved by materials with only one fiber type. In addition, a positive hybridization effect with regard to elongation at break has been demonstrated, allowing better use to be made of cost-intensive CF.

- The prediction of the stiffness of mixed fiber materials could be demonstrated using the established shear-lag modified Halpin-Tsai method. The fiber orientation evaluation using µCT proved to be suitable for this purpose. Particularly accurate results were obtained for materials with well-impregnated fibers, while large discrepancies between model and experimental values were observed for CF_{LFT}. The observed discrepancies could be attributed to fiber bundles, wherein only a subset of the fibers were engaged in the load-bearing. However, an adjustment of the model parameters to the experimental data could lead to an improvement in the prediction.

- The experimental values and modeling results of all three LFT materials demonstrate significant orientation dependent mechanical properties. This is a consequence of the fiber orientation induced by the flow, which, deviates slightly from the anticipated orientation due to inhomogeneities in the density or temperature distribution in the initial charge resulting in an inclined flow front during compression molding.

- The bundles within the CF_{LFT} were identified as the initiation for the critical failure. These act like macroscopic inclusions around which excessive stresses and strains occur. The propagation of the crack from the initial point follows a well-known failure mechanism for Dico-FRPs.

- In the tensile test, minimal differences in effective mechanical properties were observed between the charge and flow area. However, when subjected to bending loading, significant differences were observed due to the shell structures in the charge area located at the edge of the specimen, at the point of highest stress.

CoDico-LFT

- The charge and flow areas exhibit distinct differences in the quality of the interface between Co and Dico-LFT, which can be attributed to insufficient temperature and pressure in the charge area during manufacturing.

- The directional dependence of the effective mechanical properties is further reinforced by the hybridization in the direction of the Co orientation. When subjected to tensile loading, the strength of CoDico-LFT can be well approximated with RoM, whereas the stiffness is underestimated with RoM. However, this may also be due to the strain measurement on the surface of the Co phase, which may underestimate it.

- Under tensile loading bundles in the Dico phase cause localized excessive strain, which are transferred to the Co phase and initiate there the critical failure of the CoDico-LFT.

- In the context of flexural loads, the Co phase exhibits a disproportionate increase in effective mechanical properties due to its position at the edge of the CoDico-LFT. A significantly elevated degree of strengthening and stiffening can be observed, which also extends over a larger angle range under the condition of a satisfactory interface.

- The inhomogeneous stress distribution under flexural load causes the initiation of critical failure in the Co phase. Buckling was observed on the compression side, while fracture was observed on the tension side.

The bundles within the Dico phase are in the area of lowest load and, therefore, are not critical for the development of damage under flexural load.

The influence of temperature and humidity on the mechanical properties of Dico-LFT and CoDico-LFT

- The incorporation of fiber reinforcement serves to mitigate the effects of the primary softening range of PA6 on the modulus, contingent upon fiber length, fiber content, and alignment of the fibers within the load direction. The position of the main softening or the glass transition area is only slightly influenced by the reinforcing fibers.

- Volume-adapted analytical models are suitable for predicting the temperature-dependent course of the modulus from LFTs, provided that the known course of the matrix material is available. This methodology permitted the estimation of the anisotropic stiffness over a broad temperature range.

- The experimental determination of the modulus of the Co is challenging due to the strong directional dependence, whereby minor angular deviations have a significant impact on the outcomes. Nevertheless, a remarkably low temperature sensitivity was observed.

- At 0° orientation, the tensile modulus of Co, Dico-LFT and CoDico-LFT are clearly different, while at 90° orientation, a more matrix-dominated curve is shown for all materials, which is very similar. The tensile modulus versus temperature curve of CoDico-LFT can be accurately predicted using RoM. Suitable curves can be generated for both the 0 and 90° orientations.

- The absorption of water in polyamide 6 results in a β stiffening and an α softening. Conversely, in Co, Dico-LFT, and CoDico-LFT, an α softening occurs, whereas β stiffening shows no discernible effect.

7.2 Recommendations

- In order to fully exploit the properties of CF in the LFT-D-ILC process and of the Co reinforcement in CoDico-LFT, adaptations should be introduced that lead to better dispersion and impregnation of the fibers in the Dico-LFT, thus avoiding bundles. A combination of mixing elements, lower fiber content and the use of rovings with a lower tex number is the recommended approach here. However, it should be noted that the L_{crit} should not be undercut. A comparison between the measurement of fiber length and the calculated critical fiber length as a function of operating temperature $L_{\mathrm{crit}}(T)$ can provide parameters for optimizing the process setting.

- To predict the stiffness of bundled LFT materials, it is necessary to use representative volume elements in which the bundles and the effects of fiber curvature can be accounted for. Established analytical homogenization methods offer sufficiently good results for well-dispersed LFT materials and can also be used for bundled materials by adapting the parameters.

- To ensure a satisfactory interface in the charging area as well, it is recommended that heating concepts be employed as a means of process adaptation, with the objective of ensuring a sufficient temperature at the points involved in the interface formation in the charge area. The use of microwave antennas seems particularly suitable for robot-supported processes. For manual processes, infrared emitters are recommended.

- The utilization of CoDico-LFT structures is particularly well-suited to the incorporation of composite materials based on hygroscopic thermoplastics. The simultaneous reduction of both temperature and moisture sensitivity ensures that such structures can be employed in a diverse array of applications.

Bibliography

[1] European Court of Auditors. Reducing carbon dioxide emissions from passenger cars. *Puplication Office of the European Union*: Visited on 2024-06-17. [Online] Available: https://www.eca.europa.eu/ECAPublications/SR-2024-01/SR-2024-01_EN.pdf.

[2] F. Del Pero, M. Delogu, and M. Pierini. The effect of lightweighting in automotive lca perspective: Estimation of mass-induced fuel consumption reduction for gasoline turbocharged vehicles. *Journal of Cleaner Production*, 154:566–577, 2017.

[3] A. T. Mayyas, A .R. Mayyas, and M. Omar. Sustainable lightweight vehicle design: a case study in eco-material selection for body-in-white. In *Lightweight composite structures in transport*. 267–302, 2016.

[4] K. K. Chawla. *Composite Materials*. Springer Nature Switzerland AG, Cham, Switzerland, 4th edition, 2019.

[5] T. Böhlke, F. Henning, A. N. Hrymak, L. Kärger, K. A. Weidenmann, and J. T. Wood. *Continuous-discontinuous fiber-reinforced polymers: An integrated engineering approach*. Carl Hanser Verlag, Munich, Germany, 1st edition, 2019.

[6] S. J. Joo, M. H. Yu, W. Seock Kim, J. W. Lee, and H. S. Kim. Design and manufacture of automotive composite front bumper assemble component considering interfacial bond characteristics between over-molded chopped glass fiber polypropylene and continuous glass fiber polypropylene composite. *Composite Structures*, 236:111849, 2020.

[7] M. Rohde-Tibitanzl. *Direct processing of long fiber reinforced thermoplastic composites and their mechanical behavior under static and dynamic load*. Hanser eLibrary. Carl Hanser Verlag, Munich, Germany, 2016.

[8] E. Bürkle, M. Sieverding, and J. Mitzler. Spritzgießverarbeitung von langglasfaserverstärktem PP. *Kunststoffe*, 93(3):47–50, 2003.

[9] T. Ishikawa, K. Amaoka, Y. Masubuchi, T. Yamamoto, A. Yamanaka, M. Arai, and J. Takahashi. Overview of automotive structural composites technology developments in Japan. *Composites Science and Technology*, 155:221–246, 2018.

[10] Y. Wan and J. Takahashi. Development of carbon fiber-reinforced thermoplastics for mass-produced automotive applications in Japan. *Journal of Composites Science*, 5(3):86, 2021.

[11] M. D. Wakeman, E. Eble, P. Beyeler, T. Herrmann, and J-A. E. Månson. Hybrid thermoplastic composite beam structures integrating UD tow, stamped fabric, and over-injection/compression moulding. In *Proceedings of ECCM-11*. Rhodes, Greece, 2004.

[12] N. Meyer. *Mesoscale simulation of the mold filling process of Sheet Molding Compound*. PhD thesis, Karlruhe Institute of Technology, Karlsruhe, Germany, 2022.

[13] M. F. Ashby. *Materials selection in mechanical design*. Butterworth-Heinemann, Burlington MA, United States of America, 4th edition, 2011.

[14] D. Nestler. *Beitrag zum Thema Verbundwerkstoffe - Werkstoffverbunde: Status quo und Forschungsansätze*. Habilitation thesis, Technische Universität Chemnitz, Chemnitz, Germany, 2012.

[15] T. W. Clyne and D. Hull. *An Introduction to Composite Materials*. Cambridge University Press, Cambridge, England, 2019.

[16] P. Eyerer, H. Schüle, and P. Elsner. *Polymer Engineering 3*. Springer Vieweg, Berlin, Germany, 2020.

[17] Alfred Puck. *Festigkeitsanalyse von Faser-Matrix-Laminaten: Modelle für die Praxis*. Carl Hanser Verlag, Munich, Germany, 1996.

[18] G. W. Ehrenstein. *Faserverbund-Kunststoffe*. Carl Hanser Verlag, Munich, Germany, 2006.

[19] F. Henning and E. Moeller. *Handbuch Leichtbau: Methoden, Werkstoffe, Fertigung*. Carls Hanser Verlag, Munich, Germany, 2011.

[20] M. Bonnet. *Kunststoffe in der Ingenieuranwendung: Verstehen und zuverlässig auswählen*. Vieweg + Teubner Verlag, Wiesbaden, Germany, 1st edition, 2009.

[21] S. Mouton, D. Teissandier, P. Sébastian, and J. P. Nadeau. Manufacturing requirements in design: The rtm process in aeronautics. *Composites Part A: Applied Science and Manufacturing*, 41(1):125–130, 2010.

[22] E. J. Barbero. *Introduction to composite materials design*. CRC Press, Boca Raton, United States of America, 3rd edition, 2018.

[23] T. Kloska and X. Fang. Lightweight chassis components—the development of a hybrid automotive control arm from design to manufacture. *International Journal of Automotive Technology*, 22:1245–1255, 2021.

[24] S. Revfi, M. Mikus, K. Behdinan, and A. Albers. On the bead design in LFT structures: the influence of manufacturing-induced residual stresses. *Design Science*, 7:1–22, 2021.

[25] U. Gandhi, T. A. Osswald, S. Goris, and Y. Y. Song. *Discontinuous fiber-reinforced composites: Fundamentals and applications*. Hanser Publications, Cincinnati, United States of America, 1st edition, 2020.

[26] J. N. Reddy. *Mechanics of laminated composite plates and shells: Theory and analysis*. CRC Press, Boca Raton, United States of America, 2nd edition, 2003.

[27] K. L. Goh. *Discontinuous-Fibre Reinforced Composites*. Springer London, London, England, 2017.

[28] J. Rösler, H. Harders, and M. Bäker. *Mechanisches Verhalten der Werkstoffe*. Springer Fachmedien Wiesbaden, Wiesbaden, Germany, 2016.

[29] W. Voigt. Über die Beziehung zwischen den beiden Elasticitätsconstanten isotroper Körper. *Annalen der Physik*, 274(12):573–587, 1889.

[30] A. Reuss. Berechnung der Fließgrenze von Mischkristallen auf Grund der Plastizitätsbedingung für Einkristalle. *ZAMM - Zeitschrift für Angewandte Mathematik und Mechanik*, 9(1):49–58, 1929.

[31] H. L. Cox. The elasticity and strength of paper and other fibrous materials. *British journal of applied physics*, 3(3):72, 1952.

[32] J. A. Nairn. On the use of shear-lag methods for analysis of stress transfer in unidirectional composites. *Mechanics of Materials*, 26(2):63–80, 1997.

[33] C. M. Landis and R. M. McMeeking. A shear-lag model for a broken fiber embedded in a composite with a ductile matrix. *Composites Science and Technology*, 59(3):447–457, 1999.

[34] A. Kelly and W. R. Tyson. Tensile properties of fibre-reinforced metals: copper/tungsten and copper/molybdenum. *Journal of the Mechanics and Physics of Solids*, 13(6):329–350, 1965.

[35] S. Y. Fu and B. Lauke. The elastic modulus of misaligned short-fiber-reinforced polymers. *Composites Science and Technology*, 58(3-4):389–400, 1998.

[36] B. Schultrich, W. Pompe, and H. J. Weiss. The influence of fibre discontinuities on the stress-strain behaviour of composites. *Fibre Science and Technology*, (11):1–18, 1978.

[37] V. K. Mohonee and K. L. Goh. Effects of fibre–fibre interaction on stress uptake in discontinuous fibre reinforced composites. *Composites Part B: Engineering*, 86:221–228, 2016.

[38] J. Henry and S. Pimenta. Semi-analytical simulation of aligned discontinuous composites. *Composites Science and Technology*, 144:230–244, 2017.

[39] S. Y. Fu, B. Lauke, and Y. W. Mai. *Science and engineering of short fibre-reinforced polymer composites*. Woodhead Publishing series in composites science and engineering. Woodhead Publishing, Duxford, England, 2nd edition, 2019.

[40] M. Schemme. Langfaserverstärkte Thermoplaste. *Kunstoffe*, 93(8):106–109, 2003.

[41] J. L. Thomason and M. A. Vlug. Thomason jl, vlug ma. influence of fibre length and concentration on the properties of glass fibre-reinforced polypropylene: 1. tensile and flexural. *Composites Part A: Applied Science and Manufacturing*, (27A):477–484, 1996.

[42] J. L. Thomason, M. A. Vlug, G. Schipper, and H. Krikor. Influence of fibre length and concentration on the properties of glass fibre-reinforced polypropylene: Part 3. strength and strain at failure. *Composites Part A: Applied Science and Manufacturing*, (27A):1075–1084, 1996.

[43] J. L. Thomason and Vlug M. A. Influence of fibre length and concentration on the properties of glass fibre-reinforced polypropylene: 4. impact properties. *Composites Part A: Applied Science and Manufacturing*, (28A):277–288, 1997.

[44] S. Fliegener. *Micromechanical finite element modeling of long fiber reinforced thermoplastics*. PhD thesis, Karlsruhe Institute of Technology, Karlsruhe, Germany, 2015.

[45] T. W. Chou. Microstructural design of fiber composites. *NASA STI/Recon Technical Report A*, 92:50452, 1992.

[46] Deutsches Institut für Normung e.V. DIN EN ISO 22314. Plastics — Glass-fibre-reinforced products — Determination of fibre length. Beuth Verlag GmbH, Berlin, Germany, May 2006.

[47] B. N. Nguyen, S. K. Bapanapalli, J. D. Holbery, M. T. Smith, V. Kunc, B. J. Frame, J. H. Phelps, and C. L. Tucker III. Fiber length and orientation in long-fiber injection-molded thermoplastics — Part I: Modeling of microstructure and elastic properties. *Journal of composite materials*, 42(10):1003–1029, 2008.

[48] Y. Masubuchi, M. Terada, A. Yamanaka, T. Yamamoto, and T. Ishikawa. Distribution function of fiber length in thermoplastic composites. *Composites Science and Technology*, 134:43–48, 2016.

[49] N. J. Lee and J. Jang. The effect of fibre-content gradient on the mechanical properties of glass-fibre-mat/polypropylene composites. *Composites Science and Technology*, 60(2):209–217, 2000.

[50] J. L. Thomason. The influence of fibre length and concentration on the properties of glass fibre reinforced polypropylene. 6. The properties of injection moulded long fibre PP at high fibre content. *Composites Part A: Applied Science and Manufacturing*, 36(7):995–1003, 2005.

[51] J. L. Thomason. The influence of fibre length and concentration on the properties of glass fibre reinforced polypropylene: 7. Interface strength and fibre strain in injection moulded long fibre PP at high fibre content. *Composites Part A: Applied Science and Manufacturing*, 38(1):210–216, 2007.

[52] J. G. Ahn, S. E. Kim, S. Ahn, K. Y. Kim, and H. Y. Yang. Investigation of fiber content and porosity effects on tensile strength in long-fiber-reinforced thermoplastics using artificial neural network. *Fibers and Polymers*, 24(4):1389–1400, 2023.

[53] A. Kelly and N. H. MacMillan. *Strong Solids*. Oxford Science Publications, Oxford, England, 3rd edition, 1986.

[54] C. L. Tucker III. *Fundamentals of fiber orientation: Description, measurement and prediction*. Carl Hanser Verlag GmbH & Co. KG, Munich, Germany, 2022.

[55] J. H. Phelps and C. L. Tucker III. An anisotropic rotary diffusion model for fiber orientation in short-and long-fiber thermoplastics. *Journal of Non-Newtonian Fluid Mechanics*, 156(3):165–176, 2009.

[56] S. G. Advani and C. L. Tucker III. The use of tensors to describe and predict fiber orientation in short fiber composites. *Journal of Rheology*, 31(8):751–784, 1987.

[57] M. Eik, J. Puttonen, and H. Herrmann. The effect of approximation accuracy of the orientation distribution function on the elastic properties of short fibre reinforced composites. *Composite Structures*, 148:12–18, 2016.

[58] J. K. Bauer and T. Böhlke. Variety of fiber orientation tensors. *Mathematics and Mechanics of Solids*, 27(7):1185–1211, 2022.

[59] C. Krauß, J. K. Bauer, J. Mitsch, T. Böhlke, and L. Kärger. On the averaging and closure of fiber orientation tensors in virtual process chains. *Journal of Elasticity*, 1–28, 2024.

[60] P. Pinter, S. Dietrich, B. Bertram, L. Kehrer, P. Elsner, and K. A. Weidenmann. Comparison and error estimation of 3d fibre orientation analysis of computed tomography image data for fibre reinforced composites. *NDT & E International*, 95:26–35, 2018.

[61] S. Mortazavian and A. Fatemi. Effects of fiber orientation and anisotropy on tensile strength and elastic modulus of short fiber reinforced polymer composites. *Composites Part B: Engineering*, 72:116–129, 2015.

[62] J. C. Halpin and S. W. Tsai. Environmental factors in composite materials design. *US Air Force Technical Report AFML TR*, 67423:749–767, 1967.

[63] J. C. Halpin and J. L. Kardos. The halpin-tsai equations: a review. *Polymer Engineering & Science*, 16(5):344–352, 1976.

[64] S. W. Tsai and H. T. Hahn. *Introduction to composite materials, technomic*. Technomic Publishing Company, Westport, United States of America, 1980.

[65] S. Y. Fu, G. Xu, and Y. W. Mai. On the elastic modulus of hybrid particle/short-fiber/polymer composites. *Composites Part B: Engineering*, 33(4):291–299, 2002.

[66] I. M. Daniel and O. Ishai. *Engineering mechanics of composite materials*. Oxford Univ. Press, New York, United States of America, 2nd edition, 2006.

[67] C. L. Tucker III and E. Liang. Stiffness predictions for unidirectional short-fiber composites: Review and evaluation. *Composites Science and Technology*, 59(5):655–671, 1999.

[68] Z. M. Huang, C. C. Zhang, and Y. D. Xue. Stiffness prediction of short fiber reinforced composites. *International Journal of Mechanical Sciences*, 161:105068, 2019.

[69] D. Zhou, X. Tong, H. Liu, S. Lv, T. S. Srivatsan, and X. Gao. A modified Halpin–Tsai model for predicting the elastic modulus of composite materials. *AIP Advances*, 14(1):015157, 2024.

[70] X. Yan, Y. Yang, and H. Hamada. Tensile properties of glass fiber reinforced polypropylene composite and its carbon fiber hybrid composite fabricated by direct fiber feeding injection molding process. *Polymer Composites*, 39(10):3564–3574, 2018.

[71] F. Garesci and S. Fliegener. Young's modulus prediction of long fiber reinforced thermoplastics. *Composites Science and Technology*, 85:142–147, 2013.

[72] Z. Maekawa, H. Hamada, and A. Yokoyama. Lamination theory of composite material with complex fiber orientation distribution. *Composite structures*, 5:701–714, 1989.

[73] C. Mittelstedt and W. Becker. *Strukturmechanik ebener Laminate*. Studienbereich Mechanik Technische Universität Darmstadt, Darmstadt, Germany, 1st edition, 2016.

[74] U. S. Koruche and S. F. Patil. Application of classical lamination theory and analytical modeling of laminates. *International Research Journal of Engineering and Technology*, 2(02):958, 2015.

[75] Y. Cc Ng. Deriving composite lamina properties from laminate properties using classical lamination theory and failure criteria. *Journal of composite materials*, 39(14):1295–1306, 2005.

[76] F. Ularych, M. Sova, J. Vokrouhlecḱy, and B. Turčić. Empirical relations of the mechanical properties of polyamide 6 reinforced with short glass fibers. *Polymer composites*, 14(3):229–237, 1993.

[77] S. Y. Fu, Y. W. Mai, B. Lauke, and C. Y. Yue. Synergistic effect on the fracture toughness of hybrid short glass fiber and short carbon fiber reinforced polypropylene composites. *Materials Science and Engineering: A*, 323(1-2):326–335, 2002.

[78] F. Lionetto, F. Montagna, D. Natali, F. De Pascalis, M. Nacucchi, F. Caretto, and A. Maffezzoli. Correlation between elastic properties and morphology in short fiber composites by x-ray computed microtomography. *Composites Part A: Applied Science and Manufacturing*, 140:106169, 2021.

[79] H. Ahmadi, M. Hajikazemi, E. Rashidinejad, Y. Sinchuk, and W. Van Paepegem. A hierarchical multi-scale analytical approach for predicting the elastic behavior of short fiber reinforced polymers under triaxial and flexural loading conditions. *Composites Science and Technology*, 225:109452, 2022.

[80] A. Trauth and K. A. Weidenmann. Continuous-discontinuous sheet moulding compounds – effect of hybridisation on mechanical material properties. *Composite Structures*, 202:1087–1098, 2018.

[81] K. P. Menard and N. Menard. *Dynamic mechanical analysis*. CRC press, Boca Raton, United States of America, 2nd. edition, 2020.

[82] J. D. Ferry. *Viscoelastic Properties of Polymers*. John Wiley & Sons, New York, United States of America, 1976.

[83] J. S. Vrentas, J. L. Duda, and W. J. Huang. Regions of fickian diffusion in polymer-solvent systems. *Macromolecules*, 19(6):1718–1724, 1986.

[84] N. G. McCrum, B. E. Read, and G. Williams. *Anelastic and dielectric effects in polymeric solids*. John Wiley, London, England, 1967.

[85] E. Parodi, L. E. Govaert, and G. W. M. Peters. Glass transition temperature versus structure of polyamide 6: A flash-dsc study. *Thermochimica Acta*, 657:110–122, 2017.

[86] J. Heijboer. Secondary loss peaks in glassy amorphous polymers. *International Journal of Polymeric Materials*, 6(1-2):11–37, 1977.

[87] ASTM International. ASTM E1640. Standard Test Method for Assignment of the Glass Transition Temperature By Dynamic Mechanical Analysis. ASTM Internationa, West Conshohocken, United States of America, August 2023.

[88] V. Sessner. *Charakterisierung und Modellierung des Dämpfungsverhaltens von hybriden Faser-Metall-Elastomer-Laminaten*. PhD thesis, Karlsruhe Institute of Technology, Karlsruhe, Germany, 2021.

[89] G. Schenkel. Verfahren zum Bestimmen der Poissonzahl insbesondere bei Kunststoffen. *Kunststoffe*, 63:49–53, 1973.

[90] J. Kunz. Die Querkontraktionszahl in der Konstruktionspraxis. *Kunststoff Extra*, 6:27–30, 2011.

[91] J. Dassow. *Messung und Beschreibung der Querkontraktionszahl von teilkristallinen Thermoplasten als nichtlinearer viskoelastischer Materialkennwert*. PhD thesis, Rheinisch-Westfälische Technische Hochschule Aachen, Aachen, Germany, 1996.

[92] B. Lewen. *Das nichtlinear viskoelastische Verhalten von Kunststoffen am Beispiel der Zeit-Temperatur-Verschiebung und der Querkontraktionszahl*. PhD thesis, Rheinisch-Westfälische Technische Hochschule Aachen, Aachen, Germany, 1991.

[93] V. Venoor, J. H. Park, D. O. Kazmer, and M. J. Sobkowicz. Understanding the effect of water in polyamides: A review. *Polymer Reviews*, 61(3):598–645, 2020.

[94] M. Arhant, P. Y. Le Gac, M. Le Gall, C. Burtin, C. Briançon, and P. Davies. Effect of sea water and humidity on the tensile and compressive properties of carbon-polyamide 6 laminates. *Composites Part A: Applied Science and Manufacturing*, 91:250–261, 2016.

[95] L. V. Pastukhov, M. J. W. Kanters, T. A. P. Engels, and L. E. Govaert. Influence of fiber orientation, temperature and relative humidity on the long–term performance of short glass fiber reinforced polyamide 6. *Journal of Applied Polymer Science*, 138(19):50382, 2021.

[96] R. Puffr and J. Sebenda. On the structure and properties of polyamides. XXVII. the mechanism of water sorption in polyamides. *Journal of polymer science: Part C*, (16):79–93, 1967.

[97] T. S. Ellis. Miscibility in blends of aliphatic polyamides and an aromatic polyamide, nylon 3me6t. *Polymer*, 29,:2015–2026, 1988,.

[98] H. Batzer and U. T. Kreibich. Influence of water on thermal transitions in natural polymers and synthetic polyamides. *Polymer Bulletin*, 5:585–590, 1981.

[99] L. T. Lim, I. J. Britt, and M. A. Tung. Sorption and transport of water vapor in nylon 6, 6 film. *Journal of applied polymer science*, 71(2):197–206, 1999.

[100] F. N. Kelley and F. Bueche. Viscosity and glass temperature relations for polymer-diluent systems. *Journal of Polymer Science*, 50(154):549–556, 1961.

[101] H. K. Reimschuessel. Relationships on the effect of water on glass transition temperature and young's modulus of nylon 6. *Journal of Polymer Science: Polymer Chemistry Edition*, 16(6):1229–1236, 1978.

[102] E. Picard, J. F. Gérard, and E. Espuche. Water transport properties of polyamide 6 based nanocomposites prepared by melt blending: On the importance of the clay dispersion state on the water transport properties at high water activity. *Journal of Membrane Science*, 313(1-2):284–295, 2008.

[103] L. Kehrer, J. Keursten, V. Hirschberg, and T. Böhlke. Dynamic mechanical analysis of pa 6 under hydrothermal influences and viscoelastic material modeling. *Journal of Thermoplastic Composite Materials*, 36(11):4630–4664, 2023.

[104] A. Fick. Über Diffusion. *Annalen der Physik*, 170(1):59–86, 1855.

[105] J. Crank. *The mathematics of diffusion*. Oxford university press, Oxford, United Kingdom, 1979.

[106] X. Fan. Mechanics of moisture for polymers: fundamental concepts and model study. In *EuroSimE 2008-International Conference on Thermal, Mechanical and Multi-Physics Simulation and Experiments in Microelectronics and Micro-Systems*. 1–14, IEEE, 2008.

[107] M. Arhant, P. Y. Le Gac, M. Le Gall, C. Burtin, C. Briançon, and P. Davies. Modelling the non fickian water absorption in polyamide 6. *Polymer Degradation and Stability*, 133:404–412, 2016.

[108] Y. Lei, L. Luo, Z. Kang, J. Zhang, and B. Zhang. Modified halpin–tsai equation for predicting interfacial effect in water diffusion process. *Science and Engineering of Composite Materials*, 28(1):180–189, 2021.

[109] L. Sang, Y. Wang, C. Wang, X. Peng, W. Hou, and L. Tong. Moisture diffusion and damage characteristics of carbon fabric reinforced polyamide 6 laminates under hydrothermal aging. *Composites Part A: Applied Science and Manufacturing*, 123:242–252, 2019.

[110] A. K. Sambale, M. Maisl, H. G. Herrmann, and M. Stommel. Characterisation and modelling of moisture gradients in polyamide 6. *Polymers*, 13(18):3141, 2021.

[111] P. Sharma, A. Sambale, M. Stommel, M. Maisl, H. G. Herrmann, and S. Diebels. Moisture transport in pa6 and its influence on the mechanical properties. *Continuum Mechanics and Thermodynamics*, 32(2):307–325, 2020.

[112] A. Launay, Y. Marco, M. H. Maitournam, and I. Raoult. Modelling the influence of temperature and relative humidity on the time-dependent mechanical behaviour of a short glass fibre reinforced polyamide. *Mechanics of Materials*, 56:1–10, 2013.

[113] N. Abacha, M. Kubouchi, and T. Sakai. Diffusion behavior of water in polyamide 6 organoclay nanocomposites. *Express Polymer Letters*, 3(4):245–255, 2009.

[114] J. C. Arnold, S. M. Alston, and F. Korkees. An assessment of methods to determine the directional moisture diffusion coefficients of composite materials. *Composites Part A: Applied Science and Manufacturing*, 55:120–128, 2013.

[115] I. Carrascal, J. A. Casado, J. A. Polanco, and F. Gutiérrez-Solana. Absorption and diffusion of humidity in fiberglass-reinforced polyamide. *Polymer Composites*, 26(5):580–586, 2005.

[116] Y. Lei, J. Zhang, T. Zhang, and H. Li. Water diffusion in carbon fiber reinforced polyamide 6 composites: Experimental, theoretical, and numerical approaches. *Journal of Reinforced Plastics and Composites*, 38(12):578–587, 2019.

[117] H. Piao, L. Chen, Y. Kiryu, I. Ohsawa, and J. Takahashi. Influence of water absorption and temperature on the mechanical properties of discontinuous carbon fiber reinforced polyamide 6. *Fibers and Polymers*, 20(3):611–619, 2019.

[118] A. Hassan, N. A. Rahman, and R. Yahya. Moisture absorption effect on thermal, dynamic mechanical and mechanical properties of injection-molded short glass-fiber/polyamide 6,6 composites. *Fibers and Polymers*, 13(7):899–906, 2012.

[119] J. Chaichanawong, C. Thongchuea, and S. Areerat. Effect of moisture on the mechanical properties of glass fiber reinforced polyamide composites. *Advanced Powder Technology*, 27(3):898–902, 2016.

[120] A. Launay, Y. Marco, M. H. Maitournam, and I. Raoult. Modelling the influence of temperature and relative humidity on the time-dependent mechanical behaviour of a short glass fibre reinforced polyamide. *Mechanics of Materials*, 56:1–10, 2013.

[121] M. Schemme. LFT – development status and perspectives. *Reinforced Plastics*, 52(1):32–39, 2008.

[122] H. Ning, N. Lu, A. A. Hassen, K. Chawla, M. Selim, and S. Pillay. A review of long fibre thermoplastic (LFT) composites. *International Materials Reviews*, 65(3):164–188, 2019.

[123] A. Hassan, R. Yahya, M. I. M. Rafiq, A. Hussin, M. R. K. Sheikh, and P. R. Hornsby. Interfacial shear strength and tensile properties of injection-molded, short- and long-glass fiber-reinforced polyamide 6,6 composites. *Journal of Reinforced Plastics and Composites*, 30(14):1233–1242, 2011.

[124] W. Krause, F. Henning, S. Tröster, O. Geiger, and P. Eyerer. LFT-D — a process technology for large scale production of fiber reinforced thermoplastic components. *Journal of Thermoplastic Composite Materials*, 16:289–302.

[125] F. Henning, H. Ernst, and R. Brüssel. LFTs for automotive applications. *Reinforced Plastics*, 49(2):24–33, 2005.

[126] C. Schelleis, B. M. Scheuring, W. V. Liebig, A. N. Hrymak, and F. Henning. Approaching polycarbonate as an LFT-D material: Processing and mechanical properties. *Polymers*, 15(9):2041, 2023.

[127] B. M. Scheuring, N. Christ, J. Blarr, W. V. Liebig, J. Montesano, and K. A. Weidenmann. Experimental and homogenized orientation-dependent properties of long mixed fiber-reinforced thermoplastic. *International journal of mechanical sciences*, Accepted for publication 2024.

[128] M. Selezneva and L. Lessard. Characterization of mechanical properties of randomly oriented strand thermoplastic composites. *Journal of Composite Materials*, 50(20):2833–2851, 2016.

[129] H. Wei, W. Nagatsuka, H. Lee, I. Ohsawa, K. Sumimoto, Y. Wan, and J. Takahashi. Mechanical properties of carbon fiber paper reinforced thermoplastics using mixed discontinuous recycled carbon fibers. *Advanced Composite Materials*, 27(1):19–34, 2018.

[130] J. U. Roh, D. J. Kwon, J. S. Guk, J. G. Kim, H. Y. Lee, and S. E. Park. Evaluation of mechanical properties and emi shielding effectiveness of long carbon fiber reinforced thermoplastic with different matrix. *Journal of Composite Materials*, 55(6):731–739, 2021.

[131] Y. Song, U. Gandhi, C. Pérez, T. Osswald, S. Vallury, and A. Yang. Method to account for the fiber orientation of the initial charge on the fiber orientation of finished part in compression molding simulation. *Composites Part A: Applied Science and Manufacturing*, 100:244–254, 2017.

[132] A. L. Isayev. *Injection and compression molding fundamentals*. CRC Press, Boca Ration, United States of America, 1987.

[133] C. Kuhn, I. Walter, O. Taeger, and T. Osswald. Experimental and numerical analysis of fiber matrix separation during compression molding of long fiber reinforced thermoplastics. *Journal of Composites Science*, 1(1):2, 2017.

[134] L. Harper and M. Clifford. *Design and manufacture of structural composites*. Woodhead publishing series in composites science and engineering. Woodhead Publishing, Oxford, England, 2023.

[135] E. Lafranche, P. Krawczak, J. P. Ciolczyk, and J. Maugey. Injection moulding of long glass fiber reinforced polyamide 66: Processing conditions/microstructure/flexural properties relationship. *Advances in Polymer Technology*, 24(2):114–131, 2005.

[136] R. S. Bay and C. L. Tucker. Fiber orientation in simple injection moldings. Part II: Experimental results. *Polymer Composites*, 13(4):332–341, 1992.

[137] B. N. Sharma, D. Naragani, B. N. Nguyen, C. L. Tucker, and M. D. Sangid. Uncertainty quantification of fiber orientation distribution measurements for long-fiber-reinforced thermoplastic composites. *Journal of Composite Materials*, 52(13):1781–1797, 2018.

[138] F. Willems, P. Reitinger, and C. Bonten. Calibration of Fiber Orientation Simulations for LFT -A New Approach. *Journal of Composites Science*, 4(4):163, 2020.

[139] S. Alwekar, P. Yeole, V. Kumar, A. A. Hassen, V. Kunc, and U. K. Vaidya. Melt extruded versus extrusion compression molded glass-polypropylene long fiber thermoplastic composites. *Composites Part A: Applied Science and Manufacturing*, 144:106349, 2021.

[140] S. A. Simon, A. Bechara Senior, and T. Osswald. Experimental validation of a direct fiber model for orientation prediction. *Journal of Composites Science*, 4(2):59, 2020.

[141] C. H. Park, W. I. Lee, Y. E. Yoo, and E. G. Kim. A study on fiber orientation in the compression molding of fiber reinforced polymer composite material. 111(1-3):223–239, 2001.

[142] J. W. Kim and D. G. Lee. Effect of fiber orientation and fiber contents on the tensile strength in fiber-reinforced composites. *Journal of nanoscience and nanotechnology*, 10(5):3650–3653, 2010.

[143] J. W. Kim and D. G. Lee. Study on the fiber orientation during compression molding of reinforced thermoplastic composites. *International Journal of Precision Engineering and Manufacturing-Green Technology*, 1(4):335–339, 2014.

[144] M. Bondy, P. Pinter, and W. Altenhof. Experimental characterization and modelling of the elastic properties of direct compounded compression molded carbon fibre/polyamide 6 long fibre thermoplastic. *Materials & Design*, 122:184–196, 2017.

[145] S. Tröster. *Materialentwicklung und –Charakterisierung für thermoplastische Faserverbundwerkstoffe im Direktverfahren*. PhD thesis, Universität Stuttgart, Stuttgart, Germany, 2003.

[146] A. Radtke. *Steifigkeitsberechnung von diskontinuierlich faserverstärkten Thermoplasten auf der Basis von Faserorientierungs- und Faserlängenverteilungen*. PhD thesis, Universität Stuttgart, Stuttgart, Germany, 2009.

[147] S. Fliegener. *Micromechanical finite element modeling of long fiber reinforced thermoplastics*. PhD thesis, Karlsruher Institut of Technology, Karlsruhe, Germany, 2015.

[148] H. Chen and D. Baird. Prediction of young's modulus for injection molded long fiber reinforced thermoplastics. *Journal of Composites Science*, 2(3):47, 2018.

[149] H. S. Perez, A. J. Román, A. Bechara Senior, and T. Osswald. Effect of fiber bundle morphology on fiber dispersion for long fiber-reinforced thermoplastics. *Polymers*, 15(13):2790, 2023.

[150] M. Bondy, W. Rodgers, and W. Altenhof. Tensile fatigue characterization of polyamide 66/carbon fiber direct/in-line compounded long fiber thermoplastic composites. *Composites Part B: Engineering*, 173:106984, 2019.

[151] N. Ranganathan, K. Oksman, S. K. Nayak, and M. Sain. Effect of long fiber thermoplastic extrusion process on fiber dispersion and mechanical properties of viscose fiber/polypropylene composites. *Polymers for Advanced Technologies*, 27(5):685–692, 2016.

[152] K. Rohan, T. J. McDonough, V. Ugresic, E. Potyra, and F. Henning. Mechanical study of direct long fiber thermoplastic carbon/polyamide 6 and its relations to processing parameters. In *Proceedings of the 14th Annual SPE Automotive Composites Conference & Exhibition*, 2015.

[153] W. Grellmann and B. Langer. *Deformation and Fracture Behaviour of Polymer Materials*, volume 247. Springer International Publishing, Cham, Switzerland, 2017.

[154] G. H. Michler and F. J. Baltá Calleja. *Nano- and micromechanics of polymers: Structure modification and improvement of properties*. Hanser Verlag, Munich, Germany, 2012.

[155] R. Talreja and C. V. Singh. *Damage and Failure of Composite Materials*. Cambridge University Press, Cambridge, England, 2012.

[156] N. Sato, T. Kurauchi, S. Sato, and O. Kamigaito. Microfailure behaviour of randomly dispersed short fibre reinforced thermoplastic composites obtained by direct sem observation. *Journal of Materials Science*, 26(14):3891–3898, 1991.

[157] J. J. Horst and J. L. Spoormaker. Fatigue fracture mechanisms and fractography of short-glassfibre-reinforced polyamide 6. *Journal of Materials Science*, (32):3641–3651, 1997.

[158] N. Sato, T. Kurauchi, S. Sato, and O. Kamigaito. Mechanism of fracture of short glass fibre-reinforced polyamide thermoplastic. *Journal of Materials Science*, (19):1145–1152, 1984.

[159] Y. Q. Li, S. S. Du, L. Y. Liu, F. Li, D. B. Liu, Z. K. Zhao, H. M. Xiao, N. Hu, and S. Y. Fu. Synergistic effects of short glass fiber/short carbon fiber hybrids on the mechanical properties of polyethersulfone composites. *Polymer Composites*, 40(S2):1725–1731, 2019.

[160] T. Pfefferkorn. From laminate to component. *Kunststoffe international*, 12:94–100, 2013.

[161] M. Kropka, M. Muehlbacher, T. Neumeyer, and V. Altstaedt. From ud-tape to final part – a comprehensive approach towards thermoplastic composites. *Procedia CIRP*, 66:96–100, 2017.

[162] AVK–Industrievereinigung Verstärkte Kunststoffe e. V. *Handbuch Faserverbundkunststoffe/Composites*. Springer Fachmedien Wiesbaden, Wiesbaden, Germany, 4th edition, 2014.

[163] M. Bartkowiak, W. V. Liebig, J. Montesano, and K. A. Weidenmann. Effects of hybridization on the tension–tension fatigue behavior of continuous-discontinuous fiber-reinforced sheet molding compound composites. *International Journal of Fatigue*, 161:106879, 2022.

[164] S. M. Lee. *Dictionary of composite materials technology*. CRC Press, Boca Raton, United States of America, 1995.

[165] M. F. Ashby and Y. J. M. Bréchet. Designing hybrid materials. *Acta materialia*, 51(19):5801–5821, 2003.

[166] G. Kickelbick. Hybrid materials-past, present and future. *Hybrid Materials*, 1:39–51, 2014.

[167] A. R. Bunsell and B. Harris. Hybrid carbon and glass fibre composites. *Composites*, 5(4):157–164, 1974.

[168] P. W. Manders, M. G. Bader. The strength of hybrid glass/carbon fibre composites. *Journal of Materials Science*, (16):2233–2245, 1981.

[169] G. Kretsis. A review of the tensile, compressive, flexural and shear properties of hybrid fibre-reinforced plastics. *Composites*, 18(1):13–23, 1987.

[170] Y. Swolfs, L. Gorbatikh, and I. Verpoest. Fibre hybridisation in polymer composites: A review. *Composites Part A: Applied Science and Manufacturing*, 67:181–200, 2014.

[171] J. Summerscales and D. Short. Carbon fibre and glass fibre hybrid reinforced plastics. *Composites*, 9(3):157–166, 1978.

[172] S. Y. Fu and B. Lauke. Hybrid effects on tensile properties of hybrid short-glass-fiber-and short-carbon-fiber-reinforced polypropylene composites. *Journal of Materials Science*, 36:1243–1251, 2001.

[173] S. Y. Fu, Y. W. Mai, B. Lauke, and C. Y. Yue. Synergistic effect on the fracture toughness of hybrid short glass fiber and short carbon fiber reinforced polypropylene composites. *Materials Science and Engineering: A*, 323(1-2):326–335, 2002.

[174] Y. Q. Li, S. S. Du, L. Y. Liu, F. Li, D. B. Liu, Z. K. Zhao, H. M. Xiao, N. Hu, and S. Y. Fu. Synergistic effects of short glass fiber/short carbon fiber hybrids on the mechanical properties of polyethersulfone composites. *Polymer Composites*, 40(S2):1725–1731, 2019.

[175] S. Alwekar, R. Ogle, S. Kim, and U. Vaidya. Manufacturing and characterization of continuous fiber-reinforced thermoplastic tape overmolded long fiber thermoplastic. *Composites Part B: Engineering*, 207:108597, 2021.

[176] N. Aliyeva, H. S. Sas, and B. Saner Okan. Recent developments on the overmolding process for the fabrication of thermoset and thermoplastic composites by the integration of nano/micron-scale reinforcements. *Composites Part A: Applied Science and Manufacturing*, 149:106525, 2021.

[177] T. Geminger and S. Jarka. Injection molding of multimaterial systems. In *Specialized injection molding techniques*. 165–210, 2016.

[178] R. Giusti and G. Lucchetta. Analysis of the welding strength in hybrid polypropylene composites as a function of the forming and overmolding parameters. *Polymer Engineering & Science*, 58(4):592–600, 2018.

[179] R. Akkerman, M. Bouwman, and S. Wijskamp. Analysis of the thermoplastic composite overmolding process: Interface strength. *Frontiers in Materials*, 7:27, 2020.

[180] K. Tanaka, Y. Kondo, and T. Katayama. Effect of mold temperature on interfacial welded strength and outer shell laminate strength of cf/pa6 composites manufactured by press and injection hybrid molding. In *High Performance and Optimum Design of Structures and Materials II*, 317–327, 2016.

[181] K. B. Thattaiparthasarathy, S. Pillay, D. Bansal, H. Ning, and U. K. Vaidya. Processing and characterization of continuous fibre tapes comoulded with long fibre reinforced thermoplastics. *Polymers and Polymer Composites*, 21(8):483–494, 2013.

[182] T. Link, S. Baumgärtner, D. Dörr, M. Hohberg, and F. Henning. Hybrid thermoplastic composites for automotive applications–development and manufacture of a lightweight rear floor structure in multi-material design. In *Proceedings of the 18th European Conference on Composite Materials*, 1–8, 2018.

[183] B. A. Behrens, F. Bohne, R. Lorenz, H. Arndt, S. Hübner, and M. Micke-Camuz. Numerical and experimental investigation of gmt compression

molding and fiber displacement of ud-tape inserts. *Procedia Manufacturing*, 47:11–16, 2020.

[184] Deutsches Institut für Normung e.V. Kunststoffe - Bestimmung der linearen Maße von Probekörpern (DIN EN ISO 16012:2015). Beuth Verlag GmbH, Berlin, Deutschland, February 2016.

[185] J. Blarr, P. Kunze, N. Kresin, W. V. Liebig, K. Inal, and K. A. Weidenmann. Novel thresholding method and convolutional neural network for fiber volume content determination from 3D μCT images. *NDT & E International*, 144:103067, 2024.

[186] A. Trauth. *Characterisation and Modelling of Continuous-Discontinuous Sheet Moulding Compound Composites for Structural Applications*. PhD thesis, Karlsruhe Institute of Technology, Karlsruhe, Germany, 2018.

[187] Deutsches Institut für Normung e.V. DIN EN ISO 527-4. Kunststoffe - Bestimmung der Zugeigenschaften - Teil 4: Prüfbedingungen für isotrop und anisotrop faserverstärkte Kunststoffverbundwerkstoffe. Beuth Verlag GmbH, Berlin, Germany, November 2023.

[188] Deutsches Institut für Normung e. V. DIN EN ISO 14125. Faserverstärkte Kunststoffe - Bestimmt der Biegeeigenschaften. Beuth Verlag GmbH, Berlin, Deutschland, May 2011.

[189] ZOLTEK. *Material data sheet PX35 Commercial Carbon Fiber*. ZOLTEK, Bridgeton, United States of America, 2018.

[190] Johns Manville. *Material data sheet StarRov ® 895 Direct Roving*. Johns Manville, Denver, United States of America, November, 2023.

[191] Rhodia Polyamide. *Material data sheet Technyl® polyamide range*. Rhodia, Saint-Fons, France, 2009.

[192] J. Müssig and H. Fischer. Fibreshape — über 15 Jahre Einsatz in Forschung, Lehre & Dienstleistung. In *Benutzertreffen Fibreshape 2017, Potsdam, Germany, 16.10.2017 – 17.10.2017*, 2017.

[193] L. A. Feldkamp, L. C. Davis, and J. W. Kress. Practical cone-beam algorithm. *Journal of the Optical Society of America A*, 1(6):612–619, 1984.

[194] D. Grauer, B. Hangs, M. Reif, A. Martsman, and S. T. Jespersen. Improving mechanical performance of automotive underbody shield with unidirectional tapes in compression-molded direct-long fiber thermoplastics (D-LFT). In *SAMPE journal*, Society for the Advancement of Material and Process Engineering, Diamond Bar, United States of America, 2012.

[195] ASTM International. ASTM D3039 Test Method for Tensile Properties of Polymer Matrix Composite Materials. ASTM International, West Conshohocken, United States of America, June 2014.

[196] ASTM International. ASTM E111-17 Standard Test Method for Young's Modulus, Tangent Modulus, and Chord Modulus. ASTM Internationa, West Conshohocken, United States of America, September 2017.

[197] Deutsches Institut für Normung e.V. DIN EN ISO 6721-1. Kunststoffe – Bestimmung dynamisch-mechanischer Eigenschaften – Teil 1: Allgemeine Grundlagen . Beuth Verlag GmbH, Berlin, Germany, September 2019.

[198] ASTM International. ASTM D4065-20 Standard Practice for Plastics: Dynamic Mechanical Properties: Determination and Report of Procedures. ASTM Internationa, West Conshohocken, United States of America, September 2020.

[199] A. Trauth, K. Kirchenbauer, and K. A. Weidenmann. Dynamic-mechanical-thermal analysis of hybrid continuous–discontinuous sheet molding compounds. *Composites Part C: Open Access*, 5:100148, 2021.

[200] B. N. Sharma, S. A. Kijewski, L. S. Fifield, Y. Shin, C. L. Tucker, and M. D. Sangid. Reliability in the characterization of fiber length distributions of injection molded long carbon fiber composites. *Polymer Composites*, 39(12):4594–4604, 2018.

[201] M. McLeod, É. Baril, J. F. Hétu, T. Deaville, and M. N. Bureau. Morphological and mechanical comparision of injection and compression moulding in-line compounding of direct long fibre thermoplastics. *Proceedings of the ACCE*, pages 109–118, 2010.

[202] Y. Kim and O. Park. Effect of fiber length on mechanical properties of injection molded long-fiber-reinforced thermoplastics. *Macromolecular Research*, 28:433–444, 2020.

[203] S. Y. Fu, B. Lauke, E. Mäder, X. Hu, and C. Y. Yue. Fracture resistance of short-glass-fiber-reinforced and short-carbon-fiber-reinforced polypropylene under charpy impact load and its dependence on processing. *Journal of Materials Processing Technology*, 89-90:501–507, 1999.

[204] L. Schreyer, J. Blarr, K. Höger, N. Meyer, and L. Kärger. Generation of initial fiber orientation states for long fiber reinforced thermoplastic compression molding simulation. In *Composites Meet Sustainability: Proceedings of the 20th European Conference on Composite Materials, ECCM20. 26.06.2022-30.06.2022, Lausanne, Switzerland. Bd.: 4*, 687, 2022.

[205] M. Bondy and W. Altenhof. Low velocity impact testing of direct/inline compounded carbon fibre/polyamide-6 long fibre thermoplastic. *International Journal of Impact Engineering*, 111:66–76, 2018.

[206] P. Mohammadkhani, J. Magliaro, F. Rahimidehgolan, T. Khapra, and W. Altenhof. Moisture influence on anisotropic mechanical behavior of direct compounded compression molded PA6/Glass LFTs. *Composites Part B: Engineering*, 264:110927, 2023.

[207] F. Truckenmüller and H. G. Fritz. Injection molding of long fiber-reinforced thermoplastics: A comparison of extruded and pultruded materials with direct addition of roving strands. *Polymer Engineering & Science*, 31(18):1316–1329, 1991.

[208] A. Tezvergil, L. V. J. Lassila, and P. K. Vallittu. The effect of fiber orientation on the thermal expansion coefficients of fiber-reinforced composites. *Dental Materials*, 19(6):471–477, 2003.

[209] N. Christ, B. M. Scheuring, J. Montesano, and J. Hohe. A python package for homogenization procedures in fiber reinforced polymers. *Journal of Open Source Software*, 8(87):5295, 2023.

[210] H. Luo, G. Xiong, C. Ma, D. Li, and Y. Wan. Preparation and performance of long carbon fiber reinforced polyamide 6 composites injection-molded from core/shell structured pellets. *Materials & Design*, 64:294–300, 2014.

[211] H. J. An, J. S. Kim, K. Y. Kim, D. Y. Lim, and D. H. Kim. Mechanical and thermal properties of long carbon fiber-reinforced polyamide 6 composites. *Fibers and Polymers*, 15(11):2355–2359, 2014.

[212] R. F. Eduljee, R. L. McCullough, and J. W. Gillespie. The influence of inclusion geometry on the elastic properties of discontinuous fiber composites. *Polymer Engineering & Science*, 34(4):352–360, 1994.

[213] S. Goris, T. Back, A. Yanev, D. Brands, Di. Drummer, and T. A. Osswald. A novel fiber length measurement technique for discontinuous fiber–reinforced composites: A comparative study with existing methods. *Polymer Composites*, 39(11):4058–4070, 2018.

[214] N. Mentges, H. Çelik, C. Hopmann, M. Fagerström, and S. M. Mirkhalaf. Micromechanical modelling of short fibre composites considering fibre length distributions. *Composites Part B: Engineering*, 264:110868, 2023.

[215] E. Wollan. Glass & carbon fiber reinforcement combine in hybrid long fiber thermoplastic composites to bridge price & performance gap. *Reinforced Plastics*, 61(1):55–57, 2017.

[216] T. Vu-Khanh and J. Denault. Fracture behaviour of long fibre reinforced thermoplastics. *Journal of Materials Science*, 29(21):5732–5738, 1994.

[217] M. Bartkowiak, M. Kizak, W. V. Liebig, and K. A. Weidenmann. Fatigue behavior of hybrid continuous-discontinuous fiber-reinforced sheet molding compound composites under application-related loading conditions. *Composites Part C: Open Access*, 8:100265, 2022.

[218] D. Chukov, S. Nematulloev, M. Zadorozhnyy, V. Tcherdyntsev, A. Stepashkin, and D. Zherebtsov. Structure, mechanical and thermal properties of polyphenylene sulfide and polysulfone impregnated carbon fiber composites. *Polymers*, 11(4):684, 2019.

[219] N. G. Karsli and A. Aytac. Tensile and thermomechanical properties of short carbon fiber reinforced polyamide 6 composites. *Composites Part B: Engineering*, 51:270–275, 2013.

[220] J. Liang, Y. Xu, Z. Wei, P. Song, G. Chen, and W. Zhang. Mechanical properties, crystallization and melting behaviors of carbon fiber-reinforced PA6 composites. *Journal of Thermal Analysis and Calorimetry*, 115(1):209–218, 2014.

[221] M. H. Liu, R. Li, G. Wang, Z. Y. Hou, and B. Huang. Morphology and dynamic mechanical properties of long glass fiber-reinforced polyamide 6 composites. *Journal of Thermal Analysis and Calorimetry*, 126(3):1281–1288, 2016.

[222] M. S. Vishkaei, M. A. M. Salleh, R. Yunus, D. R. A. Biak, F. Danafar, and F. Mirjalili. Effect of short carbon fiber surface treatment on composite properties. *Journal of Composite Materials*, 45(18):1885–1891, 2011.

[223] C. M. Stokes-Griffin, A. Kollmannsberger, P. Compston, and K. Drechsler. The effect of processing temperature on wedge peel strength of CF/PA 6 laminates manufactured in a laser tape placement process. *Composites Part A: Applied Science and Manufacturing*, 121:84–91, 2019.

[224] M. Nikforooz, J. Montesano, M. Golzar, and M. M. Shokrieh. Assessment of the thermomechanical performance of continuous glass fiber-reinforced thermoplastic laminates. *Polymer Testing*, 67:457–467, 2018.

[225] J. Wolfrum, G. W. Ehrenstein, and and M. A. Avondet. Dynamical mechanical thermo analysis of high performance composites-influences and problems. *Journal of Composite Materials*, 34(21):1788–1807, 2000.

[226] J. B. Jackson. The effect of absorbed water on the dynamic mechanical properties of some polyamides. *Polymer*, 10:159–165, 1969.

[227] P. Avakian, R. R. Matheson Jr, and H. W. Starkweather Jr. Implications of dielectric response for the mechanism of changes in oxygen transport due to traces of moisture in amorphous nylons. *Macromolecules*, 24(16):4698–4700, 1991.

[228] K. P. Pramoda and T. Liu. Effect of moisture on the dynamic mechanical relaxation of polyamide–6/clay nanocomposites. *Journal of Polymer Science Part B: Polymer Physics*, 42(10):1823–1830, 2004.

[229] J. F. Mano, R. L. Reis, and A. M. Cunha. Effects of moisture and degradation time over the mechanical dynamical performance of starch-based biomaterials. *Journal of Applied Polymer Science*, 78(13):2345–2357, 2000.

[230] R. P. Chartoff, J. D. Menczel, and S. H. Dillman. Dynamic mechanical analysis (DMA). In *Thermal analysis of polymers: fundamentals and applications*. 387–495, 2009.

[231] Y. Park, J. Ko, T. K. Ahn, and S. Choe. Moisture effects on the glass transition and the low temperature relaxations in semiaromatic polyamides. *Journal of Polymer Science Part B: Polymer Physics*, 35(5):807–815, 1997.

[232] Y. Lei, T. Zhang, J. Zhang, and B. Zhang. Dimensional stability and mechanical performance evolution of continuous carbon fiber reinforced polyamide 6 composites under hygrothermal environment. *Journal of materials research and technology*, 13:2126–2137, 2021.

[233] K. Tanaka, S. Mizuno, H. Honda, T. Katayama, and S. Enoki. Effect of water absorption on the mechanical properties of carbon fiber/polyamide

composites. *Journal of Solid Mechanics and Materials Engineering*, 7(5):520–529, 2013.

[234] B. Schmid. Spritzgießen von langfaserverstärkten thermoplasten. *Kunststoffe*, 79(7):624–630, 1989.

[235] G. A. Vincent, T. A. de Bruijn, S. Wijskamp, M. I. A. Rasheed, M. van Drongelen, and R. Akkerman. Characterisation and improvement of the quality of mixing of recycled thermoplastic composites. *Composites Part C: Open Access*, 4:100108, 2021.

[236] K. Rohan, T. J. McDonough, V. Ugresic, E. Potyra, and F. Henning. Mechanical study of direct long fiber thermoplastic carbon/polyamide 6 and its relations to processing parameters. In *Proc. 14th-Annual SPE Automotive Composites Conference & Exhibition*, 2015.

[237] W. Dong and P. Gijsman. Influence of temperature on the thermo-oxidative degradation of polyamide 6 films. *Polymer degradation and stability*, 95(6):1054–1062, 2010.

[238] M. N. Grigg. *Thermo-oxidative degradation of polyamide 6*. PhD thesis, Queensland University of Technology, Queensland, United States of America, 2006.

[239] W. I. Lee and G. S. Springer. Microwave curing of composites. *Journal of Composite Materials*, 18(4):387–409, 1984.

[240] Y. Li, X. Hang, N. Li, and X. Hao. A temperature distribution prediction model of carbon fiber reinforced composites during microwave cure. *Journal of Materials Processing Technology*, 230:280–287, 2016.

[241] Y. Li, N. Li, J. Zhou, and Q. Cheng. Microwave curing of multidirectional carbon fiber reinforced polymer composites. *Composite Structures*, 212:83–93, 2019.

[242] T. Kim, J. Lee, and K. H. Lee. Microwave heating of carbon-based solid materials. *Carbon letters*, 15(1):15–24, 2014.

[243] Y. Li, L. Cheng, and J. Zhou. Curing multidirectional carbon fiber reinforced polymer composites with indirect microwave heating. *The International Journal of Advanced Manufacturing Technology*, 97:1137–1147, 2018.

[244] K. Tanaka, N. Hosoo, T. Katayama, Y. Noguchi, and K. Izui. Effect of temperature on the fiber/matrix interfacial strength of carbon fiber reinforced polyamide model composites. *Mechanical Engineering Journal*, 3(6):16–00158, 2016.

List of Publications

Journal articles

[245] N. Afrasiabian, A. Elmoghazy, J. Blarr, B. Scheuring, A. Prahs, D. Schneider, W. V. Liebig, K. A. Weidenmann, C. Denniston, and B. Nestler. Crystallization and crystal morphology of polymers: A multiphase-field study. *Journal of Thermoplastic Composite Materials*, page 08927057241296472, 2024.

[209] N. Christ, B. M. Scheuring, J. Montesano, and J. Hohe. A python package for homogenization procedures in fiber reinforced polymers. *Journal of Open Source Software*, 8(87):5295, 2023.

[247] N. Christ, B. M. Scheuring, C. Schelleis, W. V. Liebig, J. Montesano, K. A. Weidenmann, and J. Hohe. Characterization and simulation of the interface between a continuous and discontinuous carbon fiber reinforced thermoplastic by using the climbing drum peel test considering humidity. *Polymers*, 16(7):976, 2024.

[248] F. Frölich, L. Bechtloff, B. M. Scheuring, A. L. Heuer, F. Wittemann, L. Kärger, and W. V. Liebig. Evaluation of mechanical properties characterization of additively manufactured components. *Progress in Additive Manufacturing*, pages 1–13, 2024.

[249] L. Kehrer, B. M. Scheuring, J. Blarr, and T. Böhlke. Hydrothermal behavior of pure PA 6 and homogenization of discontinuous long carbon fiber-reinforced PA 6. In *Proceedings in Applied Mathematics and Mechanics*, Accepted for publication, 2024.

[126] C. Schelleis, B. M. Scheuring, W. V. Liebig, A. N. Hrymak, and F. Henning. Approaching polycarbonate as an LFT-D material: Processing and mechanical properties. *Polymers*, 15(9):2041, 2023.

[127] B. M. Scheuring, N. Christ, J. Blarr, W. V. Liebig, J. Montesano, and K. A. Weidenmann. Experimental and homogenized orientation-dependent properties of long mixed fiber-reinforced thermoplastic. *International journal of mechanical sciences*, page 109470, 2024.

[252] A. Schwarz, T. Lichti, F. Wenz, B. M. Scheuring, C. Hübner, C. Eberl, and P. Elsner. Development of a scalable fabrication concept for sustainable, programmable shape-morphing metamaterials. *Advanced Engineering Materials*, 24(11):2200386, 2022.

Conference contributions

[253] N. Christ, B. M. Scheuring, J. Montesano, and J. Hohe. Characterization and simulation of the interface between continuously and dicontinuously fiber-reinforced theroplastics. *23rd International Conference on Composite Materials, Belfast, Northern Ireland, 31.07.2023–04.08.2023*, 2023.

[254] N. Christ, J. Hohe, J. Montesano, and B. M. Scheuring. Charakterisierung und Simulation der Grenzfläche zwischen kontinuierlich und diskontinuierlich faserverstärkten Thermoplasten . *24. Symposium Verbundwerkstoffe und Werkstoffverbunde, Freiburg im Brteisgau, 22.05.2024-24.05.2024*, 2024.

[255] F. Froelich, L. Bechtloff, B. M. Scheuring, A. L. Heuer, L. Kaerger, and W. V. Liebig. Development of a test-method for characterization of the orientation dependent material properties of fff structures. *23rd International Conference on Composite Materials, Belfast, Northern Ireland, 31.07.2023–04.08.2023*, 2023.

[256] S. Ilinzeer, M. Wilhelm, B. M. Scheuring, and F. Henning. Process development and characterization of a locally reinforced thermoplastic sheet molding compound. *SAMPE Europe Conference 2023 Madrid - Spain, 03.10.2023–05.10.2023*.

[257] C. Schelleis, B. M. Scheuring, A. Hrymak, and F. Henning. Study on mechanical characteristics of glass fiber-reinforced polycarbonate lft for codico structures. *23rd International Conference on Composite Materials, Belfast, Northern Ireland, 31.07.2023–04.08.2023*, 2023.

[258] C. Schelleis, B. M. Scheuring, F. Henning, and A. K. Hrymak. Polycarbonat im LFT-D Fließpressprozess: Erkenntnisse aus Material- und Prozessentwicklung . *24. Symposium Verbundwerkstoffe und Werkstoffverbunde, Freiburg im Breisgau, 22.05-24.05.2024*, 2024.

[259] B. M. Scheuring, J. Blarr, N. Christ, J. Hohe, W. Liebig, J. Montesano, and K Weidenmann. Experimentelle Untersuchung und Homogenisierung der richtungsabhängigen Zugeigenschaften von mono und mischfaser verstärktem LFT . *24. Symposium Verbundwerkstoffe und Werkstoffverbunde, Freiburg im Brteisgau, 22.05-24.05.2024*, 2024.

[260] B. M. Scheuring, H. Leo, W. V. Liebig, J. Montesano, and K. A. Weidenmann. Comparison of influence of hydrothermal aging on the mechanical properties glass and carbon long fiber-reinforced polyamide 6. *ECCM 2022 - Proceedings of the 20th European Conference on Composite Materials: Composites Meet Sustainability*, 3:1071–1078, Lausanne, Switzerland, 26.06.2022–30.06.2022, 2022.

[261] B.M. Scheuring, C. Schelleis, W.V. Liebig, J. Montesano, and K.A. Weidenmann. Effect of hybridization on the mechanical properties of continous-discontinous long fiber reinforced thermoplastics. *23rd International Conference on Composite Materials , Belfast, Northern Ireland, 31.07.2023–04.08.2023*, 2023.

[262] L. Schreyer, B.M. Scheuring, N. Christ, J. Blarr, C. Krauß, W.V. Liebig, K.A. Weidenmann, T. Böhlke, A. Hrymak, and L. Kärger. Continuous simulation of a continuous-discontinuous fiber-reinforced thermoplastic (codicofrtp) compression molding process. *23rd International Conference on Composite Materials, Belfast, Northern Ireland, 31.07.2023–04.08.2023*, 2023.